An Optimal Control Approach to Helicopter Noise and Emissions Abatement Terminal Procedures

An Optimal Control Approach to Helicopter Noise and Emissions Abatement Terminal Procedures

European Clean Helicopter Optimization Suite

Proefschrift

ter verkrijging van de graad van doctor
aan de Technische Universiteit Delft,
op gezag van Rector Magnificus Prof. Ir. K.C.A.M. Luyben,
voorzitter van het College voor Promoties,
in het openbaar te verdedigen
op woensdag 04 maart 2015 om 15:00 uur

door

Sander HARTJES
ingenieur in de Luchtvaart- en Ruimtevaarttechniek
geboren te Geldrop.

Dit proefschrift is goedgekeurd door de

promotor: Prof. Dr. R. Curran en
copromotor: Dr. Ir. H.G. Visser

Samenstelling promotiecommissie:

Rector Magnificus	voorzitter
Prof. Dr. R. Curran	Technische Universiteit Delft, promotor
Dr. Ir. H.G. Visser	Technische Universiteit Delft, copromotor

onafhankelijke leden:

Prof. Dr. Ir. S.P. Hoogendoorn	Technische Universiteit Delft
Prof. Dr. M. Gennaretti	Universita Roma Tre
Prof. Dr. M. Price	Queens University Belfast
Dr. M.D. Pavel	Technische Universiteit Delft
Dr. J-P. Clarke	Georgia Insititute of Technology

reservelid:

Prof. Dr. Ir. L.L.M. Veldhuis	Technische Universiteit Delft

ISBN 978-94-6295-100-6

Keywords: optimal control, helicopter, noise abatement, community noise impact

Published by Uitgeverij BOXPress, 's-Hertogenbosch.

Summary

Civil aviation plays an irreplaceable role in the current global civilization. Even though the 2008 economic crisis has limited growth in the western world, it can only be expected that due to continuing development in the Far East, South America and Africa this role will increase further over the years to come. Also in the field of helicopter operations continuous growth is predicted, mainly attributed to the growth of the private and corporate transport sectors.

To reduce and control the negative impacts of aviation – mainly noise nuisance and pollutant emissions – both in Europe and the United States major research efforts have been initiated with the main objective to provide step changes in the development of environmentally friendly or *green* aircraft. Although the larger part of the research effort has been focused on the development of new air vehicles, also the development of green operations is being researched, especially with a focus on noise abatement. Researchers have mainly focused on the development of noise abatement departure and arrival procedures for fixed-wing aircraft in an effort to reduce the noise impact in near-airport communities, with promising results. With the current fleet of helicopters the total noise nuisance caused by helicopter operations is significantly smaller than that of fixed-wing aircraft. However, due to their specific types of operations – often flying in close proximity to densely populated areas – individual operations can lead to unacceptable levels of nuisance, which require a specific approach in the development of noise abatement procedures. Therefore, in this research the *European Clean Helicopter Optimization (ECHO)* software suite has been developed which provides an efficient and sufficiently accurate means to numerically optimize site-specific helicopter approach trajectories, focusing specifically (but not exclusively) on noise mitigation in the surrounding communities.

To provide a step change in helicopter optimization frameworks, the *ECHO* suite has been developed with a strong emphasis on computational efficiency. For this purpose, an advanced optimization methodology based on optimal control theory has been selected. In this method, the infinite-dimensional optimal control problem is discretized, and the time, state and control variables at the discretization point are treated as the variables of a large-scale Non-Linear Programming (NLP) problem. The method – more specifically a direct solution method based on pseudospectral collocation using Radau quadrature – has been chosen as it offers the best trade-off between accuracy and computational efficiency for three main reasons. Firstly, the use of a direct solution method to solve the optimal control problem requires significantly less complex problem setups, and as such results in a more flexible and versatile optimization suite. In addition, the selected methodology allows for a relatively easy imposition of constraints on both the state and

control variables, and the use of collocation based on Gaussian quadrature reduces the overall problem size for a given level of accuracy. Finally, the specific use of Radau quadrature has been shown to provide good convergence behavior, specifically in open ended trajectory optimization problems such as considered in this study.

To model the free motion of a helicopter an eight Degrees-of-Freedom (DoF) helicopter flight dynamics model with quasi-steady inflow angles for both the main and tail rotor has been integrated in *ECHO*. The model ensures that the motion of the helicopter is simulated sufficiently accurate, and ensures that the required input parameters to determine the helicopter source noise are directly available. The model has been adapted to simulate operations in non-standard atmospheric conditions including stationary wind fields. In addition, a fuel and gaseous emissions model has been integrated in the flight dynamics model to determine the total fuel burn and total emission of nitrogen oxides based on the required engine power. This allows for the optimization of trajectories with respect to fuel and NO_x emissions. Although the model is a generic flight dynamics model, to test the capabilities of the suite a set of parameters representing a Messerschmitt-Bölkow-Blohm (MBB) Bo-105 has been used. These include a set of generic limits and constraints related to passenger comfort and the helicopter's flight envelope.

To allow assessment of and hence optimization with respect to the noise impact on the ground, the *ECHO* suite contains a helicopter noise model consisting of three main components. The first component determines the source noise levels emitted by the helicopter. To model this, a database of source noise levels for different frequencies and different flight conditions is available, projected on a hemisphere centered around the helicopter's main rotor hub. The database has been derived aeroacoustically based on the disc-tilt angles and the advance ratio following from the flight dynamics model. Source noise levels corresponding to the actual flight conditions encountered in the optimization process are found through interpolation between the hemispheres.

The second step in determining the noise exposure on the ground is the assessment of the propagation loss between source and receiver. An efficient model to determine the propagation loss was developed specifically for integration in the *ECHO* suite to comply with the continuity requirements following from the selected optimization methodology and to maintain relatively short execution times. The propagation model uses a geometrical approach to ray-tracing to determine the path of sound rays traveling from the source to the receiver. This approach allows for a significantly lower number of integration steps – and hence shorter runtimes – with sufficient accuracy for the atmospheric conditions considered in this research. The propagation model integrated in *ECHO* accounts for spreading loss, ground effect and atmospheric absorption, and includes a model to approximate the noise penetrating the shadow zone to ensure continuity in all observer locations and hence in the objective function.

The final component of the helicopter noise model determines the total noise impact on the ground in order to allow for the optimization of noise abatement trajectories. A number of generic and site-specific noise impact assessment criteria is available in *ECHO* to quantify the total noise impact in the area surrounding the trajectory.

To exemplify the capabilities of the *ECHO* suite a number of case studies with increasing complexity and different optimization criteria is presented. The first scenario, a relatively simple two-dimensional approach, shows that in order to minimize the noise Sound Exposure Level (SEL) footprint areas in general flight at low altitude and high airspeeds are preferred. Apart from the relatively low source noise levels at high airspeeds, also the total exposure time is reduced, reducing the SEL values. Furthermore, the presence of shadow zones and the dissipation of sound energy by the ground surface results in lower noise levels astride the helicopter's trajectory when flying at low altitudes. Consequently, SEL contours remain relatively narrow, and hence the generic noise footprint becomes smaller.

In the second case study a more complex three-dimensional trajectory is optimized in a densely populated area. In addition, for this scenario the site-specific awakenings criterion was used in the objective function, and different atmospheric and ground surface conditions were assessed. Similar to the conclusions drawn from the first scenario, again low altitude flight at high airspeeds reduce the SEL values on which the awakenings criterion is partly dependent. In addition, the use of a site-specific noise criterion and a three-dimensional flight path allows the helicopter not only to reduce the noise levels astride or below the trajectory, but also to avoid densely populated areas. In the cases where wind from different directions and different strengths were considered, it was found that even though the effect of wind on the total number of awakenings was significant, the effect on the relative improvements to be gained through optimization was small when compared to optimization in standard atmospheric conditions. The effect on the total number of awakenings can be attributed mainly to changes in ground speed on the one hand, and the positioning of the helicopter such that significant parts of the population are inside the shadow zone on the other. In cold atmospheric conditions the atmospheric absorption loss increases, resulting in a generally higher flight profile in order to increase the slant range between source and receiver. The opposite is true in case softer ground surfaces (such as e.g. snow) are modeled. The soft ground surface leads to an increased dissipation of sound energy on the ground, and hence to a larger lateral attenuation leading to a stronger preference for low altitude flight.

Finally, the third case study was set up to assess the effect of different site-specific noise optimization criteria on a complex three-dimensional arrival trajectory. The third scenario further supported the findings with respect to noise abatement found in the first two case studies, and additionally showed that the different site-specific criteria do not lead to significant changes in the helicopter trajectory when minimizing the total noise impact.

In addition to the main conclusions from the case studies regarding noise abatement, with respect to the efficiency of the *ECHO* suite – one of the main objectives of the software, the case studies have shown that the suite is capable of optimizing helicopter trajectories with a complex set of constraints imposed with relatively short runtimes, depending highly on the overall problem size and problem complexity.

From the development and the analysis of the capabilities of the *ECHO* suite it can be concluded that the objective of providing an efficient means to optimize helicopter trajectories with respect to different environmental and economic criteria has been met.

Although the objectives with respect to total problem runtimes were not met in all cases, further development of the suite has seen a further step change in the overall efficiency, showing the potential to indeed meet the challenging requirements.

Although the case studies have shown the potential of the suite, and *ECHO* meets the accuracy requirements to indeed prove to be a step change with respect to state of the art research, further improvements were identified. Especially the source noise model requires an expansion of the database to allow modeling of flight conditions other than steady forward level or descending flight at different airspeeds. This, in combination with the modeling of noise other than the main rotor would allow for a more accurate assessment of the noise impact for a wider range of flight conditions.

Furthermore, the capabilities of the *ECHO* suite should be assessed for different helicopter classes, and in more realistic case studies, better accounting for all operational constraints encountered in real-world operations.

Finally, although the *ECHO* suite has been developed specifically for the optimization of conventional helicopter trajectories, the flight dynamics, noise modeling and model integration in general could easily be adapted for the optimization of novel helicopter concepts or fixed-wing aircraft trajectories, further extending the research scope of the suite.

Samenvatting

De burgerluchtvaart speelt een onmisbare rol in de huidige globale maatschappij. Ondanks de crisis die in 2008 de economische groei in de westerse wereld beperkte zal de voortdurende groei in het Verre Oosten, Zuid-Amerika en Afrika deze rol waarschijnlijk verder doen groeien in de komende jaren. Ook op het gebied van helikopter operaties wordt een continue groei voorspeld. Dit is vooral toe te kennen aan de groei van de zakelijke markt.

Om de negatieve invloeden van de luchtvaart – vooral geluidsoverlast en vervuilende gassen – te beheersen en verminderen zijn zowel in Europa als in de Verenigde Staten onderzoeksprojecten opgestart om de ontwikkeling van milieuvriendelijke ofwel *groene* vliegtuigen te bevorderen. Ondanks dat het grootste deel van deze onderzoeken gericht is op het ontwikkelen van nieuwe typen vliegtuigen, wordt ook het ontwikkelen van nieuwe procedures onderzocht, met name om geluidsoverlast te verminderen. Onderzoeken hebben zich hierbij tot nu toe vooral gericht op het ontwikkelen van nieuwe start- en landingsprocedures voor vliegtuigen om de geluidsoverlast te verminderen in bevolkte gebieden nabij vliegvelden. De resultaten van deze onderzoeken zijn veelbelovend. In tegenstelling tot bij vliegtuigen is de totale geluidsoverlast door helikoptervluchten relatief klein. Echter, door het typische karakter van helikoptervluchten – vaak in en rondom binnensteden – is de overlast van individuele vluchten vaak juist groot. Dit vraagt om de ontwikkeling van nieuwe geluidsarme procedures specifiek gericht op helikopters. Het *European Clean Helicopter Optimization (ECHO)* pakket is dan ook speciaal ontwikkeld binnen dit onderzoek om als efficient en voldoende accuraat middel te kunnen fungeren om landingsprocedures van helikopters te optimaliseren, met name om de geluidsoverlast in omliggende bevolkte gebieden te verminderen.

Om een grote stap te maken in de ontwikkeling van optimalisatie software voor helikopters is het *ECHO* pakket ontwikkeld met een sterke nadruk op rekentijd. Om die reden is een geavanceerd optimalisatiealgorithme gekozen gebaseerd op *optimal control theorie*. Bij de gekozen methode wordt het originele continue probleem gediscretiseerd, en worden de tijds-, toestands- en stuurvariabelen op de discretisatiepunten beschouwd als variabelen van een groot Non-Linear Programming (NLP) probleem. De methode, die een *directe methode* op basis van pseudospectrale collocatie en Radau quadratuur genoemd wordt, is gekozen omdat deze het beste compromis biedt tussen nauwkeurigheid en rekentijd om de volgende drie redenen. Ten eerste is het initiëren van een probleem bij een directe methode eenvoudiger dan bij andere methodes, wat leidt tot een flexibeler en veelzijdiger optimalisatiepakket. Verder biedt de gekozen methode de mogelijkheid om relatief eenvoudig restricties op zowel de toestands- als de stuurvariabelen toe te

passen, terwijl het gebruik van een op Gaussiaanse quadatuur gebaseerde collocatie een relatief kleine probleemgrootte tot gevolg heeft voor een bepaalde nauwkeurigheid. Tenslotte is aangetoond dat het specifieke gebruik van Radau quadratuur leidt tot goed convergentiegedrag, voornamelijk in optimalisatieproblemen waarvan het eindpunt niet gedefiniëerd is, zoals in dit onderzoek gebruikelijk is.

Om de beweging van de helikopter te modelleren wordt gebruik gemaakt van een vliegdynamica model met acht vrijheidsgraden waarin de instroomhoeken van zowel de hoofd- als de staartrotor quasi-stationair gemodelleerd worden. Het model simuleert de vlucht van een helikopter voldoende nauwkeurig, en de parameters die nodig zijn om het geluid van de helikopter te bepalen zijn direct beschikbaar. Het model is aangepast om ook vluchten in niet-standaard atmosferische condities te kunnen simuleren, waaronder vluchten in stationaire windvelden. Verder zijn een brandstof- en een emissiemodel geïntegreerd in het vliegdynamica model om de totale brandstof en emissies van een vlucht te kunnen bepalen op basis van het benodigde motorvermogen. Ondanks dat het model een generiek vliegdynamica model is, worden in dit onderzoek de parameters van een Messerschmitt-Bölkow-Blohm (MBB) Bo-105 gebruikt. Hiertoe behoren ook generieke limieten en restricties om het comfort van de passagiers te garanderen en binnen de operationele limieten van de helikopter te blijven.

Het geluidsmodel dat geïntegreerd is in *ECHO* bestaat uit drie componenten. Het brongeluid wordt afgeleid uit een database met brongeluidssterktes voor verschillende frequenties en verschillende vliegcondities. De geluidssterktes zijn geprojecteerd op een halve bol gecentreerd in de naaf van de hoofdrotor. De database is aeroacoustisch bepaald gebaseerd op de hoek van de rotorschijf en de voorwaartse snelheid van de helikopter, die beiden direct afgeleid kunnen worden uit het vliegdynamica model. Om de brongeluidssterkte te bepalen die behoort bij de actuele vliegcondities wordt interpolatie toegepast tussen de hemisferen.

De tweede stap in het bepalen van de geluidsbelasting op de grond is het bepalen van de geluidsverzwakking tussen de bron en de ontvanger. Hiervoor is een efficiënt model ontwikkeld om te voldoen aan de continuïteitseisen van de optimalisatiemethode en om te garanderen dat de rekentijden relatief kort blijven. Het propagatiemodel is gebaseerd op een geometrische variant op ray-tracing om het pad van de geluidsgolven tussen de bron en de ontvanger te bepalen. Hierdoor is een kleiner aantal integratiestappen nodig, terwijl de resultaten voor het modelleren van de geluidsoverdracht in verschillende atmosferische condities voldoende nauwkeurig zijn. Het propagatiemodel berekent de geluidsverzwakking als gevolg van spreiding, grondeffect en atmosferische absorptie, en bevat ook een model om de geluidssterkte in de schaduwzone te schatten, zodat continuïteit in alle observatiepunten – en dus in de kostenfunctie – gewaarborgd is.

Tenslotte bevat *ECHO* een model om de totale geluidsbelasting op de grond te kwantificeren. Voor het optimaliseren van vliegbanen met betrekking tot geluid is er de keuze uit een aantal generieke en specifieke lokale criteria om de totale geluidsbelasting te bepalen.

Om de mogelijkheden van het *ECHO* pakket aan te tonen worden drie voorbeeldscenarios gepresenteerd met verschillende optimalisatiecriteria en verschillende maten van complexiteit. Het eerste scenario – een relatief eenvoudige twee-dimensionale aanvliegroute – toont aan dat om het contouroppervlak van een bepaalde geluidssterkte op de grond te verminderen over het algemeen relatief laag en met hoge snelheid gevlogen moet worden. Door laag te vliegen wordt weliswaar de geluidsbelasting direct onder het vliegpad hoger, maar het grondeffect en de aanwezigheid van schaduwzones zorgen voor een sterkere laterale geluidsverzwakking naast de vliegbaan, met als gevolg een smallere contour. Verder zorgt de hoge snelheid voor lagere brongeluidssterktes en een kortere belastingstijd, met lagere Sound Exposure Level (SEL) waarden tot gevolg.

In het tweede scenario wordt een uitgebreider drie-dimensionaal probleem geoptimaliseerd voor de lokale geluidsbelasting in een dichtbevolkt gebied. Hiervoor wordt het totaal aantal slaapverstoorden bepaald als gevolg van het overvliegen van de helikopter. Verder wordt de vlucht geoptimaliseerd in verschillende weersomstandigheden en met verschillende bodemtypes. Evenals bij het eerste scenario zorgt laag vliegen bij hoge snelheden voor lage SEL waarden, en daarmee ook voor een kleiner aantal slaapverstoorden. Verder geeft het modelleren van een drie-dimensionale vliegbaan ook de mogelijkheid om niet alleen de geluidsbelasting te verminderen, maar ook om dichtbevolkte gebieden te vermijden, met een verdere verlaging van de geluidsbelasting tot gevolg. In de gevallen waar verschillende windsnelheden en -richtingen gemodelleerd zijn blijkt dat, ondanks dat het absolute aantal slaapverstoorden toeneemt, de relatieve verbetering die te behalen is door optimalisatie vergelijkbaar blijft voor alle windcondities. Het totale aantal slaapverstoorden wordt daarbij vooral beïnvloed door de aanwezigheid van schaduwzones en de verandering van de grondsnelheid als gevolg van de wind. Bij koude weersomstandigheden neemt de atmosferische absorptie toe, met als gevolg dat over het algemeen een hoger vliegprofiel beter is om de afstand tussen bron en ontvanger te vergroten. Wanneer echter zachte bodemtypes (zoas bijvoorbeeld sneeuw) gemodelleerd worden, is het juist weer beter om laag te vliegen door de toenemende dissipatie van geluidsenergie, en de daaruit volgende verhoogde laterale geluidsverzwakking.

Tenslotte worden in het derde scenario verschillende lokale specifieke geluidscriteria bekeken aan de hand van een complex drie-dimensionaal probleem. Dit scenario bevestigt en versterkt de conclusies uit de eerdere scenarios met betrekking tot de vliegcondities die leiden tot een lagere geluidsbelasting op de grond. Verder blijkt dat het optimaliseren voor het aantal slaapverstoorden of het aantal mensen dat blootgesteld wordt aan een bepaalde geluidsbelasting niet leidt tot significant andere vliegbanen.

De voorbeeldscenarios hebben niet alleen aangetoond welke vliegcondities leiden tot lagere geluidsbelasting, maar hebben ook de efficiëntie van het *ECHO* pakket aangetoond voor verschillende probleemstellingen.

Er kan geconcludeerd worden dat het hoofddoel van het *ECHO* pakket – het ontwikkelen van een efficiënt pakket om vliegbanen van helikopters te optimaliseren – behaald is. Ondanks dat de vereisten met betrekking tot de totale rekentijden niet voor alle gepresenteerde scenarios behaald zijn, heeft verdere ontwikkeling van het pakket inmiddels al aangetoond dat dit doel alsnog behaald kan worden.

De voorbeeldscenarios hebben de mogelijkheden van het *ECHO* pakket aangetoond, maar er zijn ook mogelijkheden tot verdere ontwikkeling geïdentificeerd. Vooral het brongeluidsmodel zou uitgebreid kunnen worden om niet alleen stationaire vluchten te modelleren. Verder zouden ook andere geluidsbronnen – buiten de hoofdrotor – aan het model toegevoegd kunnen worden.

Verder zou het pakket uitgebreid kunnen worden met verschillende helikoptertypen, en zouden nog realistischere scenarios bekeken kunnen worden waarin beter rekening gehouden wordt met de limitaties die gelden bij daadwerkelijke helikopteroperaties.

Tenslotte kan nog opgemerkt worden dat ondanks dat het *ECHO* pakket specifiek ontwikkeld is voor conventionele helikopters, de vliegdynamica, geluidsmodellering en de integratie van modellen relatief eenvoudig aangepast kunnen worden om vliegbanen van nieuwe helikopterconcepten en vliegtuigen te optimaliseren, waarmee het onderzoeksgebied verder uitgebreid kan worden.

Contents

Summary **vii**

Samenvatting **xi**

List of Notations **xix**

Acronyms **xxvii**

List of Figures **xxxi**

List of Tables **xxxv**

1 Introduction **1**
1.1 Background 1
1.2 Previous Research 5
1.3 Research Objectives 7
1.4 Thesis Structure 8

2 European Clean Helicopter Optimization Suite **9**
2.1 Introduction 9
2.2 *ECHO* 9
2.2.1 *ECHO* Structure 9
2.2.2 Optimization Algorithm 10
2.2.3 Helicopter Flight Dynamics 11
2.2.4 Noise Modeling 12
2.3 Reflection on Methodology 14
2.4 Limitations 16

3 Optimization Methodology **17**
3.1 Introduction 17
3.2 Optimal Control Theory 17
3.2.1 General Problem Definition 17
3.2.2 First-Order Optimality Conditions 18
3.2.3 Solution Methods 20
3.3 Radau Pseudospectral Method 24
3.3.1 Radau Quadrature 24

3.3.2 Orthogonal Collocation . . . 25
3.3.3 Discretization of the Continuous Bolza Problem . . . 27
3.3.4 First-Order Optimality Conditions . . . 28
3.3.5 Multi-Phase Problem Definition . . . 29
3.4 NLP Solver . . . 30
3.5 Conclusions . . . 32

4 Helicopter Modeling **33**
4.1 Introduction . . . 33
4.2 Model Overview . . . 34
4.2.1 Modeling Assumptions . . . 34
4.2.2 Equations of Motion . . . 34
4.2.3 Component Forces . . . 38
4.2.4 Total Forces and Moments on the Helicopter . . . 44
4.2.5 Required Engine Power . . . 44
4.2.6 Effect of Wind . . . 45
4.2.7 Helicopter Parameters . . . 47
4.3 Control Damping . . . 50
4.4 Fuel and Emissions . . . 51
4.5 Limits and Constraints . . . 52
4.6 Conclusions . . . 54

5 Noise Modeling **55**
5.1 Introduction . . . 55
5.2 Source Noise Modeling . . . 56
5.2.1 Introduction . . . 56
5.2.2 Helicopter Noise Sources . . . 56
5.2.3 Aeroacoustic-Elastic Source Noise Modeling . . . 58
5.3 Noise Propagation . . . 62
5.3.1 Introduction . . . 62
5.3.2 Propagation of Sound in the Atmosphere . . . 63
5.3.3 Ray Path Construction . . . 64
5.3.4 Source Noise Levels . . . 68
5.3.5 Propagation Loss . . . 71
5.3.6 Propagation Model Validation . . . 81
5.4 Total Noise Levels . . . 81
5.4.1 Frequency Weighting . . . 81
5.4.2 Sound Exposure Level . . . 82
5.5 Noise Impact Assessment . . . 83
5.5.1 Introduction . . . 83
5.5.2 Contour Area . . . 84
5.5.3 Number of People Enclosed in Contour . . . 85
5.5.4 Expected Awakenings . . . 86
5.6 Conclusions . . . 87

6 Scenario 1: 2D Arrival **89**
6.1 Scenario Description . . . 89
6.2 Case 1: Single Phase . . . 91
6.2.1 Case Description . . . 91
6.2.2 Results . . . 91
6.3 Case 2: Two Phases . . . 96
6.3.1 Case Description . . . 96
6.3.2 Results . . . 97
6.4 Case 3: Alternate Glideslope Capture . . . 100
6.4.1 Case Description . . . 100
6.4.2 Results . . . 100
6.5 Conclusions . . . 101

7 Scenario 2: Rotterdam City Center **105**
7.1 Introduction . . . 105
7.2 Scenario Description . . . 106
7.3 Case 1: Headwind . . . 109
7.4 Case 2: Tailwind . . . 116
7.5 Case 3: Crosswind . . . 122
7.6 Case 4: Ground Surface . . . 123
7.7 Trajectory Analysis . . . 128
7.8 Conclusions . . . 132

8 Scenario 3: Amsterdam SNI **135**
8.1 Introduction . . . 135
8.2 Scenario Description . . . 136
8.3 Results . . . 139
8.3.1 Expected Number of Awakenings . . . 139
8.3.2 People Enclosed in the 65 dBA SEL Contour . . . 143
8.4 Conclusions . . . 147

9 Conclusions and Recommendations **149**
9.1 Conclusions . . . 149
9.1.1 Introduction . . . 149
9.1.2 *ECHO* Development . . . 149
9.1.3 *ECHO* Components . . . 150
9.1.4 Example scenarios . . . 151
9.2 Recommendations . . . 153

A Source Noise Model **155**
A.1 Microphone Locations . . . 155
A.2 Source Noise Levels . . . 155
A.3 Directivity Patterns . . . 156

B Propagation Model Validation **161**
B.1 Introduction 161
B.2 Case 1: International Standard Atmosphere 161
B.3 Case 2: ISA, 15 Knot Tailwind 162
B.4 Case 3: ISA, 15 Knot Headwind 163
B.5 Case 4: Cold atmosphere, soft ground surface 164

C Scenario 1 Results **171**

D Scenario 2 Results **173**

E Scenario 3 Results **177**

Acknowledgments **179**

About the author **181**

Publications **183**

List of Notations

A	Ray tube area	m^2
A	Sound source strength	$N{\cdot}m^{-1}$
$A_{>SEL_{thr}}$	Contour area above SEL_{thr}	m^2
$C_{T_{mr}}^{Gl}$	Main rotor thrust coefficient in Glauert theory	
$C_{T_{tr}}^{Gl}$	Tail rotor thrust coefficient in Glauert theory	
$C_{T_{mr}}^{elem}$	Main rotor thrust coefficient in blade-element theory	
$C_{T_{tr}}^{elem}$	Tail rotor thrust coefficient in blade-element theory	
C_d	Main rotor blade drag coefficient	
$C_{l_{\alpha_{fin}}}$	Vertical fin lift curve slope	rad^{-1}
$C_{l_{\alpha_{hs}}}$	Horizontal stabilizer lift curve slope	rad^{-1}
$C_{l_{\alpha_{mr}}}$	Main rotor blade lift curve slope	rad^{-1}
$C_{l_{\alpha_{tr}}}$	Tail rotor blade lift curve slope	rad^{-1}
EI_{NO_x}	NO_x emission index	$g{\cdot}kg^{-1}$
F_x	Force component along the body x-axis	N
F_y	Force component along the body y-axis	N
F_z	Force component along the body z-axis	N
F_0	Fuselage parasite drag area	m^2
GS_x	Ground speed component along the Earth-fixed x-axis	$m{\cdot}s^{-1}$
GS_y	Ground speed component along the Earth-fixed y-axis	$m{\cdot}s^{-1}$
H	Relative air humidity	%
I_x	Helicopter moment of inertia about the body x-axis	$kg{\cdot}m^2$
I_y	Helicopter moment of inertia about the body y-axis	$kg{\cdot}m^2$

I_z	Helicopter moment of inertia about the body z-axis	kg·m^2
I_{bl}	Main rotor blade moment of inertia	kg·m^3
J	Cost functional	
J_a	Augmented cost functional	
J_{xz}	Helicopter product of inertia about the body x- and z-axis	kg·m^2
K_e	Maximum power ratio, all engines operating	
K_{fus}	Fuselage pitch coefficient correction factor	
L	Helicopter total roll moment	N·m
L_e	Blade hinge eccentricity moment about the body x-axis	N·m
L_{AE}	Sound Exposure Level	dBA
L_{fin}	Vertical fin moment about the body x-axis	N·m
L_{mr}	Total main rotor moment about the body x-axis	N·m
L_{tr}	Total tail rotor moment about the body x-axis	N·m
$\mathcal{L}$	Lagrange cost contribution	
M	Helicopter total pitch moment	N·m
M_e	Blade hinge eccentricity moment about the body y-axis	N·m
M_{fus}	Fuselage moment about the body y-axis	N·m
M_{hs}	Horizontal stabilizer moment about the body y-axis	N·m
M_{mr}	Total main rotor moment about the body y-axis	N·m
M_{tr}	Tail rotor figure of merit	
N	Helicopter total yaw moment	N·m
N_A	Number of expected awakenings due to a single nighttime movement	
N_e	Number of engines	
N_{fin}	Vertical fin moment about the body z-axis	N·m
N_{mr}	Total main rotor moment about the body z-axis	N·m
N_m	Number of main rotor blades	
N_{tr}	Total tail rotor moment about the body z-axis	N·m
N_t	Number of tail rotor blades	

P_a	Available engine power	W
P_c	Climb power	W
P_e	Available power per engine	W
$P_{>SEL_{thr}}$	Population above SEL_{thr}	
P_{ind}	Induced drag power	W
P_{par}	Parasite drag power	W
P_{ppd}	Profile drag power	W
P_{req}	Required engine power	W
P_{tr}	Tail rotor power	W
Q	Reflection factor	
R	Main rotor radius	m
R	Sound ray radius of curvature	m
R	Specific gas constant for air	$\mathrm{J\cdot kg^{-1}\cdot K^{-1}}$
R	Turn radius	m
R_{fus}	Fuselage parasite drag force	N
R_{tr}	Tail rotor radius	m
S_{fin}	Vertical fin surface area	$\mathrm{m^2}$
S_{hs}	Horizontal stabilizer surface area	$\mathrm{m^2}$
T	Temperature	K
T_{mr}	Main rotor thrust force	N
T_{tr}	Tail rotor thrust force	N
V	True airspeed	$\mathrm{m\cdot s^{-1}}$
V_w	Total wind velocity	$\mathrm{m\cdot s^{-1}}$
V_{fin}	Vertical fin total airspeed	$\mathrm{m\cdot s^{-1}}$
V_{hs}	Horizontal stabilizer total airspeed	$\mathrm{m\cdot s^{-1}}$
V_{w_x}	Wind velocity component along inertial x-axis	$\mathrm{m\cdot s^{-1}}$
V_{w_y}	Wind velocity component along inertial y-axis	$\mathrm{m\cdot s^{-1}}$
Vol_{fus}	Fuselage equivalent volume	$\mathrm{m^3}$

W	Helicopter weight	kg
X_{fus}	Fuselage forces along the body x-axis	N
X_{mr}	Main rotor forces along the body x-axis	N
Y_{fin}	Vertical fin forces along the body y-axis	N
Y_{mr}	Main rotor forces along the body y-axis	N
Y_{tr}	Tail rotor forces along the body y-axis	N
Z_g	Surface impedance	kg·s^{-1}·m^{-2}
Z_n	Normal surface impedance	kg·s^{-1}·m^{-2}
Z_{fus}	Fuselage forces along the body z-axis	N
Z_{hs}	Horizontal stabilizer forces along the body z-axis	N
Z_{mr}	Main rotor forces along the body z-axis	N
a_0	Coning angle	rad
a_1	Longitudinal tilt of the rotor disc plane w.r.t. the control plane	rad
a_n	Area of grid cell n	m^2
b_1	Lateral tilt of the rotor disc plane w.r.t. the control plane	rad
c	Main rotor blade chord length	m
c	Speed of sound	m·s^{-1}
e	Normalized flapping hinge offset	
f	Frequency	s^{-1}
f_{tr}	Tail rotor fin blockage factor	
g	Gravitational acceleration	m·s^{-2}
g_{tr}	Tail rotor gearing ratio	
k	Non-uniform induced velocity correction factor	
k	Wave number	rad·m^{-1}
$k_{1_{tr}}$	Main rotor downwash factor at tail rotor	
l	Segment length	m
$\dot{m}_f$	Fuel mass flow	kg·s^{-1}
$\dot{m}_{NO_x}$	Emission rate for NO_x	g·s^{-1}

m	Helicopter mass	kg
m_f	Total fuel burn	kg
m_{NO_x}	Total $\mathrm{NO_x}$ emission	g
m_{mr}	Main rotor mass	kg
n	Profile drag velocity correction factor	
p	Helicopter roll rate	rad·s^{-1}
p	Loudness level	phon
p	Sound pressure	N·m^{-2}
p_n	Population in grid cell n	
q	Helicopter pitch rate	rad·s^{-1}
r	Helicopter yaw rate	rad·s^{-1}
s	Sound ray path length	m
t	Time	s
t_0	Initial time	s
t_f	Final time	s
u	Helicopter airspeed component along the body x-axis	m·s^{-1}
u_w	Wind velocity component along the body x-axis	m·s^{-1}
u_{1-4}	Helicopter control rates	rad·s^{-1}
v	Helicopter airspeed component along the body y-axis	m·s^{-1}
v_i	Main rotor induced velocity	m·s^{-1}
v_w	Wind velocity component along the body y-axis	m·s^{-1}
v_x	Helicopter airspeed along the inertial x-axis	m·s^{-1}
v_y	Helicopter airspeed along the inertial y-axis	m·s^{-1}
v_z	Helicopter airspeed along the inertial z-axis	m·s^{-1}
w	Helicopter airspeed component along the body z-axis	m·s^{-1}
w_w	Wind velocity component along the body z-axis	m·s^{-1}
x	Helicopter x-position in inertial system	m
x	Horizontal distance traveled by sound ray	m

x_{fin}	Vertical fin offset in the body x-axis	m
x_{hs}	Horizontal stabilizer offset in the body x-axis	m
x_{mr}	Main rotor offset in the body x-axis	m
x_{tr}	Tail rotor offset in the body x-axis	m
y	Helicopter y-position in inertial system	m
z	Helicopter z-position in inertial system	m
z_0	Roughness length	m
z_r	Sound receiver height	m
z_s	Sound source height	m
z_w	Height for wind speed definition	m
z_{fin}	Vertical fin offset in the body z-axis	m
z_{mr}	Main rotor offset in the body z-axis	m
z_{tr}	Tail rotor offset in the body z-axis	m
ΔSPL_A	Atmospheric attenuation loss	dB
ΔSPL_G	Ground effect	dB
ΔSPL_S	Spreading loss	dB
ΔSPL_{AW}	Frequency A-weighting filter	dBA
ΔSPL_{sz}	Shadow zone loss correction	dB
Θ	Helicopter pitch angle	rad
Φ	Mayer cost contribution	
Φ	Helicopter roll angle	rad
Ψ	Helicopter yaw angle	rad
Ω	Main rotor angular velocity	rad$\cdot$s^{-1}
Ω_{tr}	Tail rotor angular velocity	rad$\cdot$s^{-1}
α	Atmospheric attenuation coefficient	0.01 dB$\cdot$m^{-1}
α_r	Shaft plane angle of attack	rad
$\alpha_{0_{hs}}$	Horizontal stabilizer angle of incidence	rad
α_{fus}	Fuselage angle of attack	rad

α_{hs}	Horizontal stabilizer angle of attack	rad
$\beta_{0_{fin}}$	Vertical fin angle of incidence	rad
β_{fin}	Vertical fin angle of attack	rad
γ	Adiabatic index of air	
γ	Lock number	$\mathrm{m}^2 \cdot \mathrm{rad}$
γ_a	Aerodynamic flight path angle	rad
γ_g	Geometric flight path angle	rad
γ_s	Main rotor forward shaft tilt	rad
γ_{GS}	Glideslope angle	rad
δ_0	Main rotor blade zero-lift drag coefficient	
δ_2	Main rotor blade lift-induced drag coefficient	
ϵ_β	Flapping hinge offset	m
η	Humidity lapse rate	m^{-1}
η_m	Engine mechanical efficiency	
θ	Angle of incidence	rad
θ_0	Blade collective pitch	rad
θ_0	Launch angle	rad
θ_f	Final angle of incidence	rad
$\theta_{0_{tr}}$	Tail rotor collective pitch	rad
θ_{1c}	Lateral cyclic pitch	rad
θ_{1s}	Longitudinal cyclic pitch	rad
θ_{tw}	Main rotor blade twist angle	rad
λ	Azimuth angle	rad
λ	Temperature lapse rate	$\mathrm{K} \cdot \mathrm{m}^{-1}$
$\lambda_{i_{mr}}$	Non-dimensional uniform induced downwash of the main rotor	
$\lambda_{i_{tr}}$	Non-dimensional uniform induced downwash of the tail rotor	
μ_x	Main rotor normalized airspeed along the body x-axis	
μ_z	Main rotor normalized airspeed along the body z-axis	

$\mu_{x_{tr}}$	Tail rotor normalized airspeed along the body x-axis	
$\mu_{z_{tr}}$	Tail rotor normalized airspeed along the body z-axis	
ν_2	Main rotor flap frequency ratio	
ρ	Local air density	kg$\cdot$ m^{-3}
σ	Effective flow resistivity	N$\cdot$s$\cdot$m^{-4}
σ_{mr}	Main rotor disc solidity	
σ_{tr}	Tail rotor disc solidity	
τ	Normalized time	
$\tau_{\lambda_{i_{mr}}}$	Main rotor time constant of response	
$\tau_{\lambda_{i_{tr}}}$	Tail rotor time constant of response	
υ	Control damping weighting factor	
ϕ	Elevation angle	rad
ϕ	Phase change	rad
ω	Angular frequency, $\omega = 2\pi f$	rad$\cdot$s^{-1}

Acronyms

ACARE	Advisory Council on Aviation Research and Innovation in Europe.
AD	Automatic Differentiation.
AGL	Above Ground Level.
AHE	Above Helipad Elevation.
AMS	Amsterdam Airport Schiphol.
BEM	Boundary Element Method.
BERP	British Experimental Rotor Programme.
BET	Blade Element Theory.
BPF	Blade Passage Frequency.
BVI	Blade-Vortex Interaction.
CBS	Centraal Bureau voor de Statistiek (Statistics Netherlands).
DAR	Design of Aircraft and Rotorcraft.
DoF	Degrees-of-Freedom.
ECHO	European Clean Helicopter Optimization.
EMC	Erasmus Medical Center.
EMS	Emergency Medical Services.
FFP	Fast Field Programme.
FICAN	Federal Interagency Committee on Aviation Noise.
FOCA	Federal Office of Civil Aviation.
GA	Genetic Algorithm.
GDP	Gross Domestic Product.
GIS	Geographic Information System.
GPOPS	General Pseudospectral OPtimal control Software.
GRC	Green Rotorcraft.

HBVP	Hamiltonian Boundary-Value Problem.
HSI	High-Speed Impulsive.
INM	Integrated Noise Model.
ISA	International Standard Atmosphere.
ITD	Integrated Technology Demonstrator.
JTI	Joint Technology Initiative.
LDP	Landing Decision Point.
LG	Legendre-Gauss.
LGL	Legendre-Gauss-Lobatto.
LGR	Legendre-Gauss-Radau.
MBB	Messerschmitt-Bölkow-Blohm.
NLP	Non-Linear Programming.
OEI	One Engine Inoperative.
PE	Parabolic Equation.
QP	Quadratic Programming.
REACH	Registration, Evaluation, Authorisation and Restriction of CHemical substances.
RPM	Radau Pseudospectral Method.
SAMA	Surrogate-Assisted Memetic Algorithm.
SEL	Sound Exposure Level.
SFC	Specific Fuel Consumption.
SGO	Systems for Green Operations.
SHP	Shaft Horsepower.
SNI	Simultaneous Non-Interfering.
SNOPT	Sparse Nonlinear OPTimizer.
SOCS	Sparse Optimal Control Software.
SPL	Sound Pressure Level.
SQP	Sequential Quadratic Programming.
TAS	True Airspeed.

List of Figures

1.1 BERP rotor blade . . . 3
1.2 Blue Edge^{TM}rotor blade . . . 3
1.3 Fenestron tail, Eurocopter EC-135 . . . 3
1.4 NOTAR System, MD Explorer . . . 3
1.5 Green Rotorcraft ITD goals (adapted from [1]) . . . 5

2.1 *ECHO* Suite structure . . . 10
2.2 *ECHO* Suite flight dynamics . . . 12
2.3 *ECHO* Suite final structure . . . 14

3.1 Selection process of the optimization method . . . 22
3.2 Lagrange interpolating polynomial . . . 26
3.3 Potential phase connections . . . 30

4.1 Helicopter forces and moments: side view . . . 35
4.2 Helicopter forces and moments: top view . . . 35
4.3 Helicopter forces and moments: rear view . . . 36
4.4 Definition of helicopter position with respect to a fixed system . . . 36
4.5 Dutch National Police Messerschmitt-Bölkow-Blohm Bo-105 . . . 49
4.6 Control damping . . . 51
4.7 Bo-105 Height-velocity diagram, 2300 kg [57] . . . 54

5.1 Main rotor directivity . . . 57
5.2 Main and tail rotor noise contribution [60] . . . 58
5.3 Main rotor flow conditions . . . 59
5.4 Far- and near-wake decomposition [64] . . . 60
5.5 Noise prediction tool methodology (adapted from [73]) . . . 60
5.6 Helicopter noise hemisphere example . . . 61
5.7 Refraction: a) Negative temperature gradient, b) Positive temperature gradient, c) Wind . . . 64
5.8 Refracted ray path . . . 65
5.9 Ray path integration . . . 65
5.10 Layered speed of sound approximation . . . 67
5.11 Refraction in a linear speed of sound profile . . . 67
5.12 Refraction in a linear speed of sound profile . . . 69
5.13 Azimuth angle geometry . . . 71

5.14 Spherical spreading 72
5.15 Ray tubes in a refracting and non-refracting medium 72
5.16 Ground reflection geometry 75
5.17 Reflection and refraction on a ground surface 77
5.18 Illuminated and shadow zones 79
5.19 Equal loudness contours [89] 82
5.20 Frequency weighting filters 82
5.21 Sound Exposure Level 83
5.22 Sound level in grid cells 85
5.23 Step approximation 85
5.24 Population density, Rotterdam area 86
5.25 FICAN Dose-response relationship (adapted from [92]) 87

6.1 Field landing profile (adapted from [57]) 90
6.2 Altitude and speed profiles, single objective 92
6.3 Altitude and speed profiles, fuel and noise optimized 93
6.4 Sideline noise levels 94
6.5 SEL contours, fuel and noise optimized 95
6.6 Flight path angle, fuel and noise optimized 96
6.7 Altitude and speed profiles, single objective 98
6.8 Altitude and speed profiles, fuel and noise optimized 99
6.9 Altitude and speed profiles, single objective 101
6.10 Altitude and speed profiles, fuel and noise optimized 102

7.1 Rotterdam area (©Google) 106
7.2 Population density (CBS) 106
7.3 Scenario 2 overview (©Google) 107
7.4 EMC Helipad (©Google) 107
7.5 Vertical landing profile (adapted from [57]) 108
7.6 Ground tracks, no wind 111
7.7 Altitude and airspeed profiles, no wind 111
7.8 Flight path angle in phase 1, no wind 112
7.9 50.5 dBA SEL Contours, case C01_01 and C01_16 115
7.10 Δ% Awakenings, C01_16 - C01_01 115
7.11 Flight time vs. awakenings, increasing headwind 116
7.12 Ground tracks, increasing tailwind 117
7.13 Altitude and ground speed profiles, increasing tailwind 118
7.14 Turn to final approach heading, case C02_01 and C02_16 119
7.15 Descent phase, case C02_01 and C02_16 119
7.16 Altitude and ground speed profiles, solutions C02_02, C02_07, C02_12 and C02_17 121
7.17 Flight time vs. awakenings, increasing tailwind 121
7.18 Ground tracks, increasing crosswind 123
7.19 50.5 dBA SEL Contours 124
7.20 Absorption and ground effect, 282.67 Hz, $z_s = 500$ m 125

7.21 50.5 and 65 dBA SEL Contours, solutions C04_05 and C04_06 126
7.22 Altitude profiles, varying ground surface and atmospheric conditions . . . 127
7.23 Altitude profiles, varying ground surface and atmospheric conditions . . . 128
7.24 3D-view of case C01_01 129
7.25 Airspeed 129
7.26 Helicopter body angles 130
7.27 Helicopter body angular rates 130
7.28 Control inputs 131

8.1 Scenario 3 overview 138
8.2 Ground tracks, optimized for time and awakenings 141
8.3 Altitude and airspeed profiles, optimized for time and awakenings 141
8.4 ΔSEL, C01_03 - C01_01 142
8.5 ΔSEL, C01_06 - C01_03 143
8.6 Ground tracks, optimized for time and people enclosed 144
8.7 65 dBA SEL contours, optimized for time and people enclosed 145
8.8 Altitude and airspeed profiles, optimized for time (left) and people enclosed (right) 146

A.1 Source noise model microphone locations 156
A.2 Hemispherical database, Overall Sound Pressure Levels 157
A.3 Source noise directivity patterns, $V = 100$ kts, $\gamma = 0°$ 158
A.4 Source noise directivity patterns, $V = 30$ kts, $\gamma = 0°$ 159

B.1 Speed of sound profiles 162
B.2 Case 1, z_s = 1,000 m, Ray-tracing (solid), *ECHO* (dotted) 165
B.3 Case 1, z_s = 500 m, Ray-tracing (solid), *ECHO* (dotted) 166
B.4 Case 1, z_s = 100 m, Ray-tracing (solid), *ECHO* (dotted) 167
B.5 Case 2, z_s = 500 m, Ray-tracing (solid), *ECHO* (dotted) 168
B.6 Case 3, z_s = 500 m, Ray-tracing (solid), *ECHO* (dotted) 169
B.7 Case 4, z_s = 500 m, Ray-tracing (solid), *ECHO* (dotted) 170

List of Tables

4.1 MBB Bo-105 parameters 48
4.2 General path constraints 53

5.1 Determination of $\eta(\delta)$ 78

6.1 Boundary conditions for Scenario 1 90
6.2 Scenario 1, Case 1 results: single objective 91
6.3 Scenario 1, Case 1 results: fuel and noise optimized 92
6.4 Additional constraints for Scenario 1, Case 2 97
6.5 Scenario 1, Case 2 results: single objective 98
6.6 Scenario 1, Case 2 results: fuel and noise optimized 99
6.7 Scenario 1, Case 3 results: single objective 100
6.8 Scenario 1, Case 3 results: fuel and noise optimized 101

7.1 Additional constrains for Case 2 109
7.2 Scenario 2, Case 1 results: no wind 110
7.3 Scenario 2, Case 1 results: increasing headwind 113
7.4 Scenario 2, Case 2 results: increasing tailwind 117
7.5 Scenario 2, Case 2 results: $k_{noise} = 0.02$ 120
7.6 Scenario 2, Case 3 results: increasing crosswind 122
7.7 Scenario 2, Case 4 results: varying ground surface and atmospheric conditions 125
7.8 Scenario 2, Case 4 results: ISA with hard ground surface 127

8.1 Constraints for Scenario 3 137
8.2 Scenario 3 Results, optimized for time and awakenings 140
8.3 Scenario 3 Results, optimized for time and people enclosed 144
8.4 Scenario 3 Results, optimized for time and people enclosed 147

B.1 Atmospheric parameters, Case 1 162
B.2 Atmospheric parameters, Case 2 163
B.3 Atmospheric parameters, Case 3 163
B.4 Atmospheric parameters, Case 4 164

C.1 Atmospheric parameters, Scenario 1 171
C.2 Scenario 1 results 172

D.1 Atmospheric parameters, Scenario 2 174
D.2 Scenario 2 results 175
D.3 Scenario 2 results (continued) 176

E.1 Scenario 3 results 178

1
Introduction

1.1 Background

In the current global society, civil aviation plays an irreplaceable role. An estimated contribution of 425 billion euro to the world's Gross Domestic Product (GDP) [1] and 2.7 billion passengers worldwide [2] indicate the social and economic importance of aviation. Although the 2008 economic crisis limited the growth in civil aviation in the Western world, continuous growth in the Far East and an expected economic recovery have the world's largest aircraft manufacturers Airbus [2] and Boeing [3] both predict a doubling of the civil aircraft fleet between 2011 and 2031.

Also in the civil helicopter market a continuous growth is expected. Although this market is more active with a larger number of manufacturers competing for the same market share, and the helicopter market seems to have been more adversely affected by the 2008 economic crisis, it is still expected that the total number of new deliveries in the period 2013-2033 will double as compared to the last decade [1, 4]. This growth is mainly attributed to the private and corporate sectors, the increasing use of helicopters by Emergency Medical Services (EMS) and an emerging market for commercial passenger transport that is expected to develop rapidly in the 2015-2020 period to two to three times its current size [4].

The economic and social importance of aviation and the expected growth of the aviation market does, however, lead to a significant burden on the environment. Air transport currently contributes to the greenhouse effect by emitting 2% of global man-made carbon dioxide emissions. This is expected to increase – despite the expected technological advances to further reduce fuel burn and hence carbon dioxide emissions – to 3% by 2050 due to the continuous growth in aviation [1]. More importantly, local emission of gaseous pollutants such as nitrogen oxides can have a significant impact on people living in the vicinity of airports. Finally, the noise exposure as a result of aircraft departing from and arriving at airports or heliports becomes an increasing nuisance for people living close to areas of high aviation activity. Especially the latter environmental impact causes a significant stream of complaints and increasing public awareness. The growth in air traffic can only be expected to increase this.

With the current fleet of helicopters, the global environmental impact due to helicopter operations is negligible as compared to fixed-wing air transport. However, on a local level the specific types of operations that helicopters are used for imply that they often operate in close proximity to the population, for example in case of corporate transport or EMS operations. In these types of operations helicopters can significantly contribute to the impact on the human environment – especially when noise nuisance is concerned – and with the predicted growth in rotorcraft operations particularly in corporate and EMS roles, this impact can only be expected to further increase.

Over the years though, significant developments have taken place contributing to the reduction of the environmental impact of helicopter operations. Initially, the main focus was on improving helicopter performance in terms of maximum speed and fuel efficiency. The introduction of turboshaft engines significantly improved engine performance and efficiency, and had a beneficial effect on the external noise generated by the helicopter. In addition, the common placement of the engine and exhausts at the top side of the helicopter generally reduced the source noise levels.

Also in the field of aerodynamic performance developments have been aimed at improving helicopter performance. An example is the *British Experimental Rotor Programme (BERP)* [5] started in the early 1970s to increase the helicopter's maximum lift and speed by using new designs and materials. The BERP III blade has a specially designed rotor tip with a backward sweep angle to reduce compressibility effects at high speeds, and was installed on the Westland Lynx that set the world speed record for helicopters in 1986. The current development, BERP IV (see Fig. 1.1) is installed on the AgustaWestland EH101 helicopters. The BERP blade design improves the aerodynamic efficiency of the blade but also reduces the noise originating at the blade tips. At Eurocopter currently a rotor blade is under development specifically to reduce the so-called *Blade-Vortex Interaction (BVI)* noise. BVI noise is generated by the rotor tip passing through the tip vortex of a preceding rotor blade, and occurs mainly in low speed approach conditions. The Blue Edge$^{\mathrm{TM}}$ [6, 7] blade tip (see Fig. 1.2) features a forward-backward sweep that significantly reduces the parallel interaction of the tip vortex with the following blades, hence significantly reducing the high intensity BVI noise.

Apart from main rotor blade development, one of the most successful measures to reduce the helicopter source noise is by replacing the conventional tail rotor. Sud-Aviation developed the *fenestron* [8] tail rotor (see Fig. 1.3) which greatly reduces the tail rotor noise. This reduction can mainly be attributed to three factors: 1) the fenestron casing reduces the amount of sound energy directed downwards, 2) the fenestron casing can prevent the formation of tip vortices, and 3) the higher number of blades increases the sound frequency leading to a higher atmospheric attenuation. Another alternative for the conventional tail rotor is the *NOTAR* (NO TAil Rotor) system [9] (see Fig. 1.4) –

Figure 1.1: BERP rotor blade

Figure 1.2: Blue Edge™rotor blade

originally developed by Hughes Helicopters – where a ducted fan uses the *Caondă effect* to generate lift from the tail boom to counteract the main rotor torque. NOTAR-equipped helicopters are among the quietest certificated helicopters currently in service.

Figure 1.3: Fenestron tail, Eurocopter EC-135

Figure 1.4: NOTAR System, MD Explorer

The design developments mentioned above have had a clear effect on helicopter performance, efficiency and on the source noise levels generated by the helicopter. As a result, the environmental impact – both in terms of gaseous emissions due to more efficient engines and in terms of source noise levels due to improved engines and aerodynamics – has been reduced significantly. To bring further significant step changes to the environmental impact of aviation in 2008 the European Union initiated the *Clean Sky Joint Technology*

Initiative (JTI) [1]. Clean Sky is a public-private partnership with a total budget of €1.6 billion, of which the main goal is to speed up technological developments and shorten the time to implement new solutions to advance towards the goals defined by the *Advisory Council on Aviation Research and Innovation in Europe (ACARE).* The ACARE goals are a set of challenging objectives for aviation in Europe for the year 2020. These objectives pertain among others quality and comfort for travelers, safety and air traffic management. Specifically for the environmental impact of aviation, the following four objectives are mentioned [10]:

- Total engagement by the industry in the task of studying and minimizing the industry's impact on the global environment.
- A reduction in perceived noise to one half of current average levels.
- Eliminate noise nuisance outside the airport boundary by day and night by quieter aircraft, better land planning and use around airports and systematic use of noise reduction procedures.
- A 50% cut in CO_2 emissions per passenger kilometer (which means a 50% cut in fuel consumption in the new aircraft of 2020) and an 80% cut in nitrogen oxide emissions.

The Clean Sky JTI consists of six *Integrated Technology Demonstrators(ITDs)*, among which the *Green Rotorcraft (GRC) ITD* focuses on the specific impact of any rotorcraft on the environment. In line with the ACARE targets, within GRC the following top-level objectives have been defined [1]:

- Reduce CO_2 emission by 25 to 40% per mission (for rotorcraft powered respectively by turbo shaft or diesel engines).
- Reduce the noise perceived on ground by 10 EPNdB or halving the noise footprint area by 50%.
- Ensure full compliance with the *Registration, Evaluation, Authorisation and Restriction of CHemical substances (REACH)* [11] directive which protects human health and environment from harmful chemical substances.

These objectives are to be reached by the year 2020 with the helicopter fleet in the year 2000 serving as a baseline. Although not mentioned explicitly, a reduction of the NO_x emission of 60% for helicopters with turbo shaft engines and 40% for diesel powered helicopters is also envisioned in GRC. The goals will be achieved by both internal GRC activities and contributions from other ITDs within Clean Sky. Among the internal activities within GRC are developments with regard to aerodynamics, focusing on airframe drag and rotor blade efficiency, engine developments and on-board electrical systems. However, these developments are mainly expected to result in improved fuel efficiency (and hence reduced CO_2 emissions), and to contribute to a reduction in NO_x emissions. Only the projected improvements in rotor blade aerodynamics are expected to reduce the external noise. To still be able to achieve the ambitious noise reduction goals, within GRC also the possibility to develop so-called *green trajectories* is being

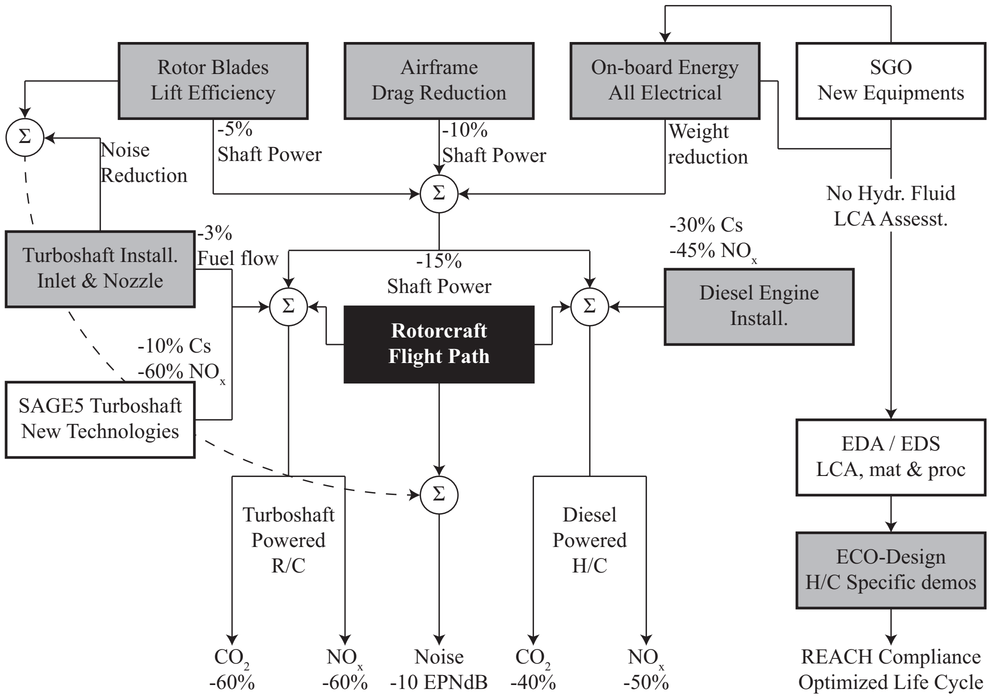

Figure 1.5: Green Rotorcraft ITD goals (adapted from [1])

examined, which is the main projected source of noise reduction. Engine performance also depends strongly on the flight conditions (air temperature, altitude, airspeed), and therefore within GRC optimal flight paths are considered to provide a reduction of 6% in total mission fuel burn as well. The specific helicopter operations in densely populated areas currently causing the most significant noise nuisance are addressed by developing new departure and arrival procedures at inner-city heliports that are tailored for noise nuisance reduction. The green terminal procedures are expected to reduce the external perceived noise levels by 5 EPNdB [1]. An overview of the means and goals for the GRC ITD can be seen in Fig. 1.5 (contributions from other ITDs in white).

1.2 Previous Research

Research on helicopter trajectories has been quite extensive over the past decades, focusing on a variety of factors such as emergency procedures and environmental impact. In the field of reducing the helicopter noise footprint specifically the German Aerospace Center DLR is performing ongoing research into arrival noise reduction [12–16]. In the proposed methodology either measured or computationally derived source noise levels are used to predict the noise impact of a given helicopter trajectory. The trajectory is modeled by defining a number of control points that define the helicopter position in three dimensions, as well as the airspeed vector. A continuous trajectory is then found by applying a spline interpolation algorithm to the control points. The work does show promising gains in terms of reducing the noise footprint during a helicopter arrival procedure, mainly by avoiding BVI noise. Although the proposed method allows imposing a realistic set of operational constraints, the large runtimes of the helicopter and noise models necessitate a relatively low number of optimization parameters to be used, and as a result significantly reduce the freedom in the optimization process. Also at helicopter manufacturer AgustaWestland research is ongoing in the field of helicopter trajectory optimization with respect to noise exposure, particularly in landing procedures [17]. In this case, source noise levels for both the main and tail rotor are determined numerically through an aeroacoustic chain prior to the optimization. Within each optimization iteration, a helicopter trajectory is simulated, and the resulting noise levels on the ground are evaluated using the predetermined source noise levels and the propagation model *HELENA* developed in the European *FRIENDCOPTER* research project. The helicopter trajectory is described in two dimensions and parametrized with five airspeed and altitude values at control points that are used to define a continuous trajectory using b-spline curves. In essence, this implies that the helicopter flight dynamics are not modeled. The optimization method applied in this study is a Surrogate-Assisted Memetic Algorithm (SAMA), which combines a Genetic Algorithm (GA) for the global search and a gradient-based algorithm for local refinement, greatly improving the efficiency of the method. The study shows a possible reduction in the noise exposure of 5 dBA SEL at some observer locations. Although a detailed source noise and propagation model is used, and the optimization method used is very efficient, in the presented study only a relatively small number of optimization parameters is evaluated, and the noise exposure is only assessed in a limited number of observer locations.

Optimal control theory has also been used extensively in helicopter trajectory optimization research, potentially greatly reducing the runtimes of a typical problem. Zhao et al. [18] and Jhemi et al. [19, 20] used trajectory optimization techniques through optimal control theory in the optimization of critical helicopter trajectories. The use of a relatively simple point-mass helicopter model and gradient-based optimization techniques are shown to result in very short problem runtimes, potentially permitting the calculation of optimized trajectories in real-time on-board helicopters, even with a significant number of optimization parameters. Okuno et al. [21, 22] and Bottasso et al. [23] also applied optimal control theory to helicopter emergency procedures, extending to a two-dimensional rigid-body helicopter model. The work again shows relatively short runtimes with a large number of optimization parameters, and even considers the modeling of tilt-rotor aircraft. However, the research presented by Zhao, Jhemi and Bottasso only considers emergency procedures, and does not consider the environmental impact of helicopter operations. Tsuchiya et al. [24] and Visser et al. [25] have shown the capabilities of combining three-dimensional point-mass helicopter models and noise models in an effort to reduce the noise impact on the ground. For this purpose, Tsuchiya used an analytical source noise model based on noise measurements of the experimental MuPAL-ϵ helicopter. Using this approach, Tsuchiya showed that a combination of optimizing the ground track and procedure allowed for significant reductions in the noise impact in a small number of discrete points. Again, avoiding BVI noise through flight path angle selection played an important role in the noise abatement. Visser applied similar flight mechanics modeling, but used the *Integrated Noise Model (INM)* instead. In this research, using the *NOISHHH* [26–30] optimization tool developed at Technische Universiteit Delft (Delft University of Technology, TUD), the noise impact on a near-airport community was assessed. For this purpose, a Geographic Information System (GIS) was integrated in the optimization tool in an effort to quantify the community noise impact through the use of a dose-response relationship. This research showed the adaptability of the optimal control methodology used, and showed a significant potential improvement for a number of community noise impact criteria.

1.3 Research Objectives

Previous research has shown several approaches towards optimizing helicopter trajectories with respect to emergency procedures or noise impact. Both DLR and AgustaWestland focused strongly on highly accurate source noise and propagation modeling. Due to the relatively long execution times for the highly detailed noise models, optimization of the trajectories for noise abatement purposes is limited to a relatively small number of parameters in the final phases of helicopter landing procedures, and noise is only assessed in a limited number of observer locations close to the helicopter's trajectory. Detailed helicopter flight mechanics are, although intended to be included in the future, only partly modeled in these studies. As a result, complex path constraints cannot be imposed, and flyability or passenger comfort considerations can only be assessed in post-processing.

The research groups using optimal control theory for helicopter trajectory optimization typically model flight mechanics through the integration of the full equations of motion. More importantly, the use of optimal control theory prescribes that all models and hence the total problem formulation is based on smooth differentiable functions. In addition, for all models involved – and hence again for the entire problem formulation – the gradients need to be provided, either numerically or analytically. Although only part of the research efforts using optimal control theory have focused on environmental optimization, in general it can be concluded that the models used are relatively simple to maintain acceptable runtimes, although the required computer runtimes are generally significantly less than for global optimization algorithms used in other studies.

Taking into consideration the status of existing research, the primary objective of this study can be defined as

to develop an optimization software suite that can optimize helicopter trajectories in non-standard atmospheric conditions with respect to (community) noise impact, fuel burn and gaseous emissions.

Although several components of this objective have indeed already been addressed in previous research, the objective of this study is to combine high-fidelity models whilst ensuring short computer runtimes. Therefore, a secondary objective is defined as follows

The optimization software suite should be based on optimal control theory to maintain computer runtimes in the order of two hours for typical problems, whilst using high-fidelity flight dynamics and noise models to achieve a required level of accuracy.

The two main research objectives can be further refined to further specify the efficiency and accuracy of the developed software suite. Firstly, the research aims to assess and optimize the environmental impact of helicopter trajectories whilst accounting for operational aspects such as fuel burn and total flight time. As a result, the selected optimization algorithm should be able to accommodate the minimization of multiple optimization criteria individually, and any combination thereof. Furthermore, the software suite should be able to synthesize optimized trajectories that are realistic and flyable. To accommodate this, the optimization algorithm should be able to solve optimal control problems with a complex set of operational constraints imposed relating to the helicopter flight envelope, regulations and passenger comfort. Thirdly, within a given search space bounded by constraints and state and control bounds, the algorithm should have sufficient freedom to find an optimal solution. To accommodate this the method should allow a relatively fine discretization of the problem (and hence a large number of optimization parameters). In addition, the optimization algorithm should be able to find an optimal solution in a sufficiently large search space. Finally, as mentioned in the secondary objective of this study, given the set of requirements defined above, the total runtime for typical problems to be solved with the software suite should be low as compared to state of the art research.

1.4 Thesis Structure

In this thesis, the development of a software suite for helicopter environmental trajectory optimization is described in detail, and some numerical examples generated with the suite are presented. In Chapter 2 the structure and modeling requirements of the software suite are presented, as well as an overview of the models integrated in the tool. Chapter 3 describes the selection process for the optimization methodology, and describes the selected method in detail. In Chapter 4 the flight mechanics model is explained. A detailed overview of the development and implementation of the noise model, including source noise, propagation and community noise impact is given in Chapter 5. In Chapters 6 to 8 the results and their analysis of three scenarios are presented in case studies to exemplify the capabilities of the new tool. Finally, in Chapter 9 the conclusions and recommendations following from this study are stated.

2

European Clean Helicopter Optimization Suite

2.1 Introduction

In Chapter 1 the high-level objectives for the development of the *European Clean Helicopter Optimization (ECHO)* research tool were stated. The main focus of this study lies on the reduction of the community noise impact in areas surrounding arrival flight paths, whereas criteria such as pollutant emissions, flight time and fuel burn are used as secondary optimization criteria. The following chapter gives a more detailed overview of the structure of the *ECHO* suite, and will discuss in more detail the modeling requirements the software has to comply with.

2.2 *ECHO*

2.2.1 *ECHO* Structure

The high-level objectives defined in the previous chapter require that the *ECHO* suite can simulate helicopter trajectories and assess the total flight time and the total fuel burn, as well as the resulting environmental impact in terms of local gaseous emissions and community noise impact. In order to achieve this, the *ECHO* suite should contain at least a helicopter flight dynamics model, a helicopter noise model and a fuel and emissions model. These are then combined with an optimization algorithm based on optimal control theory to find an optimal solution for a varying set of optimization criteria. The general structure of the suite can be seen in Fig. 2.1.

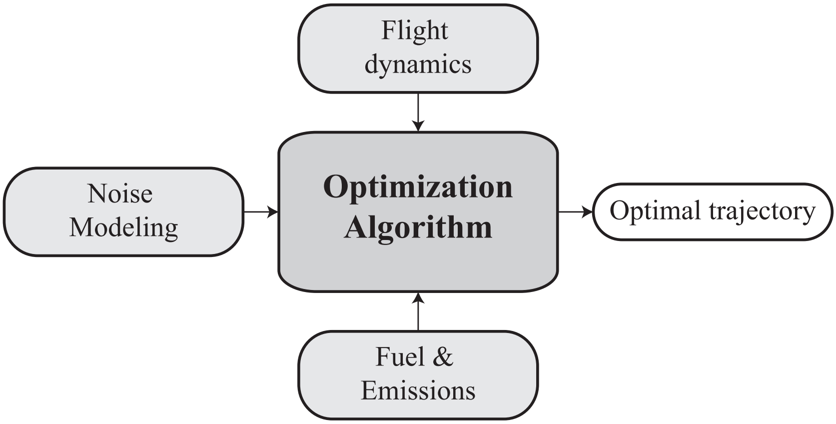

Figure 2.1: *ECHO* Suite structure

Each of the three main components has to comply with a specific set of requirements, which are discussed in detail in the following sections.

2.2.2 Optimization Algorithm

The optimization problem to be solved with the *ECHO* suite is essentially a *trajectory optimization* problem for which a significant number of potential solution methods exist. To further aid the selection of the optimization algorithm (which is discussed in detail in Chapter 3), a number of additional requirements relating to the optimization methodology should be defined. For trajectory optimization problems, the absence of discrete variables generally allows the use of optimization algorithms based on optimal control theory. Even more so, it can be argued that for trajectory optimization problems algorithms based on optimal control are the *preferred* method towards solving the problem [31]. The major benefit of optimal control algorithms is that they use *gradient* information to determine both the search direction towards an optimal solution and a termination criterion to confirm an optimal solution has been found, resulting in a relatively low computational effort. In addition, although many different solution methods exist, in general optimal control theory also allows the imposition of a complex set of constraints and the definition of composite performance indices. Due to the benefits of using gradients to find a solution and the versatility of methods based on optimal control theory, the *ECHO* suite will be based on such methods.

Although the relatively short total runtime is a major advantage of gradient-based optimization techniques, the selection of such a methodology also imposes some limits on the problem definition. Most importantly, the *direct* solution method selected for *ECHO* (see Chapter 3) requires that the trajectory dynamics differential equations used in the problem definition are smooth, differentiable functions, preferably to the second degree. Although trajectory dynamics can normally be defined as continuous functions, some models are partly based on empirical data and could rely on for instance linear interpolation which would clearly result in non-smooth functions. The same prerequisite applies to any other model contributing to the objective function or constraint vectors. In addition, discontinuities can also be introduced in the problem formulation itself. Discrete changes in the flight dynamics can occur if for instance engine failures are modeled, if the constraint vector changes in different phases of the flight, or if a trajectory is optimized for different criteria in different phases of the mission. These discontinuities also cause discrete changes in the problem formulation, and consequently will lack a continuous differential.

The need to avoid discontinuities is an important limitation to methods based on optimal control theory. It is noted, though, that in some cases discontinuities in the first derivative are acceptable and will not negatively affect the problem convergence. More importantly, many gradient-based optimization algorithms explicitly allow for discrete changes in the objective, constraint or dynamics functions through the introduction of phases – essentially coupling different individual trajectory optimization problems through an additional set of constraints. This will be discussed in further detail in Chapter 3 where the selection of the optimization methodology is presented.

2.2.3 Helicopter Flight Dynamics

As was concluded above, in the selection or design of models for integration in the *ECHO* suite continuity is an important consideration. Although apart from continuity requirements there is no strict limitation on how the flight dynamics are modeled, unnecessary complexity in modeling should be avoided in general. In fact, in applying any optimization methodology the objective should be to find the model of minimum complexity that provides a sufficiently accurate representation of the real world. To identify the requirements for the helicopter flight dynamics model to be integrated in *ECHO*, it is necessary to first consider the objectives of the research tool. One of the main objectives of the suite is to be able to optimize trajectories with respect to community noise impact. This requirement already precludes the use of a two-dimensional flight dynamics model such as used in [18–23].

The use of a three-dimensional point-mass helicopter flight mechanics model as seen in [24, 25] would allow the optimization of trajectories with respect to community noise impact. However, the noise models used in these studies are based on empirical data and only partially depend on the helicopter flight conditions. As was briefly mentioned in the previous chapter, however, helicopter source noise is highly dependent on the flight conditions, and results in a complex, asymmetric noise exposure on the ground. To be able to model the helicopter source noise in sufficient detail and in different atmospheric conditions requires the availability of rotor blade characteristics and helicopter body angles that are not readily available in a point-mass formulation. Therefore, an eight Degrees-of-Freedom (DoF) helicopter flight dynamics model has been selected for integration in *ECHO*, which will be discussed in detail in Chapter 4. The use of an eight DoF flight dynamics model does, however, also lead to an additional requirement for the optimization algorithm. To accurately model the higher-order dynamics would require a relatively fine problem discretization and hence a large number

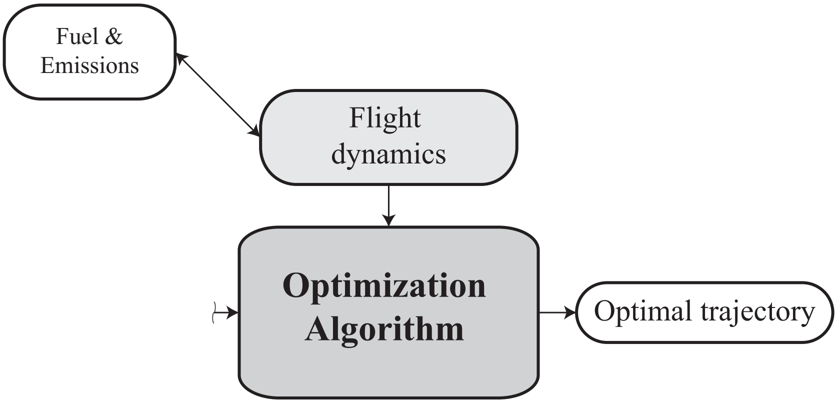

Figure 2.2: *ECHO* Suite flight dynamics

of optimization parameters. This requires more emphasis to be put on the efficiency of the optimization algorithm to ensure acceptable total runtimes.

In addition to total flight time – following directly from the flight dynamics modeling – the *ECHO* suite should also enable the optimization of helicopter trajectories with respect to total fuel burn and the emissions of pollutant gasses. Only in [25] is the fuel flow explicitly modeled using a Specific Fuel Consumption (SFC) dependent on the required engine power. This approach is considered sufficiently accurate to model the fuel flow in *ECHO*. As both fuel burn and the emissions of pollutant gasses are considered secondary objectives in the development of *ECHO*, a similar approach is deemed sufficient for the determination of pollutant emissions. Since the fuel flow and the gaseous emissions are directly related to the required engine power and hence the flight conditions, rather than adding a separate engine model the fuel flow and emissions model is integrated in the flight dynamics model, as can be seen in Fig. 2.2.

2.2.4 Noise Modeling

As this study is intended to have a strong focus on the development of noise abatement trajectories for helicopters, it is imperative to model the helicopter noise sufficiently accurate. Three general approaches can be recognized to model helicopter noise in previous optimization studies. In [24] and [25] a simplified noise model is used that does not directly include the helicopter's source noise. As a result, specific directivity patterns and to some extent the dependency of noise on the helicopter flight conditions cannot be modeled accurately. In addition, the noise levels following from the noise model do not include frequency information which is required to determine the propagation losses in non-standard atmospheric conditions.

In the studies performed at DLR and AgustaWestland [14–17], source noise is modeled through a database model, resulting in significantly more accurate results. The approach used here is to collect a large database of source noise levels for different flight conditions either based on noise measurements or determined numerically using aeroacoustical modeling. During the optimization process the flight conditions following from the flight dynamics model are then used to derive the source noise levels.

A final option to model the helicopter source noise is to explicitly model the source noise generation during the optimization process. Although this would result in the most accurate solution, the time required to solve the numerical process of aeroacoustically determining the source noise levels would be too heavy a burden on the total runtime. Also the approaches used in [24] and [25] are not suitable for implementation in *ECHO* as they only include aggregated noise levels over all frequencies, and they do not offer the required accuracy in the directivity of source noise and its dependency on the flight conditions.

Consequently, the source noise model included in *ECHO* will have to be based on a database which includes source noise levels for different frequencies and for a range of different flight conditions. As it is prohibitively difficult to create such a database from measured data derived from flight tests, the model integrated in the software suite will have to rely on numerically determined source noise levels. To determine the source noise levels at each time step, the flight conditions are obtained from the flight dynamics model to extract the corresponding database entries.

The next step in assessing the noise exposure on the ground is to determine the propagation loss between the source and the ground-based receiver. As *ECHO* is expected to be able to optimize trajectories in non-standard atmospheric conditions, so too should the propagation model integrated in the tool account for this. Noise propagation through the atmosphere depends not only on the atmospheric properties, but also on the frequency spectrum of the noise. Therefore, as was already briefly mentioned above, this precludes the use of noise models that only assess aggregated noise levels for a full frequency spectrum. In essence, this implies that the propagation model integrated in *ECHO* should be able to determine the propagation loss for all available frequencies, and should only determine the aggregated noise level at the ground-based receiver location. Although different approaches exist to model the propagation loss between a source and a ground-based receiver, the propagation model included in *ECHO* should at least be able to model the propagation loss as a result of

1. non-standard atmospheric temperatures and temperature gradients,
2. non-standard atmospheric humidity and humidity gradients,
3. the presence of wind varying with altitude, and
4. different ground surface conditions.

It should be noted that the propagation model requires additional input from both the source noise model and the flight dynamics. These models together define the source noise strength for different frequencies as a function of the helicopter flight conditions and the relative position of the helicopter with respect to a ground-based receiver.

The final step in the noise optimization process requires *ECHO* to be able to determine a set of different noise criteria in order to quantify the total noise impact due to the complete helicopter trajectory. In addition, for the specific case of *community* noise

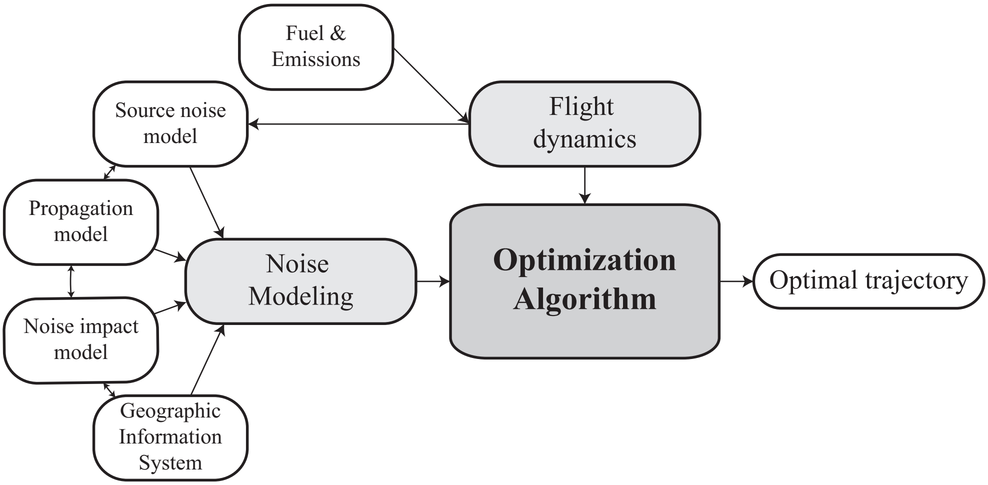

Figure 2.3: *ECHO* Suite final structure

impact, the software suite should also contain a Geographic Information System (GIS) containing geographical and demographic data of the area surrounding the trajectory.

The three components of the noise modeling are presented in detail in Chapter 5, and the complete structure of the *ECHO* suite can be seen in Fig. 2.3.

2.3 Reflection on Methodology

When the strong focus on runtime in the development of the *ECHO* suite is considered, it is also important to reflect on the performance of other available optimization approaches, and to compare the modeling accuracy in the different approaches. Although a direct comparison between different studies is difficult due to the differences in modeling accuracy, number of optimization parameters and hardware, it is possible to provide a high-level comparison between previous research and this study.

With respect to the optimization methodology, two main methods can be identified in previous research: evolutionary algorithms and algorithms based on optimal control theory. The absence of gradient information in evolutionary methods requires a significantly larger number of problem evaluations, which is furthermore highly dependent on the number of parameters to be optimized and the bounds set for those parameters. Although computer runtimes are not always stated in the literature, and are difficult to compare as they depend highly on the hardware used, for a study done at DLR [15] using an evolutionary algorithm a total problem runtime of 48 hours is stated for 80,000 problem iterations on 32 parallel processors. In this problem, 12 parameters were optimized in a helicopter approach procedure with the objective to minimize the noise footprint in a grid of 77 observer locations.

When this is compared to the optimization methodology used in *ECHO*, the benefit of using gradient information becomes readily clear. A typical problem easily exceeds 1,000 optimization parameters and as such lends more freedom to the algorithm to alter the trajectory. Also, in general in this study larger noise grids are evaluated that can include over 1,000 observer locations. It then becomes clear that the target set for a maximum runtime of 2 hours on a single core processor may indeed offer a fast alternative to methods based on evolutionary methods.

Apart from computational efficiency, it is also important to compare the modeling accuracy of each of the components. Again this is difficult to achieve as a direct comparison between different studies is not possible, and test flights to validate each of the components are prohibitively expensive. Still, a high-level comparison can be made.

As mentioned in the previous chapter, earlier studies based on optimal control theory [24, 25] mainly used simplified noise models that do not sufficiently capture the highly directive nature of helicopter noise in different flight conditions. The studies conducted at DLR and AgustaWestland [12–17] rely on a database of source noise levels projected on a hemisphere, using a similar approach as has been adapted in *ECHO*. Although the accuracy, size and completeness of the databases in the different studies may differ, in general the models are comparable. Likewise, it is difficult to directly compare the accuracy of each of the models used for noise propagation. However, the propagation model integrated in *ECHO* at least models the same atmospheric propagation effects as the indicated studies using evolutionary algorithms.

The approach taken to model the flight dynamics in previous studies is significantly different from the method adopted in *ECHO*. In the studies based on evolutionary methods, in general either a complete trajectory in terms of position and velocity is generated, or a number of waypoints along the trajectory is defined. Then a flight dynamics model is used to simulate the flight along the trajectory or through the waypoints. This approach is clearly different from the approach used in this study (or other studies relying on optimal control) where the complete trajectory is discretized and each of the vehicle states and controls in the flight dynamics model are included as optimization variables. The benefit of the latter approach is that it is significantly easier to directly impose a complex set of constraints on the trajectory. On the other hand, to maintain acceptable runtimes the problem discretization generally results in a significantly larger time step for the integration of the equations of motion as compared to regular flight simulations. Clearly the increased time step results in a less accurate representation of the trajectory, especially when the fast dynamics are concerned. However, it is assumed for this study that the trajectory definition in terms of airspeed and position is sufficiently accurate, and that the short runtimes and high number of optimization parameters outweighs this disadvantage.

2.4 Limitations

The previous sections give an overview of the detailed requirements the *ECHO* suite has to comply with - both for the individual components and the suite as a whole. The objective of this study is to integrate the models discussed above in a single suite. From this observation some limitations to the scope of this study can be derived:

1. The results presented in this study aim to show the capabilities of the *ECHO* suite to solve trajectory problems with various levels of complexity, and to identify a set of flight conditions that lead to a minimal environmental impact. This does not mean that the resulting trajectories are based on current standard operating procedures of helicopters. In addition, no test flights or simulator sessions have been conducted within the framework of this thesis to assess the level of pilot acceptance for the resulting optimal trajectories.
2. The database of source noise levels integrated in the suite provides an accurate prediction of the source noise for the flight conditions included in the database – and as such provides a significant improvement in source noise modeling accuracy as compared to previous studies using optimal control theory. It should be noted though that the database will not cover all flight conditions encountered in optimized trajectories, and as such inter- and extrapolation may be required to provide source noise information for different flight conditions.
3. The use of optimal control ensures a significant improvement in computational effort as compared to genetic optimization algorithms, and at the same time allows for a larger number of parameters to be optimized. However, it should be noted that the time step of the integration in the proposed optimal control methodology is generally significantly larger than when simulating a helicopter flight. Although the resulting trajectories in terms of helicopter position and airspeed will be sufficiently accurate, the fast dynamics may not always be captured in sufficient detail.
4. Although one of the requirements of the *ECHO* suite is to optimize trajectories with respect to community noise impact, currently no community noise impact criteria dedicated to helicopter operations are available.
5. As test flights are prohibitively expensive, the final results for the noise exposure on the ground cannot be compared to empirical data. However, all individual components contributing to the noise modeling have been validated separately.

3
Optimization Methodology

3.1 Introduction

The objective of minimizing the environmental impact of helicopter operations is in essence a trajectory optimization problem. Although several approaches exist towards solving trajectory optimization problems, the *ECHO* suite uses a *gradient-based* optimization method based on *optimal control theory*. Optimal control theory aims to find the controls that perturb a system from a fixed initial condition to a free or fixed final condition, whilst minimizing the total value of a cost functional which is itself a function of the system controls and states. Optimal control problems are constrained problems, and any number of path and boundary constraints can be applied. Although numerous methods exist to find the solution to optimal control problems, *ECHO* uses a *direct* method with *pseudospectral collocation*. The following chapter will give an overview of optimal control theory and the solution methods selected for *ECHO*.

3.2 Optimal Control Theory

3.2.1 General Problem Definition

In optimal control theory, the aim is to minimize a cost functional J which is a function of the state and control functions $x(t)$ and $u(t)$ of the dynamic system. Without loss of generality, consider as a typical example of an optimal control formulation, the so-called Continuous Bolza Problem [32]:

Determine the state $\mathbf{x}\left(t\right) \in \mathbb{R}^n$, the control $\mathbf{u}\left(t\right) \in \mathbb{R}^m$, initial time t_0 and final time t_f, that minimize the cost functional

$$J = \Phi\left(\mathbf{x}\left(t_0\right), t_0, \mathbf{x}\left(t_f\right), t_f\right) + \int_{t_0}^{t_f} \mathcal{L}\left(\mathbf{x}\left(t\right), \mathbf{u}\left(t\right), t\right) dt \tag{3.1}$$

subject to

$$\dot{\mathbf{x}}\left(t\right) = \mathbf{f}\left(\mathbf{x}\left(t\right), \mathbf{u}\left(t\right), t\right) \tag{3.2}$$

$$\boldsymbol{\phi}\left(\mathbf{x}\left(t_0\right), t_0, \mathbf{x}\left(t_f\right), t_f\right) = \mathbf{0} \tag{3.3}$$

$$\mathbf{C}\left(\mathbf{x}\left(t\right), \mathbf{u}\left(t\right), t\right) \leq \mathbf{0} \tag{3.4}$$

where J is the cost functional consisting of the *Lagrange* or *Running* cost $\mathcal{L}$, and the *Mayer* or *Endpoint* cost Φ. The problem is constrained by the *dynamic constraints* $\mathbf{f}$, the *boundary conditions* $\boldsymbol{\phi}$, and the *algebraic path constraints* $\mathbf{C}$.

3.2.2 First-Order Optimality Conditions

In order to solve the problem defined by Eqs. (3.1) to (3.4), first the *First-Order Optimality Conditions* are defined. These conditions define a set of *necessary* conditions for a solution to be optimal. In defining these conditions, the first step is to augment the cost function of Eq. (3.1). Consider again the Bolza problem defined in the previous section. The augmented cost functional can then be defined as

$$J_a = \Phi - \boldsymbol{\nu}^T \boldsymbol{\phi} + \int_{t_0}^{t_f} \left[\mathcal{L} - \boldsymbol{\mu}^T C + \boldsymbol{\lambda}^T \left(\mathbf{f} - \dot{\mathbf{x}}\right)\right] dt \tag{3.5}$$

where $\boldsymbol{\nu}$ and $\boldsymbol{\mu}$ are the *Lagrange multipliers* for the boundary and path constraints respectively, and $\boldsymbol{\lambda}$ are the *costates* or *adjoints* of the differential equations. In this equation, the *Hamiltonian* is introduced, which is defined as

$$\mathcal{H} = \mathcal{L} + \boldsymbol{\lambda}^T \mathbf{f} - \boldsymbol{\mu}^T \mathbf{C} \tag{3.6}$$

and which allows Eq. (3.5) to be rewritten as

$$J_a = \Phi - \boldsymbol{\nu}^T \boldsymbol{\phi} + \int_{t_0}^{t_f} \left[\mathcal{H} - \boldsymbol{\lambda}^T \dot{\mathbf{x}}\right] dt \tag{3.7}$$

The objective is now to find an extremal solution of Eq. (3.7) based on the *Calculus of Variations* and *Pontryagin's Minimum Principle* [33] which states that if x^* yields an extremal solution, then

$$\delta J(x^*, \delta x) = 0, \quad \forall \text{ admissible } \delta x \tag{3.8}$$

which implies that the gradient of the cost functional in any direction equals zero. When this principle is applied to Eq. (3.7) a set of first-order optimality conditions can be determined that form the *Hamiltonian Boundary-Value Problem (HBVP)*. These necessary conditions for the problem defined by Eq. (3.5) can be written as

$$\boldsymbol{\phi}\left(\mathbf{x}(t_0), t_0, \mathbf{x}(t_f), t_f\right) = \mathbf{0} \tag{3.9}$$

$$\boldsymbol{\lambda}(t_0) = -\left[\frac{\partial \Phi}{\partial \mathbf{x}(t_0)}\right]^T + \left[\frac{\partial \boldsymbol{\phi}}{\partial \mathbf{x}(t_0)}\right]^T \boldsymbol{\nu} \tag{3.10}$$

$$\boldsymbol{\lambda}(t_f) = \left[\frac{\partial \Phi}{\partial \mathbf{x}(t_f)}\right]^T + \left[\frac{\partial \boldsymbol{\phi}}{\partial \mathbf{x}(t_f)}\right]^T \boldsymbol{\nu} \tag{3.11}$$

$$\mathcal{H}(t_0) = \frac{\partial \Phi}{\partial t_0} - \boldsymbol{\nu}^T \frac{\partial \boldsymbol{\phi}}{\partial t_0} \tag{3.12}$$

$$\mathcal{H}(t_f) = -\frac{\partial \Phi}{\partial t_f} + \boldsymbol{\nu}^T \frac{\partial \boldsymbol{\phi}}{\partial t_f} \tag{3.13}$$

$$\dot{\mathbf{x}} = \mathbf{f}\left(\mathbf{x}(t), \mathbf{u}(t), t\right) \tag{3.14}$$

$$\dot{\boldsymbol{\lambda}} = -\left[\frac{\partial \mathcal{H}}{\partial \mathbf{x}}\right]^T \tag{3.15}$$

$$\left[\frac{\partial \mathcal{H}}{\partial \mathbf{u}}\right]^T = \mathbf{0} \tag{3.16}$$

It is noted that any solution complying with these necessary conditions is only a candidate optimal solution for a local minimum. Further tests are needed to assess whether the candidate solution indeed represents a local minimum. The resulting HBVP can then be solved numerically to find an extremal trajectory. To do so, two solution methods exist, referred to as *indirect* and *direct* solution methods.

3.2.3 Solution Methods

Indirect Approach

In indirect methods the aim is to solve the HBVP. Indirect methods were historically only used to solve relatively simple optimal control problems analytically, due to the absence of modern computers to find numerical solutions. With powerful computers available, nowadays also numerical solutions can be found. Although an exact solution to the optimal control problem can be found using indirect methods, in general obtaining a solution is very difficult. Firstly, indirect methods require derivation of the first-order optimality conditions from the original continuous-time problem definition. For large practical problems containing complex path constraints and possibly multiple phases – having different dynamics and constraints applied – the process of deriving the HBVP becomes very difficult. Furthermore, when changes to the problem constraints or dynamics are introduced the process has to be repeated. Apart from requiring an accurate initial guess for the system states and controls, indirect methods also require a non-intuitive initial guess to the costate variables and the corner conditions imposed at the entrance and exit of path constraints. Indeed, indirect methods tend to be highly sensitive to the initial guess, and can possibly show severe convergence problems.

Direct Approach

As mentioned in the previous section, although indirect methods result in an exact solution of the continuous problem, the problems are generally very difficult to solve, and require an accurate non-intuitive initial guess of the costates. As an alternative, *direct methods* were developed for solving optimal control problems, and do not require derivation of the optimality conditions or an accurate initial guess for the costate variables. In direct methods, the continuous, *infinite-dimensional* problem is transcribed into a *finite-dimensional NLP* problem, which can in turn be solved using numerical solvers. Although the resulting NLP problems can become very large with increasing numbers of states, controls and constraints, direct methods still provide a very efficient means to solving trajectory optimization problems. The resulting NLP problems are large but *sparse*, indicating that most of the problem derivatives are actually equal to zero. This sparsity and the availability of advanced NLP-solvers make the direct approach very computationally efficient. In addition, direct methods are more robust to initial guesses, which is beneficial in setting up large and complex practical trajectory optimization problems.

Direct methods can be generally divided in two sub-methods. In *shooting methods* only the control variables are parametrized. Although shooting methods are the simplest form of direct solution methods, they are computationally inefficient and generally lead to low-accuracy solutions. In addition, constraints on either the path or the controls are difficult to impose.

As an alternative to shooting methods, in *parametrization methods* both the control and state variables are parametrized. These methods, also referred to as *collocation methods*, provide greater accuracy than shooting methods, and allow a complex set of path constraints to be imposed. Within the subset of collocation methods another distinction is made between *local* and *global* methods.

Local methods use a local approximation of the state and control variables through for instance linear interpolation, and apply local integration techniques for the system dynamics.

In global collocation methods, the problem states and controls are approximated on the complete state interval. In the specific case of *pseudospectral methods*, the solution of the problem, $\mathbf{x}(t)$, is approximated by a sum of finite elements, $\mathbf{X}(t) = \sum_{i=1}^{N} \alpha_i \beta_i(t)$. For most common methods, the *trial functions* $\beta_i(t)$ are trigonometric functions or orthogonal polynomials such as Legendre polynomials. The *expansion coefficients* α_i are chosen in such a way that on a set of *collocation points* the residual of the basis functions and the approximating functions equals zero, such that

$$\mathbf{R}_N(t_i) = \dot{\mathbf{X}}(t_i) - \mathbf{f}(\mathbf{X}(t_i), \mathbf{U}(t_i), t) = \mathbf{0}, \qquad \forall\, i = 1, \ldots, N \tag{3.17}$$

Pseudospectral methods are generally based on a form of Gaussian quadrature to integrate the system dynamics. Although different forms exist of Gaussian quadrature, a common characteristic of these integration methods is that they require a relatively low number of discretization points whilst maintaining a high level of accuracy, thus reducing the total problem size. Three quadrature methods frequently used in trajectory optimization are the so-called *Legendre-Gauss (LG)*, *Legendre-Gauss-Lobatto (LGL)*, and *Legendre-Gauss-Radau (LGR)* quadrature rules. Of these three, the LG and LGR methods clearly show the best convergence [34] for general trajectory optimization problems. In addition, the resulting NLP problems defined using the latter two methods are smaller than when using the Lobatto approach. In the discretization process, LG quadrature does not implicitly include the initial and final time of the problem, whereas the Radau approach includes only one boundary point. It can be shown that for problems having either a fixed initial or fixed final time, the Radau method generally shows better convergence behavior [34].

ECHO Optimization Methodology

In the development of *ECHO*, one of the main objectives is to be able to solve a large variety of different helicopter optimization problems with different sets of constraints, performance indices and possibly dynamics. This requires a high level of flexibility in the setup, as well as relatively short processing times including problem runtime and setup. Considering this objective, a trade-off can be made from the proposed trajectory optimization methods presented in the previous sections.

Indirect methods would lead to an exact solution to the continuous-time optimal control problem, and would gain insight into the level of optimality of the extremal solution found (hence theoretically allowing to find the *global* optimum). However, deriving the first-order optimality conditions and then solving the HBVP is a difficult process which has to be (partly) repeated for different problem setups. Therefore, indirect methods are considered to be too inflexible and would require too much time to setup each individual helicopter optimization problem in *ECHO*.

Although *direct methods* give no indication of the optimality of the extremal solutions found (and so global optimality cannot easily be proven), the relative ease of defining different problems, the robustness with respect to initial guesses and the ease with which the resulting NLP problems can be solved show definite advantages with respect to indirect methods with regard to both flexibility and processing times. As a result, direct methods have been selected to be used in *ECHO*. Given that the practical helicopter optimization problems to be solved in *ECHO* require a complex set of operational path constraints, the inability to impose these in *direct shooting methods* make these methods unsuitable to be implemented in *ECHO*. As a result, *collocation methods*, in which both the control and state variables are discretized, have been selected. As mentioned in the previous section *pseudospectral methods* offer a higher level of accuracy through Gaussian quadrature, while resulting in a smaller required problem size. Although the differences between various quadrature methods do not consistently lead to a preferential method for the wide variety of problems to be assessed with *ECHO*, there is some benefit in selecting the Radau method since most helicopter trajectory optimization problems have at least one fixed point in time.

From the above discussion it can be concluded that to ensure flexibility, versatility and relatively low processing times in *ECHO*, a direct pseudospectral collocation method using Radau quadrature is preferable. The process for selecting this method is visualized in Fig. 3.1.

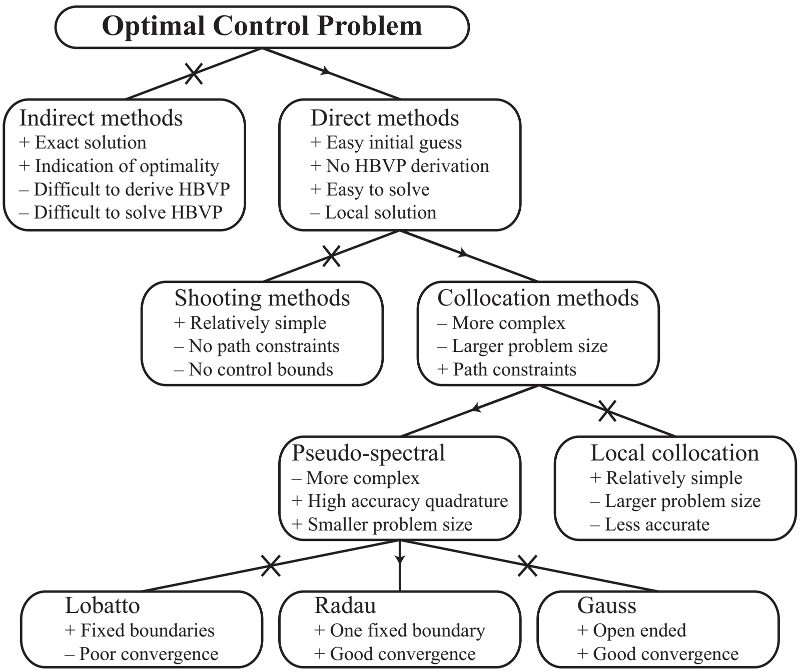

Figure 3.1: Selection process of the optimization method

For the different solution methods presented above a number of software packages exist that already integrate one of these methods, and offer some form of user interface to reduce the complexity of setting up and running new problems.

Firstly, the *EzOpt* package has been used extensively and successfully at TUD in numerous studies involving the *NOISHHH* optimization tool [26–30]. However, EzOpt only offers the possibility for local collocation, and in addition does not contain a sparse NLP solver, hence significantly reducing the computational efficiency.

Secondly, one of the more elaborate packages available is the *Sparse Optimal Control Software (SOCS)* [35] developed by Boeing. Again, only local collocation is offered, although significantly more elaborate integration schemes are available as compared to EzOpt. In addition, SOCS only allows for numerical differentiation reducing the computational efficiency. SOCS does, however, offer the possibility to assess both direct and indirect approaches.

Another well-known package is *DIDO* [36–38] developed by Elissar, LLC. DIDO applies the Legendre-Gauss-Lobatto method of pseudospectral collocation, and is fully integrated in MATLAB®, which offers numerous advantages in e.g. pre- and post-processing and user friendliness. However, DIDO requires the full problem definition to be normalized. This might require repetitive normalization for individual trajectory optimization problems, and is a cumbersome task in itself for the complex models involved in *ECHO*. In addition, it has been shown that of the various pseudospectral methods available the LGL-method shows the poorest convergence for the problems intended to be addressed with the *ECHO* suite [34].

Finally, the package called *General Pseudospectral OPtimal control Software (GPOPS)* [34, 39–45] originally developed at the University of Florida again offers a fully integrated package in MATLAB®. As opposed to DIDO, GPOPS (in different versions) offers the possibility to apply both the Legendre-Gauss and Legendre-Gauss-Radau methods. In addition, GPOPS offers a built-in scaling option to reduce the effort in problem definition, and allows for various methods for differentiation, including numerical methods, automatic differentiation and analytical differentiation. Since GPOPS offers both the selected methodology and the versatile MATLAB® environment to setup trajectory optimization problems and post-process results, GPOPS is selected as the core element of *ECHO*.

Although GPOPS offers a variety of methods to determine the derivatives of the constraints and cost functional, considering the size of the optimization problems to be solved using *ECHO*, analytical differentiation is the fastest and hence preferential method. However, analytically differentiating all models integrated in *ECHO* is certainly no trivial task and would require a large and repetitive effort in case of changing constraints. For that reason, the flight mechanics model and path constraints are differentiated using *Automatic Differentiation (AD)*. In AD, the chain rule is repeatedly applied to all arithmetic operations executed by the computer, hence providing the derivatives with machine precision. The resulting derivatives are therefore equal in value to symbolic derivatives. Although GPOPS offers an integrated package for automatic differentiation, the routines in *ECHO* onto which AD is applied are programmed in the FORTRAN programming language to reduce the computer processing time. To still benefit from automatic differentiation, the FORTRAN-based *AUTO_DERIV* package [46] has been integrated in the FORTRAN modules in *ECHO*. In addition, the derivatives of the noise model are determined numerically. Although initially the noise model – programmed in FORTRAN – was also differentiated using AD, convergence of the noise optimization problems proved to be severely affected. Therefore differentiation of the noise model is achieved with a numerical differentiation based on the midpoint rule.

With the numerical method and optimization package selected, the following sections will give a detailed overview of the direct pseudospectral method based on Radau quadrature as implemented in GPOPS.

3.3 Radau Pseudospectral Method

3.3.1 Radau Quadrature

As mentioned in the previous section, *ECHO* uses a direct collocation method based on Radau quadrature – hereafter referred to as the *Radau Pseudospectral Method (RPM)* [47, 48] – to optimize the helicopter trajectories. The first step in applying this pseudospectral collocation method is to discretize the vehicle's dynamics. In collocation methods, the location of the discretization points does not necessarily have to be fixed. However, since the RPM uses *Radau quadrature* to accurately approximate the system dynamics, the location of these points within the time domain is prescribed in order to minimize the error of the approximation. The general form of Radau quadrature looks as follows

$$\int_{-1}^{1} f(x)\,dx \approx w_1 f(-1) + \sum_{i=2}^{n} w_i f(x_i) \tag{3.18}$$

with weights w_i for the abscissae dependent on the Legendre polynomial P defined as

$$w_i = \frac{1 - x_i}{n^2 \left[P_{n-1}(x_i)\right]^2} \tag{3.19}$$

and for the initial point as

$$w_1 = \frac{2}{n^2} \tag{3.20}$$

Although strictly Radau quadrature is less accurate than Gauss quadrature, the latter is defined on the interval $x \in (-1, 1)$, as opposed to $x \in (-1, 1]$ for Radau quadrature. This characteristic – implicitly including one of the endpoints – makes Radau quadrature, and as a result the RPM, specifically suitable for finite horizon problems involving either a free initial or final time [34]. For the problems under consideration in this research, the integration interval is defined as $t \in [t_0, t_f]$. However, Radau quadrature requires an integration interval to be defined of the form $\tau \in [-1, 1]$. Therefore, the problem defined in Section 3.2.1 is first transcribed to the new interval using

$$\tau = \frac{2t}{t_f - t_0} - \frac{t_f + t_0}{t_f - t_0} \tag{3.21}$$

Given that Radau quadrature is used, the most accurate approximation of the vehicle's dynamics is then found at the so-called *LGR points*, which are the roots of $P_k(\tau) - P_{k-1}(\tau)$, with P_k the Legendre polynomial of the k^{th} order. Hence, the LGR points are used to discretize and collocate the continuous problem.

Furthermore, as with most pseudospectral methods, the RPM uses Lagrange interpolating polynomials to approximate the vehicle's states at the discretization points. When considering a set of distinct points $(x_1, y_1), \ldots, (x_i, y_i), \ldots, (x_n, y_n)$, the Lagrange polynomial is the polynomial of the least degree that satisfies the condition $f(x_i) = y_i$ for all points in the set. Now, considering a problem of N discretization points ($N-1$ LGR points and $\tau_N \equiv 1$), the problem's state is then approximated using Lagrange polynomials and discretized as

$$\mathbf{x}(\tau) \approx \mathbf{X}(\tau) = \sum_{i=1}^{N} \mathbf{X}(\tau_i)\, \mathcal{L}_i(\tau) \tag{3.22}$$

where the Lagrange polynomial $\mathcal{L}_i(\tau), (i = 1, \ldots, N)$ is defined as

$$\mathcal{L}_i(\tau) = \prod_{j=1, j\neq i}^{N} \frac{\tau - \tau_j}{\tau_i - \tau_j} \tag{3.23}$$

The process of Lagrange interpolation and discretization to the LGR points is visualized in Fig. 3.2.

3.3.2 Orthogonal Collocation

The second step in transcribing a continuous optimal control problem into an NLP problem is transforming the dynamic constraints of Eq. (3.2) into algebraic equations. for this purpose, pseudospectral methods use *orthogonal collocation* to collocate the derivatives of the approximated vehicle states of Eq. (3.22) with the dynamic constraints. The collocation points are again the roots of the orthogonal Legendre polynomials $P_k(\tau) - P_{k-1}(\tau)$. However, in contrast to the discretization points, these points do not include the terminal point $\tau_N \equiv 1$. With the RPM, this means that there are K collocation points, with $K = N - 1$ and $\mathcal{K} \subset \mathcal{N}$. So, the collocation points in the RPM are in fact the $N-1$ LGR points. The state derivative at the k^{th} collocation point can then be defined as

$$\dot{\mathbf{x}}(\tau_k) \approx \dot{\mathbf{X}}(\tau_k) = \sum_{i=1}^{N} \dot{\mathcal{L}}_i(\tau_k)\, \mathbf{X}(\tau_k) = \sum_{i=1}^{N} D_{ki} \mathbf{X}(\tau_k), \qquad (k = 1, \ldots, K) \tag{3.24}$$

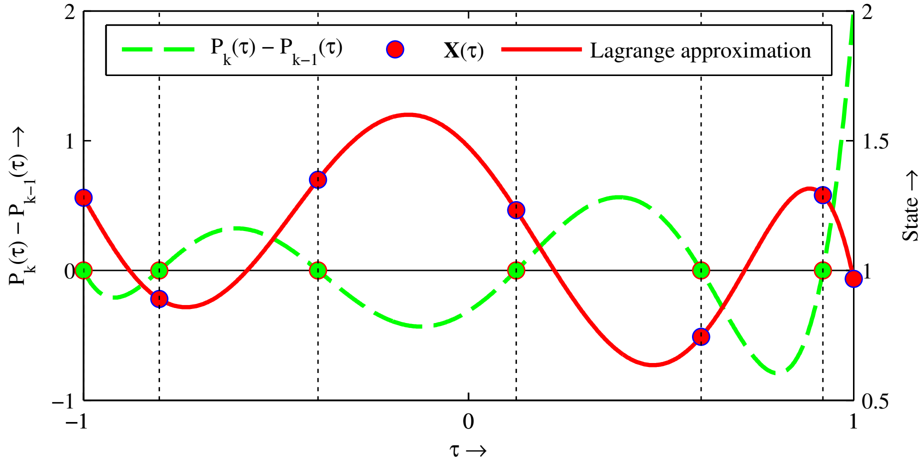

Figure 3.2: Lagrange interpolating polynomial

where the differentiation matrix $D_{ki} \in \mathbb{R}^{K \times N}$ can be defined as

$$D_{ki} = \begin{cases} \frac{\dot{g}(\tau_k)}{(\tau_k - \tau_i)\dot{g}(\tau_i)}, & \text{if } k \neq i \\ \frac{\ddot{g}(\tau_i)}{2\dot{g}(\tau_i)}, & \text{if } k = i \end{cases} \tag{3.25}$$

with

$$g(\tau_i) = (1 + \tau_i)\left[P_k(\tau_i) - P_{k-1}(\tau_i)\right] \tag{3.26}$$

The continuous dynamics as defined in Eq. (3.2) can then be collocated with the approximated vehicle states of Eq. (3.22), where Eq. (3.21) is used to define

$$\frac{\partial \mathbf{x}}{\partial \boldsymbol{\tau}} = \frac{d\mathbf{t}}{d\boldsymbol{\tau}} \frac{\partial \mathbf{x}}{\partial \mathbf{t}} = \frac{t_f - t_0}{2} \mathbf{f} \tag{3.27}$$

which subsequently leads to the collocation constraint

$$\sum_{i=1}^{N} D_{ki} \mathbf{X}(\tau_i) - \frac{t_f - t_0}{2} \mathbf{f}\left(\mathbf{X}(\tau_k), \mathbf{U}(\tau_k)\right) = \mathbf{0}, \qquad (k = 1, \ldots, K) \tag{3.28}$$

For both the collocation constraint of Equation (3.28) and the quadrature approximation of the Lagrange part of the cost functional in Eq. (3.1), the control needs to be discretized on the collocation points as well. Since the derivative of $\mathbf{U}_k$ is not required, no specific form of approximation is required as opposed to the state approximation. Therefore, GPOPS offers a number of possible control approximations, which all satisfy the requirement that $\mathbf{u}(\tau_k) = \mathbf{U}_k, \quad (k = 1, \ldots, K)$. For consistency, however, in this work Lagrange interpolation is used for the control approximation as well, resulting in

$$\mathbf{u}(\tau) \approx \mathbf{U}(\tau) = \sum_{k=1}^{K} \tilde{\mathcal{L}}_k(\tau)\,\mathbf{U}(\tau_k) \tag{3.29}$$

Note that the final control at $\tau_N = 1$ is not defined by this equation. To resolve this, Equation (3.29) is also used to extrapolate the control to the terminal point.

3.3.3 Discretization of the Continuous Bolza Problem

In summary, with the discretization and collocation process described in the previous sections, the Continuous Bolza Problem of Section 3.2.1 can be transcribed to the following NLP problem:

Minimize

$$J = \Phi(\mathbf{X}_0, t_0, \mathbf{X}_f, t_f) + \frac{t_f - t_0}{2} \sum_{k=1}^{K} w_k g(\mathbf{X}_k, \mathbf{U}_k, \tau_k; t_0, t_f) \tag{3.30}$$

subject to the dynamic constraints

$$\sum_{i=1}^{N} D_{ki}\mathbf{X}(\tau_i) - \frac{t_f - t_0}{2}\mathbf{f}(\mathbf{X}(\tau_k), \mathbf{U}(\tau_k)) = \mathbf{0}, \qquad (k = 1, \ldots, K) \tag{3.31}$$

boundary constraints

$$\boldsymbol{\phi}(\mathbf{X}_0, t_0, \mathbf{X}_f, t_f) = \mathbf{0} \tag{3.32}$$

and the path constraints

$$\mathbf{C}(\mathbf{X}_k, \mathbf{U}_k, \tau_k; t_0, t_f) \leq \mathbf{0}, \qquad (k = 1, \ldots, K) \tag{3.33}$$

For the sake of brevity, the equation for Radau quadrature from Eq. (3.18) has been written here (and onward) as

$$\int_{-1}^{1} f(x)\,dx \approx w_1 f(-1) + \sum_{i=2}^{n} w_i f(x_i) = \sum_{i=1}^{n} w_i f(x_i) \tag{3.34}$$

3.3.4 First-Order Optimality Conditions

Considering the NLP problem presented in the previous section, the next step in the optimization process is to define the first order optimality conditions. As opposed to the indirect method for solving the optimal control problem, in direct methods there is no need to derive these conditions. A solution to the NLP problem should comply with the first-order optimality conditions, but these can be determined directly from the gradients which are available through numerical, automatic, analytical or any other form of differentiation. As with indirect methods, the first step is to augment the cost function of Eq. (3.30). The cost function is augmented with *Lagrange multipliers* to find the constrained optimum of the problem. The cost function of Eq. (3.30) is augmented with the Lagrange multipliers $\tilde{\mathbf{\Lambda}}_k \in \mathbb{R}^n$, $\tilde{\boldsymbol{\mu}}_k \in \mathbb{R}^c$, $k = 1, \ldots, K$, and $\tilde{\boldsymbol{\nu}} \in \mathbb{R}^q$, yielding

$$\begin{aligned} J_a \quad = \quad & \Phi\left(\mathbf{X}_1, t_0, \mathbf{X}_N, t_f\right) + \frac{t_f - t_0}{2} \sum_{k=1}^{K} w_k g\left(\mathbf{X}_k, \mathbf{U}_k, \tau_k; t_0, t_f\right) - \\ & \sum_{k=1}^{K} \tilde{\boldsymbol{\mu}}_k^T \mathbf{C}\left(\mathbf{X}_k, \mathbf{U}_k, \tau_k; t_0, t_f\right) - \tilde{\boldsymbol{\nu}}^T \boldsymbol{\phi}\left(\mathbf{X}_1, t_0, \mathbf{X}_N, t_f\right) - \\ & \sum_{k=1}^{K} \tilde{\mathbf{\Lambda}}_k^T \left(\sum_{i=1}^{N} D_{ki} \mathbf{X}_i - \frac{t_f - t_0}{2} \mathbf{f}\left(\mathbf{X}_k, \mathbf{U}_k, \tau_k; t_0, t_f\right) \right) \end{aligned} \tag{3.35}$$

Setting the derivatives of J_a with respect to the Lagrange multipliers, $\mathbf{X}_0$, $\mathbf{X}_f$, $\mathbf{X}_k$, $\mathbf{U}_k$, t_0, and t_f equal to zero yields the first-order optimality conditions. Hence, the solution of the NLP problem defined in the previous section should satisfy

$$\mathbf{C}_k \leq \mathbf{0} \rightarrow \begin{cases} \tilde{\mu}_{jk} = 0, \text{when } C_{jk} < 0, & (j = 1, \ldots, c; k = 1, \ldots, K) \\ \tilde{\mu}_{jk} \leq 0, \text{when } C_{jk} = 0, & (j = 1, \ldots, c; k = 1, \ldots, K) \end{cases} \tag{3.36}$$

$$\boldsymbol{\phi}\left(\mathbf{X}_0, t_0, \mathbf{X}_f, t_f\right) = \mathbf{0} \tag{3.37}$$

$$\begin{aligned} & \frac{\partial \Phi}{\partial \mathbf{X}_1} + \frac{t_f - t_0}{2} \left[w_1 \frac{\partial g_1}{\partial \mathbf{X}_1} + \tilde{\mathbf{\Lambda}}_1^T \frac{\partial \mathbf{f}_1}{\partial \mathbf{X}_1} \right] - \\ & \qquad \tilde{\boldsymbol{\mu}}_1^T \frac{\partial \mathbf{C}_1}{\partial \mathbf{X}_1} - \tilde{\boldsymbol{\nu}}^T \frac{\partial \phi}{\partial \mathbf{X}_1} - \sum_{i=1}^{K} \tilde{\mathbf{\Lambda}}_i^T D_{1i}^{\dagger} \quad = \quad \mathbf{0} \end{aligned} \tag{3.38}$$

$$\frac{\partial \Phi}{\partial \mathbf{X}_N} - \tilde{\boldsymbol{\nu}}^T \frac{\partial \phi}{\partial \mathbf{X}_N} - \sum_{i=1}^{K} \tilde{\mathbf{\Lambda}}_i^T D_{iN}^{\dagger} = \mathbf{0} \tag{3.39}$$

$$\frac{t_f - t_0}{2}\left[w_k \frac{\partial g_k}{\partial \mathbf{X}_k} + \tilde{\boldsymbol{\Lambda}}_k^T \frac{\partial \mathbf{f}_k}{\partial \mathbf{X}_k}\right] - \tilde{\boldsymbol{\mu}}_k^T \frac{\partial \mathbf{C}_k}{\partial \mathbf{X}_k} - \sum_{i=1}^{K} \tilde{\boldsymbol{\Lambda}}_i^T D_{ki}^{\dagger} = \mathbf{0}, \quad (k = 1, \ldots, K) \tag{3.40}$$

$$\begin{aligned} \frac{\partial \Phi}{\partial t_0} - \frac{1}{2}\sum_{k=1}^{K}\left[w_k g_k + \tilde{\boldsymbol{\Lambda}}_k^T \mathbf{f}_k\right] + \frac{t_f - t_0}{2}\left[w_k \frac{\partial g_k}{\partial t_0} + \tilde{\boldsymbol{\Lambda}}_k^T \frac{\partial \mathbf{f}_k}{t_0}\right] - & \\ \sum_{k=1}^{K} \tilde{\boldsymbol{\mu}}_k^T \frac{\partial \mathbf{C}_k}{\partial t_0} - \boldsymbol{\nu}^T \frac{\partial \phi}{\partial t_0} &= \mathbf{0} \end{aligned} \tag{3.41}$$

$$\begin{aligned} \frac{\partial \Phi}{\partial t_f} + \frac{1}{2}\sum_{k=1}^{K}\left[w_k g_k + \tilde{\boldsymbol{\Lambda}}_k^T \mathbf{f}_k\right] + \frac{t_f - t_0}{2}\left[w_k \frac{\partial g_k}{\partial t_f} + \tilde{\boldsymbol{\Lambda}}_k^T \frac{\partial \mathbf{f}_k}{t_f}\right] - & \\ \sum_{k=1}^{K} \tilde{\boldsymbol{\mu}}_k^T \frac{\partial \mathbf{C}_k}{\partial t_f} - \boldsymbol{\nu}^T \frac{\partial \phi}{\partial t_f} &= \mathbf{0} \end{aligned} \tag{3.42}$$

$$\frac{2}{t_f - t_0}\left[w_k \frac{\partial g_k}{\partial \mathbf{U}_k} + \tilde{\boldsymbol{\Lambda}}_k^T \frac{\partial \mathbf{f}_k}{\partial \mathbf{U}_k}\right] - \tilde{\boldsymbol{\mu}}_k^T \frac{\partial \mathbf{C}_k}{\partial \mathbf{U}_k} = \mathbf{0}, \qquad (k = 1, \ldots, K) \tag{3.43}$$

$$\sum_{i=1}^{N} D_{ki} \mathbf{X}_i - \frac{t_f - t_0}{2} \mathbf{f}_k = \mathbf{0}, \qquad (k = 1, \ldots, K) \tag{3.44}$$

where the vehicle's dynamics, the Lagrange cost contribution and the path constraints are defined as $\mathbf{f}_k = \mathbf{f}(\mathbf{X}_k, \mathbf{U}_k, \tau_k; t_0, t_f)$, $g_k = g(\mathbf{X}_k, \mathbf{U}_k, \tau_k; t_0, t_f)$, and $\mathbf{C}_k = \mathbf{C}(\mathbf{X}_k, \mathbf{U}_k, \tau_k; t_0, t_f)$.

3.3.5 Multi-Phase Problem Definition

To allow different phases of the trajectories to have different dynamics or path constraints, GPOPS offers the possibility to use multiple phases to define the full trajectory optimization problem. In case a multi-phase problem definition is required, the total cost functional of all phases can be defined as

$$J = \sum_{p=1}^{P} J^p \tag{3.45}$$

for P phases. In addition, each phase may have its own set of differential equations $\dot{\mathbf{x}}^p$, boundary conditions $\boldsymbol{\phi}^p$, and state constraints $\mathbf{C}^p$. Any two phases can be connected provided that the independent variable t does not change direction. Some possible phase linkages can be seen in Fig. 3.3. The total number of connecting points is L. Then consider the phase to the left of the linkage point, $(p_l^s \in [1, \ldots, P], (s = 1, \ldots, L))$. This phase has to be connected to the phase to the right of the connecting point, $(p_u^s \in [1, \ldots, P], (s = 1, \ldots, L))$. The L linkage constraints define the constraint connecting these phases, and are used to ensure continuity in the state, parameter and time vector if required. The linkage constraint $\mathbf{P}^s$ can be defined as

$$\begin{aligned} &\mathbf{P}^s \left(\mathbf{x}^{p_l^s}(t_f), t_f^{p_l^s}; \mathbf{q}^{p_l^s}, \mathbf{x}^{p_u^s}(t_0), t_0^{p_u^s}; \mathbf{q}^{p_u^s} \right) = \mathbf{0}, \\ &\qquad (p_l^s, p_u^s \in [1, \ldots, P], s = 1, \ldots, L) \end{aligned} \tag{3.46}$$

where $\mathbf{x}^p \in \mathbb{R}^{n_p}$, $\mathbf{q}^p \in \mathbb{R}^{m_p}$ and $t \in \mathbb{R}$ are the state, parameter and time in phase p.

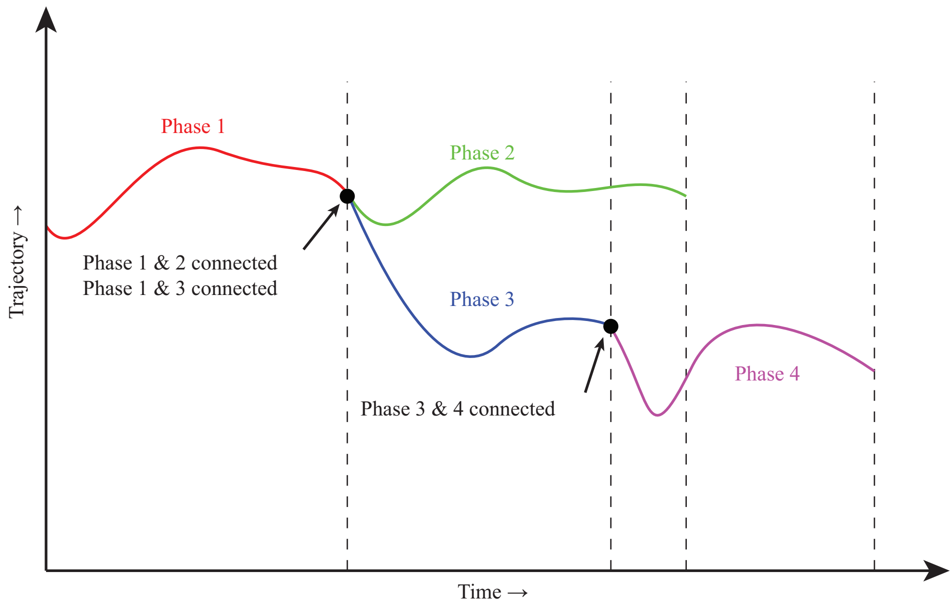

Figure 3.3: Potential phase connections

3.4 NLP Solver

The Radau Pseudospectral Method described in the previous sections is applied to the optimal control problem to discretize the continuous problem and transcribe it to a finite-dimensional Non-Linear Programming (NLP) problem of the general form

$$\begin{aligned} &\underset{x}{\text{minimize}} \quad F(\mathbf{x}) \\ &\text{subject to} \quad \mathbf{l} \le \begin{pmatrix} \mathbf{f}(\mathbf{x}) \\ A_L \mathbf{x} \end{pmatrix} \le \mathbf{u} \end{aligned} \tag{3.47}$$

with $F(\mathbf{x})$ the objective functional, $\mathbf{f}(\mathbf{x})$ the set of non-linear constraints and $\mathbf{A}_L\mathbf{x}$ the set of linear constraints. The lower and upper bounds to the constraints are defined as $\mathbf{l}$ and $\mathbf{u}$. To solve the problem defined in equation (3.47), a numerical solver called *Sparse Nonlinear OPTimizer (SNOPT)* [49, 50] is employed in GPOPS. SNOPT is a well-known solver for the minimization of constrained large-scale NLP problems, and was developed at the University of California. Providing the first derivatives for the cost functional and the constraints further increases the efficiency of SNOPT to solve the problem.

SNOPT uses *Sequential Quadratic Programming (SQP)* to solve the NLP problem. Therefore, first all constraints have to be defined as equality constraints through the introduction of *slack* variables as follows

$$\begin{pmatrix} \mathbf{f}(\mathbf{x}) \\ \mathbf{A}_L\mathbf{x} \end{pmatrix} - \mathbf{s} = \mathbf{0} \tag{3.48}$$

where $\mathbf{s}$ is a vector containing linear and non-linear slack variables, $\mathbf{s}_L$ and $\mathbf{s}_N$ respectively. The objective of the SQP is now to generate a sequence of iterates $\mathbf{x}_k$ that converge to a solution satisfying the first-order optimality conditions. At each iterate $\mathbf{x}_k$ a *Quadratic Programming (QP)* sub-problem can be defined by linearizing the non-linear constraints at the solution $\mathbf{x}_k$. This yields the following set of constraints

$$\begin{pmatrix} \mathbf{f}'(\mathbf{x}_k)\mathbf{x} - \mathbf{s}_N \\ \mathbf{A}_L\mathbf{x} - \mathbf{s}_L \end{pmatrix} = \begin{pmatrix} -\mathbf{f}(\mathbf{x}_k) + \mathbf{f}'(\mathbf{x}_k)\mathbf{x}_k \\ \mathbf{0} \end{pmatrix} = \mathbf{b} \tag{3.49}$$

where $\mathbf{f}'_k(\mathbf{x}_k)$ denotes the Jacobian matrix whose elements are the first derivatives of the constraints $\mathbf{f}(\mathbf{x})$ evaluated at the iterate $\mathbf{x}_k$. Next, a quadratic approximation of the Lagrangian is defined which, along with the linearized constraints forms the QP sub-problem at the iterate $\mathbf{x}_k$

$$\begin{aligned} &\underset{x}{\text{minimize}} && \mathbf{q}(\mathbf{x}, \mathbf{x}_k) = \mathbf{g}_k^T(\mathbf{x} - \mathbf{x}_k) + \tfrac{1}{2}(\mathbf{x} - \mathbf{x}_k)^T H_k (\mathbf{x} - \mathbf{x}_k) \\ &\text{subject to} && \begin{pmatrix} \mathbf{f}'(\mathbf{x}_k) \\ \mathbf{A}_L \end{pmatrix} \mathbf{x} - \mathbf{s} = \mathbf{b} \end{aligned} \tag{3.50}$$

where H_k is a quasi-Newton approximation of the Hessian matrix of the Lagrangian function. The solution to the QP sub-problem satisfies the linear constraints and provides a search direction for the next iterate $\mathbf{x}_{k+1}$ that progresses towards an optimal solution. Similar to the method described in Section 3.3.4 an *augmented Lagrangian merit function* is defined as follows

$$\mathcal{M}(\mathbf{x}, \mathbf{s}, \boldsymbol{\lambda}) = F(\mathbf{x}) - \boldsymbol{\lambda}^T (\mathbf{f}(\mathbf{x}) - \mathbf{S}_N) + \frac{1}{2} (\mathbf{f}(\mathbf{x}) - \mathbf{S}_N)^T D (\mathbf{f}(\mathbf{x}) - \mathbf{S}_N) \tag{3.51}$$

where $\boldsymbol{\lambda}$ are the costates for the nonlinear constraints and D is a diagonal matrix of penalty parameters ($D_{ii} \geq 0$). The augmented Lagrangian merit function is then evaluated using a line search. For this line search, the solution to the QP sub-problem determines the search direction, which leaves the step size to be determined. Then consider the current estimate $(\mathbf{x}_k, \mathbf{s}_k, \boldsymbol{\lambda}_k)$ and the solution to the QP $(\hat{\mathbf{x}}_k, \hat{\mathbf{s}}_k, \hat{\boldsymbol{\lambda}}_k)$. The new iterate is then found by defining

$$\begin{pmatrix} \mathbf{x}_{k+1} \\ \mathbf{s}_{k+1} \\ \boldsymbol{\lambda}_{k+1} \end{pmatrix} = \begin{pmatrix} \mathbf{x}_k \\ \mathbf{s}_k \\ \boldsymbol{\lambda}_k \end{pmatrix} + \alpha_k \begin{pmatrix} \hat{\mathbf{x}}_k - \mathbf{x}_k \\ \hat{\mathbf{s}}_k - \mathbf{s}_k \\ \hat{\boldsymbol{\lambda}}_k - \boldsymbol{\lambda}_k \end{pmatrix} \tag{3.52}$$

and looking for a step size $(0 < \alpha_k \leq 1)$ for which a sufficient decrease of the merit function is achieved. If so required the penalty parameters D are increased to ensure a sufficient progress is achieved. Once the solution $\mathbf{x}_n$ satisfies the first-order optimality conditions the optimal solution $\mathbf{x}^*$ has been reached and the process is terminated.

3.5 Conclusions

This chapter presented the selection process for the gradient-based optimization algorithm used in *ECHO*. It was concluded that a direct solution method offers the best approach to solve the trajectory problems in *ECHO*. For these methods initialization of a new problem is significantly less complex as compared to indirect solution methods, requiring less complex problem setups and hence resulting in a more flexible and versatile optimization software suite. Furthermore, a method based on pseudospectral collocation with Radau quadrature has been selected. Pseudospectral collocation allows for a relatively easy imposition of constraints on both the state and control variables, and the use of quadrature for the integration of the system state derivatives results in a higher accuracy with a smaller problem size. Finally, the use of Radau quadrature was found to show good convergence behavior, and can be shown to be specifically suitable for the open-ended problems to be solved using *ECHO*.

4
Helicopter Modeling

4.1 Introduction

In order to optimize helicopter trajectories, one of the central models in the *ECHO* suite is a high-fidelity helicopter flight dynamics model as was shown in Chapter 2. The three-dimensional free motion of the helicopter is modeled using an eight Degrees-of-Freedom (DoF) rigid-body dynamic model based on [51]. In this model, the vehicle's state is expressed by the following fourteen *state variables*:

- u, v and w describe the vehicle's speed components,
- p, q and r describe the vehicle's roll, pitch and yaw rate,
- Θ, Ψ and Φ describe the vehicle's pitch, yaw and roll angle,
- x, y and z describe the vehicle's position,
- and $\lambda_{i_{mr}}$ and $\lambda_{i_{tr}}$ describe the dynamic inflow of the main and tail rotor respectively.

In addition, the helicopter control is modeled by the following four *control variables*:

- θ_0 is the main rotor blade collective pitch,
- θ_{1c} is the main rotor lateral cyclic pitch,
- θ_{1s} is the main rotor longitudinal cyclic pitch,
- and $\theta_{0_{tr}}$ is the tail rotor collective pitch.

The following sections will give a detailed overview of the flight dynamics model implemented in *ECHO*.

4.2 Model Overview

4.2.1 Modeling Assumptions

The flight dynamics model developed in [51] and integrated in *ECHO* is expressed in a helicopter body system of reference xyz with the z-axis parallel to the main rotor shaft. The model is based on the following assumptions:

- The main rotor rotates in a counterclockwise direction.
- The total forces and moments are established by adding the component contributions of the main and tail rotor, fuselage, vertical fin and horizontal stabilizer.
- Aerodynamic forces and moments are modeled using Blade Element Theory (BET).
- The tail rotor is modeled as an actuator disc.
- Only steady-state rotor disc-tilt is considered.
- Fuselage, vertical fin and horizontal stabilizer are modeled using linear aerodynamics.
- Dynamic inflow of both the main and tail rotor is modeled as quasi-steady inflow.
- The lead-lag motion of the blades is neglected, and there are no pitch-lag or pitch-flap couplings.
- The blades are rectangular with a linear twist θ_{tw}, and the blade mass is distributed uniformly.
- There are no blade-tip losses.
- Gravitational forces are small compared to aerodynamic, inertial and centrifugal forces.
- The flapping and flow angles are small.
- The main rotor angular velocity Ω is constant.
- Rotor disc-tilt angles a_1 and b_1 are considered positive tilting backwards and to the right, respectively.
- Longitudinal cyclic θ_{1s} and lateral cyclic θ_{1c} are considered positive for forward and rightward stick movement, respectively.
- No reverse flow regions are considered, and the flow is incompressible.

4.2.2 Equations of Motion

As mentioned in the previous section, the total forces and moments are established by determining and adding the individual component contributions. These component contributions acting on the helicopter can be seen in Fig. 4.1 to 4.3, and consist of main rotor components (mr), tail rotor components (tr), vertical fin and horizontal stabilizer components (fin, hs) and fuselage components (fus). When first the total forces (F_x, F_y, F_z) and moments (L, M, N) are considered, and taking into account the position

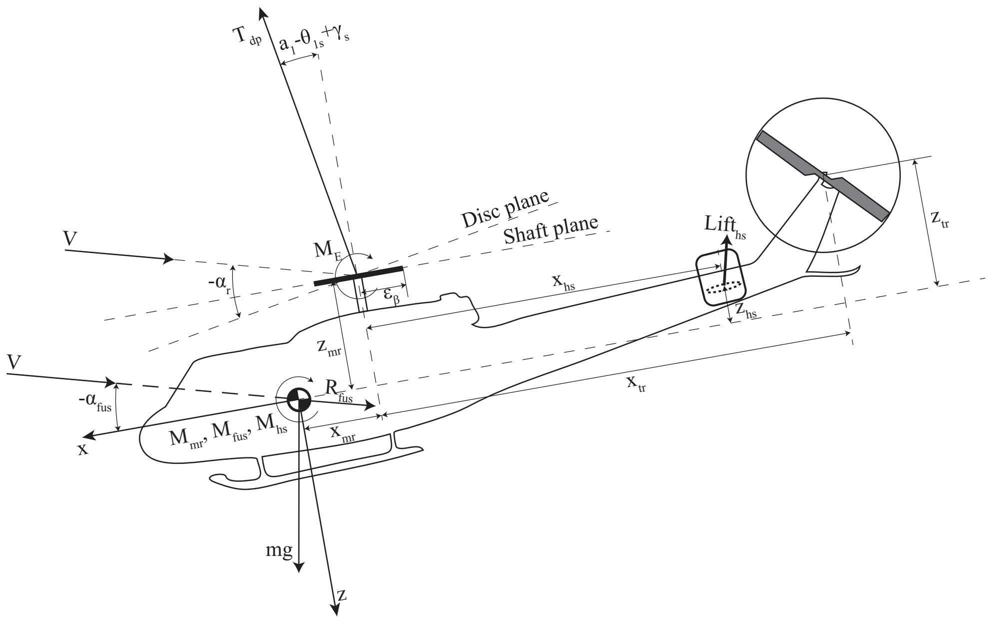

Figure 4.1: Helicopter forces and moments: side view

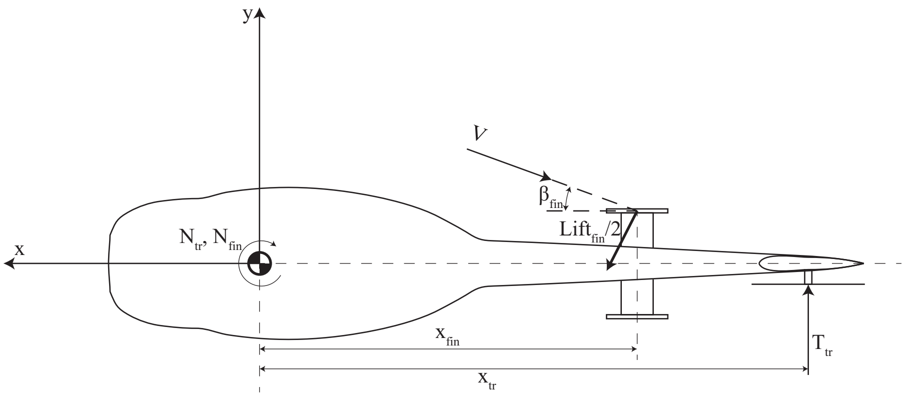

Figure 4.2: Helicopter forces and moments: top view

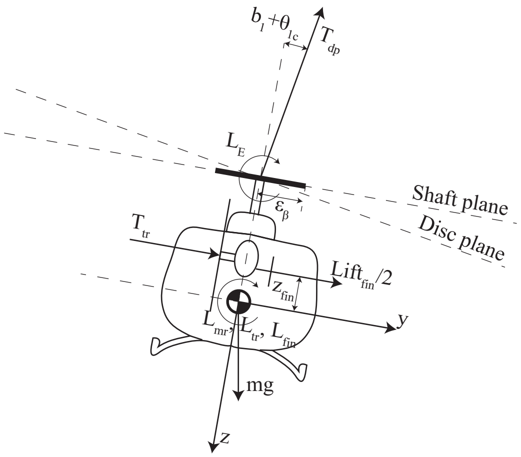

Figure 4.3: Helicopter forces and moments: rear view

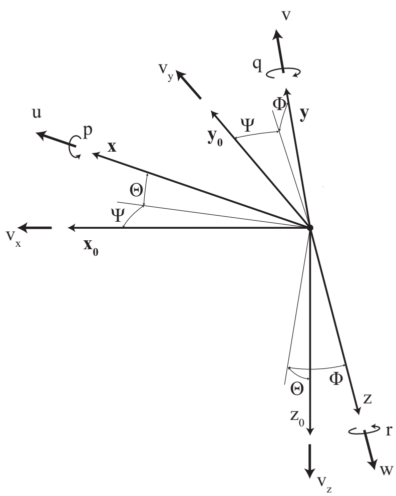

Figure 4.4: Definition of helicopter position with respect to a fixed system

of the helicopter relative to a fixed system $x_0y_0z_0$ as can be seen in Fig. 4.4, the motion of the helicopter can be described using the following equations of motion

$$\dot{u} = \frac{F_x}{m} - qw + rv \tag{4.1}$$

$$\dot{v} = \frac{F_y}{m} - ru + pw \tag{4.2}$$

$$\dot{w} = \frac{F_z}{m} - pv + qu \tag{4.3}$$

$$\dot{p} = \frac{(L - (I_z - I_y)\,qr + J_{xz}\,(\dot{r} + pq))}{I_x} \tag{4.4}$$

$$\dot{q} = \frac{\left(M - (I_x - I_z)\,rp - J_{xz}\left(p^2 - r^2\right)\right)}{I_y} \tag{4.5}$$

$$\dot{r} = \frac{\left(N - (I_y - I_x)\,pq + J_{xz}\left(\frac{(L-(I_z-I_y)qr+J_{xz}pq)}{I_x} - rq\right)\right)}{I_z - \frac{J_{xz}^2}{I_x}} \tag{4.6}$$

$$\dot{\Theta} = q\cos\Phi - r\sin\Phi \tag{4.7}$$

$$\dot{\Psi} = \frac{(q\sin\Phi + r\cos\Phi)}{\cos\Theta} \tag{4.8}$$

$$\dot{\Phi} = p + \dot{\Psi}\sin\Theta \tag{4.9}$$

$$\dot{x} = v_x \tag{4.10}$$

$$\dot{y} = v_y \tag{4.11}$$

$$\dot{z} = v_z \tag{4.12}$$

$$\dot{\lambda}_{i_{mr}} = \frac{C_{T_{mr}}^{elem} - C_{T_{mr}}^{Gl}}{\tau_{\lambda_{i_{mr}}}} \tag{4.13}$$

$$\dot{\lambda}_{i_{tr}} = \frac{C_{T_{tr}}^{elem} - C_{T_{tr}}^{Gl}}{\tau_{\lambda_{i_{tr}}}} \tag{4.14}$$

where I_x, I_y, and I_z are the moments of inertia about the body x-, y-, and z-axis, and J_{xz} is the moment of inertia about the x- and z-axis. The dynamic inflow of the main and tail rotors, $\lambda_{i_{mr}}$ and $\lambda_{i_{tr}}$, is modeled by means of the time constants $\tau_{\lambda_{i_{mr}}}$ and $\tau_{\lambda_{i_{tr}}}$. The dynamic inflow for both rotors depends on the thrust coefficients determined using both the BET [52] (C_T^{elem}) and the Glauert theory [53](C_T^{Gl}).

It is noted that in the above equations of motions the airspeed vector expressed in both a body system of reference $\mathbf{v}_B = (u, v, w)$ and an Earth-fixed system of reference $\mathbf{v}_E = (v_x, v_y, v_z)$ is used. Although the model is expressed in the body system of reference, the airspeed components in the Earth-fixed system are also determined to simplify the enforcement of constraints on the helicopter trajectories. To convert the speed components $\mathbf{v}_B$ to $\mathbf{v}_E$ the following rotation is defined

$$\begin{pmatrix} v_x \\ v_y \\ v_z \end{pmatrix} = T_{BE} \begin{pmatrix} u \\ v \\ w \end{pmatrix} \tag{4.15}$$

with the rotation matrix T_{BE} defined as:

$$\begin{bmatrix} \cos\Theta\cos\Psi & \sin\Phi\sin\Theta\cos\Psi - \cos\Phi\sin\Psi & \cos\Phi\sin\Theta\cos\Psi + \sin\Phi\sin\Psi \\ \cos\Theta\sin\Psi & \sin\Phi\sin\Theta\sin\Psi + \cos\Phi\cos\Psi & \sin\Theta\sin\Psi - \sin\Phi\cos\Psi \\ -\sin\Theta & \sin\Phi\cos\Theta & \cos\Theta \end{bmatrix} \tag{4.16}$$

in which the system is rotated about the x- (Φ), then y- (Θ) and then the z-axis (Ψ).

4.2.3 Component Forces

Main Rotor Forces and Moments

As mentioned above, to find the total body forces and moments acting on the helicopter the individual contributions of the main and tail rotors, the fuselage, and the vertical fin and horizontal stabilizer are determined. To determine the contributions of the main rotor, first the rotor thrust force vector needs to be determined. This requires the steady-state disc tilt angles to be determined, which are the coning angle a_0 and the longitudinal and lateral rotor disc tilt angles, a_1 and b_1, respectively. Given the model assumptions mentioned in the previous section, it can be shown that from the differential equations describing the flapping motion of the main rotor blades the expressions can be derived to determine the steady-state rotor disc tilt angles [51]. The angles are found by solving the system

$$A \begin{pmatrix} a_0 \\ a_1 \\ b_1 \end{pmatrix} = \mathbf{d} \tag{4.17}$$

with

$$A = \begin{bmatrix} 1 & \gamma\mu_x \frac{\left(\frac{1}{4}e^2 - \frac{e}{8}\right)}{\nu_2} & 0 \\ 0 & 1 & \frac{1-\nu_2}{\alpha_1-\alpha_2} \\ \gamma\mu_x \frac{\frac{1}{6}-\frac{e}{4}}{-\alpha_1-\alpha_2} & \frac{1-\nu_2}{-\alpha_1-\alpha_2} & 1 \end{bmatrix} \tag{4.18}$$

$$\begin{aligned} d_1 = & \frac{\gamma}{2\nu_2}\left[\theta_0\left(\left(\frac{1}{4}-\frac{e}{3}\right)+\mu_x^2\left(\frac{e^2}{4}-\frac{e}{2}+\frac{1}{4}\right)\right)+\mu_x\theta_{1s}\left(\frac{e}{2}-\frac{1}{3}\right)\right]+ \\ & \frac{\gamma}{2\nu_2}\left[\theta_{tw}\left(\frac{\mu_x^2}{6}+\frac{1}{5}-\frac{\mu_x^2 e}{4}-\frac{e}{4}\right)-\left(\frac{1}{3}-\frac{e}{2}\right)(\lambda_{i_{mr}}-\mu_z)\right]+ \\ & \frac{\gamma}{2\nu_2}\left[\frac{p\mu_x}{\Omega}\left(\frac{1}{6}-\frac{e}{4}\right)\right] \end{aligned} \tag{4.19}$$

$$\begin{aligned} d_2 = & \frac{\gamma}{\alpha_1-\alpha_2}\left[\theta_{1s}\left(\mu_x^2\left(-0.1875e^2+0.375e-0.1875\right)+\frac{e}{6}-\frac{1}{8}\right)\right]+ \\ & \frac{\gamma}{\alpha_1-\alpha_2}\left[\mu_x\theta_{tw}\left(\frac{1}{4}-\frac{e}{3}\right)-\mu_x\left(\frac{e^2}{4}-\frac{e}{2}+\frac{1}{4}\right)(\lambda_{i_{mr}}-\mu_z)\right]+ \\ & \frac{\gamma}{\alpha_1-\alpha_2}\left[\mu_x\theta_0\left(\frac{1}{3}-\frac{e}{2}\right)+\frac{p}{\Omega}\left(\frac{1}{8}-\frac{e}{6}\right)-\frac{2q}{\Omega\gamma}\right] \end{aligned} \tag{4.20}$$

$$d_3 = \frac{\frac{\gamma}{2}\left(\left(\frac{e}{3}-\frac{1}{4}+\mu_x^2\left(-\frac{e^2}{8}+\frac{e}{4}-\frac{1}{8}\right)\right)\theta_{1c}+\left(\frac{1}{4}-\frac{e}{3}\right)\frac{q}{\Omega}\right)+\frac{2p}{\Omega}}{-\alpha_1-\alpha_2} \tag{4.21}$$

where

$$\alpha_1 = \gamma\left(\frac{1}{4}e^2-\frac{e}{3}+\frac{1}{8}\right) \tag{4.22}$$

$$\alpha_2 = \gamma \left(\mu_x^2 \left(0.0625e^2 - \frac{e}{8} + 0.0625\right)\right) \tag{4.23}$$

where

- γ is the Lock number,
- μ_x and μ_z are the main rotor normalized speed components,
- ν_2 is the main rotor flap frequency ratio,
- and e is the normalized flapping hinge offset.

The steady-state disc-tilt angles determined above define the direction of the main rotor thrust. In order to determine the magnitude of the main rotor thrust force, the main rotor thrust coefficient is determined according to the BET

$$\begin{aligned} C_{T_{mr}}^{elem} &= \frac{C_{l_{\alpha_{mr}}}\sigma_{mr}}{2}\left[\theta_0\left(\frac{1}{3}+\frac{\mu_x^2}{2}\right)+\left(\theta_{1s}+\frac{p}{2\Omega}\right)\frac{\mu_x}{2}+\right]+ \\ &\quad \frac{C_{l_{\alpha_{mr}}}\sigma_{mr}}{2}\left[\frac{1}{2}\left(\mu_z-\lambda_{i_{mr}}\right)+\left(\mu_x^2+1\right)\frac{\theta_{tw}}{4}\right] \end{aligned} \tag{4.24}$$

where σ_{mr} is the main rotor disc solidity and $C_{l_{\alpha_{mr}}}$ is the main rotor blade lift curve slope. In addition, to model the quasi-steady inflow angles of the main rotor, the thrust coefficient is also determined using the Glauert theory. This follows from the requirement that in steady conditions the thrust coefficient defined above should equal the thrust coefficient following from the Glauert theory which is defined as

$$C_{T_{mr}}^{Gl} = 2\lambda_{i_{mr}}\sqrt{\mu_x^2 + \left(\lambda_{i_{mr}} - \mu_z\right)^2} \tag{4.25}$$

The total main rotor thrust force is then defined as

$$T_{mr} = C_{T_{mr}}^{elem}\rho\left(\Omega R\right)^2 \pi R^2 \tag{4.26}$$

where ρ is the local air density and R is the main rotor radius. This defines the complete main rotor thrust vector. It is assumed that the lateral and longitudinal forces of the main rotor are sufficiently small, and can therefore be neglected. As a result, the total main rotor forces along the three body axes can be defined as follows

$$X_{mr} = -T_{mr}\sin(a_1 - \theta_{1s} + \gamma_s)\cos(b_1 + \theta_{1c}) \tag{4.27}$$

$$Y_{mr} = T_{mr}\sin(b_1 + \theta_{1c}) \tag{4.28}$$

$$Z_{mr} = -T_{mr}\cos(a_1 - \theta_{1s} + \gamma_s)\cos(b_1 + \theta_{1c}) \tag{4.29}$$

where γ_s is the main rotor forward shaft tilt angle.

As a result of the flapping hinge eccentricity with respect to the main rotor shaft, ϵ_β, the main rotor also introduces moments about the main rotor hub

$$L_e = (\Omega R)^2 e m_{mr}\sin(b_1 + \theta_{1c}) \tag{4.30}$$

$$M_e = (\Omega R)^2 e m_{mr}\sin(a_1 - \theta_{1s} + \gamma_s) \tag{4.31}$$

which represent a pitch and roll moment respectively. Here, m_{mr} is the total main rotor blade mass. The flapping hinge eccentricity moments are then added to the moments about the helicopter's center of gravity induced by the main rotor forces to form the total main rotor moments defined as

$$L_{mr} = Y_{mr} z_{mr} + L_e \tag{4.32}$$

$$M_{mr} = -X_{mr} z_{mr} - Z_{mr} x_{mr} + M_e \tag{4.33}$$

$$N_{mr} = \frac{P_{req}}{\Omega} - Y_{mr} x_{mr} \tag{4.34}$$

where x_{mr} and z_{mr} define the main rotor position with respect to the helicopter's center of gravity, and P_{req} is the total required engine power.

Tail Rotor Forces and Moments

The process of determining the tail rotor thrust is similar to that of the main rotor. However, as the tail rotor is modeled as an actuator disc, only the total tail rotor thrust force is required. Therefore first the thrust coefficients following from the BET and Glauert theory are defined as follows

$$C_{T_{tr}}^{elem} = \frac{C_{l_{\alpha_{tr}}}\sigma_{tr}}{2}\left[\theta_{0_{tr}}\left(\frac{1}{3} + \frac{\mu_{x_{tr}}^2}{2}\right) + \frac{1}{2}\left(\mu_{z_{tr}} - \lambda_{i_{tr}}\right)\right] \tag{4.35}$$

$$C_{T_{tr}}^{Gl} = 2\lambda_{i_{tr}}\sqrt{\mu_{x_{tr}}^2 + \left(\lambda_{i_{tr}} - \mu_{z_{tr}}\right)^2} \tag{4.36}$$

Next, the total tail rotor thrust can be determined by

$$T_{tr} = C_{T_{tr}}^{elem} \rho \left(\Omega_{tr} R_{tr}\right)^2 \pi R_{tr}^2 \tag{4.37}$$

which yields the following forces and moments

$$Y_{tr} = T_{tr} f_{tr} \tag{4.38}$$

$$L_{tr} = Y_{tr} z_{tr} \tag{4.39}$$

$$N_{tr} = -Y_{tr} x_{tr} \tag{4.40}$$

where f_{tr} is the tail rotor fin blockage factor and x_{tr} and z_{tr} describe the position of the tail rotor with respect to the helicopter's center of gravity. The normalized speed components $\mu_{x_{tr}}$ and $\mu_{z_{tr}}$ for the tail rotor are defined as

$$\mu_{x_{tr}} = \frac{\sqrt{u^2 + \left(w + k_{1_{tr}} \lambda_{i_{mr}} \Omega R + q x_{tr}\right)^2}}{\Omega_{tr} R_{tr}} \tag{4.41}$$

$$\mu_{z_{tr}} = \frac{-\left(v - x_{tr} r + z_{tr} p\right)}{\Omega_{tr} R_{tr}} \tag{4.42}$$

where $k_{1_{tr}}$ is the main rotor downwash factor at the tail rotor.

Fuselage Forces and Moments

The fuselage only exerts a parasite drag force on the helicopter. This drag force can be defined as follows

$$R_{fus} = \frac{1}{2} \rho V^2 F_0 \tag{4.43}$$

where V is the total airspeed and F_0 is the fuselage parasite drag area. The resulting fuselage forces and moments then depend on the fuselage angle of attack α_{fus}, the fuselage equivalent volume, Vol_{fus} and the fuselage pitch coefficient correction factor K_{fus}. The fuselage forces and moments can then be described by

$$X_{fus} = -R_{fus} \cos \alpha_{fus} \tag{4.44}$$

$$Z_{fus} = -R_{fus} \sin \alpha_{fus} \tag{4.45}$$

$$M_{fus} = \rho V^2 K_{fus} Vol_{fus} \alpha_{fus} \tag{4.46}$$

Horizontal Stabilizer Forces and Moments

For the horizontal stabilizer, only the lift force is considered, which first requires the local airspeed and angle of attack to be determined from

$$\alpha_{hs} = \alpha_{0_{hs}} + \tan^{-1}\left(\frac{w + qx_{hs}}{u}\right) \tag{4.47}$$

$$V_{hs} = \sqrt{u^2 + (w + qx_{hs})^2} \tag{4.48}$$

where $\alpha_{0_{hs}}$ is the horizontal stabilizer angle of incidence. The horizontal stabilizer lift force and the resulting moment can then be defined as

$$Z_{hs} = -\frac{1}{2}\rho V_{hs}^2 0.65 S_{hs} C_{l_{\alpha_{hs}}} \alpha_{hs} \tag{4.49}$$

$$M_{hs} = Z_{hs} x_{hs} \tag{4.50}$$

where $C_{l_{\alpha_{hs}}}$ is the horizontal stabilizer lift curve slope, S_{hs} is the surface area and x_{hs} is the distance between the horizontal stabilizer and the helicopter's center of gravity along the x-axis.

Vertical Fin Forces and Moments

As with the horizontal stabilizer, the vertical tail is only considered for its lift force, again requiring the angle of attack and the local velocity to be determined using

$$\beta_{fin} = \beta_{0_{fin}} + \tan^{-1}\left(\frac{v - rx_{fin} + pz_{fin}}{u}\right) \tag{4.51}$$

$$V_{fin} = \sqrt{u^2 + (v - rx_{fin} + pz_{fin})^2} \tag{4.52}$$

The lift force and resulting moments can then be defined as

$$Y_{fin} = -\frac{1}{2}\rho V_{fin}^2 S_{fin} C_{l_{\alpha_{fin}}} \beta_{fin} \tag{4.53}$$

$$L_{fin} = z_{fin} Y_{fin} \tag{4.54}$$

$$N_{fin} = -x_{fin} Y_{fin} \tag{4.55}$$

4.2.4 Total Forces and Moments on the Helicopter

In the previous section the component contributions to the forces and moments of the main and tail rotor, horizontal stabilizer, vertical fin and fuselage were defined. With the component contributions known, the total forces acting on the helicopter can be expressed as follows

$$F_x = -W \sin\Theta + X_{mr} + X_{fus} \tag{4.56}$$

$$F_y = W \cos\Theta \sin\Phi + Y_{mr} + Y_{tr} + Y_{fin} \tag{4.57}$$

$$F_z = W \cos\Theta \cos\Phi + Z_{mr} + Z_{fus} + Z_{hs} \tag{4.58}$$

where W is the total helicopter weight. Also the total moments about the helicopter's center of gravity can now be defined

$$L = L_{mr} + L_{tr} + L_{fin} \tag{4.59}$$

$$M = M_{mr} + M_{fus} + M_{hs} \tag{4.60}$$

$$N = N_{mr} + N_{tr} + N_{fin} \tag{4.61}$$

4.2.5 Required Engine Power

Although the previous sections define the equations of motion of the helicopter, and would suffice to model the helicopter dynamics in *ECHO*, also the required engine power needs to be determined. This is required to determine the main rotor moment about the helicopter's z-axis, but also to determine the helicopter fuel flow and emissions. In addition, the required engine power is required to ensure helicopter operations within the available power limits. The total power required can be defined as

$$P_{req} = P_{par} + P_{ind} + P_{ppd} + P_{tr} + P_c \tag{4.62}$$

and consists of the parasite drag power P_{par}, the induced power P_{ind}, the profile drag power P_{ppd}, the tail rotor power P_{tr}, and finally the climb power P_c. The parasite drag is approximated by using an assumed equivalent flat plate area $\sum(C_D S)_S$. The parasite drag power can then be defined as

$$P_{par} = \frac{1}{2}\sum(C_D S)_S \rho V^3 \tag{4.63}$$

The induced power requires the main rotor induced velocity

$$v_i = \lambda_{i_{mr}} \Omega R \tag{4.64}$$

corrected with a non-uniform induced velocity correction factor k. The induced power can then be expressed as

$$P_{ind} = |k T_{mr} v_i| \tag{4.65}$$

The profile drag power is defined as

$$P_{ppd} = \frac{1}{8} \sigma_{mr} C_d \rho \left(\Omega R\right)^3 \pi R^2 \left(1 + n\mu_x^2\right) \tag{4.66}$$

with the drag coefficient defined as

$$C_d = \delta_0 + \delta_2 \left(C_{T_{mr}}^{elem}\right)^2 \tag{4.67}$$

The tail rotor power, P_{tr} is determined by

$$P_{tr} = \frac{|T_{tr}|}{M_{tr}} \sqrt{\frac{|T_{tr}|}{2\rho\pi R_{tr}^2}} \tag{4.68}$$

where M_{tr} is the figure of merit of the tail rotor. Finally, the climb power is dependent on the vertical speed and the helicopter weight, and can be defined as

$$P_c = -v_z W \tag{4.69}$$

It is noted that as the z-axis is defined as positive downward, a minus sign appears in the expression for the climb power.

4.2.6 Effect of Wind

The flight dynamics model as defined in the previous sections assumes flight in a stationary atmosphere. However, one of the objectives of *ECHO* is to model flight in non-standard atmospheric conditions including wind. Therefore, the velocity components in the Earth-fixed reference frame defined by Eq. (4.15) need to be corrected for wind speeds. In *ECHO* a stationary wind field is assumed that is only dependent on the altitude. This implies that the wind speed vector is not dependent on time, and that the wind speed components are constant in the $x_0 y_0$-plane. The wind velocity can then be defined in the Earth-fixed reference frame and parallel to the ground plane as

$$\mathbf{V}_{w_E} = \begin{pmatrix} V_{w_x} \\ V_{w_y} \end{pmatrix} \tag{4.70}$$

As a result of the wind vector, in Eqs. (4.10) and (4.11) the wind velocity components need to be accounted for to yield the ground speed

$$GS_x = \dot{x} = v_x + V_{w_x} \tag{4.71}$$

$$GS_y = \dot{y} = v_y + V_{w_y} \tag{4.72}$$

Although the wind vector itself is not dependent on time, changing the helicopter's speed vector will result in a change of the wind components relative to the helicopter's motion. This will result in a time-dependency in the effective wind vector which needs to be accounted for in the body accelerations defined in Eqs. (4.1) to (4.3). From [54] it can be derived that the change in the effective wind velocity affects the accelerations as follows

$$\dot{u} = \frac{F_x}{m} - q(w + w_w) + r(v + v_w) - \dot{u}_w \tag{4.73}$$

$$\dot{v} = \frac{F_y}{m} - r(u + u_w) + p(w + w_w) - \dot{v}_w \tag{4.74}$$

$$\dot{w} = \frac{F_z}{m} - p(v + v_w) + q(u + u_w) - \dot{w}_w \tag{4.75}$$

In Eqs. (4.73) to (4.75), the wind velocity components are expressed in the helicopter's body system, $\mathbf{V}_{w_B} = (u_w, v_w, w_w)$. This requires the wind vector to be transformed from the Earth-fixed system to the body-fixed system defined as using the following transformation

$$\mathbf{V}_{w_B} = T_{EB}\mathbf{V}_{w_E}, \tag{4.76}$$

with the rotation matrix T_{EB} defined as

$$\begin{bmatrix} \cos\Theta\cos\Psi & \cos\Theta\sin\Psi \\ \sin\Phi\sin\Theta\cos\Psi - \cos\Phi\sin\Psi & \sin\Phi\sin\Theta\sin\Psi + \cos\Phi\cos\Psi \\ \cos\Phi\sin\Theta\cos\Psi + \sin\Phi\sin\Psi & \cos\Phi\sin\Theta\sin\Psi - \sin\Phi\cos\Psi \end{bmatrix} \tag{4.77}$$

In addition, Eqs. (4.73) to (4.75) also contain the time derivatives of $\mathbf{V}_{w_B}$. The derivative of Eq. (4.76) can then be defined as

$$\dot{\mathbf{V}}_{w_B} = T_{EB}\dot{\mathbf{V}}_{w_E} + \dot{T}_{EB}\mathbf{V}_{w_E} \tag{4.78}$$

where $\dot{\mathbf{V}}_{w_E} = \frac{\partial \mathbf{V}_{w_E}}{\partial t} = \frac{\partial \mathbf{V}_{w_E}}{\partial z}\frac{\partial z}{\partial t}$. The derivative of the rotation matrix T_{EB}, $\dot{T}_{EB}$ is defined as [54]

$$\begin{bmatrix} \begin{array}{c} -(\sin\Theta\cos\Psi)\dot{\Theta} \\ -(\cos\Theta\sin\Psi)\dot{\Psi} \end{array} & \begin{array}{c} -(\sin\Theta\sin\Psi)\dot{\Theta} \\ +(\cos\Theta\cos\Psi)\dot{\Psi} \end{array} & \cdots \\ \\ \begin{array}{c} (\cos\Phi\sin\Theta\cos\Psi)\dot{\Phi} \\ +(\sin\Phi\sin\Psi)\dot{\Phi} \\ +(\sin\Phi\cos\Theta\cos\Psi)\dot{\Theta} \\ -(\sin\Phi\sin\Theta\sin\Psi)\dot{\Psi} \\ -(\cos\Phi\cos\Psi)\dot{\Psi} \end{array} & \begin{array}{c} (\cos\Phi\sin\Theta\sin\Psi)\dot{\Phi} \\ -(\sin\Phi\cos\Psi)\dot{\Phi} \\ +(\sin\Phi\cos\Theta\sin\Psi)\dot{\Theta} \\ +(\sin\Phi\sin\Theta\cos\Psi)\dot{\Psi} \\ -(cos\Phi\sin\Psi)\dot{\Psi} \end{array} & \cdots \\ \\ \begin{array}{c} -(\sin\Phi\sin\Theta\cos\Psi)\dot{\Phi} \\ +(\cos\Phi\sin\Psi)\dot{\Phi} \\ +(\cos\Phi\cos\Theta\cos\Psi)\dot{\Theta} \\ -(\cos\Phi\sin\Theta\sin\Psi)\dot{\Psi} \\ -(\sin\Phi\cos\Psi)\dot{\Psi} \end{array} & \begin{array}{c} -(\sin\Phi\sin\Theta\sin\Psi) \\ -(\cos\Phi\cos\Psi)\dot{\Phi} \\ +(\cos\Phi\cos\Theta\sin\Psi)\dot{\Theta} \\ +(\cos\Phi\sin\Theta\cos\Psi)\dot{\Psi} \\ +(\sin\Phi\sin\Psi)\dot{\Psi} \end{array} & \cdots \end{bmatrix} \tag{4.79}$$

Note that the third column in $\dot{T}_{EB}$ is not required as $V_{w_z} = 0$.

4.2.7 Helicopter Parameters

Although the eight DoF helicopter model integrated in *ECHO* is a generic model and can be used to simulate different helicopter models, numerical results generated with the *ECHO* suite use the parameters of a *MBB Bo-105*. The MBB Bo-105 (see Fig. 4.5) is a light twin-engine utility helicopter commonly used for Emergency Medical Services (EMS), police reconnaissance and various military missions. An overview of the required parameters for the helicopter model used in this study is given in Table 4.1.

Table 4.1: MBB Bo-105 parameters

Parameter	Description	Value	
m	Helicopter mass	2200	kg
I_x	Helicopter moment of inertia about the body x-axis	1433	kg·m^2
I_y	Helicopter moment of inertia about the body y-axis	4973	kg·m^2
I_z	Helicopter moment of inertia about the body z-axis	4099	kg·m^2
J_{xz}	Helicopter product of inertia about the body x- and z-axis	660	kg·m^2
x_{mr}	Main rotor offset in the body x-axis	0.08	m
z_{mr}	Main rotor offset in the body z-axis	1.48	m
N_e	Number of engines	2	
P_e	Available power per engine	313000	W
η_m	Engine mechanical efficiency	0.95	
K_e	Maximum power ratio, all engines operating	0.8643	
P_a	Available engine power ($N_e P_e \eta_m K_e$)	514	kW
Ω	Main rotor angular velocity	44.4	rad·s^{-1}
N	Parasite drag velocity correction factor [55]	0.65	
R	Main rotor radius	4.912	m
c	Main rotor blade chord length	0.27	m
N_m	Number of main rotor blades	4	
σ_{mr}	Main rotor solidity ($\frac{N_{mr}c}{\pi R}$)	0.070	
$C_{l_{\alpha_{mr}}}$	Main rotor blade lift curve slope	6.113	rad^{-1}
δ_0	Main rotor blade zero-lift drag coefficient	0.0074	
δ_2	Main rotor blade lift-induced drag coefficient	38.66	
γ_s	Main rotor forward shaft tilt	3	deg
I_{bl}	Main rotor blade moment of inertia	231.7	kg·m^3
θ_{tw}	Main rotor blade twist angle	-0.14	rad
ϵ_β	Flapping hinge offset	0.746	m
e	Normalized flapping hinge offset ($\frac{\epsilon_\beta}{R}$)	0.1519	
m_{mr}	Main rotor mass	27.3	kg
ν_2	Main rotor flap frequency ratio	1.248	
$\tau_{\lambda_{i_{mr}}}$	Main rotor time constant of response	0.1	
k	Non-uniform induced velocity correction factor	1.15	
F_0	Fuselage parasite drag area	0.949	m^2
K_{fus}	Fuselage pitch coefficient correction factor	0.83	
Vol_{fus}	Fuselage equivalent volume	6.126	m^3
$\sum(C_D S)_S$	Equivalent flat plate area	1.2	m^2
$C_{l_{\alpha_{hs}}}$	Horizontal stabilizer lift curve slope	4	rad^{-1}
$\alpha_{0_{hs}}$	Horizontal stabilizer angle of incidence	0.0698	rad
S_{hs}	Horizontal stabilizer surface area	0.803	m^2

Parameter	Description	Value	
x_{hs}	Horizontal stabilizer offset in the body x-axis	4.64	m
$C_{l_{\alpha_{fin}}}$	Vertical fin lift curve slope	4	rad^{-1}
S_{fin}	Vertical fin surface area	0.805	m^2
$\beta_{0_{fin}}$	Vertical fin angle of incidence	−0.06116	rad
x_{fin}	Vertical fin offset in the body x-axis	5.3	m
z_{fin}	Vertical fin offset in the body z-axis	0.97	m
R_{tr}	Tail rotor radius	0.95	m
f_{tr}	Tail rotor fin blockage factor $(1 - \frac{3S_{fin}}{4R_{tr}^2\pi})$	0.787	
g_{tr}	Tail rotor gearing ratio	5.25	
x_{tr}	Tail rotor offset in the body x-axis	6.08	m
z_{tr}	Tail rotor offset in the body z-axis	1.72	m
$C_{l_{\alpha_{tr}}}$	Tail rotor blade lift curve slope	5.7	rad^{-1}
N_t	Number of tail rotor blades	2	
σ_{tr}	Tail rotor solidity $(\frac{N_{tr}c_{tr}}{\pi R_{tr}})$	0.121	
$k_{1_{tr}}$	Main rotor downwash factor at tail rotor	1	
$\tau_{\lambda_{i_{tr}}}$	Tail rotor time constant of response	0.3	
M_{tr}	Tail rotor figure of merit	0.7	

Figure 4.5: Dutch National Police Messerschmitt-Bölkow-Blohm Bo-105

4.3 Control Damping

Initial testing of the *ECHO* suite showed the tool was capable of finding optimized trajectories within very short computer runtimes. However, analysis of these results indicated that control input rates were excessively high, and as a result the controls and some state variables (such as the angular rates p, q and r) were fluctuating significantly. This behavior also negatively affected the convergence rate of the problems, requiring a significantly larger number of iterations to converge to an optimal solution.

A solution for this issue was found by implementation of a so called *control damping*. This is achieved by penalizing excessive control inputs by representing the controls in the cost functional of Eq. (3.1) as an additional Lagrangian contribution $\mathcal{L}_u$. Adding the controls to the objective function, however, could result (in extreme cases) in a minimization of the control inputs themselves, which is highly undesirable. Rather than minimizing the controls, the objective of control damping is to dampen the *control rates*. Therefore, the helicopter controls $(\theta_0, \theta_{1c}, \theta_{1s}, \text{and } \theta_{0_{tr}})$ are now considered as state variables, and added to the state vector $\mathbf{x}$, increasing the number of vehicle state variables from fourteen to eighteen. The derivatives of the original controls – and hence the control rates – are then used as control variables $\mathbf{u}$. It is noted that these *pseudo-controls* $\mathbf{u}$ have no direct physical meaning, but are merely introduced to reduce the excessive control rates and as such to improve the convergence of the tool. This yields four new differential equations to be added to the equations of motion described in Section 4.2.2

$$\dot{\theta_0} = u_1 \tag{4.80}$$

$$\dot{\theta_{1c}} = u_2 \tag{4.81}$$

$$\dot{\theta_{1s}} = u_3 \tag{4.82}$$

$$\dot{\theta_{0_{tr}}} = u_4 \tag{4.83}$$

To dampen the control rates the new control vector is accounted for in the objective function of Eq. (3.1) by defining a Lagrange cost contribution J_u as follows

$$J_u = \upsilon \int_{t_0}^{t_f} \sum_{i=1}^{4} u_i^2 \tag{4.84}$$

where υ is a weighting factor. The weighting factor υ is chosen such that the contribution of J_u to the total objective function is sufficiently large to dampen the control rates, but sufficiently small not to significantly influence the final solution. Although it is difficult

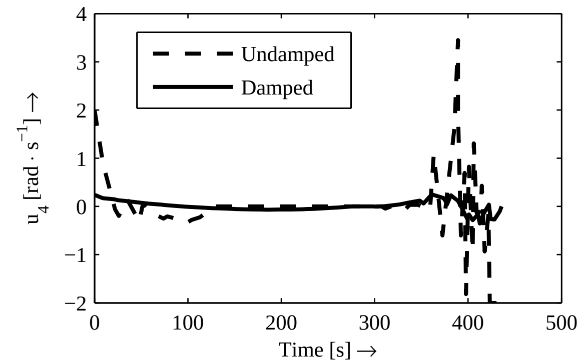

Figure 4.6: Control damping

to predict the value of J_u, it was found that when the value of the weighting factor is based on the (predicted) objective value as $v = \frac{J}{5000}$, the resulting control damping is sufficient without dominating the solution. As an example, consider the control rate u_4 plotted in Fig. 4.6 for a damped and undamped case. In this case, the *intended* optimization objective, the final time t_f, was increased by 1% due to the application of control damping. However, the number of required iterations for the problem to converge was reduced from 94 to 21.

4.4 Fuel and Emissions

In order to assess and optimize the environmental impact of helicopter operations in terms of gaseous emissions, and to reflect the financial interests of helicopter operators, a fuel and emission model has been integrated in *ECHO*. As the model depends on input from the flight mechanics model, it was chosen to directly integrate the fuel and emissions model therein. To account for gaseous emissions, the emission of nitrogen oxides (NO_x) can be selected as one of the optimization criteria in *ECHO*. In addition, the total fuel burn m_f is determined to assess the impact of optimized trajectories on direct operating costs. Apart from a cost perspective, the total fuel burn can also serve as a proxy for the total emission of carbon dioxide (CO_2).

The model integrated in *ECHO* is based on research initiated by the Swiss Federal Office of Civil Aviation (FOCA) [56] in an effort to assess the environmental impact of helicopter operations and to enforce emissions regulations. The model is based on measurements performed at RUAG Aerospace in Switzerland and the German Aerospace Center DLR in Germany, as well as on confidential engine data provided by helicopter manufacturers. The data gathered has been used to define basic polynomial relationships only based on the engine power required P_{req}, and distinguishes between different classes of helicopters. For the Bo-105 helicopter in this study, with a total available engine power of less than 600 hp per engine, the following set of equations have been defined. First, the fuel flow is determined (after converting the power required to Shaft Horsepower

(SHP)) as follows

$$\begin{aligned} SHP &= 1.34102209 \cdot 10^{-3} P_{req} \\ \dot{m}_f &= 2.197 \cdot 10^{-15} SHP^5 - 4.4441 \cdot 10^{-12} SHP^4 + 3.4208 \cdot 10^{-8} SHP^3 \\ &\quad -1.2138 \cdot 10^{-6} SHP^2 + 2.414 \cdot 10^{-4} SHP + 0.004583 \end{aligned} \tag{4.85}$$

The emission rate of NO_x is found by first determining the emission index EI_{NO_x} and then multiplying with the fuel flow.

$$\begin{aligned} EI_{NO_x} &= 0.2113 SHP^{0.5677} \\ \dot{m}_{NO_x} &= \dot{m}_f EI_{NO_x} \end{aligned} \tag{4.86}$$

To determine the total fuel burn m_f and total emission of nitrogen oxides m_{NO_x}, both equations have been added to the equations of motion, hence adding m_f and m_{NO_x} as two additional state variables. This leads to a total of 20 helicopter state variables in the flight mechanics model.

4.5 Limits and Constraints

The control damping described in the previous section already leads to more realistic and flyable trajectories, but to further enhance the realism of the solutions determined by *ECHO* a set of constraints is required to account for for instance the helicopter's flight envelope and passenger comfort. Although in many scenarios specific constraints may be required due to local legislation, atmospheric conditions and helicopter model, for the Bo-105 helicopter used in the examples in this study a set of limits and constraints can be defined that are applicable to all scenarios. First the list containing all bounds on the state variables can be found below

$$|v_x, v_y| \leq 60 \ m \cdot s^{-1} \tag{4.87}$$

$$-1500 \leq v_z \leq 0 \ fpm \tag{4.88}$$

$$|p, q, r| \leq 10^\circ \cdot s^{-1} \tag{4.89}$$

$$|\Theta| \leq 15^\circ \tag{4.90}$$

$$|\Psi| \leq 360^\circ \tag{4.91}$$

$$|\Phi| \leq 30^\circ \tag{4.92}$$

$$|\lambda_{i_{mr}}, \lambda_{i_{tr}}| \leq 25^\circ \tag{4.93}$$

It is noted that the state bounds mentioned above have mostly mathematical meaning following from the requirement to define finite upper and lower bounds to the state and control variables in the optimization methodology. As such, the bounds presented above are not directly related to the flight envelope or other constraints. To account for operational restrictions, a second set of (in)equality constraints is defined in the form of path constraints enforced along the full trajectory. The operational constraints can be found in Table 4.2. It is noted that in normal conditions, a small component of side slip would occur as a result of the tail rotor force, and hence $v \neq 0$. However, the helicopter model integrated in *ECHO* does not account for a parasite drag increase due to side slip. Initial tests showed that the helicopter yaw angle Ψ would be constantly changing, indicating an unacceptable constant rotation around the body z-axis. This allows the tail rotor force to be minimized and hence the total power required could be significantly lower. Clearly this is an unacceptable result which was initially overcome by defining small but sufficient bounds on the airspeed component in the body y-axis, v, hence precluding sideways flight. However, this solution proved to severely affect the convergence rate of the optimization problems. To overcome this, side slip was disallowed as a whole. To still be able to counter the effect of the tail rotor force, in straight and level flight a so-called *crabbed* flight condition is maintained. In this condition, a constant but small bank angle ($\Phi \approx 2^\circ$) is used to overcome the lateral force of the tail rotor.

Table 4.2: General path constraints

Constraint	**(In)equality**	**Notes**
True airspeed	$30 \leq V \leq 100\ kts$	Limited by noise database
Aerodynamic flight path angle	$0^\circ \leq \gamma \leq 10^\circ$	Limited by noise database
Maximum turn rate	$\lvert\dot{\chi}\rvert \leq 3^\circ \cdot s^{-1}$	Rate one turn
Maximum deceleration	$-2 \leq \dot{V} \leq 0\ kts \cdot s^{-1}$	Passenger comfort
Maximum vertical acceleration	$\lvert\dot{w}\rvert \leq 0.1\ g$	Passenger comfort
Power ratio	$0.1 \leq \frac{P_{req}}{P_a} \leq 1$	Do not exceed available power
Side slip	$v = 0\ m \cdot s^{-1}$	No side slip allowed

Although engine failures are not considered in this study, the *height-velocity diagram* (or *dead-man's curve*) still provides a set of airspeed and altitude combinations that should be avoided to safely land in case of an engine failure. The height-velocity diagram for the Bo-105 is presented in Fig. 4.7. Operations within the cross-hatched areas should be avoided [57]. When the constraints defined in Table 4.2 and the height-velocity diagram are considered it is clear that operations within the cross-hatched areas will be avoided, especially when considering that for a lower gross mass (as modeled in this

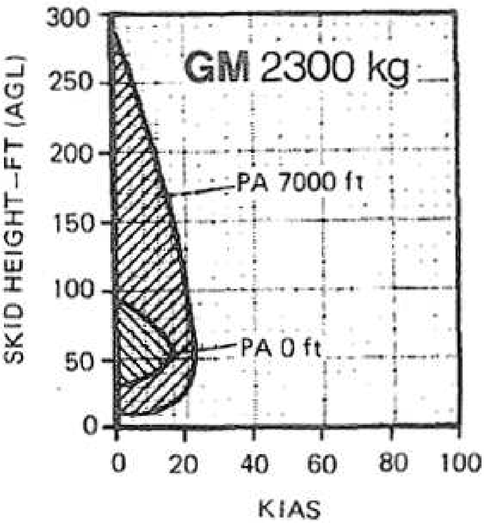

Figure 4.7: Bo-105 Height-velocity diagram, 2300 kg [57]

study) the height-velocity diagram will be less restrictive.

Constraints and limits applicable to specific scenarios can be found in the case studies in Chapters 6 to 8.

4.6 Conclusions

This chapter introduced the helicopter flight dynamics model integrated in *ECHO*. An eight DoF helicopter flight dynamics model is used with quasi-steady inflow angles for both the main and tail rotor. Although the model is generic, in this study the parameters of the twin-engine light helicopter Bo-105 are used. The model is adapted to simulate flights in non-standard atmospheric conditions which includes stationary logarithmic wind profiles. Furthermore, a fuel and gaseous emissions model is integrated which is based on empirical data from helicopter engine manufacturers and uses a set of polynomial equations to determine the fuel flow and emission index based on the required engine power. Finally, a set of generic limits and constraints imposed on all optimization problems is introduced to ensure the optimized trajectories are within the helicopter's flight envelope and comply with passenger comfort constraints.

5
Noise Modeling

5.1 Introduction

Although a much less common sight than fixed-wing aircraft, helicopters cause very specific noise problems due to their characteristic mission profiles. Emergency Medical Services (EMS), corporate charters, police and news helicopters all have in common that they often operate in densely populated areas. As opposed to fixed-wing traffic, which normally operates from airports located in less densely populated areas, and for which the frequency of flights contributes most to the noise annoyance, each helicopter movement in itself can become a cause of noise annoyance or sleep disturbance. In addition, helicopter source noise is significantly different from fixed-wing aircraft noise. The latter is typically symmetrical with respect to the direction of flight, and is mostly dependent on the engine thrust and the aircraft configuration. Helicopters, however, cause a highly asymmetrical noise profile due to the rotation of the main rotor and the position of the tail rotor. This effect is furthermore dependent on the direction of motion of the helicopter, and the airspeed. During acceleration, deceleration, climb or descent, the changing main rotor wake causes significant changes in both the magnitude of the noise as well as its directivity, and might under some conditions even lead to a specifically annoying noise state where the main rotor passes through its own wake - the so-called *Blade-Vortex Interaction (BVI)*, clearly recognizable by the typical *chopping* sound helicopters may produce.

In order to correctly model the characteristics of helicopter noise, a noise model was developed specifically to be used in *ECHO*. The noise model essentially consists of two modules; the first module is a database model containing the source noise characteristics of a helicopter for a range of typical flight conditions. The second module is a propagation model that determines the loss in sound energy through the atmosphere between the source (i.e. the helicopter) and the observer on the ground.

The following sections will present a detailed discussion of the complete noise model integrated in *ECHO*.

5.2 Source Noise Modeling

5.2.1 Introduction

For a ground-based observer the sound of a helicopter flying over is very distinctive and easily distinguished from fixed-wing aircraft noise. This is mainly caused by the typically tonal characteristics of the noise. In addition, due to the rotational motion of the main rotor and the forward motion of the helicopter itself, a highly asymmetrical sound field exists, resulting in a significantly different frequency spectrum and corresponding Sound Pressure Level (SPL) depending on the position of the observer relative to the helicopter. Finally, the aerodynamic characteristics of the main rotor blades depend heavily on the helicopter maneuver, and as a result the sound field generated by the rotor can change significantly during maneuvers.

The asymmetric and maneuver-dependent characteristics of helicopter noise require a high level of accuracy in order to correctly assess sound levels on the ground and the associated community noise impact. Therefore, *ECHO* uses an extensive database of *hemispherical* helicopter noise data to accurately predict the source noise in a given direction of propagation. The following sections will give an overview of the noise sources on a helicopter, and how they are modeled in *ECHO*.

5.2.2 Helicopter Noise Sources

Noise originating from helicopters can essentially be attributed to three main components of the helicopter [58]:

- Engine(s)
- Gearbox and transmission
- Main and tail rotors

The engine provides power to drive the main and tail rotors, and to secondary systems such as electronics and hydraulics. Most modern medium to large helicopters are powered by one or more turboshaft engines. Although not the most dominant noise source on a helicopter, engine noise can clearly be distinguished at some angles with respect to the helicopter, and is, in case of turboshaft engines, mostly dominated by the combustion noise. Other engine noise sources include the compressor and turbine, and to a lesser degree jet noise. Combustion noise appears as a broadband noise which peaks at 400 Hz, whereas turbine and compressor noise generally feature higher frequencies.

The smallest contribution to helicopter noise arises from the gearbox and transmission system used to power the main rotor, tail rotor and other systems. The noise, caused mainly by mechanical friction, is generally only distinguishable inside the cabin of the helicopter and not by external observers.

The main source for external helicopter noise that remains is the rotor noise, contributed to by both the main and tail rotor in a conventional helicopter. Main rotor noise can again be divided in three different sources [59]:

- *Thickness noise and loading noise* – also referred to together as *rotational noise* – are caused by the displacement of air of a passing blade section and the acceleration of the air due to the drag exerted by the passing blade surface, respectively. Rotational noise is mainly dependent on the blade shape and the motion of the blade with respect to the undisturbed air. It is a *tonal* or discrete-frequency noise correlated to the rotational velocity of the blades, and is generated by both the main and tail rotor blades.
- *High-Speed Impulsive (HSI) noise* occurs at high advancing-tip speeds – and thus higher speeds – and is highly directive in the tip path plane. It is associated with transonic flow at the blade tips, and peak levels are generated ahead of the helicopter.
- *Blade-Vortex Interaction (BVI) noise* is the result of the tip vortex of a blade interacting with a following blade, and is composed of tonal and broadband noise. The broadband component is caused by blade loading in a turbulent flow, whereas the tonal component is directly related to the *Blade Passage Frequency (BPF)*. BVI noise is generally considered a highly annoying type of noise, and occurs mainly in slow descending flight.

The typical directivity patterns for each of the components of the main rotor noise are visualized in Fig. 5.1.

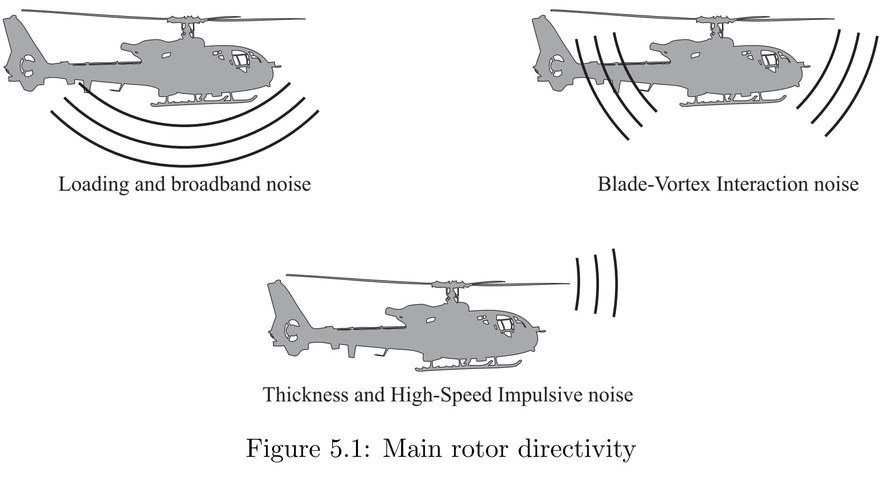

Figure 5.1: Main rotor directivity

Due to the difference in scale, isolated tail rotor noise is generally considered less important than main rotor noise. Especially in conditions when HSI or BVI noise occurs the tail rotor noise can be considered negligible [60] as can be seen in Fig. 5.2. The figure shows the sound pressure measured during 1 revolution of the main rotor, where the pressure peaks due to BVI and HSI noise are clearly distinguishable. In other conditions, however, tail rotor noise might still contribute to annoyance and early detection [61], especially due to the interaction with the main rotor wake which is highly turbulent.

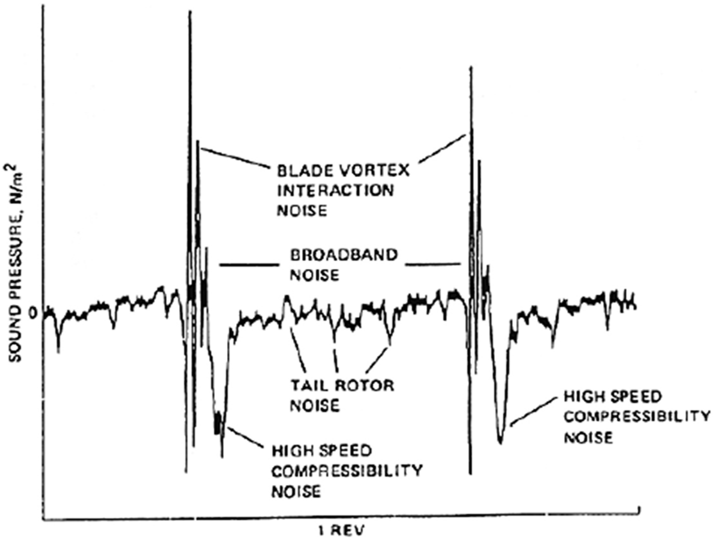

Figure 5.2: Main and tail rotor noise contribution [60]

Although all the components mentioned above contribute to the total helicopter noise profile, in most flight conditions the rotor noise contribution is highly dominant over engine and transmission noises. The tail rotor contribution cannot generally be considered negligible, but in flight conditions that are particularly noisy – and hence of special interest in noise abatement studies – its contribution to the total helicopter noise profile can be considered sufficiently small, even if the interaction with the main rotor wake is considered. Hence, in most helicopter noise studies only main rotor noise is modeled [60], as is the case in this study. It should be noted, though, that modeling only the main rotor noise contribution is not a limitation of the *ECHO* suite itself, but rather of the available source noise database. As such, additional noise sources could relatively easily be modeled when an extended source noise database would be available.

5.2.3 Aeroacoustic-Elastic Source Noise Modeling

As mentioned in the previous section, helicopter noise is highly directive. As can be seen in Fig. 5.3, the blades on the *advancing* side of the main rotor move at a speed of $V_{adv} = \Omega r + V_{helicopter}$ with respect to the undisturbed air, whereas blades on the *retreating* side encounter air at $V_{ret} = \Omega r - V_{helicopter}$, causing significant speed differences on both sides. Also, since the local blade speeds depend on the radius r, along each blade the local airspeeds vary significantly, ranging from negative speeds near the blade root at the retreating side to transonic flow near the advancing blade tip. This horizontal directivity in combination with the vertical directivity displayed in Fig. 5.1 can clearly be distinguished from the ground if a helicopter flies over from different directions. This, in combination with the dependency of the source noise on the helicopter maneuvers, however, also makes helicopter noise difficult to measure and thus to create a substantial empirical database for noise modeling. To overcome this, *ECHO* makes use of a noise database with numerically determined SPLs for a range of flight conditions.

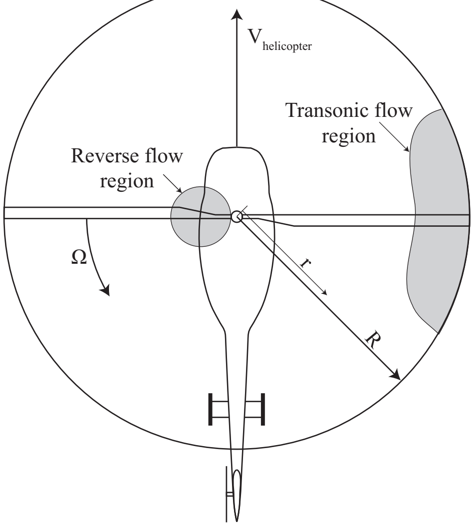

Figure 5.3: Main rotor flow conditions

The first step in determining the SPLs at the source is to determine the *trim conditions* for a given steady flight condition. The helicopter flight dynamics model described in Chapter 4 is used to numerically determine the control inputs ($\theta_0, \theta_{1s}, \theta_{1c},$ and $\theta_{0_{tr}}$) and the resulting shaft plane angle of attack α_r that ensure the steady flight conditions are maintained.

The aeroelastic solver [62–65] then couples a blade structural dynamics model and an unsteady aerodynamics model. The blade structural dynamics model uses a beam-like model based on a non-linear bending-torsion formulation, and is valid for slender, homogeneous, isotropic, non-uniform, twisted, curved blades undergoing moderate displacement [66]. The approach, derived from [67, 68], defines a set of coupled nonlinear differential equations governing the bending of the elastic axis in two dimensions (lead-lag and flap) and the blade torsion. These equations are integrated using the Galerkin approach while the periodic blade response is determined by a harmonic balance approach [65]. The aeroelastic solver yields the periodic blade deformations as a result of the aerodynamic loads on the blades.

The aerodynamic solver receives the periodic blade displacements from the aeroelastic solver, and feeds back the aerodynamic loads. The aerodynamics module consists of a potential-flow, free-wake, Boundary Element Method (BEM) solver capable of predicting

BVI effects [63]. The solver is applicable to a wide range of steady-state rotor conditions – and hence helicopter flight conditions. The wake from the rotor blade is divided in two parts (see Fig. 5.4); the first part, the near (potential) wake, is close to the trailing edge and cannot come into contact with any of the following blades. The far (vortex) wake uses a zero-thickness wake, where the vortices are expressed as thick Rankine vortices. With the potential field in the wake defined, the pressure distribution on the following rotor blade can be determined [64], which yields the aerodynamic loads that are used to determine the new state of the periodic elastic deformation in the blade structural model.

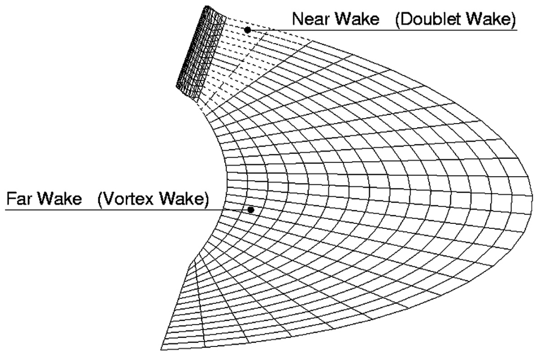

Figure 5.4: Far- and near-wake decomposition [64]

In addition, the body pressure determined by the aerodynamics solver is employed to determine the acoustic field. The aeroacoustic model uses a *Ffowcs Williams and Hawkings* formulation [69]. This in turn is solved using the so-called Farassat Formulation 1A [70, 71]. A schematic overview of the methodology can be seen in Fig. 5.5.

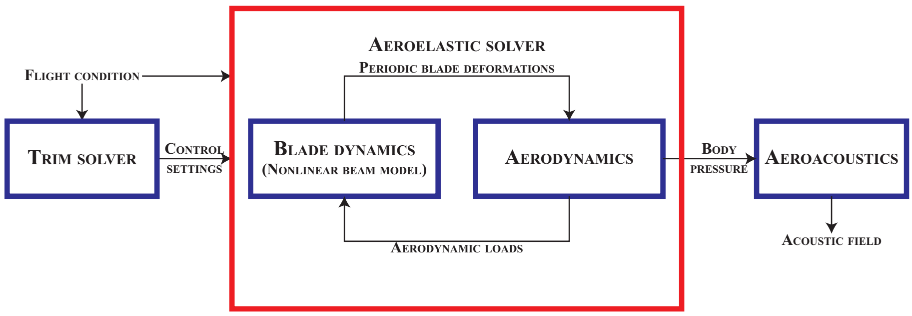

Figure 5.5: Noise prediction tool methodology (adapted from [73])

The resulting SPLs are then projected onto a *hemisphere* around the center of the rotor hub with the equatorial plane of the hemisphere parallel to the ground plane. The *Ffowcs Williams and Hawkings surface* – and hence the hemisphere – is placed at a distance of 150 m from the source. It has been numerically verified that at 150 m distance from the source the wave fronts are parallel, and the hemisphere lies in the *far field* of the noise source. As opposed to the *near field*, where the sound intensity oscillates with range, in the far field the sound intensity can be determined based on the propagation losses as described in Section 5.3. An example of a noise hemisphere can be found in Fig. 5.6. The hemisphere contains SPL data at 145 locations at incremental azimuth and elevation angles of 15°.

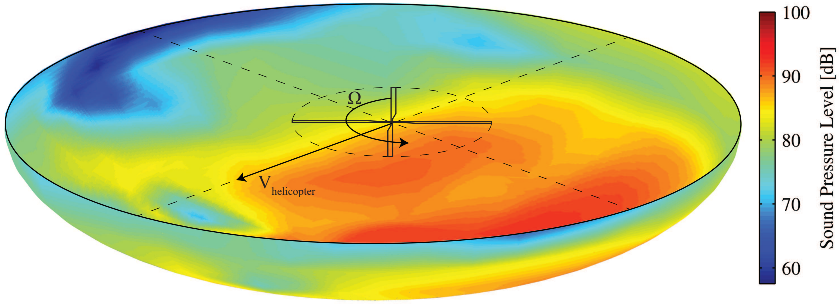

Figure 5.6: Helicopter noise hemisphere example

In trajectory optimization studies where a large number of problem evaluations may be required [12, 13, 15, 17, 24], a source noise database depending on two or three parameters generally offers a good trade-off between accuracy and computational efficiency. The database in this study depends on two parameters, *viz.* the advance ratio μ and the flight path angle γ and has been created using the method described above. One of the limitations of this database is that the database does not account for high load factor variations which would for instance occur in high-bank turns. Based on the load factor constraint defined in Table 4.2 in the previous chapter, it is, however, assumed that the load factor variations are low and that hence the source noise levels are predicted sufficiently accurate.

The database used in this study contains source noise data for 12 different flight conditions; 3 airspeeds (30, 65 and 100 knots) and 4 flight path angles (0°, −5°, −7.5° and −10°). These flight conditions sufficiently cover the ranges of airspeeds and flight path angles used in helicopter arrival and approach procedures considered in this study. The database model integrated in *ECHO* contains for each of the 12 hemispheres SPL data for the first 20 BPF harmonics, yielding a database containing a total of 240 hemispheres. The frequencies available for the Bo-105 helicopter considered in this study (see Chapter 4) can be defined as

$$f_i = \frac{\Omega N_m}{2\pi} i, \qquad i = 1, \ldots, 20 \tag{5.1}$$

where N_m is the number of main rotor blades and Ω is the angular velocity of the main rotor.

Although the source noise database available in *ECHO* covers an extensive range of steady-state flight conditions, a number of observations need to be made on the implementation of the database in the optimization software.

Firstly, when points in the trajectory are evaluated for airspeeds or flight path angles not directly represented in the database, interpolation is applied. This is further discussed in Section 5.3.4. To avoid *extrapolation* of the database the trajectory is constrained to remain within the limits of the database.

Secondly, it should be noted that the trajectory is evaluated as a sequence of steady-state points, which means maneuvers (deceleration, accelerations or turning flight) are not modeled. For decelerating flight, quasi-steady noise modeling [72] may allow for a better prediction of the source noise with a database based on steady-state flight conditions. In that case, the source noise in decelerating flight is approximated by an equivalent steady descending flight. However, applying this method in this study would further limit the allowed flight conditions. Consider that in [72] acoustically a 2 kts$\cdot$s^{-1} deceleration is considered equivalent to a 5.7° descent. In that case, if the helicopter would be descending at more than 4.3°, it would no longer be possible to decelerate at the maximum allowed rate of 2 kts$\cdot$s^{-1} without extrapolating the database. Although it should be noted that the effect of not modeling decelerations can be significant, to avoid extrapolation of the database quasi-steady noise modeling is not used in this study.

Finally, even though the trajectories are evaluated as a sequence of steady-state points, in case of maneuvers still the hemisphere should be rotated along with the helicopter's pitch and roll angles. As a result, the hemispheres would be tilted with respect to the observers leading to different source noise levels. This is not taken into account in this study as the equatorial plane of the hemispheres is always modeled as parallel to the ground.

5.3 Noise Propagation

5.3.1 Introduction

To calculate the difference in Sound Pressure Levels between the noise emitted at the source (helicopter) and received by a ground-based observer, *ECHO* requires the integration of a noise propagation model. The model needs to be sufficiently accurate to correctly model the behavior of sound waves for a variety of atmospheric conditions, and needs to accurately predict the propagation losses between noise source and receiver. In addition, the selection of a gradient-based optimization method prescribes that the models used in *ECHO* are preferably smooth differential functions. Although in some cases deviations from this rule may prove possible, in designing or selecting models – and thus the selection of the propagation model – continuity is an essential requirement.

A multitude of numerical methods exists to accurately model the behavior of sound in given atmospheric conditions. In a *Fast Field Programme (FFP)*, a Fourier transform of the acoustic wave equation [74] – describing the propagation of sound waves in a two-dimensional atmosphere – is used to solve the wave equation. A FFP uses a layered atmosphere to numerically solve the wave equation, where the number of layers required is dependent on the complexity of the atmosphere under consideration to accurately account for changes in the gradient of the speed of sound. Although the FFP method offers an accurate solution for a wide range of atmospheric conditions, it requires a very fine, frequency-dependent discretization of the grid which makes the method too computationally demanding to be integrated in *ECHO*.

An alternative numerical method was originally developed to assess electromechanical wave propagation [75]. The *Parabolic Equation (PE)* was later applied in fields such as quantum mechanics, plasma physics, seismic wave propagation and acoustics [76]. Although significantly faster than FFP and therefore possibly suitable for integration in *ECHO*, as with FFP methods the PE depends on the frequency, requiring repetitive evaluation for a full frequency domain, and hence affecting the total runtime. More importantly, the PE can only be used to assess sound at shallow angles. The region where PE methods provide accurate results lies typically between ± 10 to ± 40 degrees with respect to horizontal [77]. This implies that in the area directly below the helicopter trajectory the noise exposure cannot be determined using the PE method. Since at these locations the largest absolute noise impact can be expected, the PE method is not considered for employment in *ECHO*.

For the atmospheric conditions considered in the development of *ECHO*, so-called *ray-tracing* methods offer sufficient accuracy and calculation speeds for trajectory optimization. Ray-tracing – originally developed for optical waves [78] – is based on the integration of *sound rays*; a sound ray is constructed by tracing parts of the wave front that propagates in time. As such, the sound path is evaluated as the sound travels from source to receiver. During each integration step the propagation loss is determined. As ray-tracing is not dependent on the frequency, the ray path only has to be evaluated once for a complete frequency spectrum. Due to the flexibility, relatively short calculation times and attainable accuracy of a ray-tracing method, it has been selected to be integrated in *ECHO* to assess the propagation of sound through the atmosphere.

The following sections will give a detailed overview of sound propagation in the atmosphere, and the propagation model developed for the *ECHO* suite.

5.3.2 Propagation of Sound in the Atmosphere

In a homogeneous atmosphere, temperature and humidity are not varying with altitude, and no wind is present. Under these conditions, sound rays always travel in a straight line between source and receiver. In reality, temperature and wind gradients bend sound wave fronts, and as such the sound rays. This process, called *refraction*, is caused by the change in the effective speed of sound with changing temperature or wind speed, and results in sound rays traveling in the direction of a lower speed of sound. As an example, on normal days the temperature will decrease with increasing altitude, and as a result the speed of sound will be lower at higher altitudes. In that case, sound waves are bent upwards and away from the ground. During the night on the other hand, often positive temperature gradients occur as the ground surface might cool down faster than the air. In that case, the speed of sound closer to the surface will be lower, and so the sound waves will be bent downwards. When wind is present, the sound waves will be bent in the direction of the wind. These three cases are visualized in Fig. 5.7.

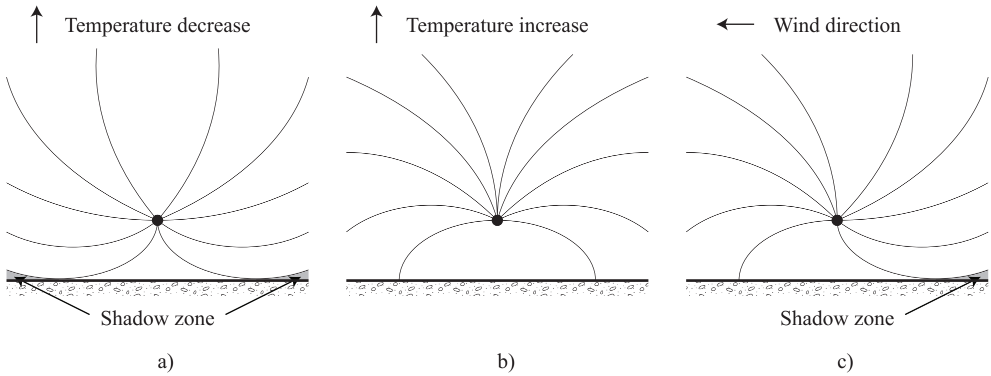

Figure 5.7: Refraction: a) Negative temperature gradient, b) Positive temperature gradient, c) Wind

In a refracted atmosphere, the total propagation loss, i.e. the difference between the source strength and the sound level observed on the ground, can be attributed to four effects:

- *Spreading loss*: as a result of the sound energy emitted from the source being spread over an ever increasing surface area at increasing distance from the source, the sound power at the receiver decreases with distance.
- *Ground reflection*: an observer can receive a direct ray from the source, as well as a ray reflected on the ground. Based on the phase difference between the two rays, the observed sound level can be significantly higher or lower than the sound level of both separate rays.
- *Atmospheric attenuation* or *absorption*: a sound wave traveling through the atmosphere loses energy through the friction the air exerts on it.
- *Shadow zones*: as can be seen in Fig. 5.7, in some cases sound rays are refracted upwards and away from the ground. In such cases shadow zones will exist were no *direct* sound ray reaches the observer. Although through *ground waves*, *diffraction* and *scatter due to turbulence* still some sound may be observed on the ground, the total sound power levels are significantly lower than in the *illuminated* zone.

In order to determine the total propagation loss between a sound emitted at the helicopter source and received at an observer location, the first step is to determine the ray path using a ray-tracing method, as described in the next section.

5.3.3 Ray Path Construction

In ray-tracing methods, the ray path is constructed by numerically integrating the movement of the wave front over time. In an atmosphere with a varying gradient of the speed of sound, the sound ray can be refracted in different directions along its path, as can be seen in Fig. 5.8.

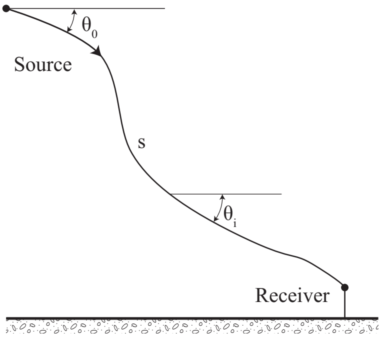

Figure 5.8: Refracted ray path

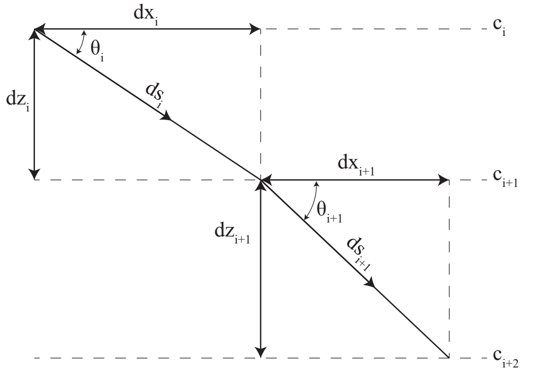

Figure 5.9: Ray path integration

The ray path is now integrated numerically with a time step dt under the assumption that within each time step the ray behaves as in a homogeneous atmosphere, i.e. the ray is straight, as can be seen in Fig. 5.9. With these assumptions, for each time step dt the characteristics of a section ds_i are defined by

$$ds_i = c_i dt \tag{5.2}$$

$$dx_i = ds_i \cos\theta_i \tag{5.3}$$

$$dz_i = ds_i \sin\theta_i \tag{5.4}$$

Using *Snell's Law of Refraction* [79], the angle of incidence in the following segment can be determined to be

$$\theta_{i+1} = \cos^{-1}\left(\sqrt{1 - \left(\frac{c_i}{c_{i+1}}\right)^2 (1 - \cos^2\theta_i)}\right) \tag{5.5}$$

If θ_{i+1} is complex, the ray is (internally) reflected.

Although this method is sufficiently fast for implementation in *ECHO*, a disadvantage of this *forward* method is that for a given launch angle at the source θ_0 the total distance traveled between source and receiver is not known. As a result, the ray path between a source and a predefined observer position is not explicitly known. In *ECHO*, however, the goal is to determine the sound levels in a relatively small number of fixed observer locations. To find the sound levels in these points, a forward method would either require a large number of rays to be assessed, and the resulting sound levels to be interpolated to find the actual sound level at the observer location, or to numerically determine the launch angle leading to a direct ray path between source and receiver. Both methods would significantly complicate the propagation model, and, more importantly, would significantly increase the execution time of the model. Still based on the numerical determination of the launch angle at the source, θ_0, the propagation model employed in *ECHO* uses an alternative approach to construct the ray path between source and receiver, permitting a significant reduction in the execution time of the model.

Consider an atmosphere with a linear temperature gradient λ, a logarithmic wind speed profile $V_w(z)$ and a temperature T_0 at ground level. The effective speed of sound profile can then be defined by

$$\begin{aligned} c(z) &= \sqrt{\gamma R\left(T_0 + \lambda z\right)} + V_w(z) \\ &= \sqrt{\gamma R\left(T_0 + \lambda z\right)} + A \ln\left(\frac{z}{z_0} + 1\right) \end{aligned} \tag{5.6}$$

where z_0 is the roughness length and A is a constant to define the logarithmic wind speed profile. The roughness length z_0 is related to surface roughness elements (such as for instance grass or crops) and defines the wind speed profile near the ground surface. Typically, the roughness length is approximately 10% of the length of the surface roughness elements ($z_0 \approx 0.02$ m for grass). A is dependent on $V_w(z_w)$, which is the wind speed component in the direction of propagation at height z_w, and can be defined as [80, 81]

$$A = \frac{V_w(z_w)}{\ln\left(\frac{z_w}{z_0} + 1\right)} \tag{5.7}$$

In the method presented in Eqs. (5.2) to (5.5) the ray path is integrated with respect to time, for each time step a constant speed of sound is assumed, and refraction is accounted for by applying Snell's law. In the method used in *ECHO*, the ray path is constructed geometrically based on a constant speed of sound gradient. For this purpose, the speed of sound profile is divided over a number of layers, and for each layer the speed of sound gradient g is considered constant. This can be seen in Fig. 5.10. The layers are logarithmically equally spaced to ensure the closest approximation to the logarithmic speed of sound profile.

As can be seen in Fig. 5.10, at the transition between layers the linearized speed of sound profile is continuous. As a result, refraction is not determined by applying Snell's law at the layer transitions. Rather, the gradient in the speed of sound profile causes the rays to be curved, where linear gradients cause a constant radius of curvature. Hence, by determining in each layer the radius of curvature and the center of the curvature, the total path of the ray can be determined geometrically. Based on Fig. 5.11, the sequence to determine the ray path for the i^{th} layer starts by determining the radius of curvature as follows [79]

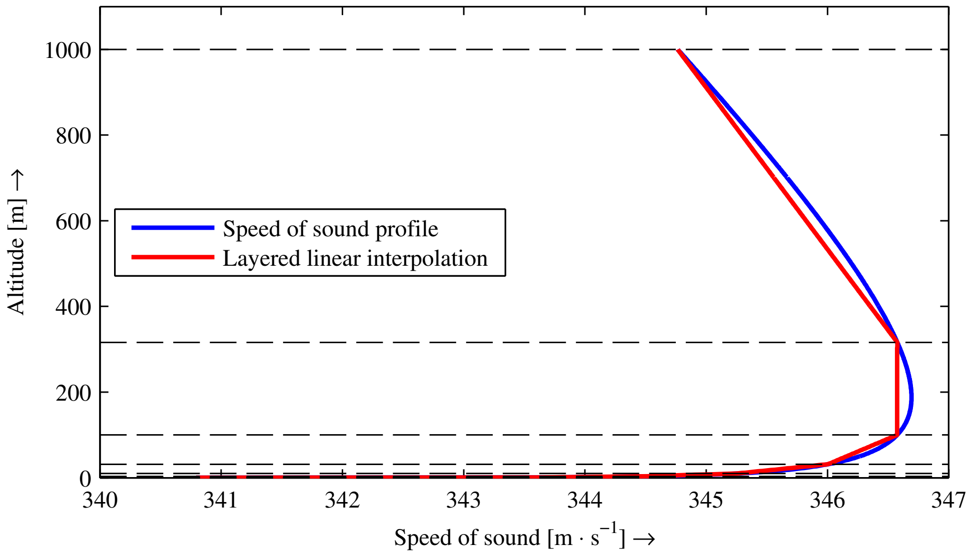

Figure 5.10: Layered speed of sound approximation

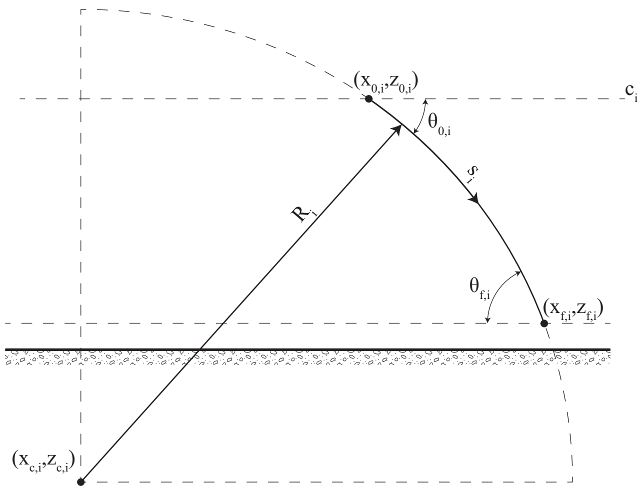

Figure 5.11: Refraction in a linear speed of sound profile

$$R_i = \frac{-c_i}{g_i \cos\theta_{0,i}} \tag{5.8}$$

where c_i is the speed of sound at the top of the layer, and g_i the linearized gradient in the layer. The center of curvature is then defined by

$$x_{c,i} = x_{0,i} + R_i \sin\theta_{0,i} \tag{5.9}$$

$$z_{c,i} = z_{0,i} + R_i \cos\theta_{0,i} \tag{5.10}$$

With these variables known, the final angle of incidence $\theta_{f,i}$, final distance $x_{f,i}$ and arc segment length s_i can be determined with

$$\theta_{f,i} = \cos^{-1}\left(\frac{z_c - z_{f,i}}{R_i}\right) \tag{5.11}$$

$$x_{f,i} = x_c - R_i \sin\theta_{f,i} \tag{5.12}$$

$$s_i = |R_i\left(\theta_{f,i} - \theta_{0,i}\right)| \tag{5.13}$$

Repeating this process for each layer, the total distance traveled x, the total ray path length s, and the final angle of incidence θ_f can be determined.

As mentioned before, in *ECHO* the noise exposure on the ground is only required to be known in a limited number of fixed observer locations. Rather than analyzing a large number of ray paths at different launch angles to determine the noise impact at an irregular grid on the ground, for the fixed number of observer locations used in this study it is more efficient to numerically determine only the ray paths between the source and the observer locations. With the source and receiver positions known, Eqs. (5.9) to (5.13) can be used to numerically solve for the launch angle θ_0. The launch angle θ_0 then defines the elevation angle at which the ray path intersects the source noise hemisphere, whereas the bearing angle between the helicopter and the observer determines the azimuth angle, as explained in the following section.

5.3.4 Source Noise Levels

Given the flight conditions following from the helicopter flight dynamics model and the sound ray path following from the previous section, the next step is to determine the source noise level at which the sound ray is initiated. This process consists of two steps:

first the hemisphere corresponding to the flight conditions is selected, and then a single source noise level corresponding to the ray path between the source and the receiver is determined.

When the hemispherical database presented in Section 5.2.3 is considered, it is readily clear that some form of interpolation is required between the different hemispheres for flight conditions different than the conditions available in either of the 12 sets of hemispheres to ensure a continuous source noise model as required by the optimization methodology employed in *ECHO*. Although linear interpolation – and the resulting discontinuity in the first derivative – might not be preferred in the optimization methodology, it was shown during the development of *ECHO* that convergence was not negatively affected by linearly interpolating between hemispheres. Therefore, the source noise model uses a bi-variate interpolation for both airspeed V and flight path angle γ. Consider an airspeed V and flight path angle γ within the bounds of the database, $V_i \leq V < V_{i+1}$ and $\gamma_j \leq \gamma < \gamma_{j+1}$, where i, $i+1$ and j, $j+1$ indicate database entries. The corresponding $SPL_{V,\gamma,k}$ for the k^{th} location at the hemisphere ($k = 1, \ldots, 145$) can then be defined as

$$\begin{aligned}
SPL_{V,j,k} &= SPL_{i,j,k} + (V - V_i)\,\frac{(SPL_{i+1,j,k} - SPL_{i,j,k})}{(V_{i+1} - V_i)} \\
SPL_{V,j+1,k} &= SPL_{i,j+1,k} + (V - V_i)\,\frac{(SPL_{i+1,j+1,k} - SPL_{i,j+1,k})}{(V_{i+1} - V_i)} \\
SPL_{V,\gamma,k} &= SPL_{V,j,k} + (\gamma - \gamma_j)\,\frac{(SPL_{V,j+1,k} - SPL_{V,j,k})}{(\gamma_{j+1} - \gamma_j)}
\end{aligned} \tag{5.14}$$

This essentially yields a single hemisphere for a given flight condition (V, γ) containing the SPLs for all 20 frequencies on all 145 source locations. The next step is to determine the single source noise level to initiate the ray path between source and observer.

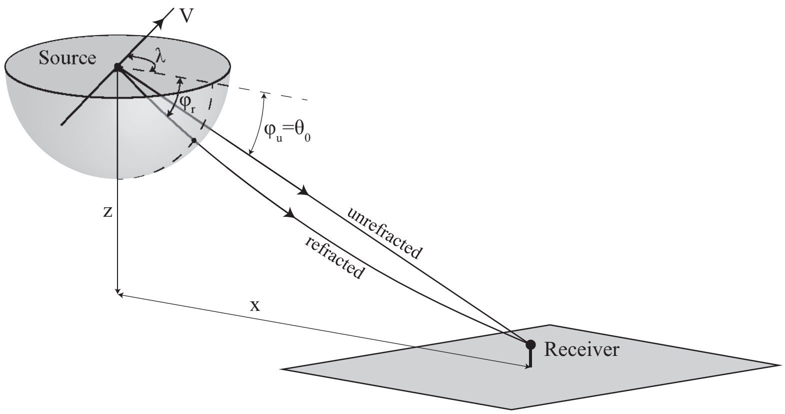

Figure 5.12: Refraction in a linear speed of sound profile

In the previous section the process for determining the launch angle θ_0 was presented. Now consider a helicopter passing by a receiver as can be seen in Fig. 5.12. It immediately follows that in a *non-refracting* atmosphere the launch angle θ_0 equals the elevation angle ϕ_u at which the ray passes through the hemisphere. However, in a *refracting* atmosphere refraction between the source and the radius of the hemisphere ($R = 150$ m) causes a difference between the launch angle and the required elevation angle, hence $\phi_r \neq \theta_0$. However, in the definition of the source noise model no atmospheric effects were taken into account within the radius of the hemisphere, and the 150 m radius is mainly used to ensure that the sound levels are determined in the far field. As a result, the SPLs at the hemisphere can be propagated *backwards* to a distance of 1 m from the source based on the assumption that only spherical spreading applies (see Section 5.3.5). It can then be shown that the source noise levels need to be increased with a value of $20\log_{10} R$ to essentially define a new hemisphere at 1 m from the source [79]. The smaller hemisphere is then used to determine the source noise levels initiating the ray paths. It can be assumed that refraction between the actual source and the smaller hemisphere at 1 m is negligible, and hence that $\phi_r = \theta_0$.

At this point it should be noted that even though an equivalent hemisphere is defined at 1 m from the source, this hemisphere is still only valid for observers in the far field, hence observers more than 150 m removed from the source. In some cases, however, the total distance between the source and a receiver may be less than the radius of the original hemispheres. In that case, the receiver would be placed within the near field of the noise source, and the source noise level determined from the hemispherical database can be significantly less accurate than for receivers in the far field.

Apart from the launch angle following from the ray path between source and receiver, also the azimuth angle λ needs to be determined. This angle depends on the horizontal position of the helicopter (x_H, y_H) relative to the receiver position (x_R, z_R). It is noted, however, that the hemisphere is defined with respect to the airspeed vector. In case of a crosswind component, the airspeed and ground speed vector are separated by the yaw angle Ψ, as can be seen in Fig. 5.13. The position of the observer with respect to the hemisphere – and hence the azimuth angle λ can then be defined as

$$\begin{aligned} \lambda &= -\Psi + \Gamma \\ &= -\Psi + \begin{cases} \tan^{-1}\left(\frac{y_R - y_H}{x_R - x_H}\right) & x_R - x_H > 0 \\ \tan^{-1}\left(\frac{y_R - y_H}{x_R - x_H}\right) + \pi & y_R - y_H \geq 0, x_R - x_H < 0 \\ \tan^{-1}\left(\frac{y_R - y_H}{x_R - x_H}\right) - \pi & y_R - y_H < 0, x_R - x_H < 0 \\ \frac{\pi}{2} & y_R - y_H > 0, x_R = x_H \\ -\frac{\pi}{2} & y_R - y_H < 0, x_R = x_H \\ \text{undefined} & y_R = y_H, x_R = x_H \end{cases} \end{aligned} \tag{5.15}$$

The elevation and azimuth angles define a point on the hemisphere (λ, ϕ) that determines a unique value for $SPL_{\lambda,\phi}$ for each of the 20 available frequencies. However, with elevation and azimuth angles both only available at 15° increments in the database, a second interpolation is required. In this case, however, convergence of the optimization algorithm proved to be significantly affected when using linear interpolation. Therefore, to determine the final source noise level a three-dimensional b-spline interpolation is

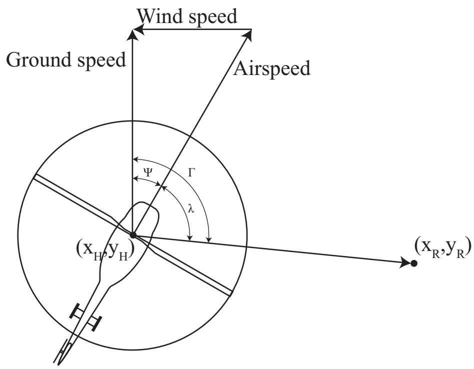

Figure 5.13: Azimuth angle geometry

applied based on [82]. The resulting $SPL_{\lambda,\phi}$ for each of the first 20 BPF harmonics is then used to initiate the ray path, and is corrected with the propagation losses described in the following sections.

Since the database model consists of hemispheres of which the equatorial plane is parallel to the ground plane, no source noise levels radiating upward are available. Although intuitively noise radiated upward might not be of interest, in the case of *refraction* noise radiated upward might still reach a ground based observer when the sound rays are bent downwards towards the ground due to a positive speed of sound gradient. Although sound rays radiated upward normally reach the ground at large distances from the source depending on the source altitude and the speed of sound gradient and can therefore be expected to have only a small contribution to the total noise impact, it needs to be noted that in all cases of launch angles above the hemisphere the source noise level of the equatorial plane is selected.

5.3.5 Propagation Loss

After the ray path has been determined as described in Section 5.3.3, the total propagation loss consisting of the four contributions mentioned in Section 5.3.2 can be calculated.

Spreading Loss

In the case of a homogeneous atmosphere and hence sound traveling along straight rays, sound from a non-directional source is spread over a spherical surface with increasing distance s (see Fig. 5.14). In that case, the *spherical spreading loss* can be defined by the *inverse-distance law* [79]

$$\Delta SPL_S = 20 \log_{10} \frac{s_0}{s} \tag{5.16}$$

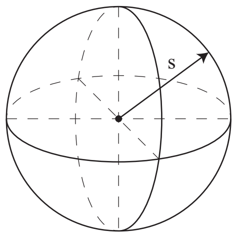

Figure 5.14: Spherical spreading

where s_0 is a reference distance at which the source levels are defined, typically 1 m. However, in a non-homogeneous atmosphere, rays can be refracted towards each other (*focusing*) or away from each other (*defocusing*), resulting in a spreading loss lower or higher than defined by Eq. (5.16). To exemplify this, consider the concept of *ray tubes* as shown in Fig. 5.15. In an atmosphere with slowly varying speed of sound, the phase of a sound wave is directly proportional to time. Then consider two sets of rays launched at the same conditions in a refracting and an unrefracting atmosphere. After a given time dt the ray tube areas are A_r and A_u respectively. The effect of (de)focusing can then be determined by comparing the area of the refracted ray tube with the conditions in a homogeneous medium. The pressure p, velocity magnitude $|v_{ray}|$ and ray tube area A_{ray} are related by the *Blokhintzev invariant* [83] of Eq. (5.17)

$$\frac{p^2|v_{ray}|A_{ray}}{\rho c^2 \Omega} = \text{constant} \tag{5.17}$$

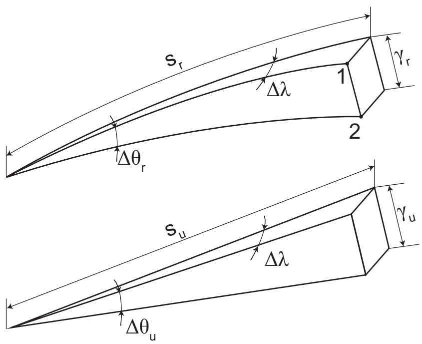

Figure 5.15: Ray tubes in a refracting and non-refracting medium

where ρ and c are the local air density and speed of sound respectively, and Ω represents the wind vector. The ray tube areas can be defined as

$$A_u = \gamma_u s_u \Delta\lambda \tag{5.18}$$

$$A_r = \gamma_r s_r \Delta\lambda \tag{5.19}$$

where the separation distances can be defined as

$$\gamma_u = 2 s_u \tan\left(\frac{\Delta\theta_u}{2}\right) \tag{5.20}$$

$$\gamma_r = \sqrt{(x_1 - x_2)^2 + (y_1 - y_2)^2} \tag{5.21}$$

Although theoretically only for stationary atmospheres, the *difference* in spreading loss due to refraction becomes

$$\Delta SPL_{S_r} = -10\log_{10}\left(\frac{\rho_u c_u^2 A_r}{\rho_r c_r^2 A_u}\right) \tag{5.22}$$

for wind speeds less than 15 knots [83]. When the ray tube areas in a refracting and non-refracting medium are compared close to the ground (and hence $V_w \approx 0$) then it can be assumed that $\rho_u = \rho_r$ and $c_u = c_r$ [83]. Since the additional spreading loss defined by Eq. (5.22) is essentially a correction with respect to the spherical spreading loss, the *total* spreading loss can then be defined as

$$\Delta SPL_S = -10\log_{10}\left(\frac{A_r}{A_u}\right) + 20\log_{10}\left(\frac{s_0}{s_r}\right) \tag{5.23}$$

In order to determine the separation distance γ_r between two refracted rays, the rays are launched at small decremental launch angles $\Delta\theta_0$ and the ray paths are integrated for a given time t to ensure the sound rays are in phase. After time t, the final positions of both rays are known and used to determine the separation distance γ_r. However, as mentioned before, the ray paths in *ECHO* are not integrated in time, but rather geometrically. As a result, first the travel time of the direct ray between source and receiver needs to be determined. With the geometry of the ray defined by Eqs. (5.8) to (5.13), the travel time along the ray path in the i^{th} layer can be defined as

$$t_i = \int_0^{s_i} \frac{1}{c_i(z)} ds_i \tag{5.24}$$

with $c_i(z) = c_{0,i} + g_i z$ the linearized speed of sound profile in the layer. With Eq. (5.9) and given that $ds_i = R_i d\theta$, the travel time in the layer can be rewritten as a function of the angle of incidence, i.e.

$$t_i = \int_{\theta_{0,i}}^{\theta_{f,i}} \frac{R_i}{c_{0,i} - g_i z_{c,i} - g_i R_i \cos\theta} d\theta \tag{5.25}$$

Evaluating this integral yields the following expression for the travel time within layer i

$$t_i = 2|R_i| \tanh^{-1}\left(\frac{(a-b)\tan\frac{1}{2}\theta}{\sqrt{a^2-b^2}}\right)\frac{1}{\sqrt{a^2-b^2}}\Bigg|_{\theta_{0,i}}^{\theta_{f,i}} \tag{5.26}$$

with

$$a = -g_i R_i$$

$$b = g_i z_{c,i} + c_{0,i}$$

In *ECHO*, each ray is only assumed to move in two dimensions, *viz.* altitude z and distance x, and as such the lateral refraction is not accounted for. As a result, the out-of-plane separation angle $\Delta\lambda$ between both rays will remain constant and only one additional ray needs to be assessed at a small decremental launch angle $\Delta\theta_0$ from the direct ray between source and receiver to determine the ray tube area. However, if this ray would be evaluated in all layers, the travel time of the second ray would not equal that of the direct ray, so $t_{direct} \neq t_{\Delta\theta_0}$. However, the Blokhintzev invariant prescribes that the rays are evaluated at the same wave front and hence are in phase. To still be able to determine the position of the second wave front at t_{direct}, the second ray is evaluated until and including the j^{th} layer where $t_j > t_{direct}$. Since a *smaller* launch angle implies that the second ray is launched *above* the direct ray, the condition $t_j > t_{direct}$ will always be met with $j \leq n$ and n the total number of layers. Then, at time t_j, also the final position (x_j, z_j) is known. To find the position $(x_{\Delta\theta_0}, z_{\Delta\theta_0})$ at $t_{\Delta\theta_0}$, linear interpolation is used between the initial and final conditions in layer j as follows

$$x_{\Delta\theta_0} = x_{j-1} + (x_j - x_{j-1})\frac{t_{\Delta\theta_0} - t_j}{t_j - t_{j-1}} \tag{5.27}$$

$$z_{\Delta\theta_0} = z_{j-1} + (z_j - z_{j-1})\frac{t_{\Delta\theta_0} - t_j}{t_j - t_{j-1}} \tag{5.28}$$

The resulting final position can be used to find the refracted ray tube area through Eqs. (5.18) to (5.21), in order to determine the total spreading loss from Eq. (5.23)

Ground Reflection

In addition to sound waves traveling directly from the source to the receiver, reflection of sound waves on the ground can increase or decrease the sound pressure level received at the observer location, depending on the phase difference between both waves. Consider a stationary source at height z_s in a homogeneous atmosphere, a flat ground surface with a roughness that is small compared to the wavelength, and an observer at height z_r above the ground. The geometry of the problem then is as presented in Fig. 5.16. To determine the phase difference between both rays, first the ray path lengths are required.

For the direct ray, the path length s_1 follows from the summation of Eq. (5.13) for all layers. Since the receiver is relatively close to the ground, the effect of refraction on the ray path length s_2 is negligible and hence s_2 can be defined as follows

$$s_2 = s_1 + 2z_r \sin\theta_f \tag{5.29}$$

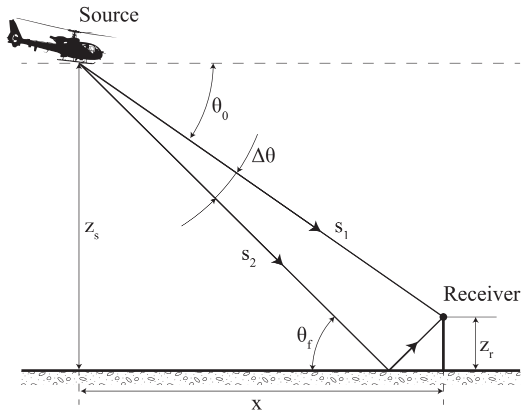

Figure 5.16: Ground reflection geometry

The difference in the direct path length s_1 and the reflected path length s_2 results in a change in the amplitude and the phase at the receiver. Following the derivation of the change in SPL at the receiver from [79] and [84], the sound pressure at the receiver can now be defined as the sum of the sound pressures from the direct and reflected rays by

$$p'(s,t) = \frac{A}{s_1} e^{i\omega\left(t - \frac{s_1}{c}\right)} + Q\frac{A}{s_2} e^{i\omega\left(t - \frac{s_2}{c}\right)} \tag{5.30}$$

Here, A is the source strength, $\omega = 2\pi f$ is the angular frequency of the source, c is the local speed of sound, and Q is the *reflection factor*. To reflect both the amplitude and the phase change in Eq. (5.30), the reflection factor can be defined as $Q = |Q|e^{i\phi}$, where ϕ is the phase change due to the ground. After subsitution in Eq. (5.30) and integration over time, the effective sound pressure at the receiver follows

$$p_e(s) = \sqrt{\frac{A^2}{2s_1^2} + |Q|^2 \frac{A^2}{2s_2^2} + |Q|\frac{A}{s_1 s_2}\cos\left(\omega\frac{s_2 - s_1}{c} + \phi\right)} \tag{5.31}$$

The effective sound pressure from the direct ray is defined as [79]

$$p_{e,direct}(s) = \frac{A}{s_1\sqrt{2}} \tag{5.32}$$

Equation (5.31) can then be rewritten as

$$p_e(s) = p_{e,direct}(s)\sqrt{1 + \left(\frac{s_1}{s_2}\right)^2 |Q|^2 + 2\frac{s_1}{s_2}|Q|\cos\left(\omega\frac{s_2 - s_1}{c} + \phi\right)} \tag{5.33}$$

Since the effect of ground interference is defined as the difference between the *actual* noise level to which the observer is exposed, and the *free field* noise level following from only a direct ray, the ground effect can be expressed as

$$\begin{aligned}
\Delta SPL_G(s,\theta) &= SPL_{actual}(s,\theta) - SPL_{free}(s,\theta) \\
&= 10\log_{10}\left(\frac{p^2_{e,actual}}{p^2_{e,0}}\right) - 10\log_{10}\left(\frac{p^2_{e,direct}}{p^2_{e,0}}\right) \\
&= 10\log_{10}\left[1 + \left(\frac{s_1}{s_2}\right)^2 |Q|^2 + 2\frac{s_1}{s_2}|Q|\cos\left(\omega\frac{s_2 - s_1}{c} + \phi\right)\right]
\end{aligned} \tag{5.34}$$

where θ depicts the launch angle of the ray at the source. By now substituting $|Q|e^{i\phi} = Q$, Eq. (5.34) becomes

$$\Delta SPL_G = 20\log_{10}\left|1 + \frac{s_1}{s_2}Qe^{ik(s_2 - s_1)}\right| \tag{5.35}$$

where k is the wave number defined as

$$k = \frac{\omega}{c} = \frac{2\pi f}{c} \tag{5.36}$$

What now remains is the determination of the reflection coefficient Q. This is in itself dependent on the *surface impedance*, Z_g, which is defined as the ratio of the sound pressure at a point on the surface, and the velocity of air particles at the surface

$$Z_g = \frac{p'(s,t)}{v_g(s,t)} \tag{5.37}$$

Using Equation (5.30), and considering that at the ground $s_1 = s_2 = s$, the sound pressure at the surface is defined as

$$p'(s,t) = (1 + Q)\frac{A}{s}e^{i\omega\left(t - \frac{s}{c}\right)} \tag{5.38}$$

Assuming that plane wave theory applies, and that the ground can transmit sound in lateral direction, the particle velocity into the ground can be expressed as [79]

$$v_g(s,t) = \frac{\sin\theta_f}{\sin\theta_g}\frac{1}{\rho_0 c_0}(1 - Q)\frac{A}{s}e^{i\omega\left(t - \frac{s}{c}\right)} \tag{5.39}$$

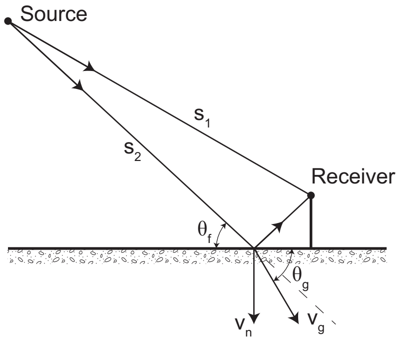

Figure 5.17: Reflection and refraction on a ground surface

The definition of the angle θ_g can be seen in Fig. 5.17. Solving Eqs. (5.37) to (5.39) for Q yields

$$Q = \frac{\frac{Z_g}{\rho_0 c_0}\sin\theta_f - \sin\theta_g}{\frac{Z_g}{\rho_0 c_0}\sin\theta_f + \sin\theta_g} \tag{5.40}$$

According to [79], it may be assumed that ground surfaces used for aviation noise modeling can be considered *locally reacting*, implying the lateral component of the propagation into the ground is negligible. As a result, the *normal surface impedance*, Z_n can be used, where v_g in Eq. (5.37) is replaced by v_n. The reflection factor in its final form then becomes

$$Q = \frac{\frac{Z_n}{\rho_0 c_0}\sin\theta_f - 1}{\frac{Z_n}{\rho_0 c_0}\sin\theta_f + 1} \tag{5.41}$$

Finally, according to [85], the *specific normal acoustic impedance* can be expressed as a function of the frequency f and the effective flow resistivity σ

$$\frac{Z_n}{\rho_0 c_0} = 1 + 0.0511\left(\frac{f}{\sigma}\right)^{-0.75} + i0.0768\left(\frac{f}{\sigma}\right)^{-0.73} \tag{5.42}$$

In case both the direct and reflected rays are in phase, a maximum theoretical increase of the total sound power level of 6 dB can be caused by the ground effect. In case the phases are exactly opposed, theoretically the sound will be canceled out all together.

Atmospheric Attenuation

In addition to spherical spreading, sound waves traveling through air – a viscous fluid – lose energy through internal friction. This atmospheric absorption loss is generally expressed by the *sound attenuation coefficient*, which defines the decrease in SPL per unit of 100 m. For the propagation model implemented in *ECHO*, the procedure defined in [86] was applied. This procedure defines the atmospheric attenuation coefficient as

$$\begin{aligned} \alpha &= 10^{\left[2.05\log_{10}\left(\frac{f_0}{1000}\right)+1.1394\cdot 10^{-3}T-1.916984\right]} + \\ &\quad \eta\left(\delta\right)\cdot 10^{\left[\log_{10}(f_0)+8.42994\cdot 10^{-3}T-2.755624\right]} \end{aligned} \tag{5.43}$$

with δ defined as

$$\begin{aligned} \delta &= \sqrt{\frac{1010}{f_0}} 10^{\left[\log_{10}H-1.328924+3.179768\cdot 10^{-2}T\right]} \times \\ &\quad 10^{\left[-2.173716\cdot 10^{-4}T^2+1.7496\cdot 10^{-6}T^3\right]} \end{aligned} \tag{5.44}$$

where T is the local air temperature in degrees centigrade and H the local air humidity. The frequency f_0 is determined through a table lookup. However, for frequencies up to 4,000 Hz – and so for the entire spectrum considered in this study – $f_0 = f$ applies. The coefficient $\eta\left(\delta\right)$ is determined using Table 5.1 [79].

Table 5.1: Determination of $\eta(\delta)$

δ	η	δ	η	δ	η
0.00	0.000	1.30	0.840	4.15	0.260
0.25	0.315	1.50	0.750	4.45	0.245
0.60	0.840	2.00	0.570	5.25	0.220
0.70	0.930	2.30	0.495	5.70	0.210
0.80	0.975	2.50	0.450	6.05	0.205
0.90	0.996	2.80	0.400	6.50	0.200
1.00	1.000	3.00	0.370	7.00	0.200
1.10	0.970	3.30	0.330	10.00	0.200
1.20	0.900	3.60	0.300		

With these parameters defined, the total sound pressure loss due to atmospheric absorption can be defined as a function of the ray path length

$$\Delta SPL_A = \frac{\alpha s}{100} \tag{5.45}$$

It is noted that as both the local air temperature and humidity are defined as functions of altitude, the atmospheric attenuation loss needs to be determined for each of the layers described in Section 5.3.3 individually. Since the temperature and humidity gradients are linear, the average values of T and H are used to solve Eq. (5.45), and the resulting attenuation losses per layer are summed to obtain the total attenuation loss.

Shadow zones

In case of upward refraction as a result of a negative gradient in the speed of sound profile, the existence of *shadow zones* significantly reduces the sound levels received at observer locations were no direct rays reach the ground (see Fig. 5.7). However, *ground waves* originating in the *illuminated zone*, *diffraction* and *scattering* due to turbulence do result in noise exposure in the shadow zone, albeit at very low SPLs. In addition, the continuity requirements following from the gradient-based optimization algorithm in *ECHO* prescribe that the noise levels in observer locations are always calculated for all helicopter positions. As a result, the noise model requires the determination of the propagation effects both in the transition to the shadow zone and in the shadow zone itself. The first step is to determine the position of the shadow zone. Consider Fig. 5.18. The launch angle θ_{sz} marking the start of the shadow zone results in a final angle of incidence $\theta_f = 0$ at the receiver height z_r. Beyond this point the shadow zone starts. To find the launch angle for this *limiting* ray, it is first noted that the *lowest layer* with a *negative speed of sound gradient*, layer j, determines the position of the shadow zone. Consider again the definition of the ray geometry per layer in Eqs. (5.8) to (5.11). These equations can be solved for the launch angle $\theta_{0,i}$ which yields

$$\theta_{0,i} = \cos^{-1}\left(\frac{\Delta z_i - \xi_i}{-\xi_i}\right) \tag{5.46}$$

with

$$\xi_i = \frac{c_i}{g_i}$$

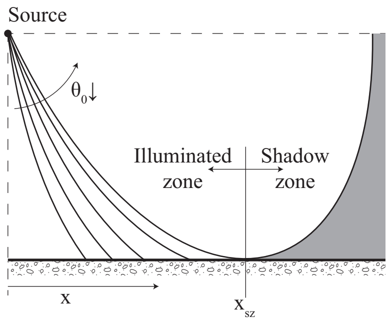

Figure 5.18: Illuminated and shadow zones

At the start of the shadow zone – and hence at the bottom of layer j – the final angle of incidence equals zero which is used to first determine the *initial* angle of incidence $\theta_{0,j}$ in this layer through Eq. (5.46). This process is then repeated until finding the launch angle at the source, yielding the limiting launch angle θ_{sz}. The limiting ray is then assessed using Eqs. (5.8) to (5.13), yielding the distance x_{sz} where the shadow zone starts.

If a receiver location lies at a distance $x_r > x_{sz}$, first the spreading loss, atmospheric attenuation and ground effect are determined at $x = x_{sz}$ – the start of the shadow zone – using the method described in the previous sections. Then the method proposed in [87] is used to determine the sound pressure levels in the shadow zone. First, upon entering the shadow zone a linear loss correction is applied based on the frequency and the local gradient of the speed of sound

$$L_{d1} = -0.0032 - 3.5 \cdot 10^{-5} f \tag{5.47}$$

$$L_{d2} = 6.7 g_n + 0.31 \tag{5.48}$$

$$L_{sz} = L_{d1} L_{d2} \left(x - x_{sz}\right) \tag{5.49}$$

where $x > x_{sz}$ and n indicates that the speed of sound gradient in the bottom layer, i.e. between the ground and the receiver height, is used. The diffraction correction L_{sz} is added to the propagation loss already determined at x_{sz} consisting of the atmospheric attenuation, spreading loss and ground effect. The ray traveling into the shadow zone is assumed to travel parallel to the ground in the bottom layer ($0 < z \leq z_r$). With the average temperature and humidity in this layer the additional attenuation loss $\Delta SPL_{A,sz}$ is determined using Eq. (5.45) over a distance $s = (x - x_{sz})$, and added to the total propagation loss. However, the correction described by Eq. (5.49) only accounts for the transition upon entering the shadow zone, and is therefore limited to a maximum of 30 dB. If the loss correction exceeds 30 dB, spherical spreading is assumed *over the full distance* $x > x_{sz}$, replacing the previously determined spreading loss at x_{sz}. Under these conditions, the total shadow zone loss can be defined as

$$\Delta SPL_{sz} = \begin{cases} \Delta SPL\Big|_{sz} + \Delta SPL_S\Big|_{sz} + L_{sz} + \Delta SPL_{A,sz}, \text{if } L_{sz} \geq 30 \text{ dB} \\ \Delta SPL\Big|_{sz} - 20\log_{10} x + \Delta SPL_{A,sz} - 30, \text{if } L_{sz} < 30 \text{ dB} \end{cases} \tag{5.50}$$

where

$$\Delta SPL\Big|_{sz} = \Delta SPL_G\Big|_{sz} + \Delta SPL_A\Big|_{sz}$$

Total Propagation Loss

With all contributions to the propagation loss defined in the previous sections, the total noise levels per frequency can be determined as follows

If an observer is within the *illuminated zone*, the total SPL per frequency n is defined by

$$SPL_n = SPL_{\lambda,\phi,n} + \Delta SPL_S + \Delta SPL_{G,n} + \Delta SPL_{A,n} \tag{5.51}$$

If an observer is within the *shadow zone*, the total SPL per frequency n is defined by

$$SPL_n = SPL_{\lambda,\phi,n} + \Delta SPL_{sz,n} \tag{5.52}$$

5.3.6 Propagation Model Validation

The propagation model described above has been validated using the work described in [87], which in turn has been validated against [88]. An overview of the validation study for different atmospheric conditions is available in Appendix B.

5.4 Total Noise Levels

5.4.1 Frequency Weighting

The source noise levels and propagation loss determined in the previous sections define the SPL contribution from a single stationary helicopter position. However, the main interest in *ECHO* is to assess the *noise impact* of helicopter trajectories on the human environment. Since the human ear can be more or less sensitive to certain pure tones, a correction is applied to account for the human perception of noise. Based on the reactions of a large number of listeners, *loudness levels p* of pure tones have been determined, which give an indication of the sensitivity of the human ear with respect to different frequencies at different SPLs. An example of equal loudness contours for pure tones can be seen in Fig. 5.19.

To reflect the loudness caused by complex sound, so-called *frequency weighting filters* are applied. Four weighting filters have been standardized [90, 91], designated A, B, C and D, as can be seen in Fig. 5.20. D-weighting was initially designed for high-level aircraft noise, specifically for low bypass-ratio aircraft engines. As B-weighting, designed for low-level noise, D-weighting has come in disuse. C-weighting was specifically designed for very high noise levels, where the human ear is less sensitive to changes in frequency. Finally, although A-weighting is based on the 40 phon contour, and hence is intended for relatively low noise levels, it is currently the standard noise metric for civil aviation noise measurements. Therefore, an A-weighting frequency filter is applied to the noise levels in *ECHO*. The weighting filter is frequency dependent, and can be expressed as follows [90, 91] for the n^{th} BPF

$$\begin{aligned} R_A(f_n) &= \frac{12200^2 f_n^4}{(f_n^2+20.6^2)\sqrt{(f_n^2+107.7^2)(f_n^2+737.9^2)}(f_n^2+12200^2)} \\ \Delta SPL_{AW,n} &= 2.0 + 20\log_{10} R_A(f_n) \end{aligned} \tag{5.53}$$

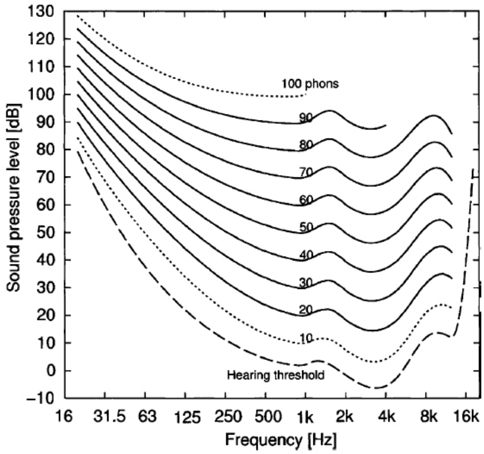

Figure 5.19: Equal loudness contours [89]

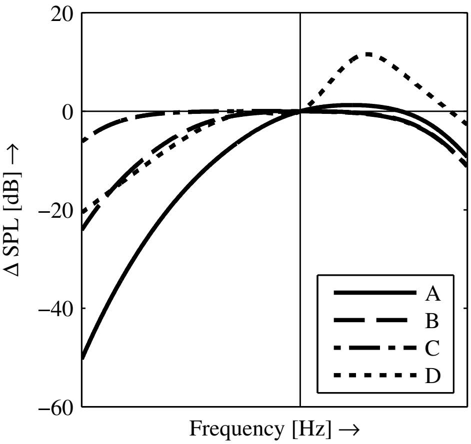

Figure 5.20: Frequency weighting filters

This is added to the source noise level and propagation loss determined in the previous sections to yield the *A-weighted sound level* in dBA defined as

$$L_{A,n} = SPL_n + \Delta SPL_{AW,n} \tag{5.54}$$

5.4.2 Sound Exposure Level

The A-weighted sound level defined above still only applies to discrete frequencies and single helicopter positions. However, rather than assessing discrete frequencies, the contribution of the complete frequency spectrum needs to be accounted for by defining the total A-weighted sound level as follows

$$L_A = 10 \log_{10} \left(\sum_{n=1}^{20} 10^{\frac{L_{A,n}}{10}} \right) \tag{5.55}$$

In reality though, not only the instantaneous sound level, but also the *duration* of the sound exposure affects the human perception of noise, and hence the nuisance caused by noise. To account for both magnitude and duration of the noise exposure the *Sound Exposure Level (SEL)* is introduced. Consider in Fig. 5.21 the effect of a helicopter passing over a ground based observer.

As the helicopter approaches the A-weighted sound level increases, to decrease again once the helicopter has passed. To account for the time variation of the noise exposure of a ground-based observer, the total amount of sound energy due to a complete trajectory is determined by integrating the A-weighted sound level over time. To eliminate the effect of different exposure times and as such to allow comparison of the noise exposure

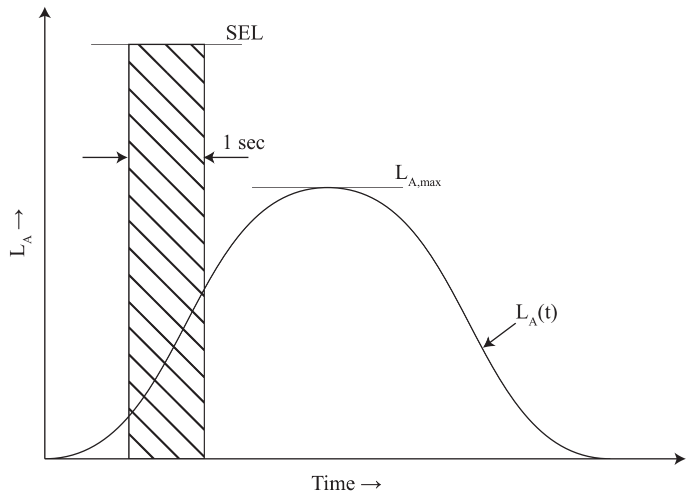

Figure 5.21: Sound Exposure Level

between different trajectories, the integrated A-weighted sound level is normalized to a period of 1 second. This yields the SEL which can be defined as

$$L_{AE} = 10 \log_{10} \left[\frac{1}{T_1} \int_0^T 10^{\frac{L_A(t)}{10}} dt \right] \tag{5.56}$$

where T_1 is the reference time of 1 second and $L_A(t)$ is the A-weighted sound level as a function of time. As *ECHO* discretizes the helicopter flight dynamics (see Chapter 3), so too are the noise levels only known for a discrete number of helicopter positions, precluding the continuous integration of the noise level to obtain the SEL. For consistency with the integration of the helicopter flight dynamics, the integration of the noise levels in *ECHO* is based on the Radau Quadrature as described in Section 3.3.1.

5.5 Noise Impact Assessment

5.5.1 Introduction

At this point in the noise model evaluation, the SEL is known on a set of discrete points or on a complete grid surrounding the helicopter trajectory, depending on the selected optimization criterion. The final step in assessing the impact of helicopter noise – and hence to be able to develop noise abatement helicopter trajectories – is to quantify the total noise impact of a full trajectory. For this a number of generic and site-specific noise performance criteria are calculated in the noise impact assessment model. The following sections will discuss these performance criteria in more detail.

5.5.2 Contour Area

The generic noise optimization criterion integrated in *ECHO* is the *contour area*. The contour area is essentially determined by calculating the area on the ground that is exposed to a noise level greater than or equal to a predefined threshold value. This performance criterion is also commonly used to assess and minimize the noise impact of generic departure and arrival procedures. Depending on the cell sizes of the grid on which the noise is calculated, the contour area can simply be determined by counting all cells with noise levels above the threshold value. However, for the implementation of this performance criterion in *ECHO* two problems arise. Firstly, this method requires a very fine grid to ensure a sufficient level of accuracy, and hence a large number of grid cells, significantly increasing the runtime of a single noise model evaluation. This, in combination with the iterative process of the optimization algorithm would lead to unacceptably high total problem runtimes. More importantly, however, is the fact that counting discrete cells will lead to discontinuities in the objective function, leading to severe convergence problems. To exemplify this, consider a cutout of two neighboring cells as seen in Fig. 5.22. The figure shows the continuous noise level in two cells. Since the noise calculated in *ECHO* is determined in the middle of each grid cell, it clearly follows that Cell 2 is above the threshold value and hence would be counted, whereas Cell 1 is not. However, if due to a change in the helicopter trajectory the value in Cell 2 would drop just below the threshold value, the cell would no longer contribute to the objective function. This discontinuous step function applying to a large number of cells would lead to severe convergence problems. In addition, it is noted that in the example Cell 2 is not fully exposed to noise levels above the threshold value, leading in this case to an overestimation of the contour area. To overcome both issues, the calculation of the contour area in *ECHO* is achieved by using an approximation to the Heaviside step function, also referred to as a switch function [25]. This can be seen in Fig. 5.23. Below the threshold value cells are not counted ($\beta_{switch} = 0$), and above the threshold value cells are counted ($\beta_{switch} = 1$). This process is approximated with the switch function β_{switch}, which is defined as

$$\beta_{switch} = \frac{1}{\pi} \tan^{-1} \left(SEL - SEL_{thr} \right) + 0.5 \tag{5.57}$$

The total contour area can then be determined from

$$A_{>thr} = \sum_{n=1}^{N} \beta_{switch}(SEL_n) a_n \tag{5.58}$$

where a_n is the area of the n^{th} grid cell.

As can be seen in the figure, near the threshold SEL value, the value of $\beta_{switch} \neq 0$. As a result, cells that are exposed to SELs close to the threshold level are still partly contributing to the objective function. In this approach all cells in the grid contribute to the objective value, and, more importantly, the total objective function is a smooth differentiable function as required. Although the gradient of the switch function can be

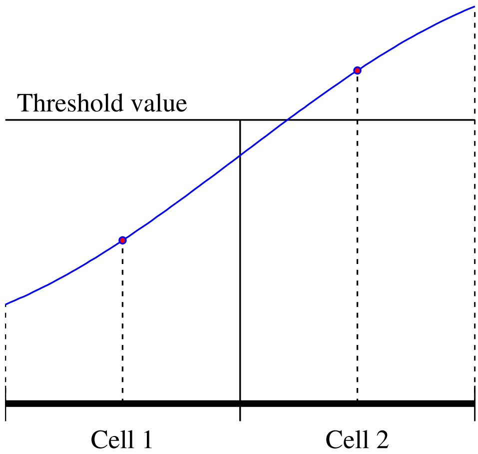

Figure 5.22: Sound level in grid cells

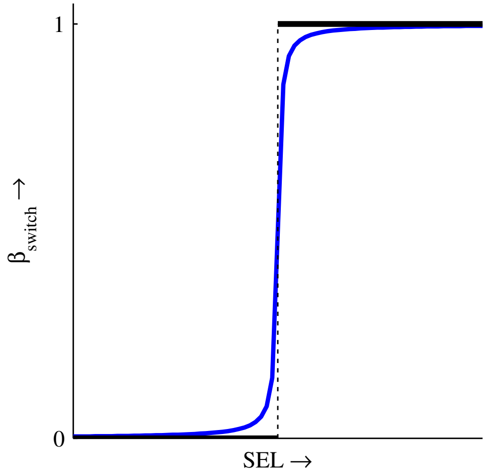

Figure 5.23: Step approximation

changed to improve the approximation of the Heaviside step function, test cases with *ECHO* have shown that the switch function defined in Eq. (5.57) proves a good trade-off between an accurate approximation and good problem convergence.

5.5.3 Number of People Enclosed in Contour

Although the noise performance criterion described above allows for generic optimization of helicopter trajectories, it is mostly used to optimize two-dimensional procedures. Since noise abatement should first and foremost be directed at reducing the noise exposure in populated areas, it is important to consider site-specific noise performance criteria, accounting for population living in the vicinity of the helicopter path. Therefore the *number of people enclosed in a contour* is introduced. This criterion counts the number of people that are exposed to noise levels above a given threshold level, and hence specifically takes into account where the trajectory is positioned with respect to population.

To accommodate site-specific noise criteria based on population data, first a *Geographic Information System (GIS)* is required. The GIS integrated in *ECHO* contains population density data for The Netherlands on a grid with 500 x 500 m cells. Expressed in the local Dutch *Rijksdriehoeks* Cartesian coordinate system, the database ranges from $x = [14,\ldots,277]$ km and $y = [307,\ldots,611]$ km, containing a total of 80520 grid cells. Of these, 29742 are populated with a total population of 16.4 million people. The data is valid for the year 2012 and is publicly available from the Dutch *Centraal Bureau voor de Statistiek (Statistics Netherlands) (CBS)*. An example of a section of the GIS data for the area around the city of Rotterdam can be seen in Fig. 5.24. To reduce the runtime of optimizations involving noise, a section of the grid can be selected in the vicinity of the helicopter trajectory. In addition, when a population-based noise optimization criterion is

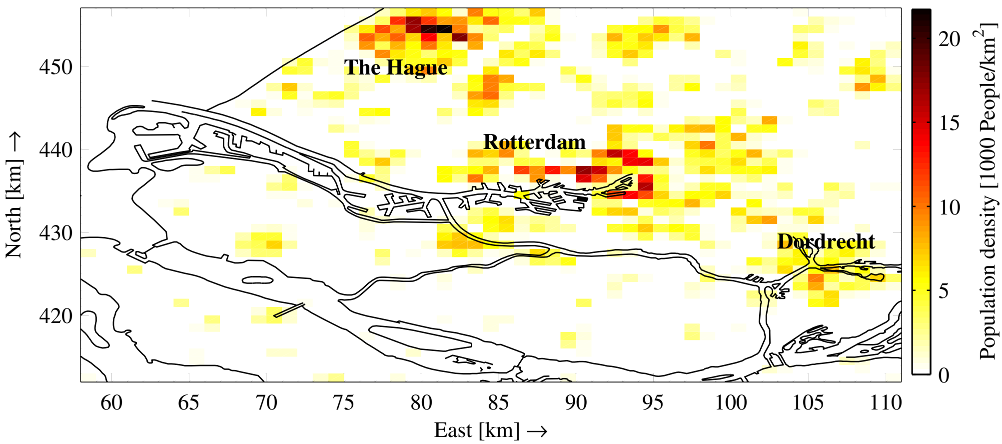

Figure 5.24: Population density, Rotterdam area

defined, *ECHO* automatically only calculates the noise in cells with population present.To determine the total number of people within a reference contour level the same procedure is followed as for the contour area. Again to avoid discontinuities the switch function of Eq. (5.57) is applied. The total number of people in a contour can then be defined as

$$P_{>thr} = \sum_{n=1}^{N} \beta_{switch}(SEL_n)p_n \tag{5.59}$$

where p_n is the number of people in cell n.

5.5.4 Expected Awakenings

The population exposed to a noise level higher than a given threshold level already clearly focuses on the effect of noise exposure on population. However, the magnitude of the noise exposure is not yet accounted for. The criterion does not offer a weighting for population exposed to excessively high noise levels, and as a result there is no direct incentive for the optimization algorithm to minimize or at least reduce the maximum noise exposure levels. Still, it is readily clear that excessively high noise levels are not acceptible, and can contribute to for instance noise nuisance, sleep disturbance or health impairment. To account for the magnitude of the noise exposure in populated areas, the final noise criterion integrated in *ECHO* uses a *dose-response relationship* to quantify sleep disturbance due to a single night time flyover. The dose-response relationship was defined by the *Federal Interagency Committee on Aviation Noise (FICAN)* [92] and defines the *maximum percent of the exposed population expected to be behaviorally awakened*. The relationship is based on three field studies [93–96] and predicts a conservative relationship based on the results of all three studies. The resulting curve can be seen in Fig. 5.25 and

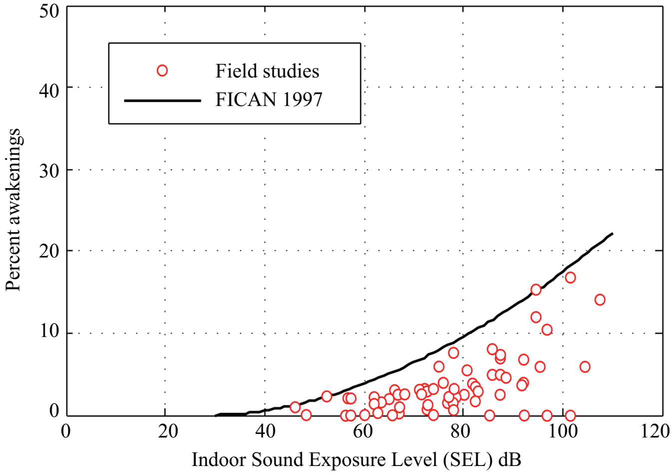

Figure 5.25: FICAN Dose-response relationship (adapted from [92])

is represented by the following expression

$$\%A_n = 0.0087\left(SEL_{indoor,n} - 30\right)^{1.79} \tag{5.60}$$

where $SEL_{indoor,n}$ is the SEL experienced inside a typical home in grid cell n. To relate the indoor SEL to the outdoor SEL calculated by the noise model in *ECHO*, a 20.5 dBA correction is applied to account for the sound absorption of a typical home [27], which yields $SEL_{indoor} = SEL - 20.5$. It is noted that the relationship of Eq. (5.60) is only applicable to indoor SELs above 30 dBA. To determine the total number of expected awakenings due to a single nighttime flyover – hereafter referred to as *awakenings* for the sake of brevity – for each cell the percent awakenings is multiplied with the population in the cell and summed. This yields the total number of awakenings N_A defined by

$$N_A = \sum_{n=1}^{N} \frac{\%A_n}{100} p_n \tag{5.61}$$

5.6 Conclusions

In this chapter the selection and development of the components of the helicopter noise model integrated in *ECHO* is described. To model the source noise, a database of source noise levels for different frequencies and projected on a hemisphere around the helicopter rotor hub was acquired. This database is derived aeroacoustically based on inputs from the flight dynamics model, *viz.* the disc-tilt angles and the advance ratio.

The propagation model to determine the attenuation loss between the source and the receiver was developed specifically for the *ECHO* suite to comply with the continuity requirements set by the selected optimization algorithm and to maintain relatively short execution times. The propagation model uses a geometrical approach of standard ray-tracing techniques allowing for a significantly lower number of integration steps and hence a shorter runtime. In addition, the benefit of using ray-tracing techniques is that the numerical process of determining the ray path between source and receiver is not dependent on the frequency, and hence has to be executed only once. The propagation model developed for *ECHO* accounts for spreading loss, ground effect and atmospheric absorption in different atmospheric conditions including moderate wind speeds. In addition, to ensure continuity in all observer locations, a model to approximate the noise penetrating the shadow zone is included.

Finally a selection of noise impact assessment criteria is presented to quantify the total noise impact in the area surrounding the trajectory. These include both generic and site-specific, population-based criteria.

6
Scenario 1: 2D Arrival

6.1 Scenario Description

As a first example of the capabilities of the *ECHO* suite, the optimization of a two-dimensional generic arrival trajectory is presented. The trajectory is assumed to start in level flight at an an initial *True Airspeed (TAS)* of 100 kts (51.44 $\text{m}\cdot\text{s}^{-1}$) and at an altitude of 2,000 ft (609.6 m) *Above Ground Level (AGL)*. The landing takes place on a conventional landing field and hence the landing profile defined in Fig. 6.1 is used as a basis to define the trajectory's terminal boundary conditions. The profile defined in the figure includes the so-called *Landing Decision Point (LDP)*. If an engine failure (*One Engine Inoperative (OEI)*) occurs before the LDP the pilot has to follow the rejected landing profile. If, however, OEI occurs after the LDP, the landing is continued. In the optimization of trajectories involving the *ECHO* suite, no emergency situations are assumed to occur. However, up to the LDP the published landing procedure still needs to be adhered to, making the LDP a suitable terminal point to be considered for this scenario. However, as the source noise database integrated in *ECHO* is only valid for speeds down to 30 knots (15.43 $\text{m} \cdot \text{s}^{-1}$), the terminal boundary conditions are defined just before the LDP to remain within the boundaries of the source noise model. As such, the final airspeed is set to 30 knots. In addition, the 300 fpm (1.524 $\text{m} \cdot \text{s}^{-1}$) rate of descent limit imposed at the LDP is not imposed as a terminal condition for this scenario. To accommodate the deceleration to the conditions at the LDP, a final altitude of 300 ft (91.44 m) *Above Helipad Elevation (AHE)* is assumed, which, for a conventional landing field, equals 300 ft AGL.

During the entire scenario, the path constraints and state bounds described in Section 4.5 are imposed unless mentioned otherwise. A complete overview of the boundary conditions imposed on this scenario can be found in Table 6.1. All optimized trajectories

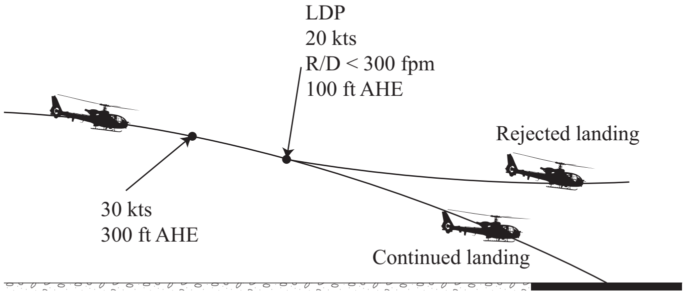

Figure 6.1: Field landing profile (adapted from [57])

Table 6.1: Boundary conditions for Scenario 1

Boundary condition	**(In)equality**
Initial speed	$V_0 = 100$ knots
Initial rate of descent	$v_{z,0} = 0$ fpm
Initial altitude	$z_0 = 2000$ ft
Initial position	$(x_0, y_0) = (0, 0)$ m
Final speed	$V_f = 30$ knots
Final altitude	$z_f = 150$ ft
Final position	$(x_f, y_f) = (15000, 0)$ m

presented below are assumed to be flown in the *International Standard Atmosphere (ISA)*.

The trajectories in Scenario 1 have been optimized with respect to total flight time, total fuel burn and total NO_x emissions. As the scenario represents a generic landing procedure, also a generic noise optimization criterion is selected. The contour area above 65 dBA SEL is added to the objective function which can then be defined as

$$J = k_{time} t_f + k_{noise} A_{>65} + \int_{t_0}^{t_f} \left(k_{fuel} \dot{m}_f + k_{NO_x} \dot{m}_{NO_x} \right) dt + \upsilon \int_{t_0}^{t_f} \sum_{i=1}^{4} u_i^2 dt \tag{6.1}$$

This includes the control damping component discussed in Section 4.3. The weighting factors $k \geq 0$ allow the assessment of different performance criteria separately (by setting all weighting factors to zero except one), or to define a composite performance index to for instance optimize for a weighted combination of flight time and noise. It is noted that in all cases total flight time, fuel burn and NO_x emissions are optimized individually, and that only in case of optimized trajectories including noise a composite performance index is used where two weighting factors are non-zero.

Table 6.2: Scenario 1, Case 1 results: single objective

Case	**Objective**	$\mathbf{t_f}$ **[s]**	$\mathbf{m_f}$ **[kg]**	$\mathbf{m_{NO_x}}$ **[g]**	$\mathbf{A_{>SEL_{65}}}$ **[km^2]**
C01_01	t_f	**304.2**	13.56	47.18	39.67
C01_02	m_f	307.1	**13.09**	46.38	46.03
C01_03	m_{NO_x}	311.1	13.39	**46.37**	44.65

6.2 Case 1: Single Phase

6.2.1 Case Description

In the first case of Scenario 1 presented here the trajectory has been configured using a single phase problem definition. As a result, the same constraints and state and control bounds apply throughout the trajectory. The trajectory has been discretized with a total number of 100 nodes, leading to a total problem size of 2,422 nonlinear variables and 2,702 nonlinear constraints (which include state and control bounds, path constraints and boundary conditions). The noise impact is calculated on a 9.5x26.5 km grid with cells of 500x500 m, leading to a total of 1,080 grid cells. For comparison, the NLP problem size is more than 9 times larger than that presented in [25] – which uses a comparable optimization method – with twice the number of grid cells.

6.2.2 Results

In Table 6.2 the first results pertaining to time, fuel and NO_x optimized trajectories are presented, where all other weighting factors are zero. As can be seen from the table the differences in the performance indicators are relatively small for the considered cases. It can also be seen from the altitude and airspeed profiles in Fig. 6.2 that the trajectories are quite similar. In fact, only the minimum time solution is significantly different as it minimizes the total path length by constantly descending. Both the minimum fuel and NO_x maintain a higher altitude to reduce the power required and as a result to reduce the fuel flow and NO_x emission rate. The largest reduction in the performance indicator – with respect to the second best performing solution – is found in the minimum fuel solution of case C01_02. A 2.2% reduction in total fuel burn is achieved mainly by avoiding high initial decelerations after the descent has been initiated. In the minimum NO_x solution the airspeed is reduced to approximately 95 knots before initiating the descent. However, as compared to the minimum fuel solution the effect on the performance indicator is negligible. A further noticeable observation is that even though the relative improvements in the objective criteria are small, the contour area above 65 dBA SEL is significantly affected. This is especially apparent in the minimum time solution, where the contour area is 11% smaller than in the minimum NO_x solution.

To identify the cause of the reduced contour area in the minimum time solution presented above, in the second set of results the contour area above 65 dBA SEL is accounted for in the objective function as well, together with fuel. Therefore, all weighting factors are set to zero, except $k_{fuel} = 1$, while k_{noise} is varied to assess the effect of

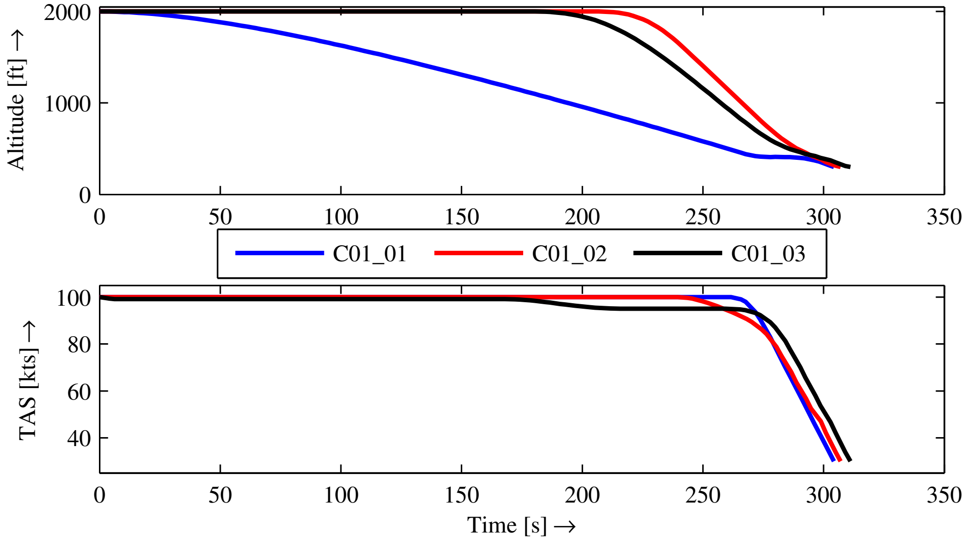

Figure 6.2: Altitude and speed profiles, single objective

Table 6.3: Scenario 1, Case 1 results: fuel and noise optimized

Case	**Objective**	$\mathbf{t_f}$ **[s]**	$\mathbf{m_f}$ **[kg]**	$\mathbf{m_{NO_x}}$ **[g]**	$\mathbf{A_{>SEL_{65}}}$ **[km^2]**
C01_02	m_f	307.1	**13.09**	46.38	46.03
C01_04	$m_f + 1.25 \cdot 10^{-7} A_{>65}$	305.0	**13.26**	47.18	**30.10**
C01_05	$m_f + 2.5 \cdot 10^{-7} A_{>65}$	306.0	**13.29**	47.20	**29.92**
C01_06	$m_f + 5 \cdot 10^{-7} A_{>65}$	311.9	**13.46**	47.23	**29.12**
C01_07	$m_f + 10^{-6} A_{>65}$	317.4	**13.62**	47.32	**28.87**

increased noise weighting on the trajectory. The results can be seen in Table 6.3. It now immediately follows that the contour area can be significantly reduced. A 37% noise reduction can be achieved with an increased fuel burn of only 4.0% with respect to the minimum fuel solution. However, although these results seem promising, when the altitude and airspeed profiles presented in Fig. 6.3 are considered, a problem caused by the single phase trajectory definition emerges. Similar to the single objective results ($k_{noise} = 0$), a high airspeed is maintained in all trajectories where noise is represented in the objective function. However, the altitude is reduced to the minimum allowed level of 300 ft directly after the start of the trajectory. Although sustained flight at an altitude of 300 ft is not acceptable for reasons such as safety and extreme nuisance in surrounding communities, these cases do clearly give an initial insight in what could be the preferred flight conditions to reduce the contour area.

The high airspeeds observed in all trajectories contribute to the reduction of the noise levels in two ways. First, consider again the expression for the Sound Exposure

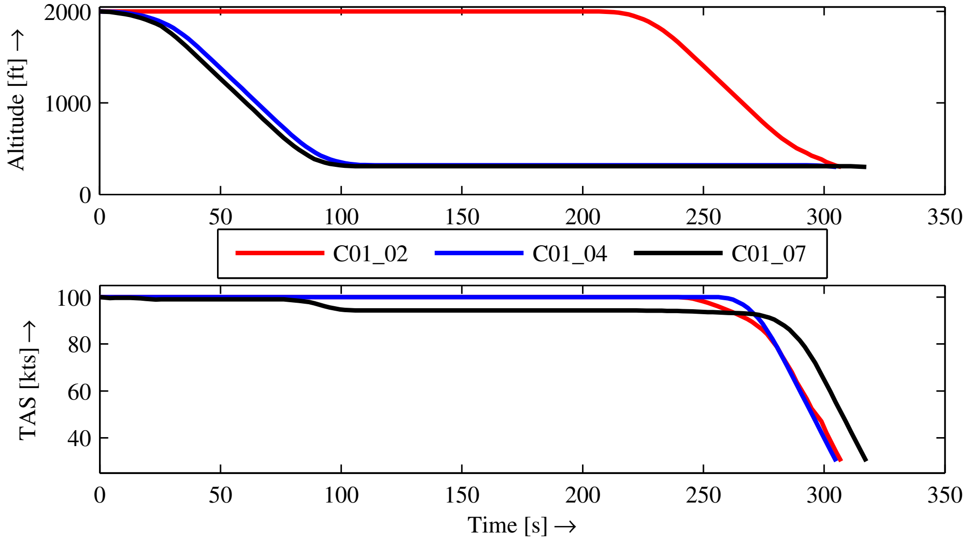

Figure 6.3: Altitude and speed profiles, fuel and noise optimized

Level (SEL) in Eq. (5.56). The SEL is an *exposure based* noise metric, indicating that the exposure time T affects the noise levels. A higher airspeed would result in a lower exposure time, and, for a given source noise level, would therefore reduce the SEL observed on the ground.

Furthermore, the high airspeeds lead to significantly lower source noise levels. Consider the overview of the source noise model in Appendix A, Fig. A.2. It is apparent that hemispheres corresponding to high speed flight at small flight path angles typically show significantly lower source noise levels. Although the source noise levels also depend on the flight path angle, it can readily be concluded that the high airspeeds observed in all trajectories will have a significant effect on the source noise levels, and as a result also on the contour area. This conclusion is fully supported by the flight test data presented in [14].

In addition to the high airspeeds, in all cases where $k_{noise} \neq 0$ the altitude is reduced to the minimum allowed level directly after the start of the trajectory. This reduces the slant range between source and receiver, hence reducing the propagation losses due to absorption and spreading. This then might be expected to lead to higher noise levels observed on the ground. This is indeed true directly below the flight path. However, the low altitude flight contributes significantly to the reduction of the contour area. As with the airspeed, the explanation is twofold. Firstly, consider again the source noise model overview in Appendix A, Fig. A.2, and the source noise levels as a function of azimuth and elevation angle in Fig. A.3. It can be seen that closer to the equatorial plane of the hemispheres source noise levels are generally lower as a result of the downward directionality of the loading and BVI noise components. Although observers directly below the flight path will experience higher noise levels due to the reduced slant range,

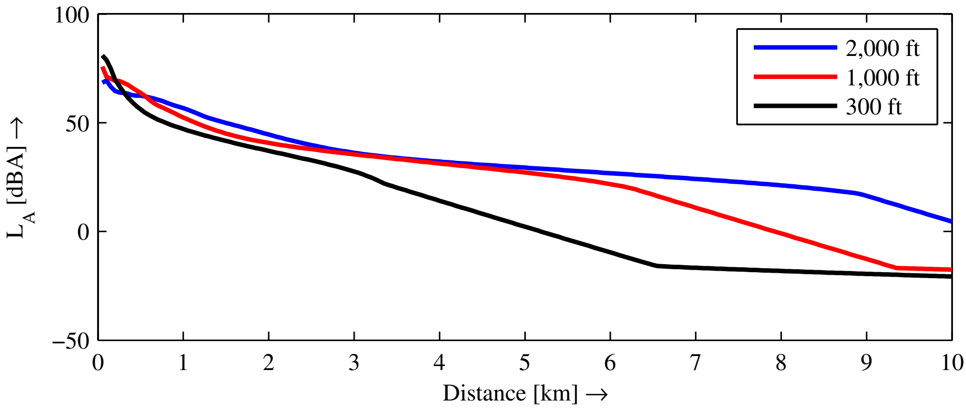

Figure 6.4: Sideline noise levels

receivers astride the trajectory are exposed to the lower source noise levels due to the low altitude flight and the resulting high incidence angles between source and receiver.

A more important effect of the low altitude path is the lateral attenuation of sound. This phenomenon can be explained by considering Fig. 6.4 where the A-weighted sound level L_A to the right side of a helicopter flying at an airspeed of 100 knots is shown for three different altitudes. The figure shows that only directly below the flight path the noise exposure is highest when flying at 300 ft. When the observer is further away from the flight path, the noise levels observed are significantly lower. Up to about 2 km this is caused by the ground effect. Recall from Eq. (5.41) that the reflection factor Q depends on the final angle of incidence θ_f on the ground. As a result, at low source height, and hence small final angles of incidence, the reflection factor Q will be smaller, and as such the contribution of the reflected ray. A more significant difference can be seen from approximately 3 km from the a source at a height of 300 ft, where the shadow zone starts. When the distance is increased even further, the noise exposure drops significantly, and in fact quickly to a level that is no longer relevant. When the sources at 2,000 ft and 1,000 ft are considered, it can be seen that the shadow zone only starts after about 9 km and 6 km, respectively, leading to significantly higher noise levels astride the flight path. The total result is a significantly narrower noise contour after the descent has been completed, as can be seen in the contour plots of Fig. 6.5.

From the above discussion it can be concluded that low altitude, high speed flight significantly reduces the noise exposure on the ground in terms of the contour area above 65 dBA SEL. The result is a relatively narrow contour with slightly higher noise exposure levels directly below the flight path. However, when the overview of the source noise model in Appendix A is considered again it can be seen that although high speed flight results in relatively low source noise levels, high flight path angles and hence steep descents have an opposite effect. In fact, closer inspection of the flight path angle history in Fig. 6.6 reveals that the maximum flight path angle is just below -8.5°, which at

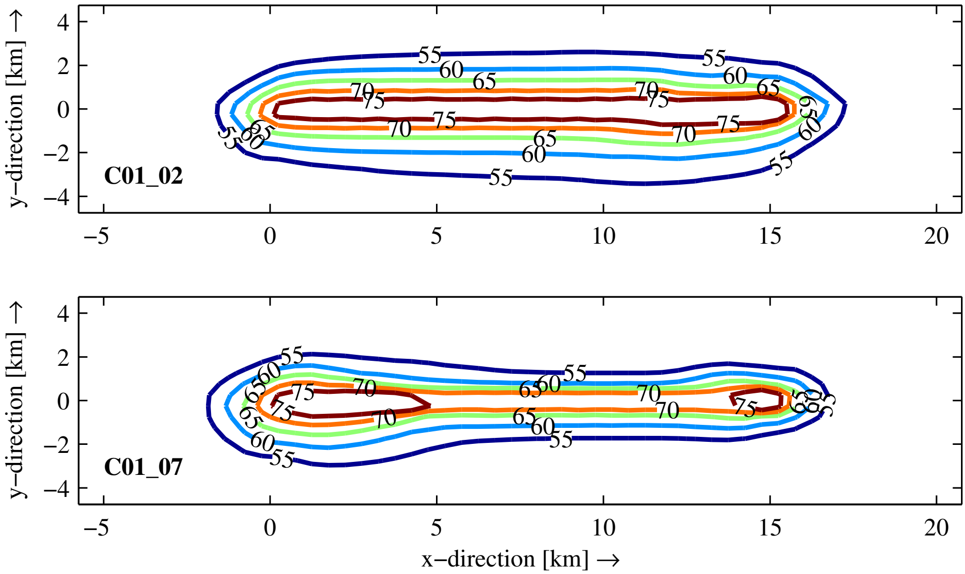

Figure 6.5: SEL contours, fuel and noise optimized

an airspeed of 100 knots corresponds to the maximum allowed rate of descent of 1,500 fpm. Although this would indeed lead to higher source noise levels as compared to level flight, the steep descent maximizes the length of the trajectories flown at the minimum altitude of 300 ft. It can only be concluded that the increased propagation loss due to low altitude flight outweighs the short period of increased source noise levels due to the high flight path angles.

A final, secondary effect to reduce the noise exposure can be identified by considering again the altitude and airspeed profiles in Fig. 6.2. In the fuel optimized case, C01_02, deceleration to meet the boundary conditions is initiated during the descent phase. This, in combination with the high flight path angles seen in Fig. 6.6 implies that relatively close to the ground the helicopter is operated at low airspeeds and high flight path angles – the least preferential conditions in terms of source noise levels. In cases where noise is accounted for in the objective function, the descent is executed at high speeds, and flight close to the ground is mostly level flight. As a result, the combination of low airspeeds and high flight path angles is avoided in the noise optimized solutions, further reducing the noise exposure and hence the contour area above 65 dBA SEL.

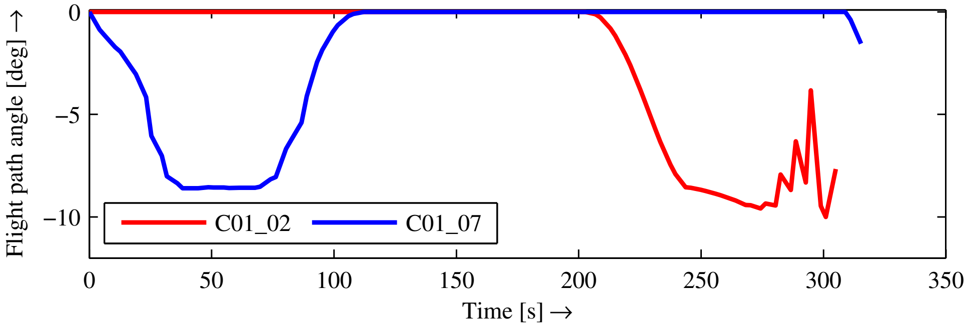

Figure 6.6: Flight path angle, fuel and noise optimized

6.3 Case 2: Two Phases

6.3.1 Case Description

Although the results presented above provide a good initial understanding of the characteristic behavior to mitigate the contour area above 65 dBA SEL, considerations such as excessively high noise levels directly below the flight path and external safety render the optimal trajectories in Case 1 unacceptable for operational implementation. To obtain more realistic trajectories, Case 2 presented herein includes a glideslope segment where the flight path angle is constant during the descent from cruise to landing altitude. As a consequence, the problem has to be described by two phases, as in the glideslope segment different path constraints will apply.

In the first of the two phases, the helicopter starts in level flight in the same initial conditions as Case 1, i.e. at 2,000 ft and 100 knots TAS, and the general constraints of Section 4.5 apply. Phase 1 ends as the helicopter is stabilized on the glideslope, which implies that the transition from level flight to a descent at a constant flight path angle is part of phase 1. To accommodate this transition, the final altitude of phase 1 is set at 1,900 ft (579.12 m), allowing a 100 ft (30.48 m) altitude margin to execute the transition. The final airspeed and positional coordinates of the first phase are not prescribed.

In the second phase the flight along the glideslope is executed. The final conditions are the same as those used for Case 1 described above. In addition to the general path constraints, during phase 2 a constant flight path angle is maintained. However, the value of the flight path angle is not prescribed, and in fact is an optimization parameter. To accommodate different glideslope angles, a design parameter associated to the flight path angle has been added to the problem setup, which ranges from - 3° to -10° to ensure that only flight within the boundaries of the source noise model is modeled.

The addition of a second phase also requires the definition of linkage constraints. For this problem setup, twenty linkage constraints are defined to ensure that all twenty vehicle states are continuous along the link between phases 1 and 2, essentially equating the states to the left of the switch to the states on the right. With 50 nodes in phase

Table 6.4: Additional constraints for Scenario 1, Case 2

Constraint	**Phase no.**	**(In)equality**
Final altitude	1	$z_f = 1900$ ft
Linkage constraints	(1,2)	$\mathbf{x}_l = \mathbf{x}_r$
Glide slope angle	2	$-10° \leq \gamma_{GS} \leq -3°$
Follow glideslope	2	$\gamma = \gamma_{GS}$

1, and 50 nodes in phase 2, the time discretization is similar to that of Case 1. The additional constraints for Case 2 are summarized in Table 6.4, which are added to the constraints listed in Table 6.1. This leads to a total problem size for Case 2 of 2,445 nonlinear variables and 2,722 nonlinear constraints.

6.3.2 Results

In Table 6.5 the results for the time, fuel and NO_x optimized cases are presented, along with the corresponding altitude and speed profiles in Fig. 6.7. It is noted that in solutions C02_03 and C02_04, both optimized for minimum fuel burn, the flight path angles are forced to -3° and -10°, respectively, to serve as reference cases and to assess the effect of the flight path angle on the various optimization criteria.

As can be seen from the results in the table, again the differences between the performance indicators are relatively small. Although the second phase of the trajectory now constitutes a fixed glideslope angle, the results are both qualitatively and quantitatively similar to those presented for Case 1 above. When the three fuel optimized solutions in Fig. 6.7 are considered, it can again be seen that a high altitude profile leads to a lower total fuel burn. Consider case C02_03 where the glideslope is prescribed at -3°. This forces the helicopter to start descending early, and hence leads to a 2.7% increase in the total fuel burn compared to the minimum fuel solution. When the glideslope angle is prescribed at -10° – and high altitude is maintained as long as possible – also a 3.1% increase in the total fuel burn is observed, even though the glideslope angle is very close to the optimal glideslope angle of -9°. This can be explained by considering that at a flight path angle of -10° the airspeed needs to be reduced to at most 85.3 kts TAS not to exceed the 1,500 fpm rate of descent limit. In fact, in solution C02_04 the airspeed is reduced even further, to 72.3 kts TAS. At the optimal glideslope angle of -9° the airspeed is not limited by the rate of descent constraint, and hence the optimal altitude and airspeed profile can be selected within the constraint bounds. In addition, the comparison between the three minimum fuel solution shows that the contour are above 65 dBA SEL depends heavily on the glideslope angle. This effect can again be attributed mainly to the source noise levels. Firstly, in descending flight the helicopter main rotor descends partly through its own wake, resulting in more Blade-Vortex Interaction (BVI) noise, and hence higher source noise levels. As can be seen in the overview of the source noise model in Appendix A, with increasing descent angles the source noise levels in general increase. In addition, when the airspeed is reduced to descend at 10°, the source noise

Table 6.5: Scenario 1, Case 2 results: single objective

Case	Objective	t_f [s]	m_f [kg]	m_{NO_x} [g]	$A_{>SEL_{65}}$ [km^2]	γ_{GS}
C02_01	t_f	**304.5**	13.50	46.88	41.06	-3.00°
C02_02	m_f	308.5	**13.14**	46.73	46.10	-8.99°
C02_03	m_f	304.6	**13.49**	46.82	41.07	*-3.00°*
C02_04	m_f	323.9	**13.55**	47.80	48.89	*-10.0°*
C02_05	m_{NO_x}	311.0	13.60	**46.71**	42.30	-3.59°

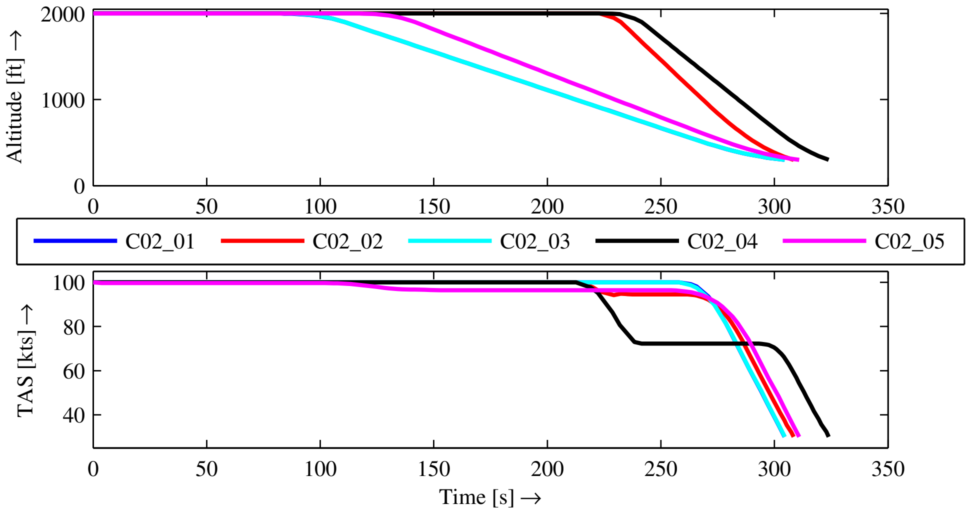

Figure 6.7: Altitude and speed profiles, single objective

levels are further increased.

When noise is added to the objective function, a 12.5% reduction in the contour area above 65 dBA SEL can be observed in Table 6.6 for case C02_08, compared to the minimum fuel solution. Although significantly less than the 37% reduction in the contour area observed in case C01_07, similar characteristic behavior to mitigate the noise exposure can be seen in the altitude and airspeed profiles in Fig. 6.8. In the noise optimize solution C02_08, the altitude is reduced as soon as possible to the final altitude of 1,900 ft in phase 1. Although the effect of an initial 100 ft descent is only marginal, the preference for low flight to reduce the contour area can again be recognized. In addition, at increasing values for k_{noise} noise becomes dominant in the objective function, and as a consequence the flight path angle is reduced to -3°. This reduces the source noise levels, but also leads to a generally lower flight profile, hence increasing the lateral attenuation of sound. As in Case 1, it can be concluded that low altitude flight at high airspeeds clearly significantly reduces the contour area above 65 dBA SEL.

Table 6.6: Scenario 1, Case 2 results: fuel and noise optimized

Case	**Objective**	$\mathbf{t_f}$ [s]	$\mathbf{m_f}$ [kg]	$\mathbf{m_{NO_x}}$ [g]	$\mathbf{A_{>SEL_{65}}}$ [km^2]	γ_{GS}
C02_02	m_f	308.5	**13.14**	46.73	46.10	-8.99°
C02_06	$m_f + 2.5 \cdot 10^{-7} A_{>65}$	307.2	**13.21**	46.71	**45.42**	-8.03°
C02_07	$m_f + 5 \cdot 10^{-7} A_{>65}$	310.3	**13.30**	46.72	**45.23**	-7.98°
C02_08	$m_f + 10^{-6} A_{>65}$	317.5	**13.85**	46.95	**40.32**	-3.00°

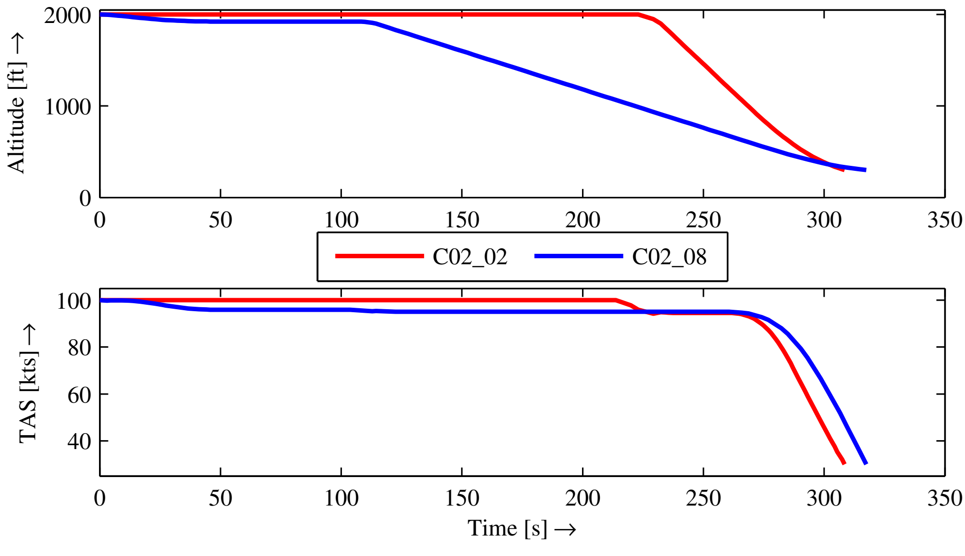

Figure 6.8: Altitude and speed profiles, fuel and noise optimized

Table 6.7: Scenario 1, Case 3 results: single objective

Case	**Objective**	$\mathbf{t_f}$ **[s]**	$\mathbf{m_f}$ **[kg]**	$\mathbf{m_{NO_x}}$ **[g]**	$\mathbf{A_{>SEL_{65}}}$ $\mathbf{[km^2]}$	$\boldsymbol{\gamma_{GS}}$
C03_01	t_f	**304.5**	13.54	47.04	39.87	-3.00°
C03_02	m_f	306.0	**13.18**	46.75	45.77	-8.36°
C03_03	m_f	304.9	**13.34**	46.70	42.11	*-3.00°*
C03_04	m_f	310.0	**13.24**	47.06	47.13	*-10.0°*
C03_05	m_{NO_x}	310.4	13.43	**46.48**	42.54	-3.31°

6.4 Case 3: Alternate Glideslope Capture

6.4.1 Case Description

Although the addition of a glideslope phase in the previous case leads to more realistic and acceptable trajectories, the inability to descend before capturing the glideslope has a clear effect on the possible reduction of the contour area above 65 dBA SEL. In the final case of Scenario 1, a glideslope segment is still enforced, but the altitude at which the glideslope is intercepted has been lowered to 1,000 ft (304.8 m) AGL. This allows the helicopter to descend to mitigate the noise exposure, but ensures that an acceptable altitude is maintained until the final approach phase.

As in Case 2, a two-phase problem definition is required to separate the arrival and glideslope segments. The constraints and boundary conditions are the same as those mentioned above for Case 2, with the exception of a final altitude of 1,000 ft AGL in the first phase. The lower glideslope intercept altitude significantly reduces the length of the glideslope phase. To ensure a time discretization comparable to the previous two cases, the first phase is discretized with 70 nodes, and the glideslope phase with 30. The problem then again contains 2,445 nonlinear variables and 2,722 nonlinear constraints.

6.4.2 Results

As in the previous cases, first the solutions for minimum time, fuel and NO_x are presented in Table 6.7, including minimum fuel solutions with fixed glideslope angles at respectively -3° and -10°.

Again, quantitative results with respect to time, fuel and NO_x are similar and only small improvements can be made for either performance criterion. The altitude and airspeed profiles in Fig. 6.9 show the characteristic behavior observed in previous cases where both fuel and NO_x optimized solutions maintain altitude, and only the time optimized solution shows a continuously descending profile.

In Table 6.8 the results for Case 3 with $k_{noise} > 0$ are presented, along with the corresponding altitude and airspeed profiles in Fig. 6.10. In all four cases the possibility to descend early is used to reduce the noise impact on the ground. However, when the contribution of noise to the objective function is still relatively low, the altitude is not reduced to the minimum allowed altitude of 1,000 ft. In case C03_06, with the smallest contribution of noise to the objective function ($k_{noise} = 1.25 \cdot 10^{-7}$), an altitude of 1,300

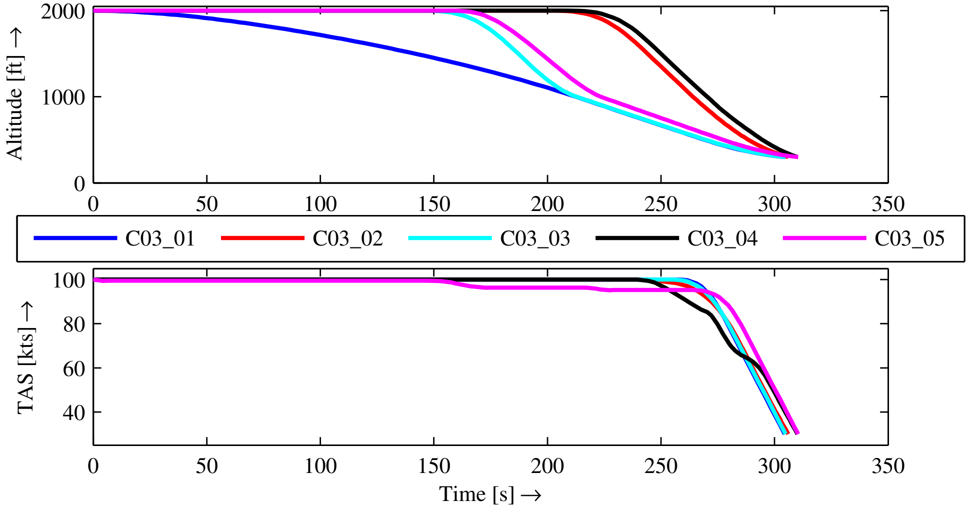

Figure 6.9: Altitude and speed profiles, single objective

Table 6.8: Scenario 1, Case 3 results: fuel and noise optimized

Case	**Objective**	$\mathbf{t_f}$ **[s]**	$\mathbf{m_f}$ **[kg]**	$\mathbf{A_{>SEL_{65}}}$ **[km^2]**	$\gamma_{\mathbf{GS}}$
C03_02	m_f	306.0	**13.18**	45.77	-8.36°
C03_06	$m_f + 1.25 \cdot 10^{-7} A_{>65}$	305.8	**13.40**	**40.97**	-7.99°
C03_07	$m_f + 2.5 \cdot 10^{-7} A_{>65}$	307.3	**13.44**	**40.72**	-8.10°
C03_08	$m_f + 5 \cdot 10^{-7} A_{>65}$	310.2	**13.46**	**38.06**	-5.54°
C03_09	$m_f + 10^{-6} A_{>65}$	317.0	**13.64**	**37.82**	-5.53°

ft is maintained as the contribution of fuel in the objective function is still dominant. In this case the contour area is reduced by 10.5% at the cost of an increase in the total fuel burn of only 1.7%. Similar observations can be made for case C03_07. In the other two cases the altitude is reduced to 1,000 ft directly after the trajectory is initiated, and similar to the results in Case 2 the selected glideslope angle is shallower. The reduced altitude and glideslope angle is found to result in a 17.4% reduction of the contour area above 65 dBA SEL while resulting in 3.5% more total fuel burn.

6.5 Conclusions

Scenario 1 was defined as an initial test case for the *ECHO* suite and was limited to a relatively simple two-dimensional arrival trajectory optimized for flight time, fuel burn, NO_x emissions and the contour area above 65 dBA SEL. It also served as an initial test for the general constraints defined in Section 4.5 and additional scenario-specific

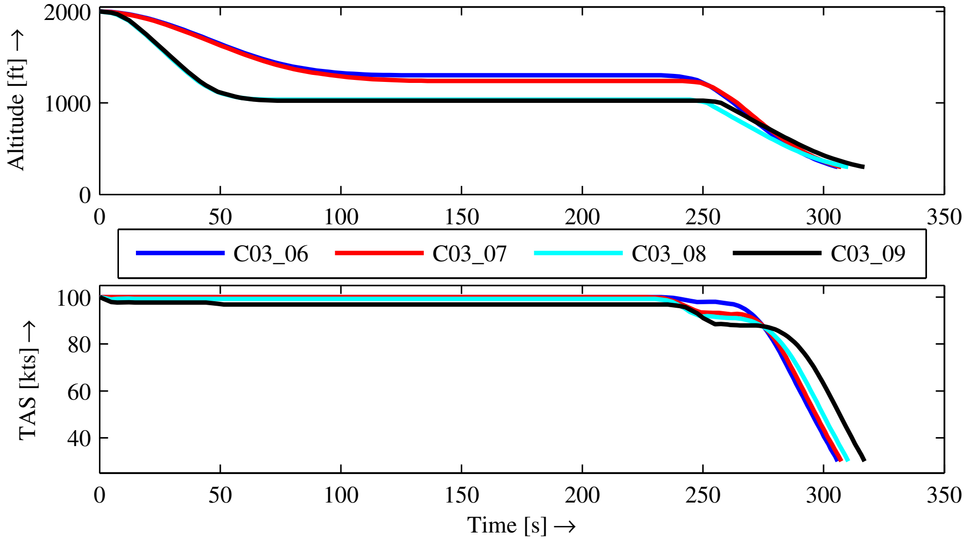

Figure 6.10: Altitude and speed profiles, fuel and noise optimized

constraints. The scenario has given an initial insight in the behavior of helicopter trajectories optimized for different criteria.

For the reduction of the contour area above 65 dBA SEL, two mechanisms can be distinguished. Firstly, in all cases considered in this scenario it was found that a high airspeed is beneficial. This can be explained by considering that the Sound Exposure Level (SEL) is an exposure based noise metric. As a consequence, a high airspeed reduces the exposure time, which, in case of equal source noise levels, leads to lower SELs on the ground. In addition, source noise hemispheres related to high airspeed generally show significantly lower source noise levels than at low airspeeds, hence further reducing the noise exposure on the ground.

Secondly, reducing the altitude also has a twofold effect towards the reduction of the contour area. At low altitude, the incidence angle between the source and ground based observers astride the flight path is larger, resulting in source noise originating closer to the equatorial plane of the source noise hemispheres. As a result of the downward directionality of most helicopter noise sources, source noise at high incidence angles is generally lower. A more significant effect of the low altitude flight is the increased lateral attenuation of sound. As the sound rays reach the ground at shallower angles of incidence, more sound energy is dissipated dependent on the reflection factor of the ground surface. In addition, in case of negative speed of sound gradients, and hence the occurrence of shadow zones, flying low significantly reduces the range direct sound rays can travel, and hence also reduces the illuminated zone with the highest noise levels. Ground effect and shadow zones ensure significantly lower noise exposure astride the trajectory when flying low, and can be concluded to have the largest contribution to reducing the contour area.

When optimal solutions for fuel burn, flight time and NO_x emissions are compared, it can be seen that in most cases results are very similar. Although in the least constrained case, Case 1, significant improvements have been found – most notably the difference between fuel and time optimal solutions – in all other cases the gains for the optimization criterion were negligible. This is partly caused by the commonality of mechanisms to reduce either criterion. For example, high speed flight is preferable for all three criteria. Only in NO_x optimized solutions a small reduction of the airspeed can be observed. This leads to a significant increase in total flight time, but does not significantly affect the emission of NO_x. When a composite objective function is used including both the total fuel burn and the contour area above 65 dBA SEL, it was found that the preference to fly low to reduce the contour area negatively affects the total fuel burn. However, it was also found that in all cases of Scenario 1 a significant reduction of the contour area can be achieved with a relatively small increase in the total fuel burn.

Finally, Scenario 1 served as an initial test of the capabilities and performance of the *ECHO* suite. Some preliminary conclusions can be drawn with respect to the performance of *ECHO*. Firstly, for this particular scenario runtimes while excluding noise from the objective function are less than 30 seconds on average. With noise included runtimes increase to an average of 1.35 hours on a standard single-core laptop computer. In addition, one of the objectives of Scenario 1 was to assess the capability of the *ECHO* suite to handle a set of complex constraints. It can be concluded from the cases presented above that in all cases constraints were successfully imposed, and that the *ECHO* suite is easily adaptable to different cases within a scenario.

An overview of the results of all solutions for Scenario 1 (including more parameters not presented here) can be found in Appendix C.

7

Scenario 2: Rotterdam City Center

7.1 Introduction

In the second scenario presented a site-specific noise optimization criterion is introduced, based on the population density surrounding the flight path. Consequently, a three-dimensional trajectory has to be optimized to also allow shaping the ground track to, for instance, avoid overflying noise sensitive areas with high population density. In addition, in this scenario the impact of atmospheric conditions on the helicopter flight mechanics, noise propagation and total noise impact in surrounding communities is assessed by simulating flights in different atmospheric conditions, looking mainly at different wind speeds.

The scenario relates to an Emergency Medical Services (EMS) flight to Rotterdam city center. Rotterdam is the second largest city in The Netherlands with a population of 1.2 million people in the metropolitan area. A map of the Rotterdam area and a plot of the corresponding population density can be found in Figs. 7.1 and 7.2, respectively. In EMS flights, obviously time is the most important factor to get a patient to a hospital as soon as possible; as a result, optimizing the total flight time appears to be most appropriate optimization criterion. However, especially at nighttime, noise nuisance might lead to strict regulations which can include limitations on the number of flights or even a ban on flights to city centers at night. The composite objective function used in *ECHO* is therefore selected to find a balanced trajectory for which the flight time is still sufficiently short, but the annoyance for the surrounding areas is reduced as well. It is noted here that the objective of this numerical case study is not to determine which is the best solution in terms of flight time and noise nuisance. Especially considering the fact that EMS operations can save human lives, flight time should in principle always be prioritized. The objective is rather to show the capabilities of the *ECHO* suite and perhaps to provide insight in the trade off between noise nuisance and flight time in an effort to improve social acceptance.

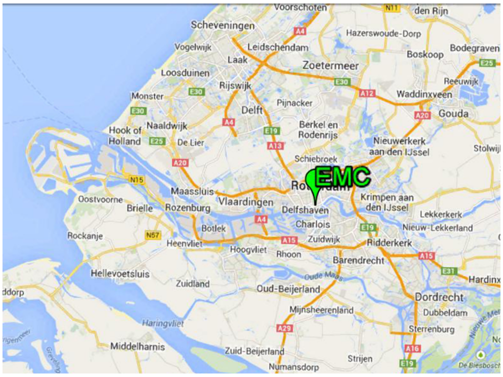

Figure 7.1: Rotterdam area (©Google)

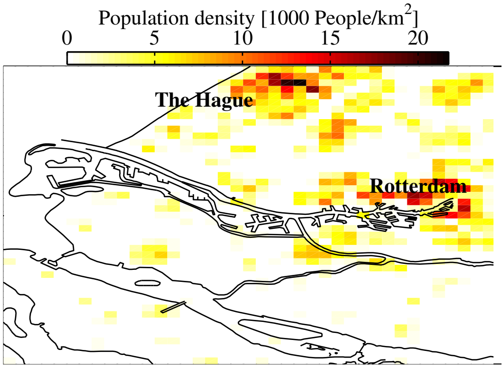

Figure 7.2: Population density (CBS)

7.2 Scenario Description

Scenario 2 starts in-flight over an unpopulated area to the west of Rotterdam and simulates a flight to the helipad of the Erasmus Medical Center (EMC) in Rotterdam city center (see Fig. 7.3). To distinguish between the *arrival* and *approach* segments of the flight, the scenario is divided into two phases, where each phase has an individual set of operational path and event constraints imposed. The general constraints to ensure operation within the flight envelope and to account for passenger comfort as discussed in Section 4.5 are imposed on the complete trajectory unless mentioned otherwise.

Apart from the set of constraints mentioned above, both phases have a specific set of event and path constraints imposed. Phase 1 is the arrival phase which essentially connects an en-route flight segment – not simulated in this scenario – to the start of the approach segment where the preparation for landing is initiated. Phase 1 starts in-flight over an unpopulated area over the Rotterdam harbor area at an altitude of 3,000 ft (914.4 m) AGL. The helicopter is in steady level flight at a true airspeed of 100 knots, and the initial heading χ_0 is free. The first phase ends at the start of the approach phase at an altitude of 1,000 ft (304.8 m) AGL. Due to the presence of the university building close to the helipad (see Fig. 7.4), the helipad can only be approached from either 66° or 246° [97]. At the end of phase 1, the objective is to be lined up for the approach phase, and hence, depending on the wind direction and magnitude, the final heading of phase 1, χ_f, is fixed at either direction.

The approach phase is intended to prepare the helicopter for landing on the helipad and starts when the helicopter is already alined with the inbound heading to the helipad. Although no flight along a glideslope is required, in phase 2 the heading angle should remain equal to the inbound heading χ_R along the complete phase. For this scenario, the

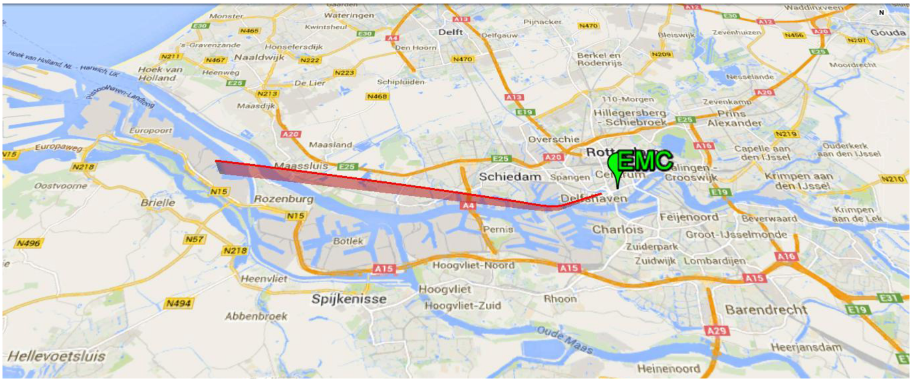

Figure 7.3: Scenario 2 overview (©Google)

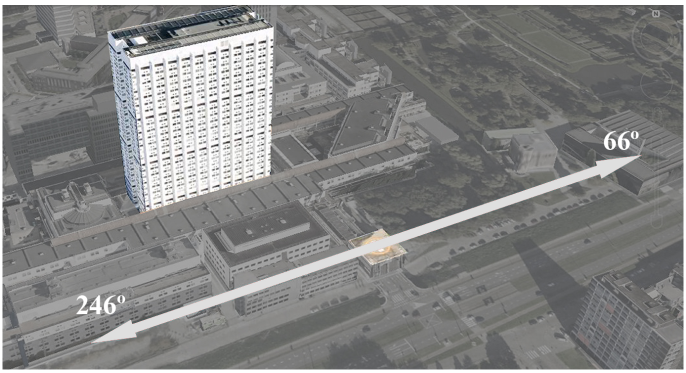

Figure 7.4: EMC Helipad (©Google)

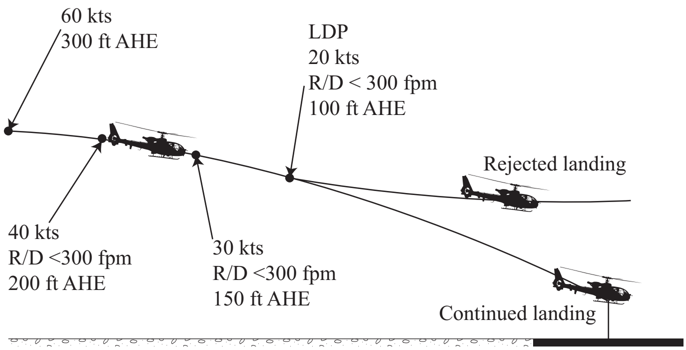

Figure 7.5: Vertical landing profile (adapted from [57])

landing is assumed to take place at the helipad, and hence a vertical landing is required. As a result, the pilot is advised to follow the landing profile defined in Fig. 7.5. As in Scenario 1, again all engines are assumed to be operating throughout the trajectory, and the trajectory ends at the point prior to the LDP. As a result, the final airspeed V_f is set to 30 knots, with a final altitude of 150 ft AHE. With an EMC helipad elevation of 120 ft (36.58 m) [97], the final altitude of phase 2 becomes 270 ft (82.30 m) AGL. During phase 2 the rate of descent is limited to 1,000 fpm, whereas the rate of descent should not exceed 300 fpm at the end of the trajectory [57]. In addition, to ensure that the helicopter descends throughout the final approach phase, the aerodynamic flight path angle is required to stay within the range of -10° to -3°. Finally, as the final phase of the approach and the landing itself are not modeled, the final position of the trajectory needs to be appropriately located as well. This position depends on the selected inbound heading, and on an assumed -3° flight path angle between the final point of the optimized trajectory and the helipad position (x_{HP}, y_{HP}). An overview of the constraints for phases 1 and 2 can be found in Table 7.1.

As mentioned in the introduction above, in EMS flights minimizing the flight time is the most important consideration. Therefore, the final time t_f of the trajectory is designated as the primary performance criterion in the problem formulation, and hence in all cases presented here the weighting factor $k_{time} = 1$. However, especially during nightly EMS flights noise nuisance in the area surrounding the helipad might still lead to significant resistance against the flight operations. Therefore, a balanced approach is used where – maintaining flight time as the primary criterion – the nightly noise nuisance is still considered in the performance index. In nighttime operations, resulting sleep disturbance is the main cause of resistance from the surrounding communities. As a result, the noise criterion selected for this scenario is the total number of expected awakenings due to a single nighttime operation (see Section 5.5). The number of awakenings N_A is then added to the performance index with a weighting factor k_{noise}. This weighting factor is parametrically varied to assess the effect of noise reduction on flight time, and hence to find an optimized solution that might provide an acceptable balance between

Table 7.1: Additional constrains for Case 2

Constraint	Phase no.	(In)equality
Initial speed	1	$V_0 = 100$ knots
Initial rate of descent	1	$v_{z,0} = 0$ fpm
Initial altitude	1	$z_0 = 3000$ ft
Initial position	1	$(x_0, y_0) = (x_s, x_s)$ m
Final altitude	1	$z_f = 1000$ ft
Linkage constraints	(1,2)	$\mathbf{x}_l = \mathbf{x}_r$
Flight path angle	2	$-10° \leq \gamma \leq -3°$
Maximum rate of descent	2	$-1000 \leq v_z \leq 0$ fpm
Maintain heading	2	$\chi = \chi_R$
Final speed	2	$V_f = 30$ knots
Final rate of descent	2	$v_{z,f} \leq -300$ fpm
Final altitude	2	$z_f = 270$ ft
Final x-position	2	$x_f = x_{HS} + \frac{z_f - z_{HS}}{\tan 3} \sin \chi_R$
Final y-position	2	$y_f = x_{HS} + \frac{z_f - z_{HS}}{\tan 3} \cos \chi_R$

both criteria. The objective of this scenario is then to minimize

$$J = t_f + k_{noise} N_A + \upsilon \int_{t_0}^{t_f} \sum_{i=1}^{4} u_i^2 \tag{7.1}$$

which again includes the control damping penalty discussed in Section 4.3.

All cases for Scenario 2 presented below have the same number of nodes (45 for phase 1, 15 for phase 2) and the same set of constraints. This results in a problem with 1,485 nonlinear variables and 1,630 nonlinear constraints. The noise exposure on the ground is determined on a 58x45 km grid with cells of 1x1 km. The 2,714 grid cells contain a total population of 2.9 million people. It is noted that during the optimization run the noise exposure is only calculated in *populated* cells within 12.5 km of the trajectory. This significantly reduces the runtime of the noise model and hence the complete optimization, whilst ensuring that all cells with a SEL value higher than the threshold value of 50.5 dBA for the awakenings criterion are inside the area in which the noise exposure is calculated. Only in post-processing is the entire grid analyzed.

7.3 Case 1: Headwind

In the first case of Scenario 2 presented here the main objective is to assess the influence of increased headwind on the flight mechanics and the noise optimization criterion. The simulated flights are performed in ISA conditions to which are added different wind speeds $V_w(z_w) = [0, 5, 10, 15]$ knots, from an eastern direction at 90°. Given the general

Table 7.2: Scenario 2, Case 1 results: no wind

Case	**Objective**	$\mathbf{t_f}$ **[s]**	$\mathbf{\Delta t_f}$ **[%]**	$\mathbf{N_A}$	$\mathbf{\Delta N_A}$ **[%]**
C01_01	t_f	**367.3**	n/a	3479	n/a
C01_02	$t_f + 0.02N_A$	**372.8**	+1.48	**2284**	-34.4
C01_03	$t_f + 0.04N_A$	**376.3**	+2.46	**2156**	-38.0
C01_04	$t_f + 0.1N_A$	**389.9**	+6.14	**1882**	-45.9
C01_05	$t_f + 0.2N_A$	**396.9**	+8.06	**1822**	-47.6

direction of the trajectory as presented in Fig. 7.3 this implies that the main wind component opposes the direction of flight. As the helicopter is not allowed to land in a strong tailwind, this also implies that the final approach heading shall be 66°.

The results without a wind vector present are available in Table 7.2. The corresponding ground tracks and altitude and airspeed profiles can be seen in Figs. 7.6 and 7.7, respectively. When first case C01_01 is considered, which is optimized to minimize the total flight time t_f, it can be seen that – as can be expected – the general behavior is very similar to that presented for Case 1 in Scenario 1. Again a continuous descent is used to reduce the total distance flown, and a high airspeed is maintained throughout phase 1. At the start of phase 2 (indicated with a dot in Fig. 7.7), the rate of descent is maximized to 1,000 fpm and the high airspeed is maintained for a few more seconds. Then the deceleration is initiated to meet the boundary conditions pertaining to the final rate of descent and final airspeed. Also from the ground track it can be seen that a direct path from the initial position to the intercept point of the final approach heading is followed. In this figure, colored and black dots indicate the problem discretization and phase link, respectively. The total flight time of this trajectory is 367.3 seconds with a total of 3,479 expected awakenings.

In the next step, the noise weighting factor k_{noise} is gradually increased, hence increasing the contribution of the number of expected awakenings to the total objective value. For this scenario, k_{noise} was varied from 0 to 0.20, where in the latter case noise constitutes almost 50% of the total objective value. As can be seen from Table 7.2, significant improvements in the noise nuisance can already be achieved at the cost of a small increase in total flight time.

In contrast to the solutions presented in Scenario 1, however, the use of a site-specific noise criterion and the three-dimensional problem setup allow for additional means to reduce the noise impact. Firstly, using a site-specific criterion based on population density allows to overfly only less noise-sensitive areas. This can be clearly seen from the ground tracks in Fig. 7.6. The solutions where $k_{noise} \neq 0$ fly over the Meuse river and the harbor area to its south, avoiding the communities of Maassluis, Rozenburg and Vlaardingen on the river bank. Only the densely populated areas near Rotterdam city center cannot be avoided due to the prescribed inbound heading of 66°.

When the vertical profile is considered, it could be expected that, as in the previous scenario, flying low would result in high noise exposure levels directly below the flight

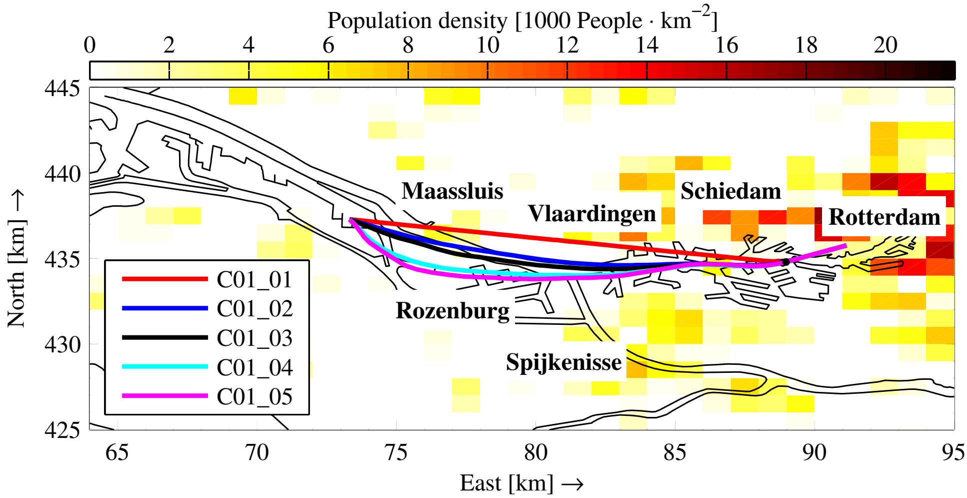

Figure 7.6: Ground tracks, no wind

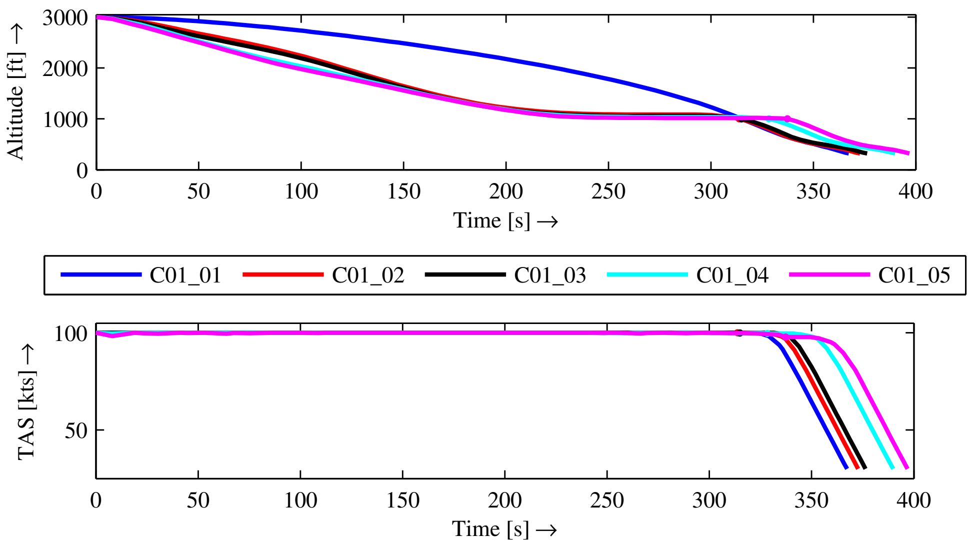

Figure 7.7: Altitude and airspeed profiles, no wind

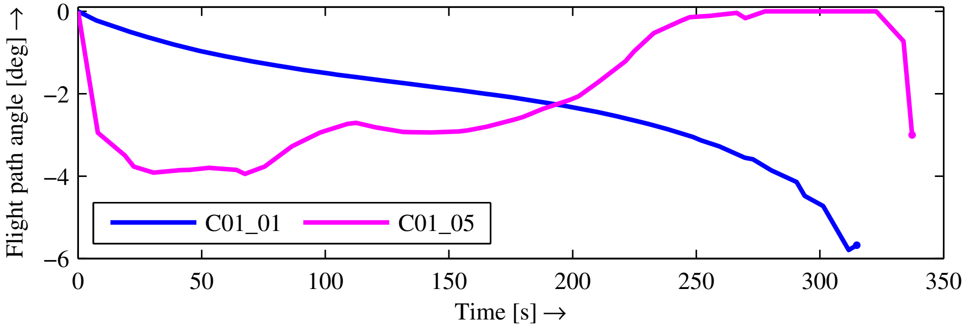

Figure 7.8: Flight path angle in phase 1, no wind

path, whereas at higher elevation angles to the side of the helicopter path the noise levels would be significantly reduced due to the dissipating ground effect and the lower source noise levels. However, in Scenario 1 only the total contour area was used as the noise performance criterion, and as a result the peak levels directly below the helicopter were not relevant in the optimization. In contrast, in Scenario 2 high noise levels below the flight path could expose communities to excessively high noise levels, and hence result in a very high number of awakenings. Still, as can be seen from Fig. 7.7, in all noise optimized trajectories the helicopter descends to almost the minimum allowed altitude of 1,000 ft in phase 1 and maintains this altitude for a large part of the trajectory. This can readily be explained by considering that in this scenario the peak levels directly below the flight path are found over less noise-sensitive areas – such as the Meuse river and harbor areas – as the ground track is shifted away from the populated areas. Although this may seem a trivial observation, it is the *combination* of low altitude and a change in the ground track that accounts for the larger part of the reduction in the number of awakenings.

Finally, also the flight conditions again play an important role in the mitigation of the noise impact. The continuously high airspeed that can be observed in Fig. 7.7 reduces the exposure time and also leads to significantly lower source noise levels. However, as opposed to Case 1 of Scenario 1, where the descent was executed at very high flight path angles, in this scenario a more gradual descent is used as can be seen in Fig. 7.8. The minimum flight path angle is almost -4° which corresponds to a rate of descent of about 700 fpm. Due to the communities of Maassluis and Rozenburg located astride of the trajectory and close to the initial position, a steep descent as in Scenario 1 would lead to very high noise levels in both communities due to the high source noise levels as can be seen in Appendix A, Fig. A.2. The selection of a shallow descent gradient reduces the noise levels at the source and hence the exposure in Maassluis and Rozenburg, but still leads to the low altitude beneficial for the communities located further ahead, most notably Vlaardingen and Schiedam.

The preferential flight conditions, avoidance of densely populated areas and the relatively low flight profile all contribute to a significant reduction in the total number of

Table 7.3: Scenario 2, Case 1 results: increasing headwind

Case	$\mathbf{V_w(z_w)}$ **[kts]**	$\mathbf{k_{noise}}$	$\mathbf{t_f}$ **[s]**	$\mathbf{\Delta t_f}$ **[%]**	$\mathbf{N_A}$	$\mathbf{\Delta N_A}$ **[%]**
C01_01	0	0.00	367.3	n/a	3479	n/a
C01_05	0	0.20	396.9	+8.06	1822	−47.6
C01_06	5	0.00	398.5	n/a	3460	n/a
C01_10	5	0.20	428.3	+7.46	1799	−48.0
C01_11	10	0.00	434.8	n/a	3570	n/a
C01_15	10	0.20	449.0	+3.27	2095	−41.3
C01_16	15	0.00	478.2	n/a	3685	n/a
C01_20	15	0.20	510.0	+6.65	1948	−47.1

awakenings of up to 47.6% in solution C01_05. This does, however, result in an almost 30 seconds or 8.1% increase in the total flight time. Still, even at the cost of increasing the flight time by just over 5 seconds, already a 34.4% reduction in the number of awakenings is achieved by a combination of the aforementioned factors.

From the results presented above a number of operational procedures were distinguished that all contribute to the reduction of the noise exposure in nearby communities. In the next set of results a wind vector is added to the atmospheric conditions, blowing from the east against the general direction of the trajectory. In Table 7.3 results for the reference cases ($k_{noise} = 0.00$) and the highest noise weighting factor ($k_{noise} = 0.20$) are presented for increasing wind speeds.

With regards to the flight dynamics, the headwind results in a lower ground speed, and hence a longer flight time as can clearly be recognized from the increase in total flight time with increasing wind speed in the table of results. When the number of awakenings is considered, however, it can be seen that for all four wind conditions both the absolute number of awakenings and the relative reduction achieved after optimization are very similar. This can be attributed to three – sometimes contradictory - effects. Firstly, it should be noted that the effect of a headwind component on the ground speed adversely affects the noise exposure. With equal airspeed, the ground speed will decrease resulting in a longer exposure time, and thus higher SELs on the ground.

To counter the effect of the increased ground speed – which also leads to a longer total flight time – the helicopter descends early, especially in the cases where only the total flight time is optimized for. Consider that the wind speed increases with altitude. As such, flying at low altitude results in a lower headwind component, and consequently a shorter total flight time. When the flight conditions that are beneficial to reduce the noise exposure are recalled, it immediately becomes clear that the low altitude flight in case of headwind also reduces the number of expected awakenings, and counters the effect mentioned above.

It should be noted, though, that this can only explain the similar numbers of awakenings in the time optimized cases; in cases including noise the early descent will be executed for all wind conditions. As such, to explain the very similar relative improvements observed in 7.3 when optimizing with $k_{noise} = 0.20$, a third effect of the headwind component needs to be discussed. Wind has a significant impact on the gradient of the speed of sound profile. Consider for instance Fig. B.1 in Appendix B. Cases 2 and 3 are the speed of sound profiles for a 15 knots tail- and headwind, respectively. In case of a headwind – i.e. sound traveling in an upwind direction – the gradient of the speed of sound profile becomes more negative than in ISA conditions. Consequently, as can be recalled from Chapter 5, the upward refraction of the sound is increased and hence the shadow zone lies closer to the source. On the other hand, on the downwind side the gradient of the speed of sound profile becomes less negative or even positive, possibly resulting in the absence of a shadow zone behind the helicopter. Then consider Fig. 7.9 where the 50.5 dBA SEL contours – the threshold noise levels for awakenings – are plotted for the time optimized cases in ISA conditions and a 15 knots headwind. As can be seen the shadow zone ahead of the helicopter results in a significant part of the densely populated area of Rotterdam city center being exposed to noise levels below 50.5 dBA. Although to the west – behind the helicopter – the contour envelopes population that was previously exposed to noise levels below the threshold level, it can clearly be seen that the reduction in Rotterdam outweighs the additional exposure to the west. The westward shift of the noise exposure counters the effect of the reduced ground speed in terms of the total number of awakenings, and can explain the similar relative improvements obtained when including noise in the objective function.

The overall effect of the eastern wind on the noise nuisance can be seen in Fig. 7.10, where the percentage of expected awakenings between both solutions C01_01 and C01_16 are compared. In the green area, the percentage of expected awakenings as a result of the noise exposure caused by case C01_16 exceeds that of solution C01_01, whereas in the blue area the case with no winds results in a higher percentage of awakenings. Due to the lower flight altitude in solution C01_16, the noise levels astride the trajectory are reduced at the cost of higher noise levels directly below the trajectory. The figure also clearly shows that as a consequence of the changed location of the shadow zone, solution C01_16 results in a higher percentage of awakenings west of the trajectories, but reduced levels in the densely populated city center of Rotterdam.

In the discussion of solutions C01_01 to C01_05, flown under ISA conditions with no wind present, four aspects that reduce the community noise impact were identified, *viz.* avoidance of high source noise levels, low flight to increase ground attenuation, high airspeeds and a ground track that avoids overflying densely populated areas. Although the presence of a headwind significantly affects the propagation of sound and the flight mechanics of the helicopter, these aspects are beneficial for both the reduction of flight time and the number of awakenings under all wind conditions considered here. As a result, both the airspeed and altitude profiles as well as the ground tracks for all solutions involving noise closely resemble the results presented in the previous section, and are therefore not visualized here.

A final overview of the complete set of results for both increasing noise weighting factors ($k_{noise} = [0.00, 0.02, 0.04, 0.10, 0.20]$) and increasing wind speeds ($V_w(z_w) = [0, 5, 10, 15]$ knots) can be seen in Fig. 7.11 where for all solutions the total flight time is plotted against the number of awakenings. This figure indeed shows that although the increasing

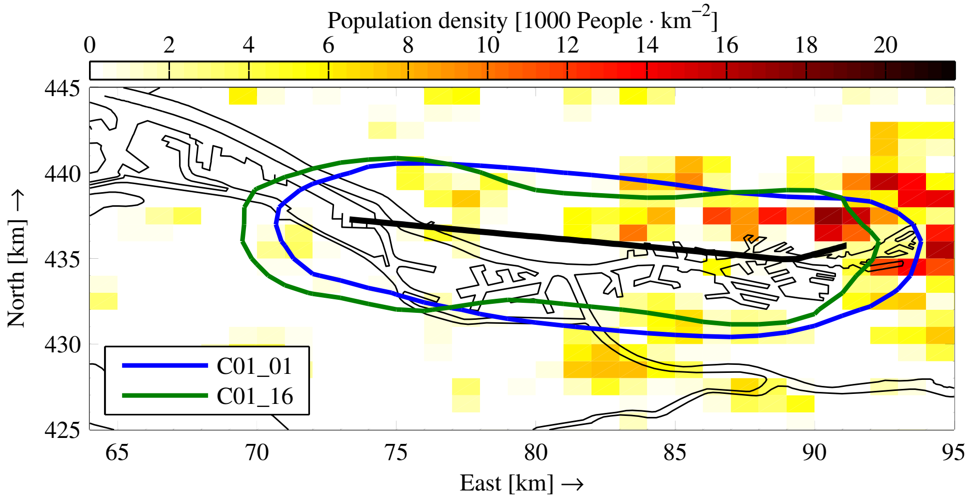

Figure 7.9: 50.5 dBA SEL Contours, case C01_01 and C01_16

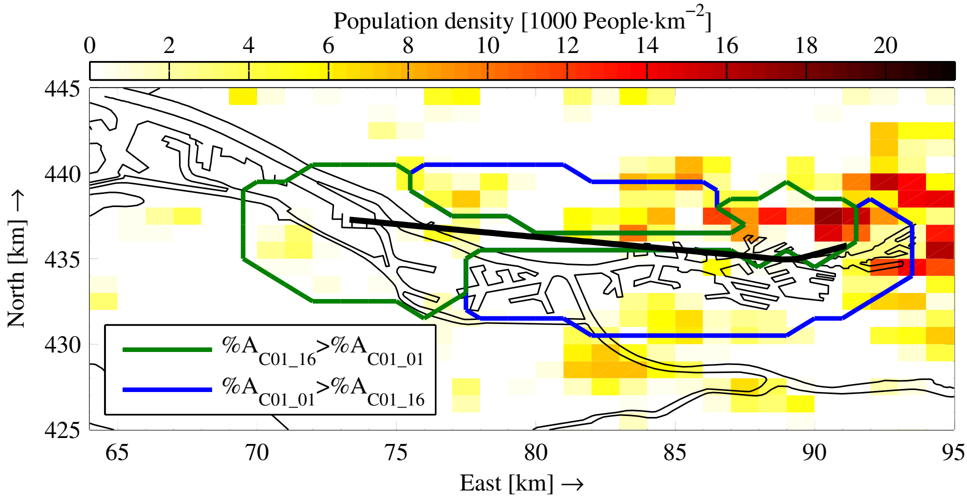

Figure 7.10: Δ% Awakenings, C01_16 - C01_01

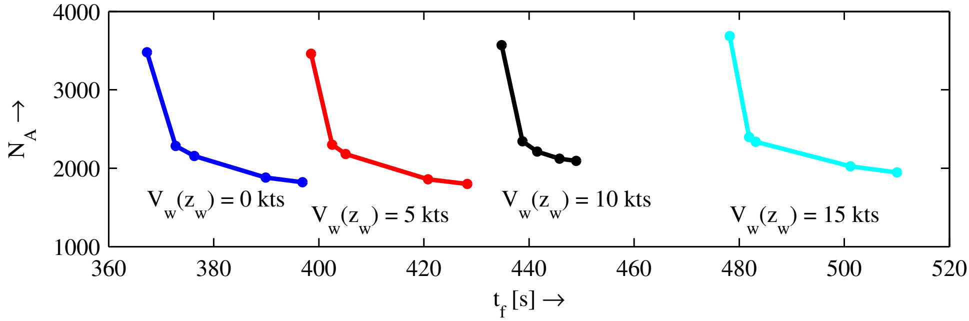

Figure 7.11: Flight time vs. awakenings, increasing headwind

wind speeds result in a significant increase in flight time, both the absolute values of the number of awakenings and the relative gains achieved with increasing noise weighting factors are very similar for all wind conditions considered here.

7.4 Case 2: Tailwind

In the second case of Scenario 2 the effect of a tailwind is assessed. With regards to the flight mechanics, in this case to reduce the flight time the helicopter should fly high to increase the tailwind velocity component and thus to maximize the ground speed. However, this opposes the effect of high elevation angles leading to relatively low source noise levels and increased lateral attenuation of the noise. In addition, as the helicopter is not allowed to land with a strong tailwind component [57] it needs to make a turn exceeding 180° to line up with the inbound heading of 246°. As with the previous case, the trajectory is flown in ISA conditions with four different wind speeds added, $V_w(z_w) = [0, 5, 10, 15]$ knots, this time from a western direction at 270°. It is noted that the solution without wind present is still approaching the helipad on the 246° inbound heading to serve as a reference case. Again, first the major results are presented in Table 7.4 for all four wind speeds, and optimized either for $k_{noise} = 0.00$ or $k_{noise} = 0.20$.

From these results a dramatic increase follows for both the total flight time and the expected number of awakenings as compared to the headwind cases. This can be almost completely attributed to the turn to the final approach heading over the densely population city center of Rotterdam at a relatively low speed. The extreme solutions for no wind and $V_w(z_w) = 15$ knots and for $k_{noise} = 0$ and $k_{noise} = 0.20$ are presented in Figs. 7.12 and 7.13.

When first both minimum time solutions C02_01 and C02_16 are considered, the significant differences in both total flight time and the number of awakenings can be explained by closer inspection of the flight mechanics. Firstly, the tailwind significantly increases the ground speed, which is more than 25 knots higher in solution C02_16. As a result, both the total flight time and the noise exposure time are reduced. Secondly, the turn onto the final heading and the final approach itself are also significantly affected

Table 7.4: Scenario 2, Case 2 results: increasing tailwind

Case	$\mathbf{V_w(z_w)}$ **[kts]**	$\mathbf{k_{noise}}$	$\mathbf{t_f}$ **[s]**	$\mathbf{\Delta t_f}$ **[%]**	$\mathbf{N_A}$	$\mathbf{\Delta N_A}$ **[%]**
C02_01	0	0.00	509.7	n/a	8074	n/a
C02_05	0	0.20	547.1	+7.34	4146	−48.7
C02_06	5	0.00	469.7	n/a	8063	n/a
C02_10	5	0.20	520.3	+10.8	3405	−57.8
C02_11	10	0.00	435.2	n/a	7634	n/a
C02_15	10	0.20	478.3	+9.90	3287	−56.9
C02_16	15	0.00	405.4	n/a	7138	n/a
C02_20	15	0.20	443.0	+9.27	3264	−54.3

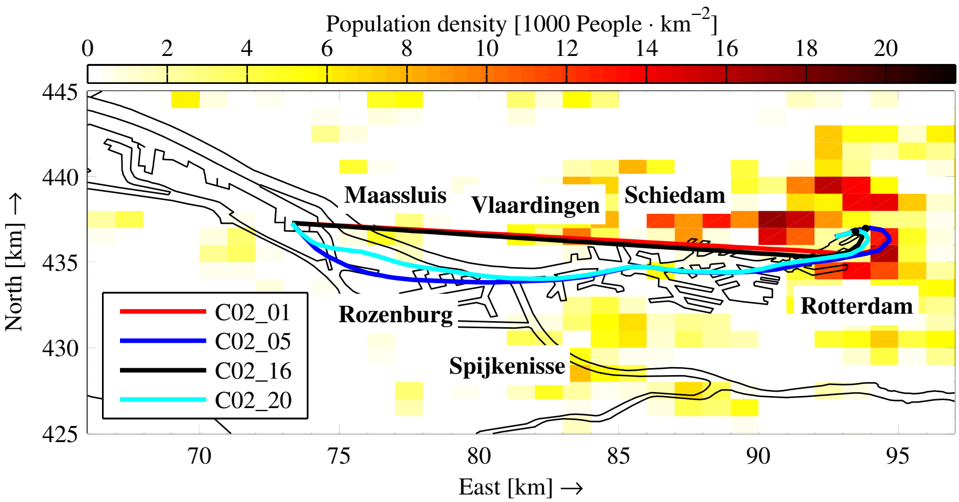

Figure 7.12: Ground tracks, increasing tailwind

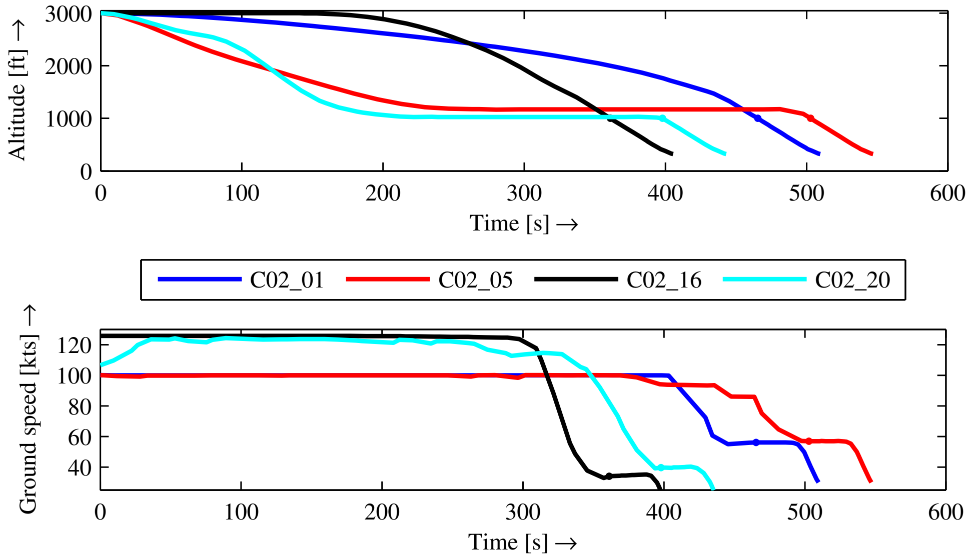

Figure 7.13: Altitude and ground speed profiles, increasing tailwind

by the wind speed. To explain the effect of wind in the final phase of the flight, first consider the expressions for the geometric and aerodynamic turn rates below

$$\dot{\chi}_a = \frac{(\dot{v}_x v_y - v_x \dot{v}_y)}{V^2} \tag{7.2}$$

$$\dot{\chi}_g = \frac{\left(\dot{GS}_x GS_y - GS_x \dot{GS}_y\right)}{GS_x^2 + GS_y^2} \tag{7.3}$$

where GS_x and GS_y are the ground speed components, which are defined as $GS_x = v_x - V_{w_x}$ and $GS_y = v_y - V_{w_y}$. Equations (7.2) en (7.3) denote the *aerodynamic* and *geometric* turn rate, respectively. The aerodynamic turn rate is limited to $\pm\, 3°{\cdot}\mathrm{s}^{-1}$ for both cases, as was defined in Section 4.5. For case C02_01, with no wind present, $\dot{\chi}_a = \dot{\chi}_g$. For solution C02_16, however, at the initial point of the turn to the final heading the tailwind results in a lower value for $\dot{\chi}_g$, so $\dot{\chi}_g < \dot{\chi}_a$. This effect is reduced and eventually reversed when turning into the wind, resulting in an elliptically shaped turn. This can clearly be seen from Fig. 7.14.

A more important effect of the wind speed can also explain part of the difference in awakenings between both optimized trajectories. Therefore first the expressions for the aerodynamic and geometric flight path angle are considered, similar to the turn rates

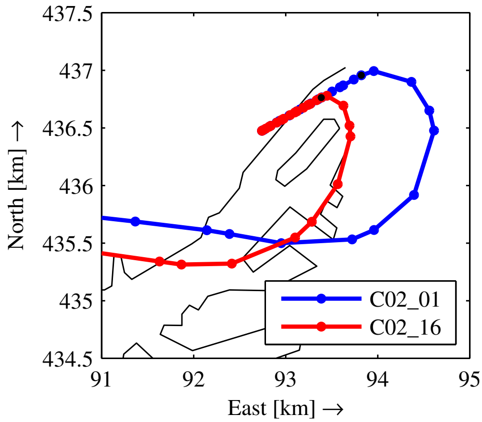

Figure 7.14: Turn to final approach heading, case C02_01 and C02_16

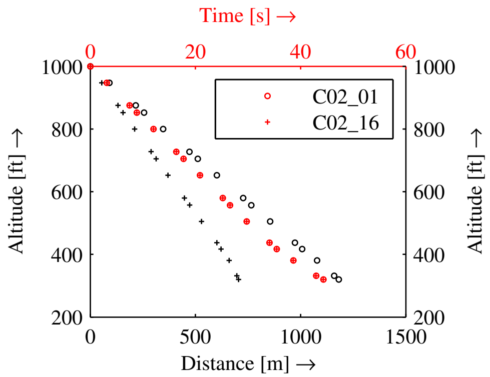

Figure 7.15: Descent phase, case C02_01 and C02_16

discussed above. The flight path angles can be defined as follows

$$\gamma_a = \tan^{-1}\left(\frac{v_z}{\sqrt{v_x^2 + v_y^2}}\right) \tag{7.4}$$

$$\gamma_g = \tan^{-1}\left(\frac{v_z}{\sqrt{GS_x^2 + GS_y^2}}\right) \tag{7.5}$$

As for the constraints imposed on the turn rate, only the *aerodynamic* flight path angle is limited, between 0° and -10°, within the bounds of the source noise model. As the helicopter lines up for final approach and turns into the wind, the ground speed is lower than the airspeed, and as a result the geometric flight path angle is greater than the aerodynamic flight path angle. This can be seen in Fig. 7.15. Here, the altitude in the final approach phase of the flight is plotted against the distance on the lower x-axis and the time on the upper x-axis. As can be seen, the descent rate in both cases is the same, indicating the aerodynamic flight path angles are indeed equal. This also leads to the same time to descend from 1,000 ft AGL to 150 ft AHE for both cases. However, when considering the distance, it can be seen that the descent in solution C02_16 is significantly shorter, indicating a higher geometric flight path angle. When the population density in e.g. Fig. 7.12 is considered, it can be seen that the relatively short descent path results in a trajectory that at least avoids directly overflying some of the most densely populated areas in Rotterdam city center, contributing partly to the reduced number of awakenings in the time optimized case when tailwind is considered.

Table 7.5: Scenario 2, Case 2 results: $k_{noise} = 0.02$

Case	$\mathbf{V_w(z_w)}$ **[kts]**	$\mathbf{k_{noise}}$	$\mathbf{t_f}$ **[s]**	$\mathbf{\Delta t_f}$ **[%]**	$\mathbf{N_A}$	$\mathbf{\Delta N_A}$ **[%]**
C02_02	0	0.02	521.1	+2.23	4597	−43.1
C02_07	5	0.02	483.0	+2.83	4170	−48.3
C02_12	10	0.02	447.6	+2.86	3994	−47.7
C02_17	15	0.02	418.1	+3.12	3826	−46.4

The tailwind component clearly has a significant impact on the vertical profile of the trajectory and its ground track, affecting both the total flight time and the total number of awakenings. However, as in the cases considering a headwind, also the propagation of sound significantly contributes to the differences in noise impact seen in Table 7.4. When the discussion on the location of the shadow zone in the previous section is recalled, it is clear that in case of a western wind the city center of Rotterdam will be exposed to higher noise levels, which, in combination with the turn to the final heading results in a significantly higher total number of awakenings. However, the relative reduction of the number of awakenings in Case 2 varies from 49% for $V_w(z_w) = 0$ to 58% for $V_w(z_w) = 5$ knots, even more than was observed in Case 1. This does result in an extended total flight time of up to 51 seconds or 11%. Still, in Table 7.4 only the results for the highest noise weighting factor $k_{noise} = 0.20$ were presented. Solutions also exist for all three wind velocities where a reduction in the number of awakenings is observed of more than 40% at the cost of only about 3% additional flight time – on average about 12 seconds. As an example, the solutions with the lowest contribution of noise to the objective value, with $k_{noise} = 0.02$, are presented for all wind conditions in Table 7.5 and Fig. 7.16. It is noted that the percentages for Δt_f and ΔN_A are expressed with respect to the corresponding minimum time solutions.

Although not presented here for the sake of brevity, it can already be seen from Fig. 7.12 that all noise optimized trajectories again overfly the unpopulated areas near the Meuse river, as was observed in Case 1. The same holds for all other solutions involving tailwind. The solutions for $k_{noise} = 0.02$ all show the same behavior both in the airspeed and in the altitude profile. The differences in the number of awakenings are mainly caused by the increased ground speed and the resulting reduced noise exposure time, and the effects of an eastward shift of the noise exposure due to the tailwind, the reverse effects of those discussed for Case 1. In addition, the wind component also has a significant effect on the final turn and the final approach phase, which is also expected to have a mitigating effect on the noise exposure.

Finally, the same overview of the results for increasing noise weighting factors ($k_{noise} = [0.00, 0.02, 0.04, 0.10, 0.20]$) and increasing wind speeds ($V_w(z_w) = [0, 5, 10, 15]$ knots) as presented for Case 1 can be seen in Fig. 7.17. Although the tailwind has a significant impact on the total flight time and number of awakenings, the relative gains that can be achieved by reducing the altitude, maintaining a high airspeed and avoiding noise sensitive areas and high source noise levels are very similar to those found for Case 1.

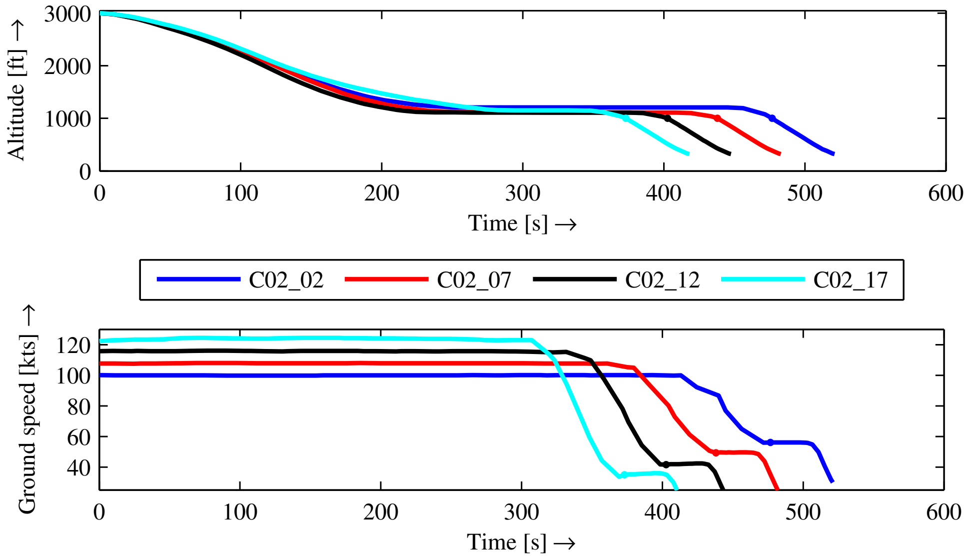

Figure 7.16: Altitude and ground speed profiles, solutions C02_02, C02_07, C02_12 and C02_17

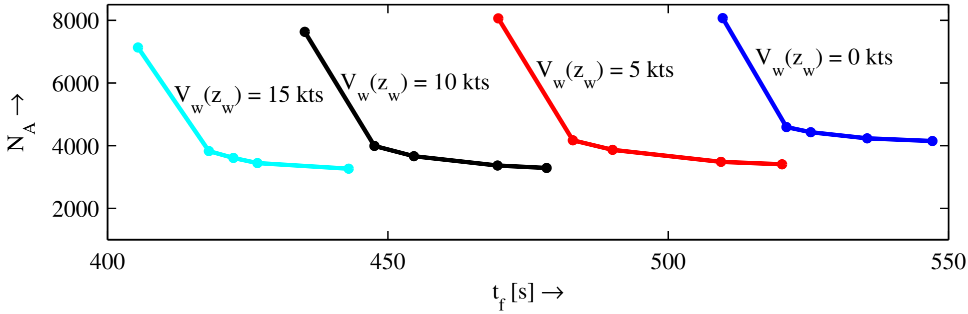

Figure 7.17: Flight time vs. awakenings, increasing tailwind

Table 7.6: Scenario 2, Case 3 results: increasing crosswind

Case	$\mathbf{V_w(z_w)}$ **[kts]**	$\mathbf{k_{noise}}$	$\mathbf{t_f}$ **[s]**	$\mathbf{\Delta t_f}$ **[%]**	$\mathbf{N_A}$	$\mathbf{\Delta N_A}$ **[%]**
C01_01	0	0.00	367.3	n/a	3479	n/a
C01_04	0	0.10	389.9	+6.14	1882	−45.9
C03_01	5	0.00	366.1	n/a	3214	n/a
C03_02	5	0.10	389.0	+6.26	1569	−51.2
C03_03	10	0.00	367.6	n/a	3204	n/a
C03_04	10	0.10	389.9	+6.07	1322	−58.7
C03_05	15	0.00	371.9	n/a	3235	n/a
C03_06	15	0.10	393.1	+5.71	1333	−58.8

7.5 Case 3: Crosswind

To also assess the impact of a crosswind on the trajectory, Case 3 is presented. The wind is blowing from a northern direction of 360°, and again the speeds are varied from 0 to 15 knots. It is noted that the maximum allowed crosswind component for a Bo-150 helicopter in landing is 17 knots [57], which is complied with when approaching the helipad from an inbound heading of 66°. In the case of crosswind, it can be expected that the total flight time is not significantly affected due to increasing wind speeds. The northern wind, however, does lead to a shadow zone north of the trajectory, which should lead to a significant reduction in the noise exposure in the populated areas on the northern banks of the Meuse river. In Case 3, solutions have only been generated for $k_{noise} = 0$ and $k_{noise} = 0.1$, and the results for $V_w(z_w) = 0$ are already available from Case 1. The complete set of results can be found in Table 7.6.

The ground tracks for the noise optimized solutions can be found in Fig. 7.18. As can be observed, the effects of crosswind on the routing are hardly discernible, and in fact all trajectories follow nearly the same ground track. Although not depicted here, also the airspeed and altitude profiles are very similar, and only minor head- or tailwind components in different sections of the trajectories influence the total flight time. The altitude and airspeed profiles again follow the same general trends already observed in Case 1; again low altitude, high speed flight and avoidance of populated areas and high source noise levels cause the reduction in the number of awakenings.

Although the results of Case 3 are very similar to those of Case 1, a clear difference can be seen when comparing the relative changes of both optimization parameters contributing to the objective function. For a typical 6% increase in flight time, the reduction in awakenings in Case 3 can be as high as 59%, more than 10% higher than the results seen in Table 7.3 which were optimized with a higher value for k_{noise}. As mentioned above, this can be explained by considering that the northern wind results in a shadow zone to the north of the trajectory, which is especially beneficial in the final approach phase where the helicopter flies low but close to densely populated areas. To exemplify this, consider the 50.5 dBA SEL contours for solutions C01_04 and C03_06 in Fig. 7.19. Both are optimized using $k_{noise} = 0.1$, and both have nearly the same ground

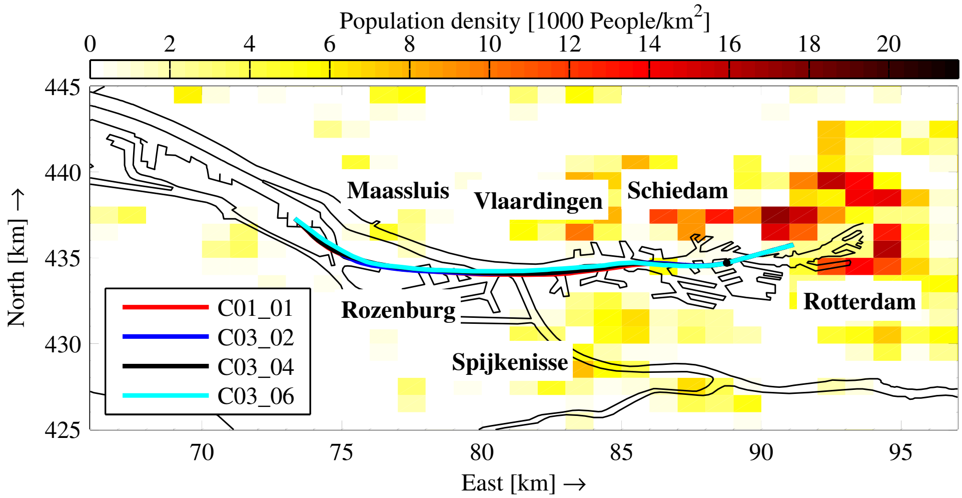

Figure 7.18: Ground tracks, increasing crosswind

track. It clearly follows from this figure that the northern wind shifts the threshold contour up to more than 1 km southward, especially in the eastern part of the trajectory where the helicopter flies low. This results in some densely populated areas to be exposed to significantly lower SEL values. To the south of the trajectory some communities are then being exposed to higher SEL values in solution C03_06, but given the relatively low population density in those areas the total number of awakenings is 29% lower than in solution C01_04, without significant changes to the ground track or the total flight time. Consequently, the reduction in the noise exposure can almost fully be attributed to the propagation of sound rather than the difference in the flight mechanics as was observed in the head- and tailwind cases presented above.

7.6 Case 4: Ground Surface

In the final case presented for Scenario 2 the effect of temperature and, more importantly, ground surface is assessed. In this case, no wind is present, but the atmospheric conditions have been changed to simulate a flight in a winter night. Firstly, the temperature at 0 m AGL is set to T_0 = - 10° centigrade, with a relative air humidity of H = 70% and a temperature lapse rate of $\lambda = +\ 0.001\ \mathrm{K} \cdot \mathrm{m}^{-1}$. Under these conditions, the atmospheric attenuation coefficient α can be significantly higher than under ISA conditions, and no shadow zones exist due to the positive gradient of the speed of sound profile. In addition, different ground surfaces are modeled. It is recalled from Section 5.3.5 that generally a hard ground surface with a high value for the effective flow resistivity σ results in a high value of the reflection factor $Q \approx 1$ and hence a relatively large contribution of the secondary ray. This can theoretically lead to a ground effect of $\Delta SPL_G \approx$ - 6 dB for

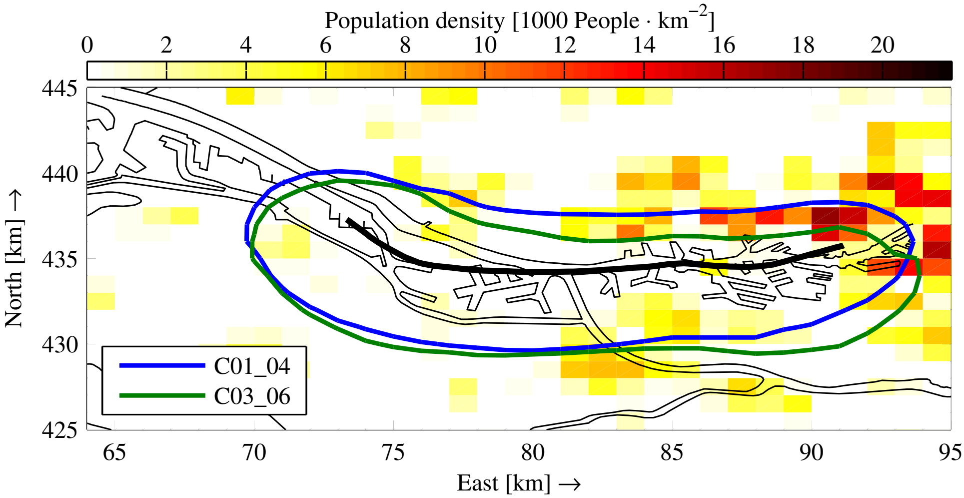

Figure 7.19: 50.5 dBA SEL Contours

a specific frequency, hence increasing the noise levels observed on the ground. In case of a soft ground surface, however, a significant part of the reflected ray's energy can be absorbed resulting in relatively low noise levels at larger distances from the source. As it was found in previous results that the contribution of ground effect in the reduction of the noise impact was significant, for Case 4 three surface types have been assessed, *viz.* snow ($\sigma = 2.5 \cdot 10^4$), grass ($\sigma = 2.5 \cdot 10^5$), and a hard reflecting surface ($\sigma = 2.5 \cdot 10^{32}$). An example of the effect of the ground conditions on the noise levels on the ground can be seen in Fig. 7.20. The figure shows the A-weighted sound level L_A to the right side of a helicopter flying at 1,000 ft at an airspeed of 100 knots. As can be seen, in general the noise levels determined using a snow ground surface are lower, up to 9 dBA as compared to a grass ground surface at distances close to 10 km from the source. When modeling a hard ground surface the noise levels at this distance are again around 4 dBA higher. Also closer to the source noise levels are lower in case of a soft ground surface, albeit that the differences are smaller.

As for Case 3, only time optimal solutions and solutions with $k_{noise} = 0.1$ have been generated, and again solutions C01_01 and C01_04 of Case 1 represent the trajectories optimized under ISA conditions. The complete set of results for Case 4 can be found in Table 7.7.

Although the general trends of the results presented in the table are similar to the trends observed in Cases 1 to 3, one number that particularly stands out is the result pertaining to the number of awakenings – both total and relative – for solutions C04_05 and C04_06, where a hard ground surface is assumed. Compared to the same atmospheric conditions, the minimum time solution C04_05 results in 54% more awakenings than solution C04_03, the same trajectory but now over a grass surface. Also compared to the result in ISA conditions with a grass ground surface solution C04_05 results in 46% more

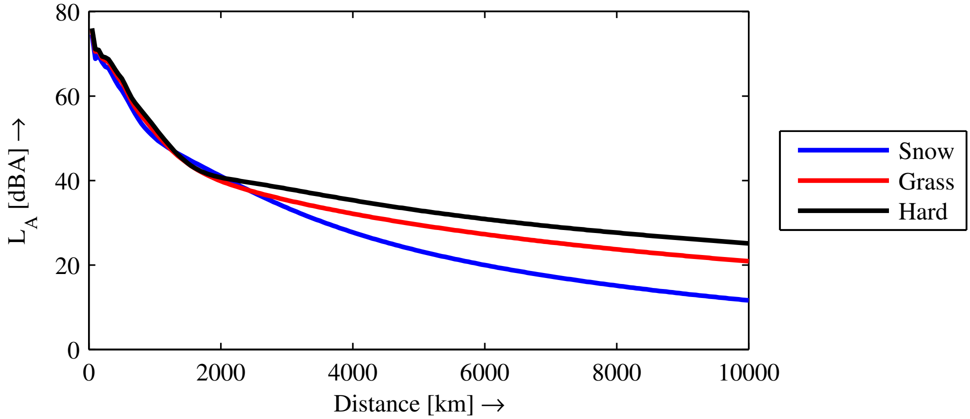

Figure 7.20: Absorption and ground effect, 282.67 Hz, z_s = 500 m

Table 7.7: Scenario 2, Case 4 results: varying ground surface and atmospheric conditions

Case	$\mathbf{V_w(z_w)}$ **[kts]**	$\mathbf{k_{noise}}$	$\mathbf{t_f}$ **[s]**	$\mathbf{\Delta t_f}$ **[%]**	$\mathbf{N_A}$	$\mathbf{\Delta N_A}$ **[%]**
C01_01	ISA, grass	0.00	367.3	n/a	3479	n/a
C01_04	ISA, grass	0.10	389.9	+6.14	1882	−45.9
C04_01	Winter, snow	0.00	367.2	n/a	3148	n/a
C04_02	Winter, snow	0.10	383.0	+4.30	1922	−45.0
C04_03	Winter, grass	0.00	367.3	n/a	3305	n/a
C04_04	Winter, grass	0.10	394.6	+7.44	1851	−44.0
C04_05	Winter, hard	0.00	367.3	n/a	5080	n/a
C04_06	Winter, hard	0.10	393.3	+7.07	3626	−28.6

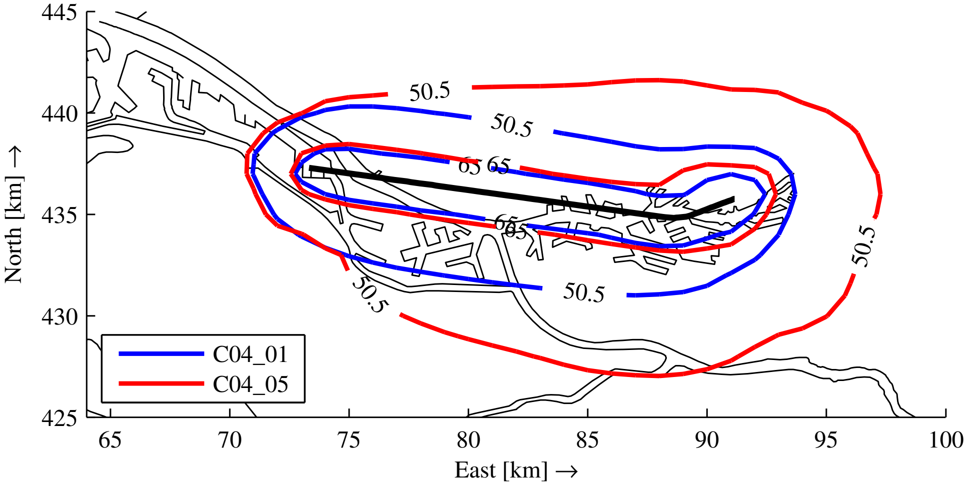

Figure 7.21: 50.5 and 65 dBA SEL Contours, solutions C04_05 and C04_06

awakenings.

When Fig. 7.20 is considered again the contribution of the differences in the number of awakenings can at least party be explained. At high incidence angles – when the helicopter is flying low or at observer locations at large distances – the absorption of the ground is significantly higher in the case of a soft ground surface as compared to the hard surface modeled in solutions C04_05 and C04_06. As a result, at large distances from the helicopter path noise levels can be significantly higher in these cases, which can clearly be seen from the contour plots in Fig. 7.21. To ensure that the trajectories under comparison in this figure are the same, the results of the minimum time solutions C04_01 and C04_05 are plotted here. It can be observed that the 50.5 dBA SEL contour – the threshold value for awakenings – is significantly larger when a hard ground surface is modeled. At larger distances the difference in ground effect results in an extended region of relatively low but still significant noise levels in case of a hard ground surface. However, when the 65 dBA contour (where just over 1% of the population is awoken) is considered, the effect is much less pronounced and in fact only significant during the final phases of the trajectory where again the incidence angles are high.

When the number of awakenings is accounted for in the objective function, it can only be expected that changing the ground surface also affects the optimized routing. However, although not plotted here, the ground tracks of all cases are in fact very similar for all four cases where $k_{noise} = 0.1$, so for all three ground surface types and both atmospheric conditions. The same holds for the airspeed profiles where a high airspeed remains preferential. When the altitude profiles in Fig. 7.22 are considered though, some significant differences can be observed though. Only solution C04_02, corresponding to a cold atmosphere and a snow ground surface, shows the typical profile seen in previous

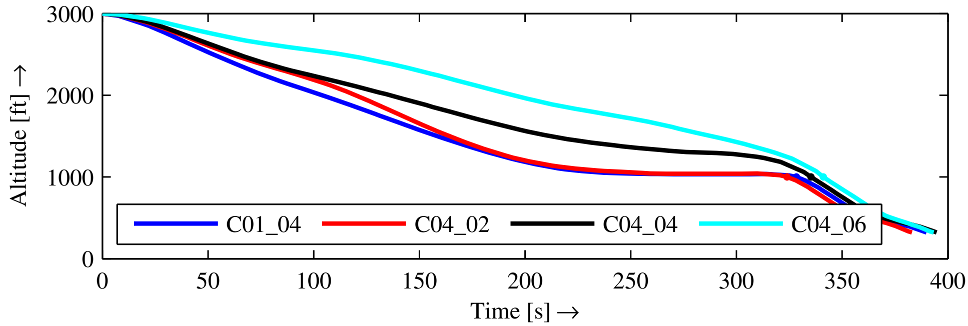

Figure 7.22: Altitude profiles, varying ground surface and atmospheric conditions

Table 7.8: Scenario 2, Case 4 results: ISA with hard ground surface

Case	$V_w(z_w)$ [kts]	k_{noise}	t_f [s]	Δt_f [%]	N_A	ΔN_A [%]
C04_07	ISA, hard	0.00	367.3	n/a	5806	n/a
C04_08	ISA, hard	0.10	393.1	+7.02	4254	−26.7

cases descending to the minimum allowed altitude in phase 1. In cases C01_04 and C04_04, flying over a grass ground surface in ISA and cold conditions, respectively, a higher altitude is maintained. This effect indicates that the effect of temperature has no significant impact on either the total flight time or the total number of awakenings, which is also reflected by the results in Table 7.7.

In solution C01_04 a low altitude was preferred to ensure lower source noise levels and high lateral attenuation. In case C04_06, with a hard ground surface, the effect of lateral attenuation is reduced significantly, and although the lower source noise levels due to high incidence angles would still be beneficial, in this case a higher altitude profile is selected indicating a more dominant contribution of absorption and spreading losses.

Although it is readily clear that the changes in the atmospheric conditions and the ground surface have a significant impact on the noise impact, both in terms of absolute numbers and relative improvements when optimizing for noise as well, lateral attenuation can only partly explain the differences in the altitude profiles. It is therefore noted that solutions C01_04 and C04_06 not only differ in terms of ground surface, but also in terms of atmospheric conditions. Already in solution C04_04, which also assumes a grass surface as in solution C01_04, the altitude is generally higher. This leads to the conjecture that the changes in the altitude are only partly caused by the changing lateral attenuation due to the ground effect, and are also contributed to by the changes in absorption. To isolate the effects of temperature and ground surface, an additional solution is presented which is flown under ISA conditions with a hard ground surface with $\sigma = 2.5 \cdot 10^{32}$, as listed in Table 7.8.

The table shows an even higher absolute number of awakenings, and again a significantly lower relative reduction after optimization, at the cost of a similar increase

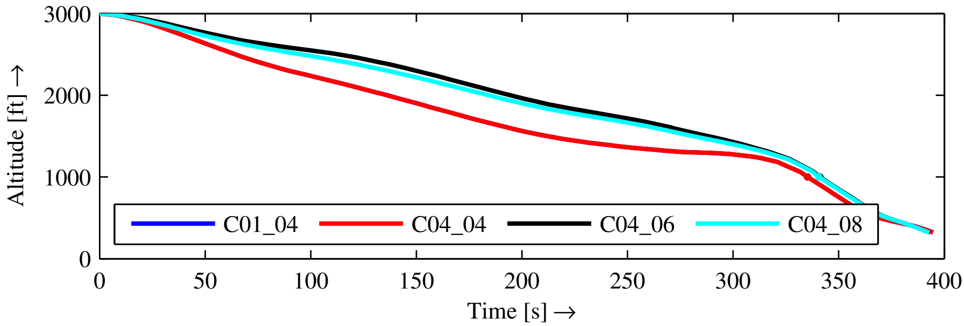

Figure 7.23: Altitude profiles, varying ground surface and atmospheric conditions

in total flight time. Finally, Fig. 7.23 shows the altitude profiles for both atmospheric conditions and both grass and hard ground surface. Both cases with a hard ground surface, C04_06 and C04_08, maintain a generally higher profile similar to the minimum fuel solution, although it cannot be concluded that a high altitude in general is preferential. The latter might result in increased absorption and spreading losses, but will also result in higher source noise levels due to smaller incidence angles, and would require a descent – with associated higher source noise levels – close to the densely populated areas. Apart from the ground effect, also the colder temperature leads to a higher flight profile, which can be observed by comparing C01_01 and C04_04, in which for both a grass ground surface is assumed. Although the ground effect is more dominant, it can be concluded that also for flight in cold atmospheric conditions the effect of increased absorption outweighs the lateral attenuation due to the ground effect, leading to a flight profile at a generally higher altitude.

7.7 Trajectory Analysis

In this chapter the first 3-dimensional optimized trajectories have been presented. Although in noise abatement the main driving parameters are the position of the helicopter and the size and direction of the airspeed vector, at this stage it is interesting to assess one case in more detail to show the control inputs, body angles and angular rates. A 3-dimensional plot of the selected case, C01_01, a trajectory optimized for minimum time in standard atmospheric conditions, can be seen in Fig. 7.24. Essentially the helicopter continuously descends to minimize the total path length, until it has to align with the inbound heading of 66° towards the helipad at the EMC. Since the initial part of the trajectory is a continuous descent at maximum allowed airspeed, only the turning and decelerating parts (indicated in blue in Fig. 7.24) will be considered in more detail.

From Fig. 7.25, depicting the airspeed components v_x, v_y, and, v_z in the Earth-fixed system, and the total airspeed V, the initiation of the turn to the final heading can be

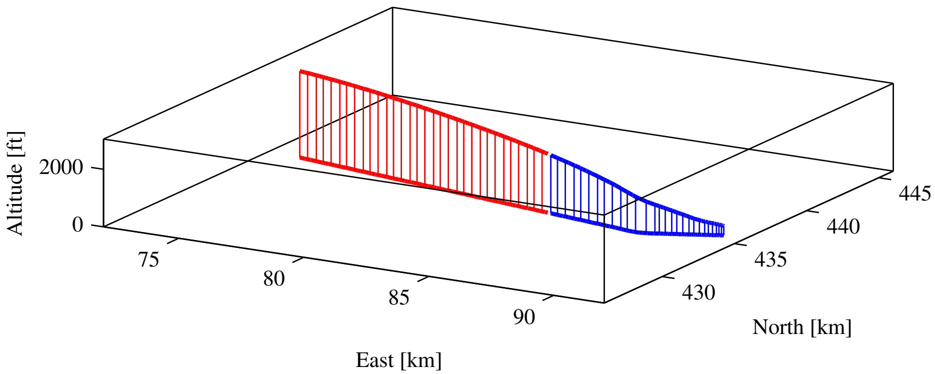

Figure 7.24: 3D-view of case C01_01

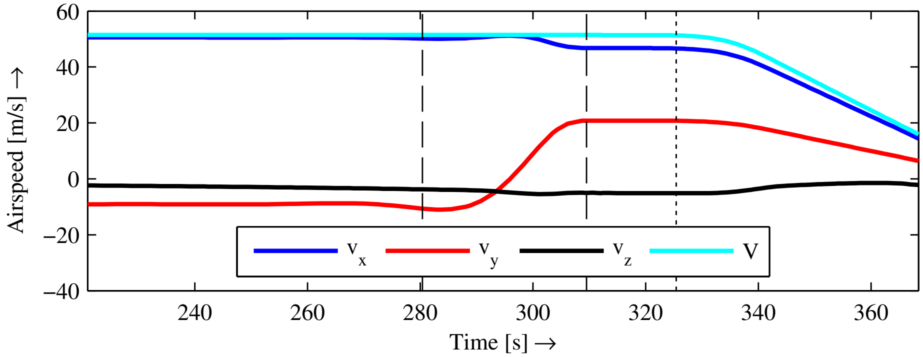

Figure 7.25: Airspeed

seen at around 260 seconds, where v_y increases indicating a northward turn. The turning maneuver, lasting for about 30 seconds, is indicated with two dashed lines in the figure. Throughout the turn the maximum total airspeed of 100 knots (51.44 m·s^{-1}) is maintained. In the final 50 seconds of the flight (starting at 315 seconds, indicated with a dotted line) the helicopter starts decelerating towards its final total airspeed of 30 knots (15.43 m·s^{-1}).

Both maneuvers – turning and decelerating – can also be recognized in the helicopter's body angles plotted in Fig. 7.26. The bank angle is increased to a maximum of 25 degrees, albeit at a relatively low roll rate as can be seen from Fig. 7.27. It should be noted here that the bank angle in this case is not limited by the bounds set to the bank angle (which was limited to 30 degrees), but rather by the constraint on the load factor allowing a maximum vertical acceleration of 1.1 g. The yaw angle logically also increases again indicating a leftward turn. The deceleration maneuver is initiated by increasing the pitch angle of the helicopter, and as such tilting the thrust vector backward to reduce the airspeed.

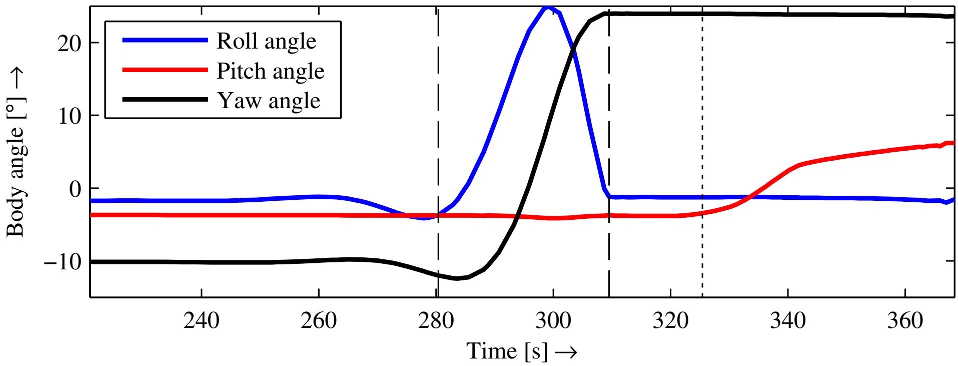

Figure 7.26: Helicopter body angles

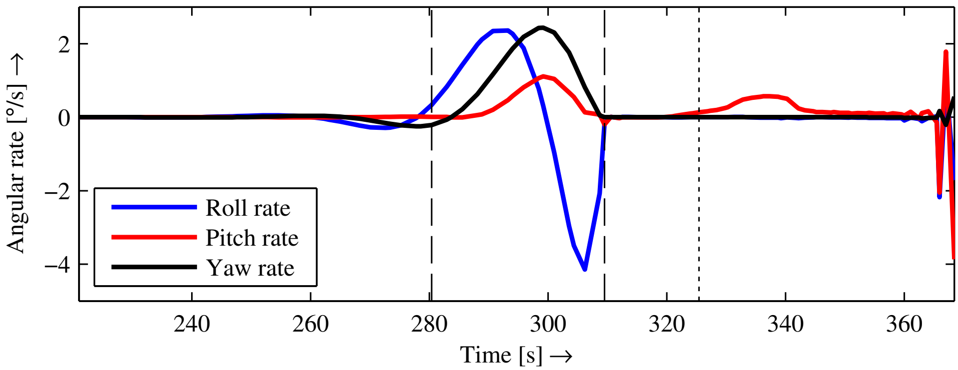

Figure 7.27: Helicopter body angular rates

Another observation can be made from the angular rates. Especially in the last 10 seconds of the trajectory all angular rates show a strong oscillation around an average value of $0° \cdot s^{-1}$. As was already mentioned in Chapter 2, the optimization methodology used in this study has a relatively large time step for the integration of the equations of motion. Similar to the control oscillations discussed in Section 4.3, the fast dynamics such as the angular rates may not be captured in sufficient detail. Especially in regions where constraints apply (such as the terminal conditions in this example) this effect becomes visible. It is noted that the oscillations hardly affect the quality of the trajectory, as ultimately the average values are integrated in time. This can also be seen from the body angles in Fig. 7.26, which hardly show any impact of the oscillations in the angular rates in the final 10 seconds of the trajectory. Although the oscillations could easily be reduced by increasing the number of nodes, the short runtimes obtained by limiting the number of nodes outweigh the possible disadvantages of this behavior.

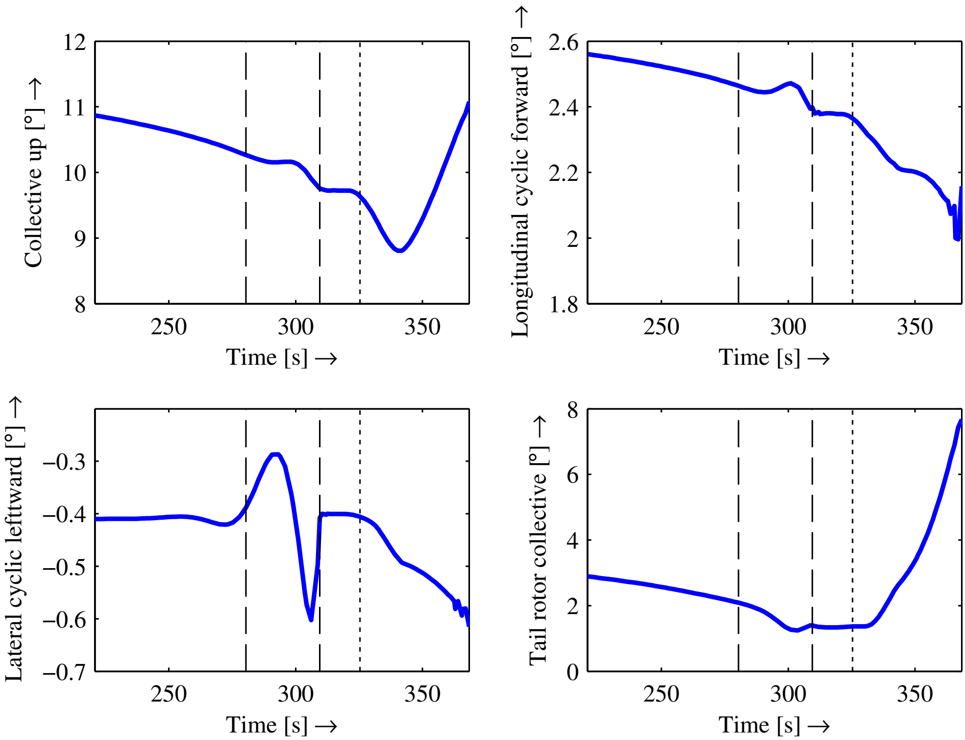

Figure 7.28: Control inputs

Finally, Fig. 7.28 shows the control inputs for the two maneuvers. In the control inputs also some oscillations can be seen for the same reason as discussed above. The turning maneuver is most clearly recognized in the lateral cyclic input at the bottom left plot where the leftward turn is initiated by a small leftward stick input at about 280 seconds. Although the turning maneuver is relatively slow, some cross-coupling effects can be distinguished during the turn. These effects are more clearly recognized in the decelerating maneuver which is initiated with a strong increase of the collective pitch angle. The increase in collective pitch requires an increase in engine torque, and as such also an increase in the tail rotor collective pitch to increase the tail rotor lift and stop the helicopter from yawing.

7.8 Conclusions

Scenario 2 was defined mainly to assess the impact of atmospheric conditions – including wind – on helicopter trajectories optimized for a site-specific noise criterion based on population density information. From this scenario a number of conclusions can be drawn which give an insight into the general preferred behavior of a helicopter in an arrival flight to mitigate the noise exposure expressed in the number of expected awakenings.

As was already observed in Scenario 1, also in Scenario 2 high airspeed and shallow descents avoid particularly high source noise levels – amongst others caused by the BVI noise – and are used as a mechanism to reduce the noise impact in all cases were $k_{noise} \neq 0$. Especially the high airspeed contributes to lower exposure times and hence lower noise exposure for ground based observers.

When a headwind is considered, it was observed that neither the absolute number of awakenings nor the relative improvements after optimizing the trajectories were significantly affected. Although different wind vectors significantly affect the helicopter's flight dynamics and the propagation of sound, it was found that the relative improvements in the number of awakenings and the consequential increase in flight time was similar for all headwind conditions considered. This was found to be the direct result of the site-specific noise criterion. Although a headwind reduces the ground speed and increases the exposure time, a significant part of the population was no longer exposed to high noise levels due to their upwind position relative to the flight track, placing them in the shadow zone.

In tailwind conditions the absolute number of awakenings was found to be significantly higher, which can mainly be attributed to a required turn over a densely populated area. The positive effect of an increased ground speed was countered by a larger part of Rotterdam city center being exposed to high noise levels due to the absence of a shadow zone in the downwind direction. However, more significant relative reductions in the number of awakenings were observed, albeit at the cost of a larger relative increase in flight time as compared to the cases involving headwind.

Finally, in the case of crosswind also larger relative improvements in the number of awakenings could be achieved with similar or shorter additional flight times required as compared to other cases. This can be explained by considering that the crosswind assessed in this scenario places the most densely populated areas to the north of the trajectory in the shadow zone.

It was also found that the atmospheric conditions and the ground surface have a significant impact on the absolute number of awakenings and the relative improvements. When cold atmospheric conditions are assumed, the propagation loss due to absorption increases. As a result, increasing the range between source and receiver results in a higher total absorption loss. This partly outweighs the effects of the lateral attenuation discussed in Scenario 1, and leads to a generally higher flight profile. A more dramatic effect was observed when changing the ground surface type. A soft ground surface significantly increases the propagation loss due to the ground effect, and as a result low flight remains preferential to further increase the contribution of the ground effect. However, when a hard ground surface is assumed, the lateral attenuation becomes negligible, and as a result both under ISA conditions as well as in cold atmospheric conditions the propagation loss is driven by absorption and spreading. As a result, low flight is no longer preferred, and the trajectory shows a gradual descent in order to avoid high source noise levels.

It was also found that with a more complex trajectory and the inclusion of community noise impact in the objective function the computer runtimes are still comparable to those found in Scenario 1. For cases not including noise in Scenario 2 runtimes averaged 45 seconds, whereas solutions runtimes for cases including noise averaged 1.34 hours.

An overview of the results of all solutions for Scenario 2 (including more parameters not presented here) can be found in Appendix D.

8

Scenario 3: Amsterdam SNI

8.1 Introduction

In the final scenario presented in this study a hypothetical *Simultaneous Non-Interfering (SNI)* approach to Amsterdam Airport Schiphol (AMS) is explored. The concept of SNI operations was initially developed in the United States and is since then being researched in both the United States and Europe. In SNI operations, helicopters are assigned specific departure and arrival procedures to separate helicopter traffic from the generally much faster fixed-wing traffic. This allows for a more efficient use of congested airspace, and can significantly reduce delays near major airports [98]. A downside to the SNI concept is, however, that previously unused airspace is now used for helicopter procedures. Although usually less frequent than fixed-wing movements, helicopter movements are now possibly diverted over populated areas previously unhindered by aviation noise. This indicates a clear need for the optimization of SNI routes to reduce the noise impact in the affected areas [25].

An SNI approach on a major commercial airport offers a different challenge than that seen in the previous scenario. Firstly, the airport itself is located in a less densely populated area. This is expected to allow for more lateral freedom to circumvent populated areas, but at a higher cost contribution of flight time and total fuel burn. Secondly, the design of an arrival route in busy airspace around a major airport offers additional challenges which will result in a more complex set of constraints to safely direct the helicopter to the designated landing area.

Two main objectives can be distinguished in Scenario 3. Firstly, the SNI approach procedure is modeled using a significantly larger number of phases and nodes, and has a more complex set of constraints imposed on it. Apart from allowing to model a more realistic trajectory, this also allows to assess the ability of the *ECHO* suite to solve a significantly more complex optimal control problem than explored in the two previous scenarios. Secondly, in Scenario 3 a second site-specific noise criterion is introduced, *viz.* the number of people living inside the 65 dBA SEL contour. In addition, the trajectories synthesized in this scenario are also optimized with respect to the number of awakenings as in Scenario 2. This allows for a comparison in the characteristic behavior of the helicopter for both criteria, and to identify any significant differences between them.

The following sections will give a more detailed overview of the setup of this scenario, and will present major results.

8.2 Scenario Description

Scenario 3 starts in-flight over the IJmeer lake to the east of Amsterdam, at an altitude of 3,000 ft AGL and an airspeed between 30 and 100 knots TAS. The objective of the flight is to approach AMS from a southern direction and to land at the helicopter landing area of AMS which is located at runway 04 highlighted in blue in Fig. 8.1. In normal operations, the helicopter could follow the same inbound route as the fixed-wing traffic to runway 36R and then make a turn towards the landing area. In the SNI concept presented in this scenario, however, the helicopter approaches the threshold of runway 04 at a heading of 353°, which is at a 10° offset with the fixed-wing traffic approaching runway 36R. The trajectory then ends 500 m before reaching the threshold of runway 04, at an altitude of 300 ft AGL and an airspeed of 40 knots TAS. With these final conditions, the helicopter trajectory is separated from the fixed-wing traffic on runway 36R by at least 350 m, and is assumed to make a visual turn onto runway 04 to land in the designated helicopter landing area, as can be seen from Fig. 8.1.

As opposed to the procedure defined in in Scenario 2, in this scenario more limitations are imposed on the design of the ground track. The ground track is defined as a sequence of waypoints with a minimum separation distance to allow stabilization criteria to be met. In essence this will result in a sequence of straight flight segments connected with turns at the waypoints. However, in previous studies on noise abatement terminal procedures for fixed-wing aircraft, it was already shown that constructing a trajectory using only straight legs and constant radius turns is beneficial for noise abatement [30, 99]. With these flight segments, a ground path is constructed using a sequence of straight legs and constant radius turns connecting the waypoints. Under the assumption that sufficiently accurate navigational equipment is available, this minimizes flight track dispersion, ensuring that the noise abatement procedures can be followed accurately in varying weather conditions. As can be derived from Fig. 8.1, this approach has been adopted for this scenario as well. As a result, the problem formulation consists of six phases, where each phase has its own set of boundary conditions and path constraints imposed. In essence, the six phases are required to first fly past the airport to approach from the south, then to line up with the final heading and finally to intercept the glideslope. In all phases the constraints defined in Section 4.5 are imposed. Additional constraints are defined in Table 8.1 below.

It is noted that phase 5 is added to ensure that the helicopter is stabilized when intercepting the glideslope, which implies that for at least one nautical mile (1,852 m) the helicopter maintains its airspeed and altitude along the final approach heading.

Table 8.1: Constraints for Scenario 3

Constraint	(In)equality
Phase 1: Straight leg	
Initial rate of descent	$v_{z,0} = 0$ fpm
Initial altitude	$z_0 = 3000$ ft
Initial position	$(x_0, y_0) = (x_s, x_s)$ m
Straight leg	$\dot{\chi} = 0^\circ \cdot s^{-1}$
Phase 2: Constant radius turn	
Constant turn radius	$R =$ constant
Bounded turn radius	$500 \leq R \leq 15000$ m
Minimum heading change	$10^\circ \leq \Delta\chi_g \leq 120^\circ$
Phase 3: Straight leg	
Straight leg	$\dot{\chi} = 0^\circ \cdot s^{-1}$
Bounded segment length	$1852 \leq l \leq 15000$ m
Phase 4: Constant radius turn	
Constant turn radius	$R =$ constant
Bounded turn radius	$500 \leq R \leq 15000$ m
Intercept final heading	$\chi_f = 353^\circ$
Descend to glideslope intercept altitude	$z_f = 1000$ ft
Decelerate for final approach	$V_f = 65$ knots
Phase 5: Straight leg	
Straight leg	$\dot{\chi} = 0^\circ \cdot s^{-1}$
Bounded segment length	$1852 \leq l \leq 5000$ m
Maintain altitude	$z_f = 1000$ ft
Maintain airspeed	$V_f = 65$ knots
Phase 6: Glideslope	
Straight leg	$\dot{\chi} = 0^\circ \cdot s^{-1}$
Glide slope angle	$-10^\circ \leq \gamma_{GS} \leq -3^\circ$
Follow glideslope	$\gamma = \gamma_{GS}$
Final airspeed	$V_f = 40$ knots
Final altitude	$z_f = 300$ ft
Final x-position	$x_f = x_{HS} - 500 \sin 353^\circ$
Final y-position	$y_f = y_{HS} - 500 \cos 353^\circ$

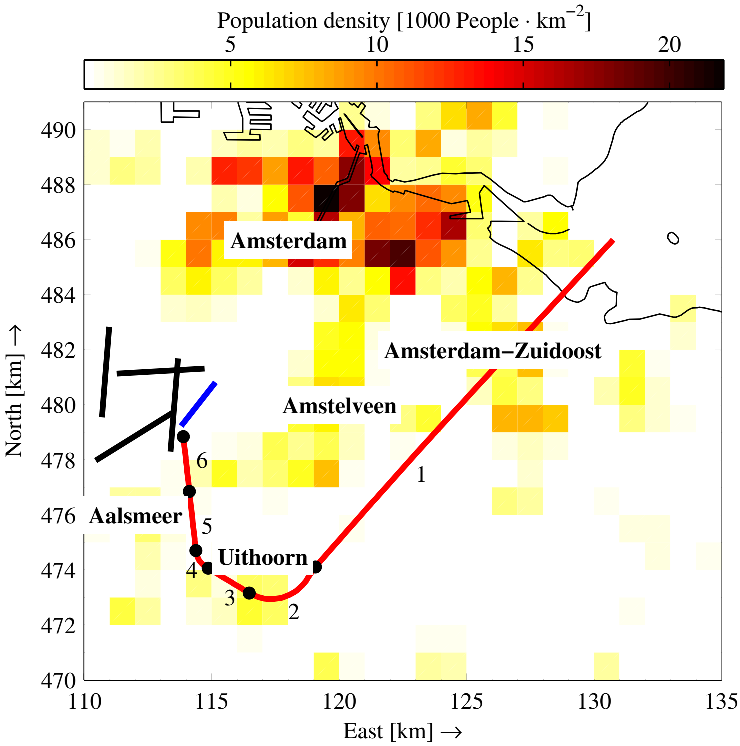

Figure 8.1: Scenario 3 overview

Furthermore, phases 2 and 4 are defined as constant radius turns, and hence require the turn radius to be determined. For this, consider that when no wind is present the turn radius can be readily determined from

$$R = \frac{\sqrt{v_x^2 + v_y^2}}{\dot{\chi}} \tag{8.1}$$

To ensure a constant turn radius, in phases 2 and 4 a design parameter is introduced. A design parameter is a parameter in the optimization problem which is constant throughout a phase. Hence, a path constraint setting the turn radius determined from Eq. (8.1) equal to the design parameter results in a constant turn radius throughout the entire phase. The design parameter itself is then bounded as well, in this case between 500 and 15,000 m for both turns.

Furthermore, it is noted that the transition from a straight leg to a constant radius turn is not modeled in this scenario. Consequently, the linkages between straight and turning legs contain discontinuities, mainly concerning the helicopter roll angle Φ. To accommodate this, the bounds on linkage constraints have been relaxed for the body angles, inflow angles and the control variables. It is noted though, that continuity in the position and airspeed vectors is still imposed.

In Scenario 3 trajectories are optimized with respect to time and two different site-specific noise optimization criteria. Firstly, the number of expected awakenings due to a single nighttime flyover – already presented in Scenario 2 – is used. In addition, the trajectories are also optimized for the number of people living in areas exposed to SEL values higher than 65 dBA. The main difference between both criteria is that in case of the number of people enclosed in a contour the value of the SEL determines only whether or not a person is counted in the objective function. Exposure to excessively high noise levels does not lead to a higher value in the objective function. In contrast, the number of people awoken depends exponentially on the actual noise exposure, and as such excessively high noise levels in populated areas are generally avoided when possible. As it is expected that both noise criteria can lead to significantly different noise abatement procedures, one of the main objectives of this scenario is to assess the differences in the characteristic behavior of the helicopter for both criteria. The performance index for Scenario 3 can then be defined as

$$J = t_f + k_{awakenings} N_A + k_{enclosed} P_{>SEL_{65}} + \upsilon \int_{t_0}^{t_f} \sum_{i=1}^{4} u_i^2 \tag{8.2}$$

which again includes the control damping penalty discussed in Section 4.3. It is noted that either $k_{awakenings}$ or $k_{enclosed}$ is non-zero, and hence that the noise criteria are never accounted for simultaneously in the objective function. In addition, the values for both noise weighting factors have been chosen such that in all cases the relative contribution to the performance index is comparable between both noise criteria.

The six phases in Scenario 3 have been discretized in time with a total of 140 nodes for all cases presented below. The resulting NLP contains 3,495 nonlinear variables and 3,918 nonlinear constraints. The noise is calculated in 2,964 cells in a 57x52 km grid. Although 3.1 million people live within the grid, the noise is only calculated in cells within 12.5 km of the trajectory, as was discussed in Scenario 2.

8.3 Results

8.3.1 Expected Number of Awakenings

Scenario 3 is only assessed for standard atmospheric conditions. First, the results optimized with respect to time and awakenings with increasing weighting factor $k_{awakenings}$ are presented in Table 8.2. As compared to the results presented for Scenario 2, the table shows that both the total number of awakenings and the possible reduction are significantly lower. This can be attributed to the population distribution around AMS which is – as can be expected in the direct vicinity of a major airport – more sparse than the city center assessed in Scenario 2. Case C01_03 shows a reduction in the

Table 8.2: Scenario 3 Results, optimized for time and awakenings

Case	**Objective**	$\mathbf{t_f}$ **[s]**	$\mathbf{N_A}$	$\mathbf{\Delta N_A}$ **[%]**	$\mathbf{kP_{>SEL_{65}}}$	$\mathbf{\Delta kP_{>SEL_{65}}}$ **[%]**
C01_01	t_f	**579.5**	2689	n/a	116.3	n/a
C01_02	$t_f + 0.04N_A$	**580.4**	**2555**	-4.98	108.6	-6.59
C01_03	$t_f + 0.1N_A$	**581.3**	**2342**	-12.9	99.93	-14.0
C01_04	$t_f + 0.2N_A$	**595.8**	**2261**	-15.9	98.00	-15.7
C01_05	$t_f + 0.5N_A$	**610.6**	**2133**	-20.7	88.58	-23.8
C01_06	$t_f + N_A$	**622.5**	**2113**	-21.4	87.36	-24.9

number of awakenings of 12.9%, whereas the total flight time is hardly affected, and, as can be seen from Fig. 8.2, the ground track is nearly identical to that of the minimum time solution, C01_01. Consequently, the reduction in the number of awakenings can only be explained by considering the altitude and airspeed profiles in Fig. 8.3. Indeed this figure confirms that as in previous scenarios the altitude is directly reduced after initiating the trajectory to increase the effect of lateral attenuation. Figure 8.4 shows the difference SEL_{C01_03} - SEL_{C01_01} in dBA plotted over the GIS of the area surrounding AMS and the ground track of C01_01 (which is nearly identical to that of case C01_03). Although for instance in the city center of Amsterdam noise levels are reduced by more than 20 dBA, in these areas the SEL is well below the threshold value for awakenings of 50.5 dBA in both cases. However, the figure also shows a significant reduction of over 5 dBA to the right of the helicopter, hence reducing the noise exposure in the communities of Ouderkerk and the southeastern part of Amsterdam. Although also an area of increased noise levels can be observed directly below the trajectory due to the reduced slant range, the relatively low population density in that area and the decreased exposure in Ouderkerk and Amsterdam-Southeast result in a net reduction in the number of awakenings.

For higher weighting factors $k_{awakenings}$, the reduction in the number of awakenings can be further increased to 21.4% as can be seen for case C01_06. However, this reduction can no longer be attributed solely to changes in the altitude and airspeed profiles. Figure 8.2 reveals that in case C01_06 the westward turn near the community of Uithoorn has a larger turn radius, increasing the distance with respect to the communities of Ouderkerk and Uithoorn. As can be seen from Fig. 8.5, showing the difference in noise exposure between cases C01_03 and C01_06, the noise exposure in Ouderkerk and parts of Uithoorn is reduced by more than 5 dBA. The larger turn also allows to partly compensate the longer ground track, which logically leads to a longer total flight time. As the trajectory has to comply with passenger comfort constraints, in cases C01_01 and C01_03, the airspeed is reduced to around 65 knots after 400 seconds, as can be seen in Fig. 8.3. In case C01_06, however, the larger turn radius allows for a higher airspeed of around 71 throughout the turn, which starts at 450 seconds. Although due to the use of an exposure based noise metric this increased airspeed will also be beneficial for the noise optimization criterion, the reduction of the SEL in this area is only 0.38 dBA. A comparison of cases C01_03 and C01_06 in Fig. 8.5 reveals that the increased turn radius has led to a noise

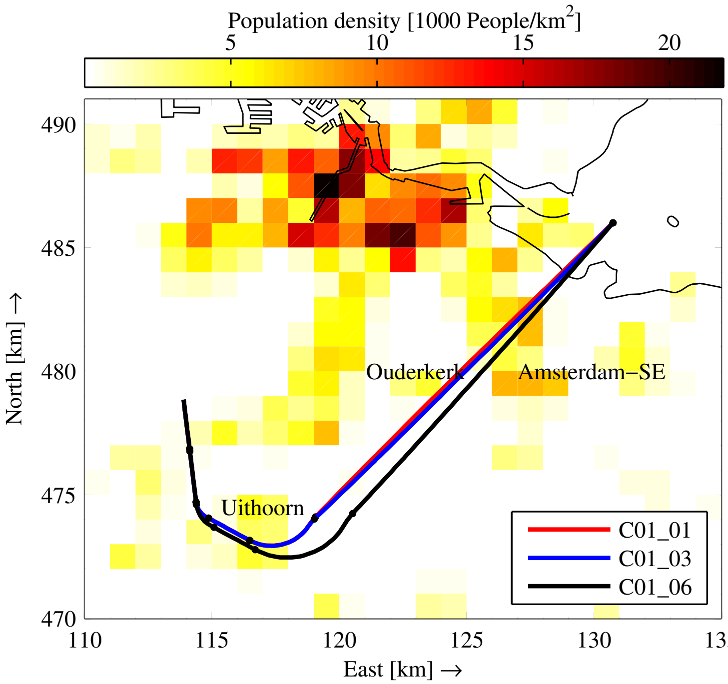

Figure 8.2: Ground tracks, optimized for time and awakenings

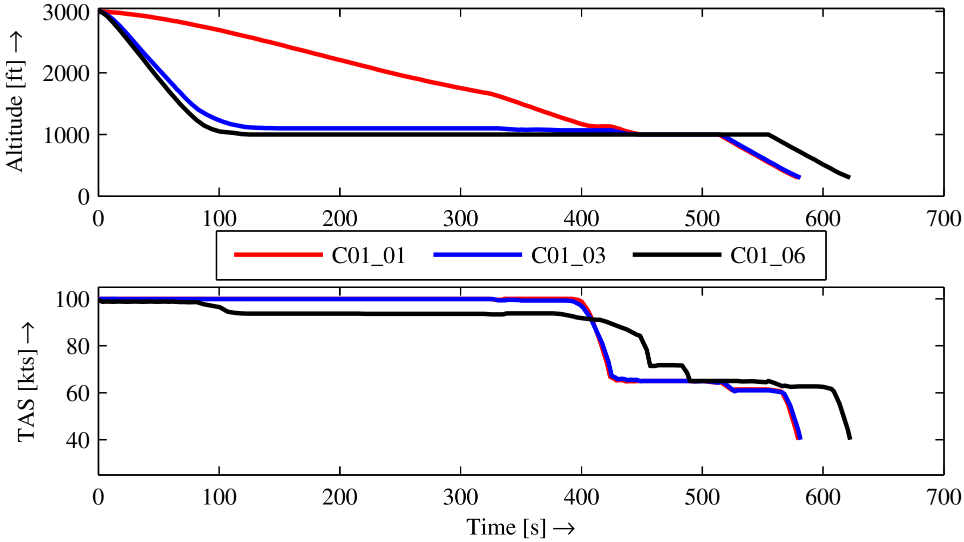

Figure 8.3: Altitude and airspeed profiles, optimized for time and awakenings

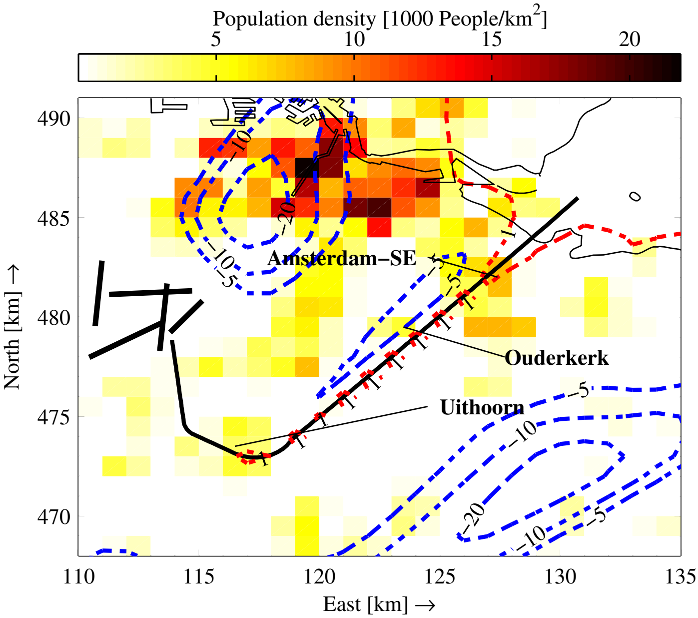

Figure 8.4: ΔSEL, C01_03 - C01_01

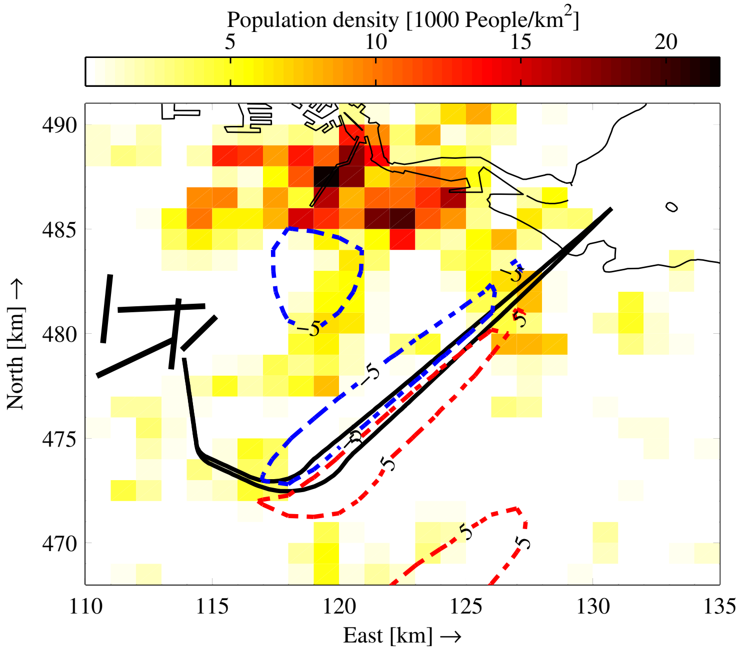

Figure 8.5: ΔSEL, C01_06 - C01_03

reduction of over 5 dBA in areas to the west of the trajectory, further reducing the number of awakenings in the communities of Ouderkerk and Uithoorn.

8.3.2 People Enclosed in the 65 dBA SEL Contour

The same process as described above has been repeated including the number of people enclosed in the 65 dBA SEL contour in the performance index. Major results can be found in Table 8.3. The values for the weighting factor $k_{enclosed}$ have been chosen such that the total value of the performance index is comparable to the results presented in Table 8.2, and hence that a comparable trade-off is ensured between flight time and the selected noise criterion. Initially the results appear similar in terms of the relative reduction of the objective value. In fact, upon closer inspection again clearly two groups of solutions can be distinguished. Cases C02_01 and C02_02 both have very similar total flight times and numbers of people enclosed, resulting from changes to the airspeed and altitude profiles only. In other cases also the ground track has changed, resulting in a longer trajectory and hence longer flight times.

As in the cases optimized with respect to flight time and the number of awakenings, an increased radius for the first turn is the main difference in the ground tracks between cases C02_01 to C02_03 and cases C02_03 and C02_04, which see a further reduction of

Table 8.3: Scenario 3 Results, optimized for time and people enclosed

Case	Objective	t_f [s]	N_A	ΔN_A [%]	$kP_{>SEL_{65}}$	$\Delta kP_{>SEL_{65}}$ [%]
C01_01	t_f	**579.5**	2689	n/a	116.3	n/a
C02_01	$t_f + \frac{1}{1000} P_{>SEL_{65}}$	**581.6**	2525	-6.10	**105.7**	-9.06
C02_02	$t_f + \frac{1}{500} P_{>SEL_{65}}$	**582.2**	2520	-6.28	**105.0**	-9.71
C02_03	$t_f + \frac{1}{200} P_{>SEL_{65}}$	**614.3**	2198	-18.3	**89.94**	-22.6
C02_04	$t_f + \frac{1}{80} P_{>SEL_{65}}$	**619.3**	2181	-18.9	**89.33**	-23.2

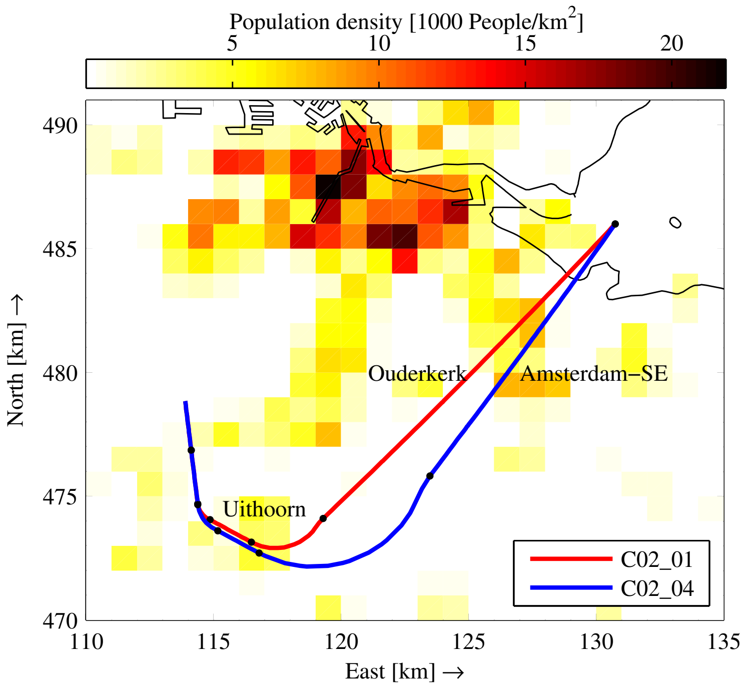

Figure 8.6: Ground tracks, optimized for time and people enclosed

the noise impact, but at the cost of a significantly higher increase in the flight time. This can be seen in Fig. 8.6. Whereas in the cases optimized with respect to awakenings the noise impact in the community of Ouderkerk was reduced significantly by the larger turn radius, Fig. 8.7 reveals that in the cases optimized with respect to the number of people enclosed this community in fact is no longer within the 65 dBA contour, and as such does not contribute to the performance index. Also the northern part of Uithoorn is now no longer within the 65 dBA contour. Although a small part of the densely populated Amsterdam-Southeast area is now placed within the threshold contour, overall a significant reduction of the noise impact is achieved. Finally, the airspeed and altitude

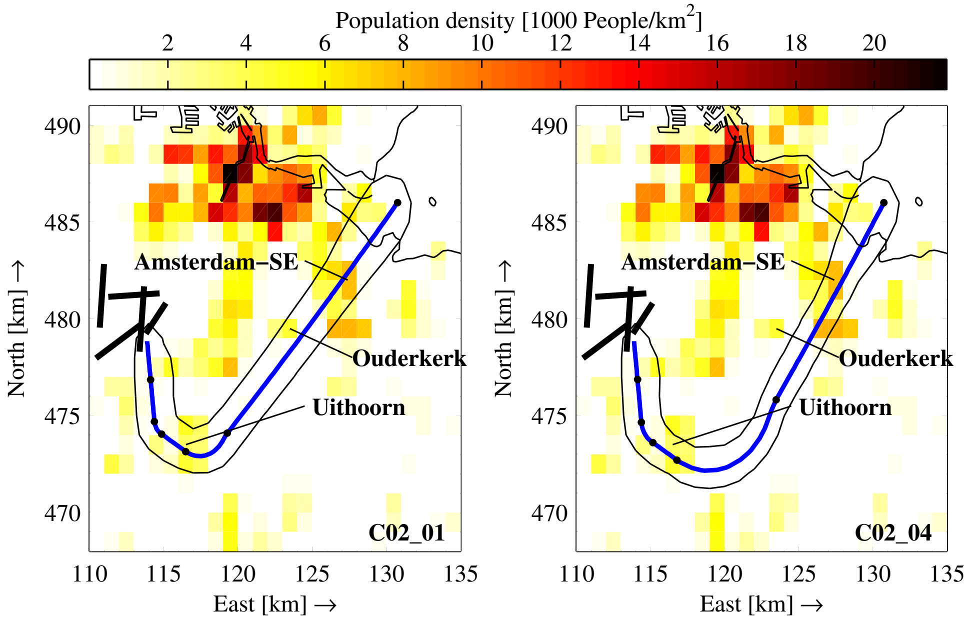

Figure 8.7: 65 dBA SEL contours, optimized for time and people enclosed

profiles in Fig. 8.8 show that the larger turn radius allows for a higher airspeed throughout the turn partly compensating the increased path length in terms of the total flight time.

It should be noted that although the general trends for both noise optimization criteria are similar, the turn radius when optimizing with respect to the number of people enclosed in the 65 dBA SEL contour is significantly larger then when optimizing with respect to the number of expected awakenings. It may be reasoned then that this larger turn radius could also be better for the cases where awakenings are accounted for in the objective function. If this would indeed occur, a local minimum has been encountered. In that case, solutions of cases C02, *evaluated using the objective functions of cases C01*, result in a lower value of the total objective value J. Even though with the optimization methodology used in this work a local optimum cannot be readily excluded, in this case it is easily recognized. In fact, although it was expected that the larger turn radius could be a better solution in terms of the number of awakenings, a detailed analysis of the results of both sets of cases proved that in fact the larger turn radius is a local minimum. To exemplify this, consider the results presented below using the performance index of case C02_04 and the results from both cases.

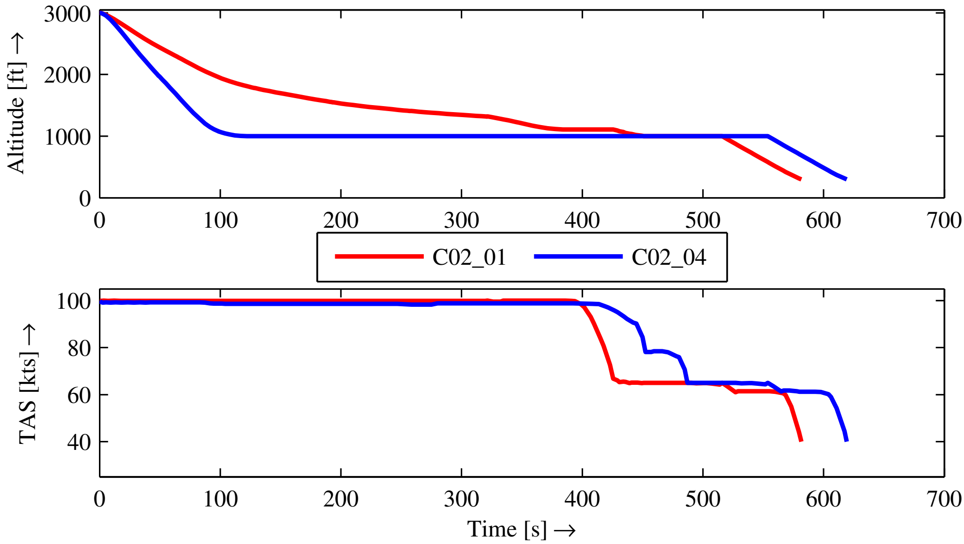

Figure 8.8: Altitude and airspeed profiles, optimized for time (left) and people enclosed (right)

$$\text{C01\_05:} \quad J = t_f + k_{enclosed}P_{>SEL_{65}} + J_u = 610.6 + \frac{1}{80} \cdot 1000 \cdot 88.58 = 1717.9 + J_u$$

$$\text{C02\_04:} \quad J = t_f + k_{enclosed}P_{>SEL_{65}} + J_u = 619.3 + \frac{1}{80} \cdot 1000 \cdot 89.33 = 1735.9 + J_u$$

Although the effect of the control penalty cannot be completely neglected, it is very likely that indeed solution C02_04 forms a local minimum. As solutions depend heavily on the initial guess used to start the optimization, a new solution is presented using C01_05 as an initial guess; the objective function of C02_04, however, is used, which allows to assess the possible further reduction in the number of people enclosed. The results of case C02_05 are presented in Table 8.4. The table confirms that a better solution has indeed been found using a different initial guess as the total objective value J is significantly lower. In addition, although previous results implied slightly different behavior when optimizing for different noise criteria, the results of case C02_05 indicate the opposite. In fact, for solutions C01_05 and C02_05 with comparable total objective function values but different noise criteria, the ground tracks, airspeed and altitude profiles are nearly identical.

Table 8.4: Scenario 3 Results, optimized for time and people enclosed

Case	Objective	$\mathbf{t_f}$ [s]	$\mathbf{N_A}$	$\mathbf{\Delta N_A}$ [%]	$\mathbf{kP_{>SEL_{65}}}$	$\mathbf{\Delta kP_{>SEL_{65}}}$ [%]
C01_01	t_f	**579.5**	2689	n/a	116.3	n/a
C02_04	$t_f + \frac{1}{80}P_{>SEL_{65}}$	**619.3**	2181	-18.9	**89.33**	-23.2
C02_05	$t_f + \frac{1}{80}P_{>SEL_{65}}$	**617.3**	2138	-20.5	**86.97**	-25.2

8.4 Conclusions

Scenario 3 was defined mainly to assess the effect of different site-specific noise optimization criteria on an arrival trajectory with a complex set of constraints imposed.

The cases presented in this scenario have shown that significantly larger and more complex problems can successfully be optimized using *ECHO*, although the computer runtimes are significantly higher than in the previous two scenarios due to a combination of a large number of discretization points and a large noise calculation grid. In fact, also the complexity of the problem definition – mainly caused by the large number of phases – contributes to long runtimes, which are typically in the order of 4 hours, exceeding the 2 hour goal defined in the objectives for this study.

In addition, the trajectories in Scenario 3 were optimized with respect to two different site-specific, population-based noise criteria. Trajectories were optimized showing significant reductions for both noise criteria at the cost of a relatively small increase in the total flight time. The number of expected awakenings is exponentially dependent on the SELs in the observer locations, whereas the number of people enclosed is discretely dependent on a single threshold value. Although significant differences could be expected in both the ground track and the vertical profile between trajectories optimized with respect to either of the two criteria, it was found that the mechanisms to reduce the noise performance criteria were nearly identical.

As in the previous scenarios, high airspeed and low altitude flight contribute significantly to the reduction of the noise exposure by reducing the source noise levels and increasing the lateral attenuation of sound. In the ground plane, for both noise optimization criteria the ground track was adjusted to circumvent communities where possible. In addition, turn radii near communities are increased to allow higher airspeeds throughout the turn, and hence to keep the total flight time in check.

The increase in the complexity of the scenario as compared to previous scenarios has led to a significant increase in computer runtime. This is partly caused by the overall increase in problem size, and partly by the decreased convergence rates due to the increased complexity of the problem. For this scenario runtimes therefore averaged to 3.34 hours when noise was included in the objective function.

An overview of the results of all solutions for Scenario 3 (including more parameters not presented here) can be found in Appendix E.

9
Conclusions and Recommendations

9.1 Conclusions

9.1.1 Introduction

This thesis presents the development of the *European Clean Helicopter Optimization (ECHO)* suite aimed at the optimization of helicopter arrival and approach trajectories with respect to environmental performance criteria. The primary objective of this study was *to develop an optimization software suite that can optimize helicopter trajectories in non-standard atmospheric conditions with respect to (community) noise impact, fuel burn and gaseous emissions.* Previous research includes multiple studies with similar objectives or components thereof. To ensure a step change in the state of the art with respect to existing studies, the secondary goal of this study requires *the optimization software suite to be based on optimal control theory to maintain computer runtimes in the order of two hours for typical problems, whilst using high-fidelity flight dynamics and noise models to achieve a required level of accuracy.*

9.1.2 *ECHO* Development

From the discussion of the *ECHO* suite and the example scenarios presented in this thesis a number of conclusions can be drawn directly related to the main objectives of this study.

Firstly, it can be concluded that the main research objective has been achieved. The *ECHO* suite is capable of optimizing helicopter trajectories with respect to different environmental and economic criteria, and in different atmospheric conditions, as has been shown in the example scenarios presented herein.

The secondary objective, however, has been only partly achieved. The requirements on total modeling accuracy and the overall efficiency of the suite have proven – as could reasonably be expected – to be competitive, and the trade-off chosen in the development of *ECHO* has resulted in meeting the accuracy requirements, but violating the efficiency requirements in some cases. However, it should be noted that ongoing development of the software suite at the time of writing – mainly including parallel computing – has seen a further reduction of the total computer runtimes by up to 75% in cases where noise is included in the objective function, showing the potential to indeed meet the efficiency requirements for the cases presented in this study.

9.1.3 *ECHO* Components

To comply with the objectives of this study, first an advanced optimization methodology was selected called the Radau Pseudospectral Method (RPM), which is a direct method for solving optimal control problems. This method discretizes the infinitely-dimensional trajectory optimization problem and transforms it to a finite-dimensional Non-Linear Programming (NLP) problem. To determine a direction towards the optimal solution, and to define a convergence criterion, however, the method requires the problem derivatives to be provided to the numerical solver. Although multiple methods are available to determine the derivatives, *ECHO* uses integrated automatic differentiation software to efficiently determine most of the problem derivatives.

To allow the optimization of helicopter trajectories with respect to noise, fuel burn and gaseous emissions, a number of models were integrated in *ECHO*.

Firstly, an eight Degree-of-Freedom helicopter flight dynamics model using quasi-static inflow for both the main and tail rotor was selected to accurately model the vehicle dynamics. The flight dynamics model was augmented with a model based on empirical data providing the fuel flow and the emission of NO_x as a function of the shaft horsepower required from the engine. These models together enable *ECHO* to optimize helicopter trajectories with respect to total flight time, fuel burn and NO_x emissions. Although both models are generic, the parameters of an MBB Bo-105 helicopter were used in the optimized trajectories presented in this study.

Secondly, to model the community noise impact, a helicopter noise model was integrated in the software suite, consisting of three separate elements.
The helicopter source noise is modeled using a database of hemispherical source noise levels. The source noise levels were determined offline using an aeroacoustic-elastic model, and are available for 12 different flight conditions typically encountered during a helicopter arrival procedure.
The second step in the noise modeling is the propagation of the source noise levels through the atmosphere. To be able to accurately model the propagation losses in non-standard atmospheric conditions, a propagation model based on ray-tracing methods was developed for integration in *ECHO*. To significantly improve the performance of the model, a geometrical approach was developed to determine the ray path between

source and receiver, rather than a classical forward integration of the sound rays. The propagation model was validated against proven ray-tracing models and a Fast Field Programme (FFP), indicating a very accurate prediction of the total propagation loss between source and receiver for the atmospheric conditions considered in this study.

To quantify the noise impact on the ground, a number of generic and site-specific noise impact criteria are determined in *ECHO*. To minimize the noise exposure in generic arrival procedures, the contour area above a threshold Sound Exposure Level (SEL) is available. Combined with a Geographic Information System (GIS) containing population density data, both the number of expected awakenings due to a single night time flyover and the number of people exposed to SELs above a predefined threshold value can be determined to optimize trajectories with respect to community noise impact.

The selected optimization methodology and the models integrated in *ECHO* allow helicopter trajectories to be optimized with respect to flight time, fuel burn, NO_x emissions and three different noise criteria, or any combination thereof. From a number of example scenarios presented in this study it can be concluded that the two main modeling components combined with the advanced optimization methodology indeed provide a significant improvement in the ability to accurately optimize helicopter trajectories with respect to environmental criteria as compared to existing studies.

9.1.4 Example scenarios

In order to demonstrate the capabilities of the *ECHO* suite, three example scenarios were defined, each addressing the assessment of specific required attributes of the optimization suite. Within the scenarios a large number of trajectories has been optimized with respect to different optimization criteria, and for different atmospheric conditions. From these scenarios a number of conclusions can be drawn regarding the development of the optimization suite, and, more importantly, with respect to preferential flight conditions to minimize the performance criteria.

Firstly, it can be concluded that the optimization suite is able to optimize helicopter trajectories with a complex set of constraints imposed to ensure flight operations within the helicopter's flight envelope and within predefined passenger comfort limits. In addition, in representative cases the total computer runtime on a standard desktop computer was well within the two hour limit defined as a development objective for *ECHO*. Only in the third scenario presented in this study was the runtime objective significantly violated due to the significantly larger problem size and complexity.

The total flight time, fuel burn and NO_x emissions all have been assessed in single objective optimization runs. In all minimum time solutions found in this study, the high airspeeds are maintained and a continuous descent path is followed to essentially minimize the total trajectory length. To minimize fuel and NO_x emissions, in general a high flight altitude and airspeed is maintained as long as possible to maximize the specific range of the helicopter, although in most minimum NO_x solutions a small reduction in the airspeed was observed, indicating a more efficient airspeed with respect to NO_x

emissions. However, compared to the minimum fuel solutions determined for the same scenario the reduction of the total NO_x emission was found to be negligible, while the total flight time increased significantly. It can be concluded that although airspeed and altitude profiles of optimal solutions found for each of the three performance criteria can differ significantly, the effect on the value of the performance index is generally very small.

In the three scenarios presented in this study all three of the available noise impact criteria have been assessed. In all cases a composite performance objective was used defining a weighted combination of the selected noise criterion and either total fuel burn or total flight time. For all noise criteria, and for all scenarios significant reductions in the noise impact were observed at the cost of relatively small increases of the second performance criterion. The optimal solutions found in all three scenarios provide a good insight in the preferential flight conditions to reduce the noise impact of a helicopter on the ground.

Firstly, when only considering the vertical profile of an approach procedure, it can be concluded that in all cases and for all noise criteria maintaining a high airspeed can significantly reduce the noise exposure. This is caused largely by a reduction of the source noise levels at high airspeeds, but is also contributed to by a reduction of the total noise exposure time reducing the SEL noise metric used in this study. Only when three-dimensional trajectories are considered in combination with a population-based noise criterion, the airspeed should in some cases be reduced to allow maneuvering around densely populated areas within the specified operational constraint boundaries.

Secondly, in all cases considered in this study reducing the altitude as soon as allowed significantly reduces the noise impact astride the helicopter trajectory. This is partly caused by the source noise levels which are generally lower near the main rotor's tip path plane, and as such for observers located at high incidence angles with respect to the helicopter. A more significant noise mitigating effect of the low flight altitude is caused by a significant increase in the propagation loss astride the trajectory. The high lateral attenuation losses are in part caused by a significant increase in the ground effect. Furthermore, shadow zones occur in atmospheric conditions with a negative speed of sound gradient, where no direct sound rays reach the ground, and consequently noise levels are generally negligible. With the noise source at a relatively low altitude, the shadow zone starts closer to the source, effectively placing a large number of the observer locations inside the shadow zone. Although the reduction of the flight altitude leads to increased noise levels directly below the source, the effect of the increased lateral attenuation on the overall noise performance criterion was in all cases found to be dominant.

Finally, it was found that the source noise levels are highly dependent on the flight conditions. Consequently, avoiding specific flight conditions can significantly contribute to the mitigation of the noise impact on the ground. Especially at steep descent angles, and especially at low airspeeds, the dominance of Blade-Vortex Interaction (BVI) noise results in significantly higher source noise levels. A high airspeed was already observed to be beneficial for all optimization criteria considered in this study. The effect of the flight path angle on the source noise levels is less significant though, and in fact in all results steep descent angles were observed. This indicates that the noise mitigating effect of flying at relatively low altitudes is significantly higher than the effect of avoiding steep descent angles, justifying the steep descents observed in all example scenarios.

In addition to different noise optimization criteria, also the influence of atmospheric conditions and different ground surfaces was assessed.

In Scenario 2 the effect of wind on the flight mechanics and on the number of people expected to awaken due to a single nighttime flyover was assessed. Especially in headwind conditions the absolute number of awakenings nor the relative improvement achieved in the optimized trajectories was significantly affected as compared to no-wind conditions. This can be fully attributed to the specific population density distribution in this specific scenario, and consequently results in very similar noise abatement trajectories. Although in both crosswind and tailwind conditions a clearer dependency on the wind speed was observed, the optimal trajectories partly followed a highly similar ground path in all wind conditions. Again this can be fully attributed to the specific population density distribution in this scenario. Also in the airspeed and altitude profiles similar behavior was observed as in cases with no wind vector present, again showing the benefits of high airspeed, low altitude flight. Consequently, it can be concluded that although the effect of wind on the absolute noise impact is significant, the effect on the trajectories optimized with respect to noise is negligible.

The atmospheric conditions and the ground surface type both significantly influence the absolute number of awakenings and the relative improvements that can be achieved. A hard ground surface partly reduces the propagation loss due to the ground surface, and consequently reduces the beneficial effect of flying at low altitudes. Consequently, the total propagation loss is no longer dominated by the ground effect but rather by the atmospheric absorption and the spreading loss, reducing the noise mitigating effect of flying at low altitudes, and leading to a generally higher flight altitude in trajectories optimized with respect to noise. When the ambient temperature is also reduced – leading to higher absorption losses – increasing the slant range between source and receiver is even more beneficial, further reducing the need to fly at low altitude.

9.2 Recommendations

Although it was shown that the *ECHO* suite largely complies with the objectives defined for the development of the suite, a number of recommendations for further research can be formulated following from the example scenarios presented in this study.

Firstly, four improvements in the noise modeling should be considered. Most importantly, it should be noted that the source noise along the trajectory is currently only modeled as a sequence of steady-state events. In reality, though, the current source noise database could be used to give a better approximation of the source noise levels in unsteady flight if the hemispheres would be rotated along with the pitch and roll angles of the helicopter. In addition, specific effects in accelerating or decelerating flight could be modeled by quasi-steady noise modeling where the effects of helicopter accelerations are approximated by simulating steady climbing or descending flight. Similarly, source noise characteristics in turning flight could be approximated by simulating a heavier helicopter in straight and steady flight. However, the latter two approximations would require an extension of the current source noise database.

Furthermore, although the specifically noisy BVI conditions are not present in a departure procedure, it is still expected that significant reductions in the total noise impact can be achieved using the same methodology for departures. An extension of the database may also allow the optimization of departure procedures.

A further improvement to the source noise database could be found in the addition of noise sources other than the main rotor. Although the main rotor counts as the main source of noise on a helicopter, sources such as the tail rotor and engines would influence both the source noise levels and the directivity pattern.

Finally, the noise criteria currently available in the optimization suite all depend on the SEL. In addition, especially the awakenings dose-response relationship was originally developed only for fixed-wing aircraft. To extend the capabilities of *ECHO*, additional, helicopter-specific noise impact assessment criteria should be added, possibly related to different noise metrics as well.

Secondly, in all scenarios assessed in this study only one helicopter type was modeled. Although the general trends observed in this study – low altitude and high speed flight – will most likely be beneficial in terms of noise nuisance for all helicopter types – and in fact for aircraft in general, it can still be expected that using helicopters from different classes may result in different trajectories. Although the models used in *ECHO* are generic and could be adapted to a different helicopter type relatively easily, it would require both the flight dynamics parameters and an extensive source noise database to be acquired.

In addition, although the *ECHO* suite was developed solely for the optimization of conventional helicopter trajectories, the concept can be readily applied to novel helicopter designs or even fixed-wing aircraft. Tilt-rotors and compound helicopters would require a replacement of the flight dynamics model and the source noise model, which would allow to optimize trajectories in the same conditions and with the same optimization criteria as presented here for conventional helicopters.

Although the example scenarios provided in this study give a good initial overview of the capabilities of the optimization suite, more focus is required on the definition and imposition of constraints to be able to optimize more realistic helicopter procedures.

In addition, a simulator experiment or test flights should be considered to assess the feasibility of the resulting trajectories and to confirm the validity of the constraints imposed in *ECHO*. In the case of actual test flights this could also be an opportunity to validate the final results in terms of the noise exposure on the ground.

A
Source Noise Model

A.1 Microphone Locations

The *ECHO* suite contains an aeroacoustic-elastic source noise model consisting of hemispheres for 12 different flight conditions dependent on the True Airspeed (TAS) and flight path angle. The data are determined on microphones positioned on six parallels at 15° increments including the equatorial plane, and 24 meridians, also at 15° increments. Including a final microphone at the bottom of the hemisphere, the source noise in a total of 145 microphone positions is determined as can be seen in Fig. A.1.

A.2 Source Noise Levels

The source noise database contains a total of 12 hemispheres for three different airspeeds (V = [30,65,100] knots) and four different flight path angles (γ = [0°, -5°, -7.5°, -10°]) to cover the typical operational ranges of a helicopter in arrival and final approach flight conditions. Each of the 12 hemispheres contains the Sound Pressure Levels(SPLs) for twenty frequencies corresponding to the first twenty Blade Passage Frequencies (BPFs). To visualize the source noise levels and the directivity patterns typically observed for helicopters in different flight conditions, Fig. A.2 shows the *overall* SPL for all 12 flight conditions. It is noted, though, that the figure shows source noise levels aggregated for all available frequencies, and that hemispheres for individual frequencies might show significantly different directivity patterns and source noise levels.

From this figure a number of observations can be made related to the development of minimum noise trajectories. Firstly, it is readily clear that source noise corresponding to the lowest airspeed of 30 knots is significantly higher than the source noise for 65 and

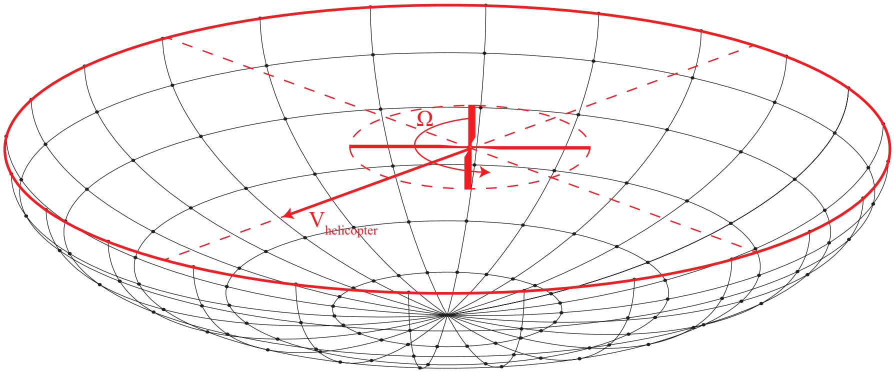

Figure A.1: Source noise model microphone locations

100 knots. In fact, all hemispheres related to 30 knots show source noise levels that are typically over 7 dB higher then source noise levels for higher airspeeds. Secondly, in low speed descending flight clearly the effect of Blade-Vortex Interaction (BVI) can be distinguished. In these conditions, where the effect of BVI is strongest, a clear increase in the SPLs behind the helicopter can be observed. Finally, at higher airspeeds also the effect of forward motion on the source noise can be seen. For both 65 and 100 knots, all hemispheres show higher source noise levels on the advancing (right) side of the helicopter. With decreasing flight path angles this effect is further exacerbated by the addition of an increasing BVI noise component.

From these hemispheres it can already be seen that the source noise levels can be significantly reduced by maintaining relatively high airspeeds, and by avoiding steep descent angles.

A.3 Directivity Patterns

To further assess the directivity patterns of helicopter noise, Figs. A.3 and A.4 show the overall SPL as a function of the azimuth angle λ for different elevation angles ϕ. In Fig. A.3, for high speed, level flight, at the equatorial plane ($\phi = 0°$) the High-Speed Impulsive (HSI) component of the source noise can be recognized in the direction of flight. At lower elevation angles, the highest source noise levels can be found on the right, advancing side of the helicopter, at approximately 90° with respect to the direction of flight. On the advancing side of the main rotor blade the source noise is typically around 4 dB higher than on the left, retreating side.

When Fig. A.4, corresponding to V = 30 knots and γ = -10°, is observed, it is readily clear that the source noise levels are significantly higher than those seen in the previous figure. In fact the average SPL for these conditions is over 10 dB higher than that observed in high speed level flight. In addition, due to the absence of a significant component of HSI noise, the lowest source noise levels are found at the equatorial plane. The figure also shows increasing source noise levels with decreasing elevation angle. This

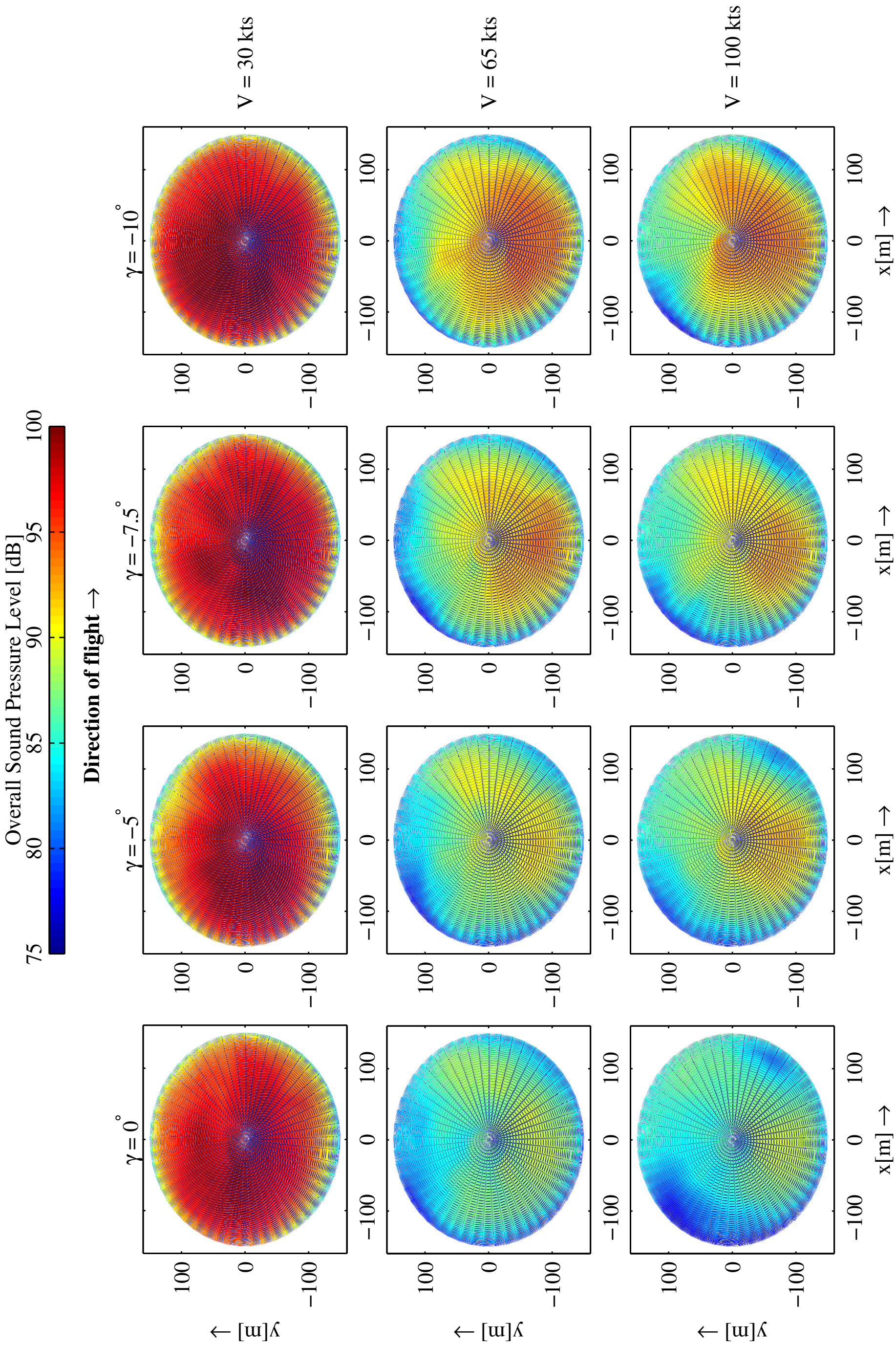

Figure A.2: Hemispherical database, Overall Sound Pressure Levels

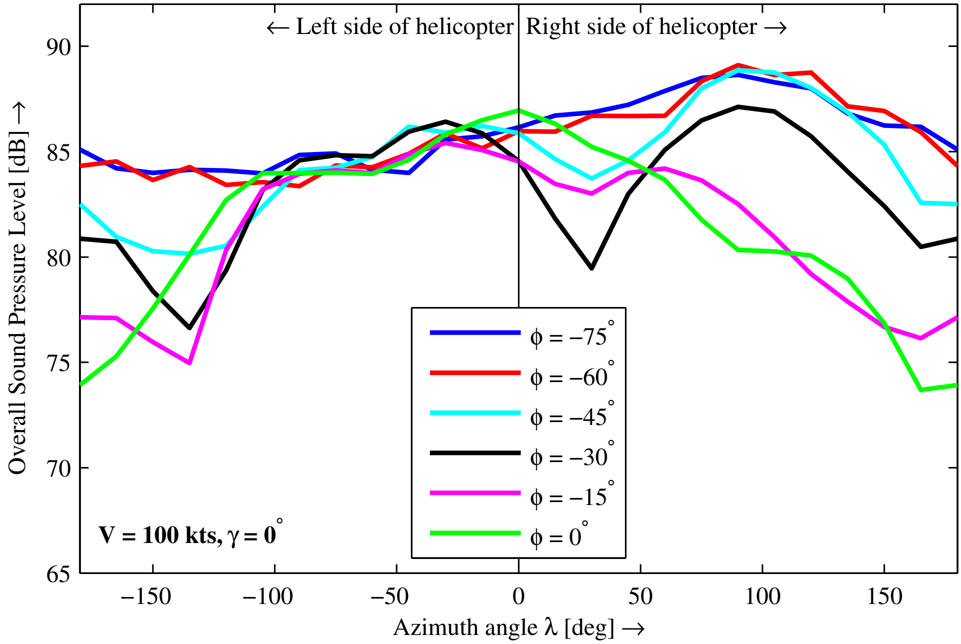

Figure A.3: Source noise directivity patterns, $V = 100$ kts, $\gamma = 0^\circ$

can be attributed partly to the downward direction of the loading and broadband noise components, and partly to the BVI component, mostly towards the rear of the helicopter.

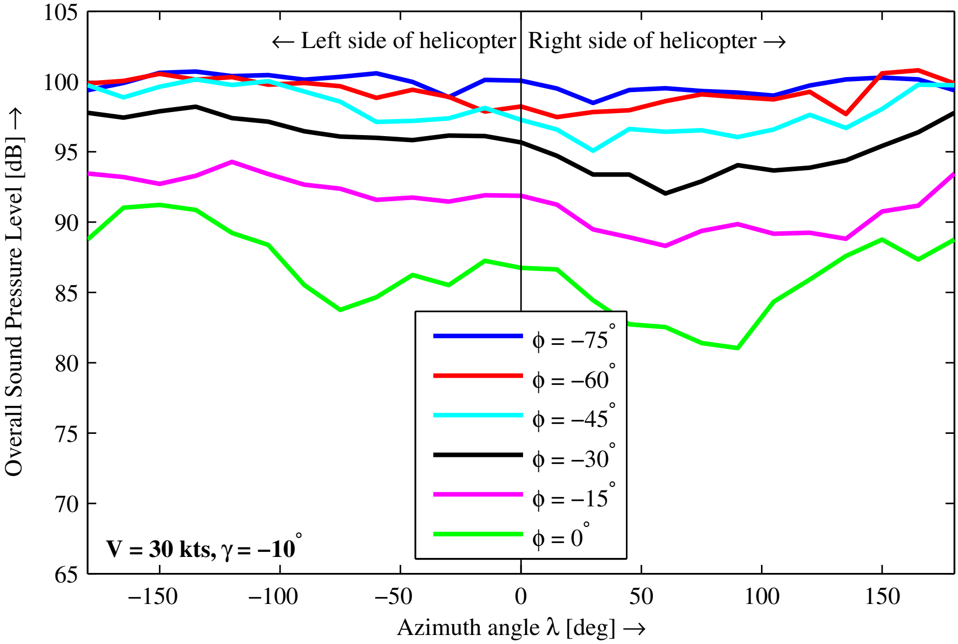

Figure A.4: Source noise directivity patterns, $V = 30$ kts, $\gamma = 0°$

B
Propagation Model Validation

B.1 Introduction

The propagation model discussed in detail in Section 5.3 has been validated against the work presented in [87]. For this purpose, the total propagation loss between a source at height z_s and an observer at $z_r = 1.2$ m has been determined as a function of distance x. The following sections show a selection of the validation study related to the comparison between the ray-tracing method described in [87] and the ray-tracing method employed in *ECHO*.

B.2 Case 1: International Standard Atmosphere

The first case presented shows the propagation loss in the International Standard Atmosphere (ISA) with a grass ground surface. The atmosphere is stationary, and hence refraction is only contributed to by the temperature gradient. The parameters required for the noise propagation model are presented in Table B.1 and the resulting speed of sound profile is visualized in Fig. B.1.

The results for all 20 Blade Passage Frequencies (BPFs) can be seen in Figs. B.2 to B.4 for source heights of 1,000, 500, and 100 meters, respectively. As can be seen from the figures the *ECHO* solutions form a close match to the ray-tracing approach. Near the source, at distances less than 5 km, the effects of ground reflection can clearly be distinguished in both methods where the sudden peaks in the propagation loss are caused by the cancellation of two rays arriving out of phase. Especially the close match in the location of these cancellations is a good indicator for the validity of the geometrical approach used in *ECHO*. In addition, Fig. B.2 also shows a good approximation of

Table B.1: Atmospheric parameters, Case 1

Parameter	Desciption	Value	
T_0	Temperature at 0 m height	288.15	K
λ	Temperature lapse rate	-0.0065	$K \cdot m^{-1}$
H	Relative humidity	70	%
η	Humidity lapse rate	0	m^{-1}
z_0	Roughness length	0.02	m
z_w	Height for wind speed definition	10	m
$V_w(z_w)$	Wind speed at z_w	0	$m \cdot s^{-1}$
σ	Effective flow resistivity	$250 \cdot 10^3$	$N \cdot s \cdot m^{-4}$

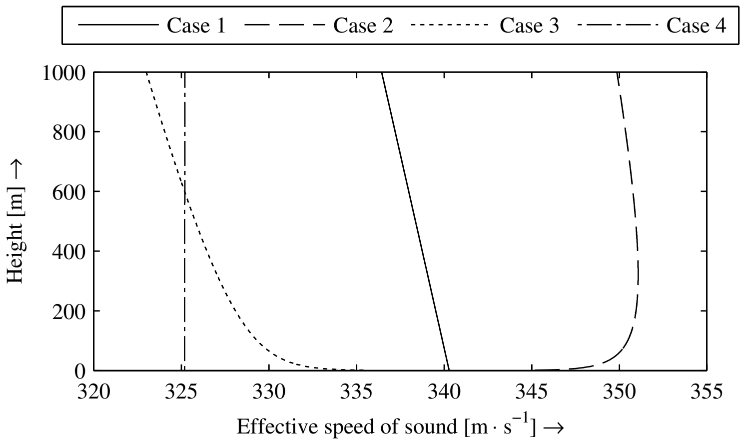

Figure B.1: Speed of sound profiles

the start of the shadow zone at 12 km. Overall it can be concluded that for the ISA the propagation model employed in *ECHO* is sufficiently accurate as compared to the ray-tracing method for the wind conditions considered in this study.

B.3 Case 2: ISA, 15 Knot Tailwind

Although the method to define the spreading loss (see Section 5.3.5) is theoretically only valid for stationary atmospheres, the effect of moderate winds is small and mostly only distinguishable at larger distances. Hence, *ECHO* has been used to generate results with winds up to 15 knots (≈ 7.7 m $\cdot$ s^{-1}) at 10 m above the ground surface. To validate the propagation model in wind conditions, first the same atmospheric conditions as in the previous sections have been assessed, but now with a logarithmic tailwind profile of 15 knots at a height of $z_w = 10$ m. The logarithmic tailwind profile results in a largely positive gradient of the speed of sound, and hence the absence of a shadow zone within the range considered. As in the previous section, a grass ground surface is assumed. The effective speed of sound profile can be found in Fig. B.1 and the parameters required for the noise propagation model are presented in Table B.2.

As can be seen from the comparison of the spreading losses for a source at 500 m in Fig. B.5 again the location of the ground interference and the long distance total propagation loss closely matches the ray-tracing method. Consequently, it can be concluded that for tail wind the propagation model used in *ECHO* is sufficiently accurate as well.

Table B.2: Atmospheric parameters, Case 2

Parameter	**Description**	**Value**	
T_0	Temperature at 0 m height	288.15	K
λ	Temperature lapse rate	-0.0065	$K \cdot m^{-1}$
H	Relative humidity	70	%
η	Humidity lapse rate	0	m^{-1}
z_0	Roughness length	0.02	m
z_w	Height for wind speed definition	10	m
$V_w(z_w)$	Wind speed at z_w	7.716	$m \cdot s^{-1}$
σ	Surface flow resistance	$250 \cdot 10^3$	$N \cdot s \cdot m^{-4}$

B.4 Case 3: ISA, 15 Knot Headwind

To also assess the effect of a headwind, the same atmosphere as above has been evaluated with a 15 knot headwind. Together with the temperature gradient the logarithmic tailwind profile results in a fully negative gradient of the speed of sound. As a result, the position of the shadow zone has moved closer to the source. The parameters for Case 3 can be found in Table B.3, the speed of sound profile is plotted in Fig. B.1 and the results can be found in Fig. B.6.

As with the previous two cases it can be concluded that the model employed in *ECHO* very closely matches the results of the ray-tracing routine.

Table B.3: Atmospheric parameters, Case 3

Parameter	**Description**	**Value**	
T_0	Temperature at 0 m height	288.15	K
λ	Temperature lapse rate	-0.0065	$K \cdot m^{-1}$
H	Relative humidity	70	%
η	Humidity lapse rate	0	m^{-1}
z_0	Roughness length	0.02	m
z_w	Height for wind speed definition	10	m
$V_w(z_w)$	Wind speed at z_w	-7.716	$m \cdot s^{-1}$
σ	Effective flow resistivity	$250 \cdot 10^3$	$N \cdot s \cdot m^{-4}$

B.5 Case 4: Cold atmosphere, soft ground surface

In the final validation case presented here mainly the effect of atmospheric attenuation and ground surface is assessed. For this purpose, a cold atmospheric scenario is defined with a slightly positive temperature lapse rate and no wind, as can be seen in Table B.4

Table B.4: Atmospheric parameters, Case 4

Parameter	**Description**	**Value**	
T_0	Temperature at 0 m height	263.15	K
λ	Temperature lapse rate	0.00001	$K \cdot m^{-1}$
H	Relative humidity	70	%
η	Humidity lapse rate	0	m^{-1}
z_0	Roughness length	0.02	m
z_w	Height for wind speed definition	10	m
$V_w(z_w)$	Wind speed at z_w	0	$m \cdot s^{-1}$
σ	Effective flow resistivity	$25 \cdot 10^3$	$N \cdot s \cdot m^{-4}$

Since the gradient of the speed of sound is always positive, no shadow zones exist as can be seen in Fig. B.7. The relatively soft ground surface dampens the effect of ground reflection and the low temperatures lead to a slightly higher absorption rate. This case again shows the validity of the propagation module in *ECHO* for the atmospheric conditions assessed in this study. For other atmospheric conditions used in the test cases presented in this study separate validation studies have been performed giving comparable results.

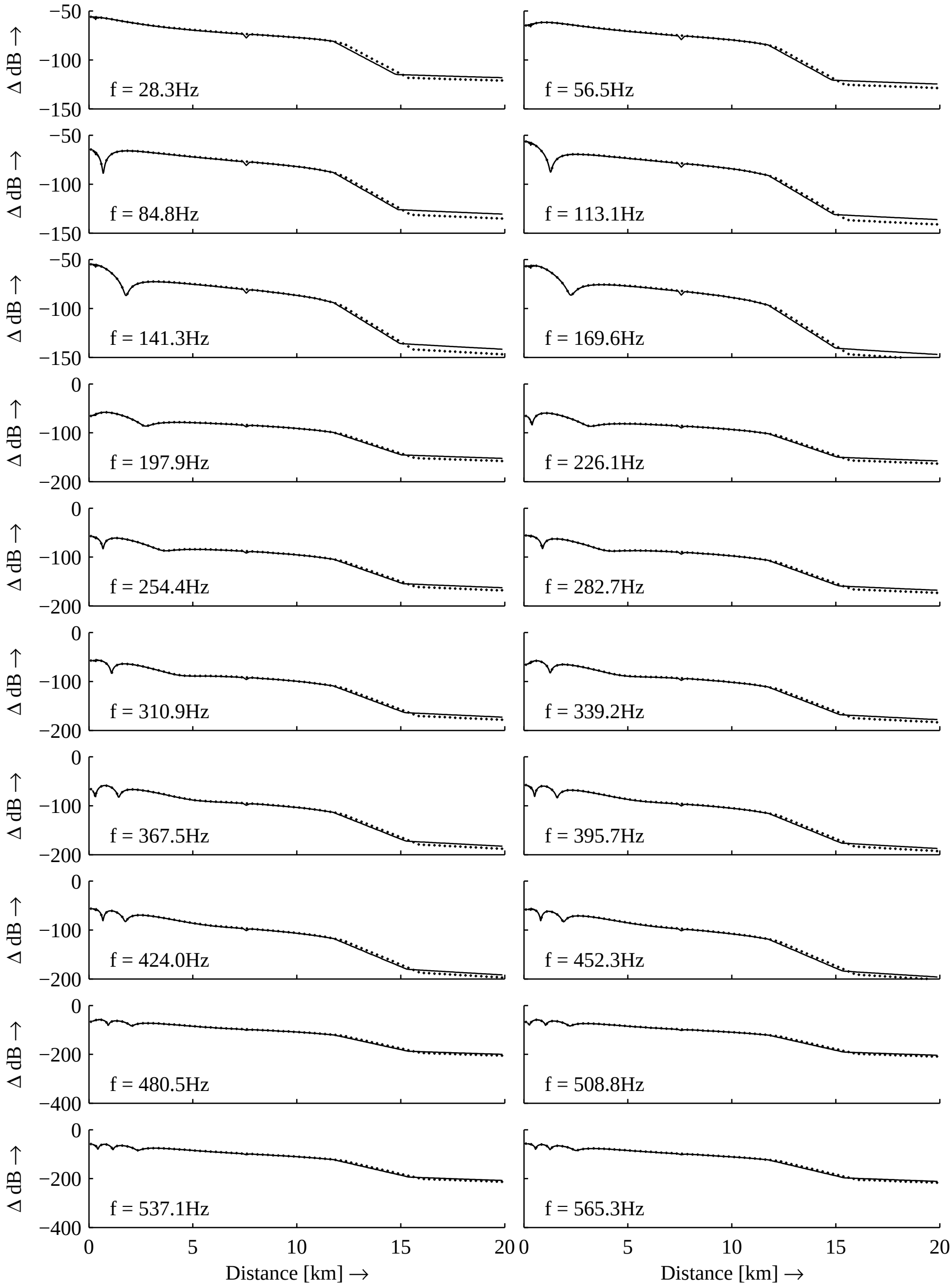

Figure B.2: Case 1, $z_s = 1{,}000$ m, Ray-tracing (solid), *ECHO* (dotted)

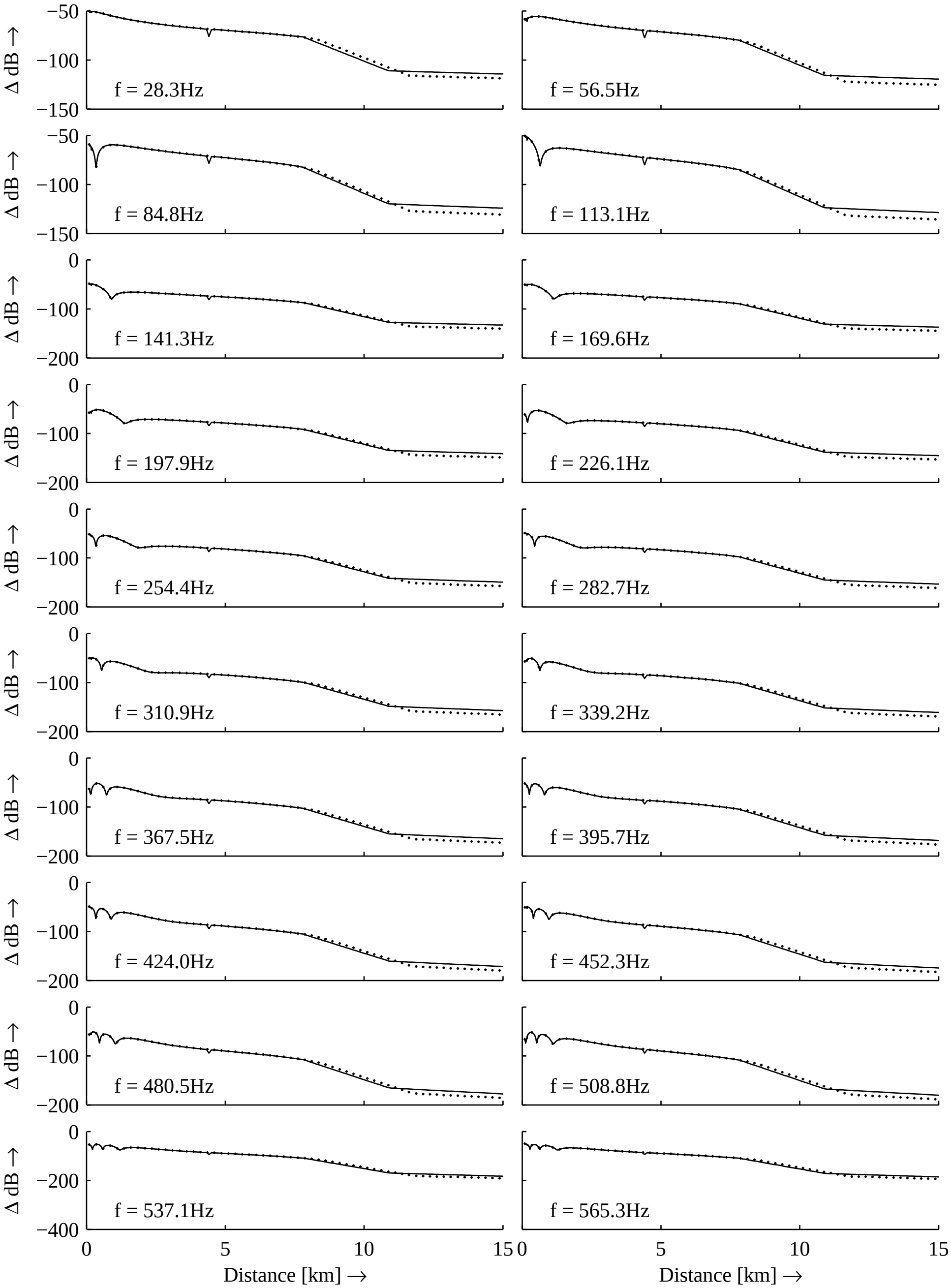

Figure B.3: Case 1, $z_s = 500$ m, Ray-tracing (solid), *ECHO* (dotted)

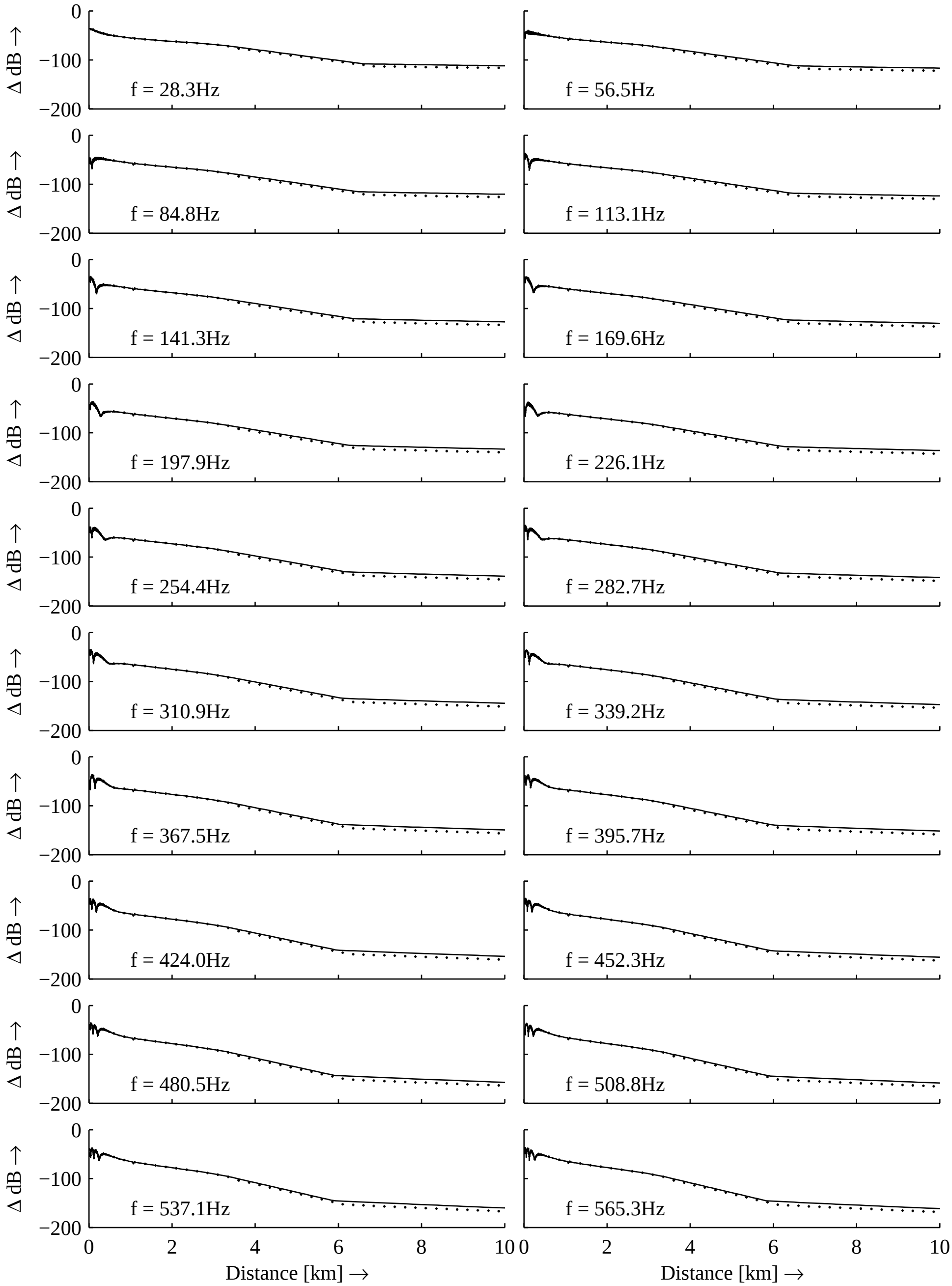

Figure B.4: Case 1, $z_s = 100$ m, Ray-tracing (solid), *ECHO* (dotted)

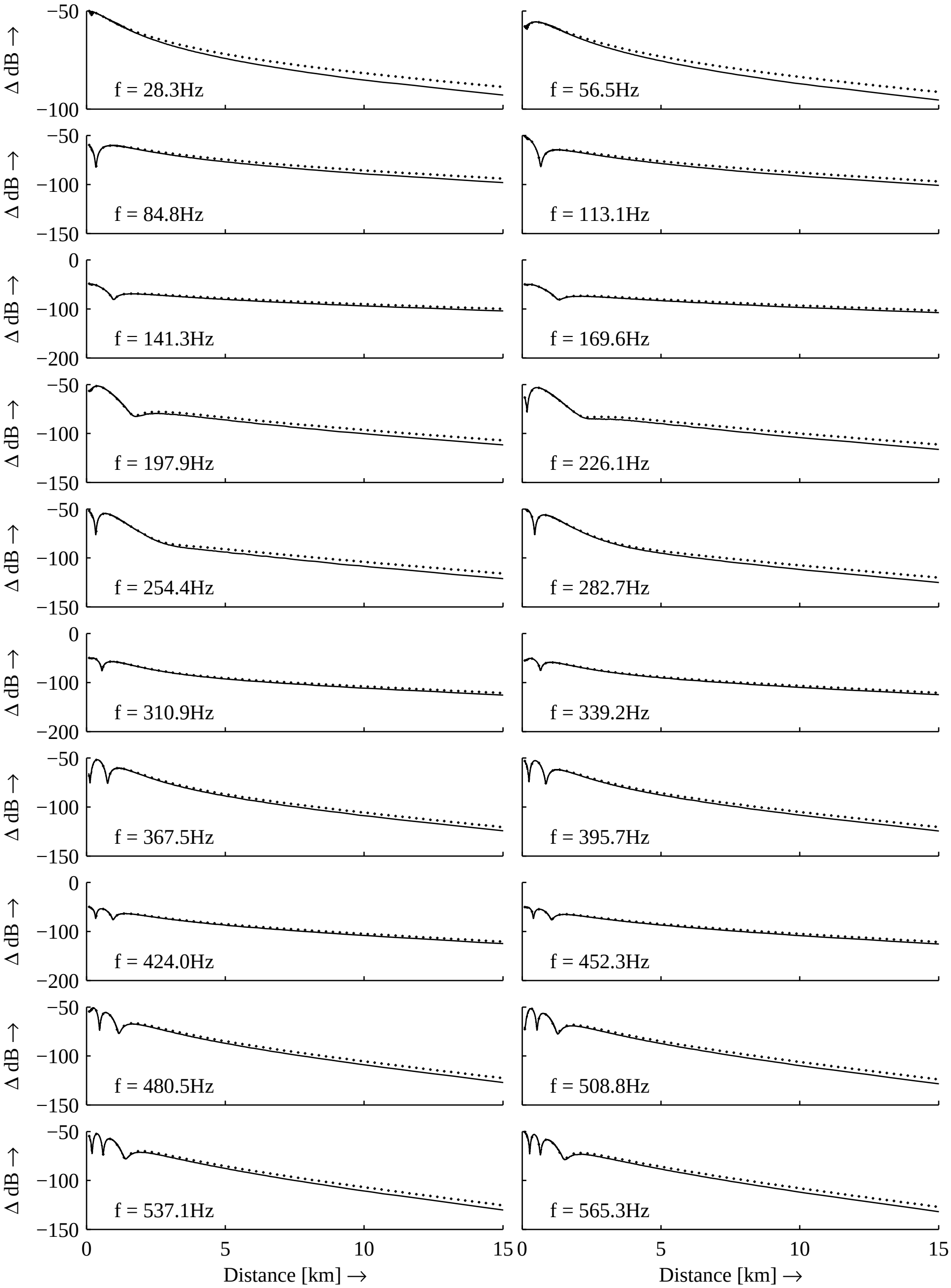

Figure B.5: Case 2, $z_s = 500$ m, Ray-tracing (solid), *ECHO* (dotted)

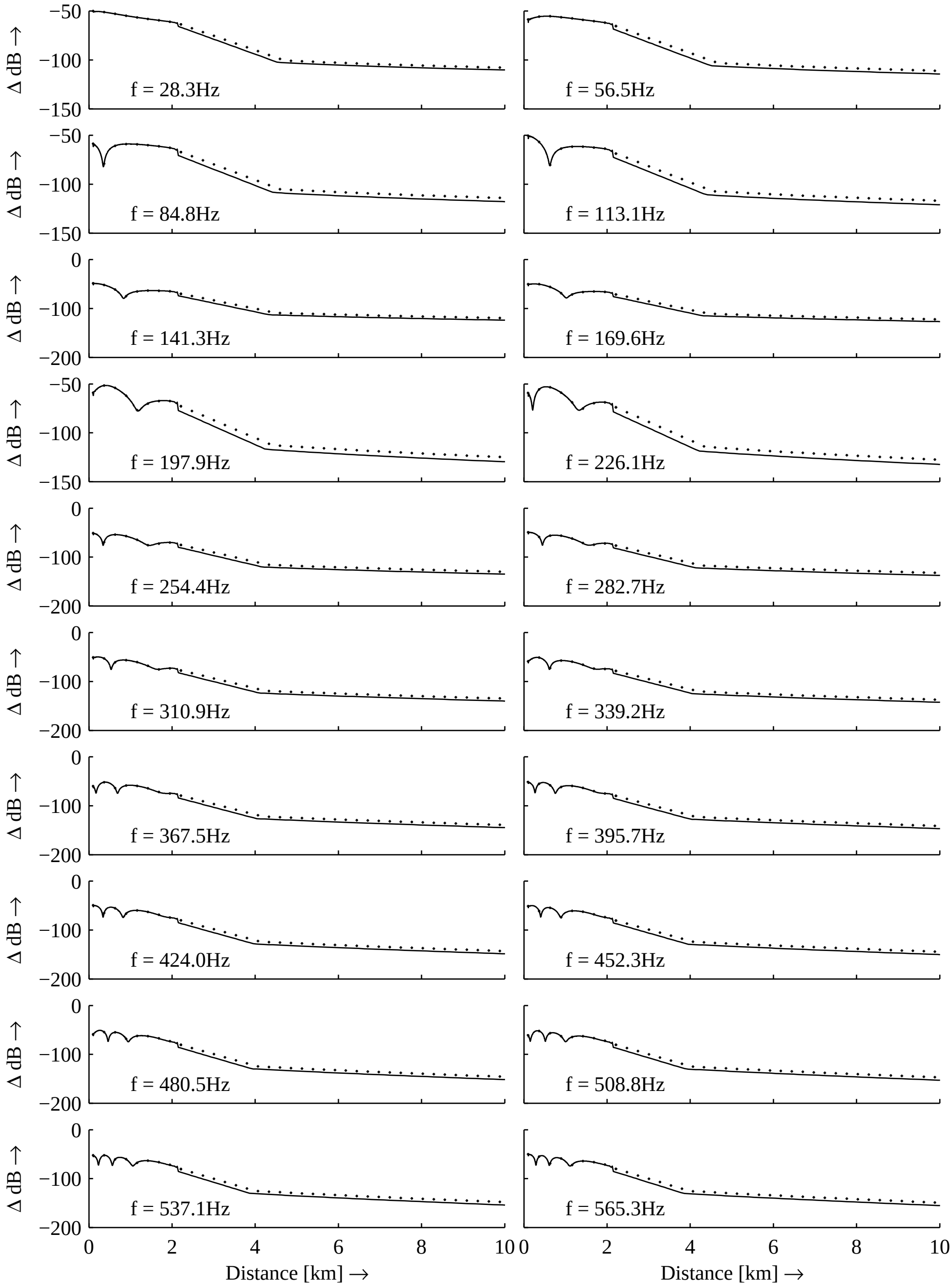

Figure B.6: Case 3, $z_s = 500$ m, Ray-tracing (solid), *ECHO* (dotted)

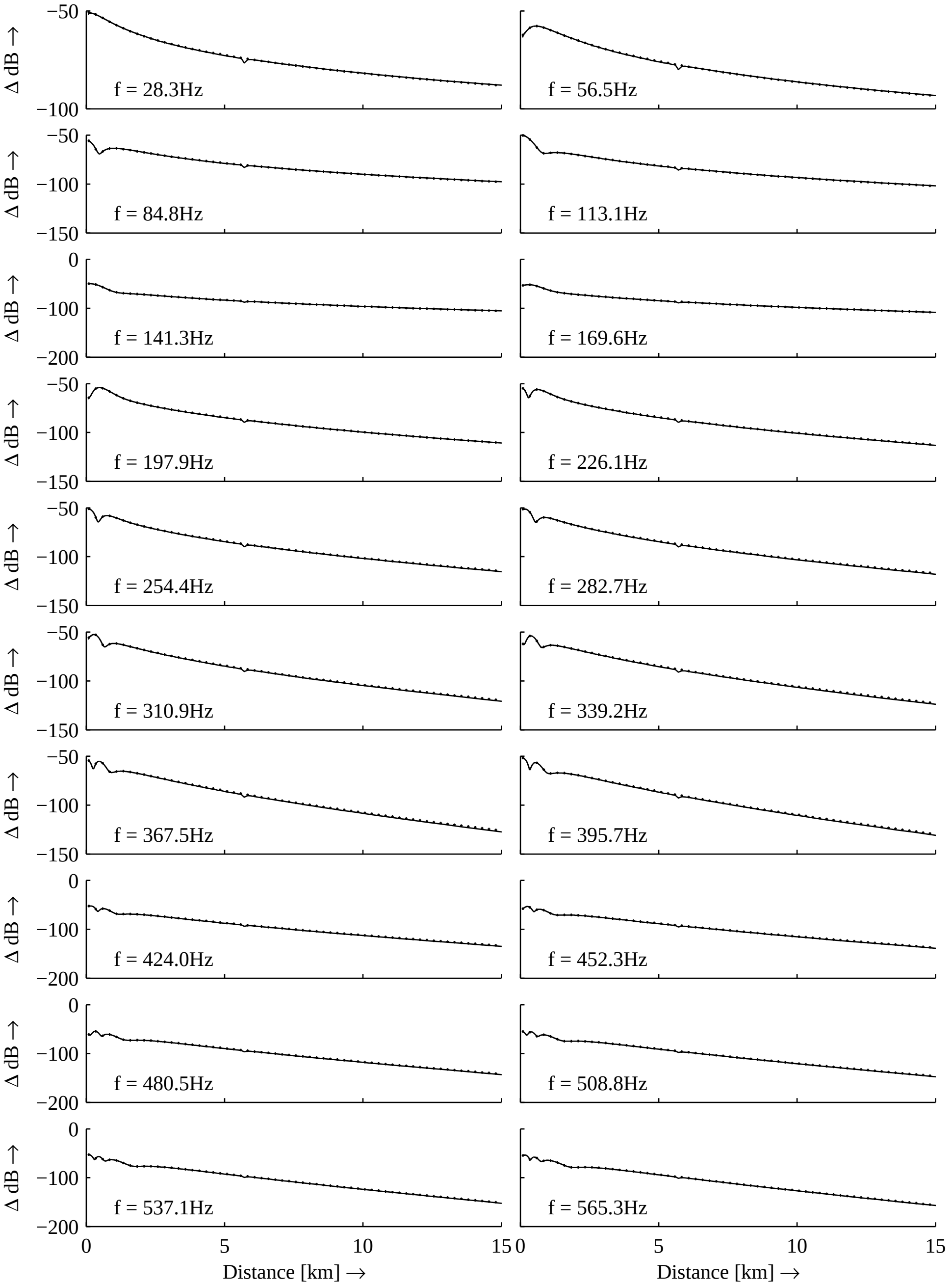

Figure B.7: Case 4, $z_s = 500$ m, Ray-tracing (solid), *ECHO* (dotted)

C
Scenario 1 Results

In total 24 trajectories have been optimized in Scenario 1. All results have been generated under ISA conditions, hereafter referred to as Atmosphere 1. The atmospheric properties as used for the flight dynamics and noise modeling in Scenario 1 are presented in Table C.1.

Table C.1: Atmospheric parameters, Scenario 1

Parameter	**Desciption**	**Value**	
T_0	Temperature at 0 m height	288.15	K
λ	Temperature lapse rate	-0.0065	$\mathrm{K} \cdot \mathrm{m}^{-1}$
H	Relative humidity	70	%
η	Humidity lapse rate	0	m^{-1}
z_0	Roughness length	0.02	m
z_w	Height for wind speed definition	10	m
$V_w(z_w)$	Wind speed at z_w	0	m kts
σ	Effective flow resistivity	$250 \cdot 10^3$	$\mathrm{N} \cdot \mathrm{s} \cdot \mathrm{m}^{-4}$

Table C.2 contains the results of all trajectories optimized in Scenario 1. The table contains the total flight time t_f, fuel burn m_f, $\mathrm{NO_x}$ emissions m_{NO_x} and the area above 65 dBA SEL $A_{>SEL_{65}}$ which were the optimization parameters in Scenario 1. In addition, the table shows the total objective value J, relative contribution of the damping penalty J_u, the problem runtime t_{run} and the set of atmospheric conditions A. Finally, when applicable the optimized glideslope angle is stated.

Table C.2: Scenario 1 results

Solution	Objective	J	t_f [s]	m_f [kg]	m_{NO_x} [g]	$A_{>SEL_{65}}$ [km^2]	$\frac{J_u}{J}$ [%]	t_{run} [s]	A	γ_{GS} [°]
C01_01	t_f	304.7	304.2	13.56	47.18	39.67	0.15	32	1	n/a
C01_02	m_f	13.24	307.1	13.09	46.38	46.03	1.14	20	1	n/a
C01_03	m_{NO_x}	46.58	311.1	13.36	46.37	44.65	0.44	18	1	n/a
C01_04	$m_f + 1.25 \cdot 10^{-7} A_{>SEL_{65}}$	17.23	305.0	13.26	47.18	30.10	1.21	8752	1	n/a
C01_05	$m_f + 2.5 \cdot 10^{-7} A_{>SEL_{65}}$	21.04	306.0	13.29	47.20	29.92	1.27	1993	1	n/a
C01_06	$m_f + 5 \cdot 10^{-7} A_{>SEL_{65}}$	28.40	311.9	13.46	47.23	29.12	1.36	4896	1	n/a
C01_07	$m_f + 10^{-6} A_{>SEL_{65}}$	43.06	317.4	13.62	47.32	28.87	1.31	5625	1	n/a
C02_01	t_f	306.1	304.5	13.50	46.88	41.06	0.51	20	1	3.00
C02_02	m_f	13.45	308.5	13.14	46.73	46.10	2.30	31	1	8.99
C02_03	m_f	13.57	304.6	13.49	46.82	41.07	0.58	24	1	3.00
C02_04	m_f	13.81	323.9	13.55	47.80	48.89	1.84	29	1	10.0
C02_05	m_{NO_x}	47.00	311.0	13.60	46.71	42.30	0.62	26	1	3.59
C02_06	$m_f + 2.5 \cdot 10^{-7} A_{>SEL_{65}}$	25.05	307.2	13.21	46.71	45.42	1.92	2821	1	8.03
C02_07	$m_f + 5 \cdot 10^{-7} A_{>SEL_{65}}$	36.58	310.3	13.30	46.72	45.23	1.82	4611	1	7.98
C02_08	$m_f + 10^{-6} A_{>SEL_{65}}$	54.41	317.5	13.85	46.95	40.32	0.46	8767	1	3.00
C03_01	t_f	306.1	304.5	13.54	47.04	39.87	0.55	21	1	3.00
C03_02	m_f	13.42	306.0	13.18	46.75	45.77	1.74	47	1	8.36
C03_03	m_f	13.51	304.9	13.34	46.70	42,11	1.30	34	1	3.00
C03_04	m_f	13.52	310.0	13.24	47.06	47.13	2.09	25	1	10.0
C03_05	m_{NO_x}	46.66	310.4	13.43	46.48	42.54	0.38	55	1	3.31
C03_06	$m_f + 1.25 \cdot 10^{-7} A_{>SEL_{65}}$	18.85	305.8	13.40	47.12	40.97	1.75	3567	1	7.99
C03_07	$m_f + 2.5 \cdot 10^{-7} A_{>SEL_{65}}$	24.04	307.3	13.44	47.16	40.72	1.74	1641	1	8.10
C03_08	$m_f + 5 \cdot 10^{-7} A_{>SEL_{65}}$	33.24	310.2	13.46	47.15	38.06	2.27	3990	1	5.54
C03_09	$m_f + 10^{-6} A_{>SEL_{65}}$	52.52	317.0	13.64	47.21	37.82	2.02	6861	1	5.53

D
Scenario 2 Results

In total 54 trajectories have been optimized in Scenario 2 for a total of 14 different atmospheric and ground surface conditions, which are presented in Tables D.1.

Table D.2 contains the results of all trajectories optimized in Scenario 2. The table contains the total flight time t_f, fuel burn m_f, $\mathrm{NO_x}$ emissions m_{NO_x} and the number of awakenings N_A which were the optimization criteria in this scenario. Furthermore, the number of people enclosed in the 65 dBA contour, $kP_{>SEL_{65}}$, and the corresponding contour area, $A_{>SEL_{65}}$, are presented. Finally, the table shows the total objective value J, contribution of the damping penalty J_u, the problem runtime t_{run} and the set of atmospheric conditions A.

Table D.1: Atmospheric parameters, Scenario 2

Parameter		**Atmosphere 1**	**Atmosphere 2**	**Atmosphere 3**	**Atmosphere 4**	**Atmosphere 5**	**Atmosphere 6**	**Atmosphere 7**
T_0	[K]	288.15	288.15	288.15	288.15	288.15	288.15	288.15
λ	[K·m^{-1}]	-0.0065	-0.0065	-0.0065	-0.0065	-0.0065	-0.0065	-0.0065
H	[%]	70	70	70	70	70	70	70
η	[m^{-1}]	0	0	0	0	0	0	0
z_0	[m]	0.02	0.02	0.02	0.02	0.02	0.02	0.02
z_w	[m]	10	10	10	10	10	10	10
$V_w(z_w)$	[kts]	0	5	10	15	5	10	15
χ_w	[°]	n/a	90	90	90	270	270	270
σ	[N·s·m^{-4}]	250·10^3	250·10^3	250·10^3	250·10^3	250·10^3	250·10^3	250·10^3

Parameter		**Atmosphere 8**	**Atmosphere 9**	**Atmosphere 10**	**Atmosphere 11**	**Atmosphere 12**	**Atmosphere 13**	**Atmosphere 14**
T_0	[K]	288.15	288.15	288.15	263.15	263.15	263.15	288.15
λ	[K·m^{-1}]	-0.0065	-0.0065	-0.0065	0.001	0.001	0.001	-0.0065
H	[%]	70	70	70	70	70	70	70
η	[m^{-1}]	0	0	0	0	0	0	0
z_0	[m]	0.02	0.02	0.02	0.02	0.02	0.02	0.02
z_w	[m]	10	10	10	10	10	10	10
$V_w(z_w)$	[kts]	5	10	15	0	0	0	0
χ_w	[°]	0	0	0	n/a	n/a	n/a	n/a
σ	[N·s·m^{-4}]	250·10^3	250·10^3	250·10^3	250·10^2	250·10^3	250·10^{3}0	250·10^{3}0

Table D.2: Scenario 2 results

Solution	**Objective**	**J**	$\mathbf{t_f}$ **[s]**	$\mathbf{m_f}$ **[kg]**	$\mathbf{m_{NO_x}}$ **[g]**	$\mathbf{N_A}$	$\mathbf{kP_{>SEL_{65}}}$	$\mathbf{A_{>SEL_{65}}}$ $\mathbf{[km^2]}$	$\mathbf{\frac{J_u}{J}}$ **[%]**	$\mathbf{t_{run}}$ **[s]**	**A**
C01_01	t_f	369.2	367.3	15.83	53.11	3479	138.5	71.77	0.50	22	1
C01_02	$t_f + 0.02N_A$	420.9	372.8	16.14	54.45	2284	82.60	66.68	0.59	2963	1
C01_03	$t_f + 0.04N_A$	465.5	376.3	16.32	55.17	2156	78.32	65.97	0.63	2369	1
C01_04	$t_f + 0.1N_A$	582.1	389.9	16.99	57.81	1882	73.59	69.72	0.69	2495	1
C01_05	$t_f + 0.2N_A$	766.6	396.9	17.31	59.06	1822	69.93	68.48	0.69	2262	1
C01_06	t_f	400.4	398.5	17.38	59.16	3460	131.8	71.70	0.47	22	2
C01_07	$t_f + 0.02N_A$	451.3	402.5	17.56	60.04	2300	83.01	68.57	0.62	2740	2
C01_08	$t_f + 0.04N_A$	495.7	405.1	17.69	60.55	2181	78.39	68.28	0.67	2565	2
C01_09	$t_f + 0.1N_A$	611.0	420.8	18.46	63.58	1859	71.79	70.81	0.70	3292	2
C01_10	$t_f + 0.2N_A$	794.0	428.3	18.82	64.95	1799	68.32	69.71	0.76	2770	2
C01_11	t_f	437.2	434.8	19.05	66.02	3570	124.7	71.11	0.55	43	3
C01_12	$t_f + 0.02N_A$	488.6	438.8	19.29	66.82	2345	82.89	69.54	0.60	3175	3
C01_13	$t_f + 0.04N_A$	533.4	441.6	19.42	67.35	2211	79.00	69.56	0.65	4402	3
C01_14	$t_f + 0.1N_A$	662.8	445.8	19.64	68.16	2121	77.17	69.92	0.74	7775	3
C01_15	$t_f + 0.2N_A$	874.8	449.0	19.78	68.68	2095	76.56	70.88	0.80	4648	3
C01_16	t_f	481.0	478.2	21.09	74.16	3685	125.1	70.22	0.57	63	4
C01_17	$t_f + 0.02N_A$	533.4	481.9	21.21	74.84	2397	82.49	67.67	0.74	5089	4
C01_18	$t_f + 0.04N_A$	581.0	483.2	21.26	75.08	2337	81.48	67.81	0.75	2856	4
C01_19	$t_f + 0.1N_A$	707.3	501.2	22.30	78.53	2024	75.78	73.48	0.53	8281	4
C01_20	$t_f + 0.2N_A$	905.6	510.0	22.73	80.19	1948	71.96	72.75	0.66	8553	4
C02_01	t_f	512.9	509.7	22.31	77.75	8074	321.2	93.11	0.62	53	1
C02_02	$t_f + 0.02N_A$	618.4	521.1	22.97	80.72	4597	176.4	82.85	0.87	5103	1
C02_03	$t_f + 0.04N_A$	708.6	525.4	23.18	81.52	4433	171.7	83.98	0.82	4457	1
C02_04	$t_f + 0.1N_A$	968.7	535.5	23.64	83.21	4235	168.3	85.53	1.00	6891	1
C02_05	$t_f + 0.2N_A$	1390	547.1	24.14	84.87	4146	165.1	85.48	1.01	6449	1
C02_06	t_f	472.9	469.7	20.32	70.15	8063	340.2	97.22	0.68	86	5
C02_07	$t_f + 0.02N_A$	572.1	483.0	21.15	73.52	4170	169.7	83.24	1.00	5087	5

Table D.3: Scenario 2 results (continued)

Solution	**Objective**	**J**	$\mathbf{t_f}$ **[s]**	$\mathbf{m_f}$ **[kg]**	$\mathbf{m_{NO_x}}$ **[g]**	$\mathbf{N_A}$	$\mathbf{P_{>SEL_{65}}}$	$\mathbf{A_{>SEL_{65}}}$ **[km^2]**	$\mathbf{J_u}$ **[%]**	$\mathbf{t_{run}}$ **[s]**	**A**
C02_08	$t_f + 0.04N_A$	652.1	490.1	21.49	74.88	3868	162.0	83.61	1.13	4460	5
C02_09	$t_f + 0.1N_A$	869.5	509.4	22.35	77.71	3485	151.2	84.75	1.34	3722	5
C02_10	$t_f + 0.2N_A$	1219	520.3	22.79	78.91	3405	148.4	84.55	1.43	4581	5
C02_11	t_f	438.2	435.2	18.65	63.78	7634	327.9	96.89	0.69	53	6
C02_12	$t_f + 0.02N_A$	533.2	447.6	19.45	66.98	3994	165.4	83.06	1.08	5067	6
C02_13	$t_f + 0.04N_A$	608.0	454.6	19.77	68.17	3666	152.4	81.98	1.10	6000	6
C02_14	$t_f + 0.1N_A$	817.9	469.5	20.46	70.61	3365	144.9	84.28	1.45	7539	6
C02_15	$t_f + 0.2N_A$	1156	478.3	20.84	71.82	3287	142.4	84.32	1.73	4783	6
C02_16	t_f	408.3	405.4	17.22	58.35	7138	308.7	95.45	0.71	50	7
C02_17	$t_f + 0.02N_A$	499.7	418.1	18.04	61.27	3826	155.2	81.34	1.02	6724	7
C02_18	$t_f + 0.04N_A$	573.3	422.4	18.24	62.07	3606	147.5	80.85	1.16	4601	7
C02_19	$t_f + 0.1N_A$	783.7	426.7	18.32	62.65	3447	144.9	80.17	1.56	6463	7
C02_20	$t_f + 0.2N_A$	1115	443.0	19.03	64.97	3264	140.9	80.83	1.70	5406	7
C03_01	t_f	367.9	366.1	15.77	52.88	3214	136.7	73.66	0.48	16	8
C03_02	$t_f + 0.1N_A$	550.0	389.0	16.95	57.66	1569	70.67	71.78	0.73	2875	8
C03_03	t_f	369.3	367.6	15.85	53.18	3204	139.3	75.15	0.46	26	9
C03_04	$t_f + 0.1N_A$	527.8	389.9	16.99	57.91	1322	63.89	71.51	1.07	4950	9
C03_05	t_f	373.5	371.9	16.08	54.04	3235	140.3	75.67	0.44	22	10
C03_06	$t_f + 0.1N_A$	530.7	393.1	17.15	58.55	1333	61.06	72.13	0.80	7420	10
C04_01	t_f	369.1	367.2	15.77	52.57	3152	135.6	71.88	0.50	21	11
C04_02	$t_f + 0.1N_A$	579.2	383.0	16.59	56.03	1922	85.66	69.99	0.70	4549	11
C04_03	t_f	369.2	367.3	15.77	52.57	3305	146.8	80.93	0.51	83	12
C04_04	$t_f + 0.1N_A$	583.7	394.6	17.17	58.09	1851	86.63	79.92	0.68	3396	12
C04_05	t_f	369.2	367.3	15.77	52.57	5080	213.6	96.97	0.51	70	13
C04_06	$t_f + 0.1N_A$	759.9	393.3	17.03	57.39	3626	146.5	97.05	0.53	4099	13
C04_07	t_f	369.2	367.3	15.83	53.11	5806	226.4	92.54	0.50	42	14
C04_08	$t_f + 0.1N_A$	822.9	393.1	17.08	57.91	4254	152.4	92.76	0.53	7618	14

E
Scenario 3 Results

In total 11 trajectories have been optimized in Scenario 3, all under ISA conditions, for which the parameters were already stated in Table C.1.

Table E.1 contains the results of all trajectories optimized in Scenario 3. The table contains the total flight time t_f, fuel burn m_f, NO_x emissions m_{NO_x}, followed by the three noise optimization criteria considered in this study. In addition, the table shows the total objective value J, the relative contribution of the damping penalty J_u, the problem runtime t_{run} and the set of atmospheric conditions A. Finally, when applicable the optimized glideslope angle is stated.

Table E.1: Scenario 3 results

Solution	**Objective**	**J**	$\mathbf{t_f}$ **[s]**	$\mathbf{m_f}$ **[kg]**	$\mathbf{m_{NO_x}}$ **[g]**	$\mathbf{N_A}$	$\mathbf{kP_{>SEL_{65}}}$	$\mathbf{A_{>SEL_{65}}}$ **[km^2]**	$\mathbf{\frac{J_u}{J}}$ **[%]**	$\mathbf{t_{run}}$ **[s]**	**A**
C01_01	t_f	597.6	579.5	25.45	87.72	2689	116.3	90.55	3.03	62	1
C01_02	$t_f + 0.04N_A$	704.0	580.4	25.48	87.95	2555	108.6	86.43	3.04	7716	1
C01_03	$t_f + 0.1N_A$	845.6	581.3	25.22	88.04	2342	99.93	82.08	3.57	10110	1
C01_04	$t_f + 0.2N_A$	1078	595.8	25.81	90.33	2261	98.00	80.07	2.80	20616	1
C01_05	$t_f + 0.5N_A$	1724	610.6	26.28	90.94	2133	88.58	80.05	2.71	20388	1
C01_06	$t_f + N_A$	2813	622.5	26.64	91.33	2113	87.36	79.30	2.74	13650	1
C02_01	$t_f + \frac{1}{1000}P_{>SEL_{65}}$	709.9	581.6	25.51	88.23	2525	105.7	85.23	3.18	5968	1
C02_02	$t_f + \frac{1}{500}P_{>SEL_{65}}$	816.7	582.2	25.53	88.34	2520	105.0	85.19	3.00	6887	1
C02_03	$t_f + \frac{1}{200}P_{>SEL_{65}}$	1093	614.3	26.72	93.89	2198	89.94	82.28	2.66	16560	1
C02_04	$t_f + \frac{1}{80}P_{>SEL_{65}}$	1786	619.3	26.87	94.10	2181	89.33	81.81	2.81	4201	1
C02_05	$t_f + \frac{1}{80}P_{>SEL_{65}}$	1752	617.3	26.50	91.38	2138	86.97	79.27	2.72	14150	1

Acknowledgments

Here before you lies the result of five years of development of a new software suite designed for the environmental optimization of helicopter trajectories. Looking back at these five years, I have come to realize that working on a Ph.D.-degree is much more than just five years of research. I look back at five years in which next to research I was involved in education, supervision of Master theses and most importantly the Green Rotorcraft and Systems for Green Operations projects, both part of the European Clean Sky research project. The self development, social contacts, experience and most importantly working pleasure I have experienced in these projects were more than worth their share of the time. These five years have made me a richer person, made me broaden my views, and have finally brought me to finishing my thesis.

This work would not have been possible without the help of some special people. First and foremost I would like to thank dr. ir. Dries Visser. During all these years Dries has been my direct supervisor, and as such my technical tower of strength, critic and counselor, and all that while remaining a very pleasant colleague to work with. Dries was always there to help me with his collection of old books, and to debate my ideas as a true sparring partner. Thanks also go out to dr. ir. Marilena Pavel, who has supported me in the field of helicopter modeling, and who has proven an indispensable source of information in a field I had yet to conquer. I would also like to thank Professor Massimo Gennaretti of Roma Tre University for so kindly providing me with the source noise database, without which the work couldn't have been where it is now. Thanks also go out to dr. ir. Michael Arntzen for his essential contribution to the development of the noise propagation model. Finally, I would like to thank Professor Ricky Curran who also supervised my work in the second phase of my research, and more importantly has given me the trust to offer me the chance to pursue an academic career in Delft.

In addition I would like to thank my friends and family. My girlfriend, Marie-Christine, for supporting me in the final phases of the thesis work and the start of my new job as an assistant professor; my parents, Rien and Jeanette, who have supported me in the choice to pursue my Ph.D. degree, and kept on supporting me until this very day; my brothers Ton and Joep, and Jenny, my sister-in-law. Special thanks also go out to Arnout, my friend who was always there when I needed him, when he needed me, and first and foremost when we needed a drink.

Finally, I would like to say thanks to all my colleagues who have made the days during these five years enjoyable and interesting. Mark, Hans, and all the other colleagues from the SEAD department where I started. Thanks also to Frank, Paul, Wim, Xiaojia, Wouter, Bruno, Alexei, Vera, Geeta, and all others from the ATO department who

cheered up my lunch, our weekly coffee break, and the numerous social events. And, finally, thanks to all my colleagues in both European projects I worked in, who are too many to mention.

The research presented in this thesis has received funding from the European Union's Seventh Framework Programme (FP7/20072013) for the Clean Sky Joint Technology Initiative under grant agreement no. CJSU-GAM-GRC2008001.

Sander Hartjes
14 November, 2014

About the author

Sander Hartjes was born in Geldrop, The Netherlands on 14 January 1979. He attended high school at the Sint Willibrord Gymnasium in Deurne, graduating in 1997. In that same year he moved to Delft to study Aerospace Engineering at Delft University of Technology, where he obtained his Bachelor of Science degree in 2006. Sander then joined the former department of Design of Aircraft and Rotorcraft (DAR) where he obtained his Master of Science degree in 2008 on a thesis called *"Optimization of RNAV noise and emission abatement departure procedure"* under the supervision of dr. ir. Dries Visser.

After his graduation, Sander got the opportunity to pursue a Ph.D. degree at Delft University of Technology under the supervision of dr. ir. Dries Visser and initially prof. dr. ir. Michel van Tooren, later replaced by prof. dr. Richard Curran. Besides his Ph.D. research, Sander was involved as a researcher in two European research projects on behalf of his university, both part of the European Clean Sky Joint Technology Initiative (JTI). In the Systems for Green Operations (SGO) ITD, Sander contributed to the development of a framework focused on the optimization of fixed-wing environmentally friendly trajectories. His main contributions were in the fields of aircraft noise abatement trajectories and aircraft noise impact assessment. In the Green Rotorcraft (GRC) ITD Sander developed the helicopter optimization framework that would serve as his Ph.D. research. During his employment as a Ph.D. researcher, Sander supported multiple courses and projects, and (co-)supervised a number of M.Sc. students.

Publications

Hartjes, S., Dons, J., Visser, H.G. (2014), “Optimization of Area Navigation Arrival Routes for Cumulative Noise Exposure”, *Journal of Aircraft*, **51**(5), pp. 1432-1438

Visser, H.G., Hartjes, S. (2013), “Economic and Environmental Optimization of Flight Trajectories Connecting a City-Pair”, *Proceedings of the Institution of Mechanical Engineers, Part G: Journal of Aerospace Engineering*, **228**(6), pp. 980-993

Hartjes, S., Visser, H.G., Hebly, S.J. (2010), “Optimisation of RNAV Noise and Emission Abatement Standard Instrument Departures”, *Aeronautical Journal*, **114**(1162), pp. 757-767

Hartjes, S., Visser, H.G., Pavel, M.D. (2014), “Helicopter Noise Abatement Arrival Trajectories”, *Conference Proceedings*, 70th American Helicopter Society Annual Forum, Montreal, Canada

Hartjes, S., Dons, J., Visser, H.G. (2013), “Terminal Route Optimization for Cumulative Noise Exposure”, *Conference Proceedings*, CEAS 2013, Linkping, Sweden

Sabbatini, D., Janssens, K., Hartjes, S., Visser, H.G., Gennaretti, M., Bernardini, G. (2013), “Sound Synthesis Approach for Noise Annoyance Assessment of Rotorcraft Operations”, *Conference Proceedings*, Noise-Con 2013, Denver, Colorado, USA

Hartjes, S., Buys, Y., Visser, H.G., Pavel, M.D., Gennaretti, M., Bernardini, G., Arntzen, M. (2012), “Optimization of Rotorcraft Noise Abatement Trajectories”, *Conference Proceedings*, Internoise 2012 Conference, New York City, New York, USA

Visser, H.G., Hartjes, S. (2012), “Economic and Environmental Optimization of Flight Trajectories Connecting a City-Pair“, *Conference Proceedings*, 2012 ATRS World Conference, Tainan, Taiwan

Braakenburg, M.L., Hartjes, S., Visser, H.G., Hebly, S.J. (2011), “Development of a Multi-Event Trajectory Optimization Tool for Noise-Optimized Approach Route Design”, *Conference Proceedings*, AIAAs 11th Annual Aviation Technology, Integration and Operations (ATIO) Technical Forum, Virginia Beach, Virginia, USA

Hartjes, S., Visser, H.G., Pavel, M.D. (2011), "Environmental Optimization of Rotorcraft Approach Trajectories", *Conference Proceedings*, 37th European Rotorcraft Forum (ERF), Gallarate, Italy

Braakenburg, M.L., Hartjes, S., Visser, H.G., Hebly, S.J. (2011), "Multi-Event Trajectory Optimization Methodology for the Design of Community Noise Optimized RNAV Approach Routes", *Conference Proceedings*, 2nd Air Transport and Operations Symposium (ATOS), Delft, The Netherlands

Hartjes, S., Visser, H.G., Pavel, M.D. (2009),"Optimization of Simultaneous Non-Interfering Rotorcraft Approach Trajectories", *Conference Proceedings*, 35th European Rotorcraft Forum (ERF), Hamburg, Germany

Hartjes, S., Visser, H.G., Hebly, S.J. (2009), "Optimization of RNAV Noise and Emissions Abatement Departure Procedures", *Conference Proceedings*, AIAAs 9th Annual Aviation Technology, Integration and Operations (ATIO) Technical Forum and Aircraft Noise and Emissions Reduction Symposium (ANERS), Hilton Head, South Carolina, USA

Bibliography

[1] Clean Sky website, available at http://www.cleansky.eu, (Accessed 14 February 2013)

[2] Airbus, "Airbus Global Market Forecast 2012-2031", available at http://www.airbus.com/company/market/forecast/ (Accessed 14 February 2013)

[3] Boeing, "Boeing Current Market Outlook 2013-2032", available at http://www.boeing.com/boeing/commercial/cmo/ (Accessed 14 February 2013)

[4] Frost & Sullivan, "Global Civil Helicopter Market Growth Dynamics with Focus on Emergency Medical Services", available at http://www.slideshare.net/FrostandSullivan/global-civil-helicopter-market-growth-dynamics (Accessed 14 February 2013)

[5] Harrison, R., Stacey, S., Hansford, B. (2008), "BERP IV:The Design, Development and Testing of an Advanced Rotorblade", *Conference Proceedings*, 64th American Helicopter Society International Annual Forum, Montreal, Canada

[6] Rauch, P., Gervais, M., Cranga, P., Baud, A., Hirsch, J.-F., Walter, A., Beaumier, P. (2011), "Blue Edge^{TM}: The Design, Development and Testing of a New Blade Concept", *Conference Proceedings*, 67th American Helicopter Society Annual Forum, Virginia Beach, Virginia, USA

[7] Gervais, M., Gareton, V. (2011), "Analysis of Main Rotor Noise Reduction due to Novel Planform Design - The Blue Edge^{TM}Blade", *Conference Proceedings*, 37th European Rotorcraft Forum, Gallarate, Italy

[8] Mouille, R. (1970), "The Fenestron, Shrouded Tail Rotor of the SA. 341 Gazelle", *Journal of the American Helicopter Society*, **15**(4), pp. 31-37

[9] Sampatacos, E.P., Morger, K.M., Logan, A.H. (1983), "NOTAR: The Viable Alternative to a Tail Rotor", *Conference Proceedings*, AIAA Aircraft Design, Systems and Technology Meeting, Fort Worth, Texas, USA

[10] Group of Personalities (2001), "European Aeronautics: A Vision for 2020 - Meeting Society's Needs and Winning Global Leadership", Luxembourg: Office for Official Publications of the European Communities

[11] European Commission website, available at http://ec.europa.eu (Accessed 01 July 2013)

[12] Yin, J., Buchholz, H. (2007), "Toward Noise Abatement Flight Procedure Design: DLR Rotorcraft Noise Ground Footprints Model", *Journal of the American Helicopter Society*, **52**(2), pp. 90-98

[13] Le Duc, A., Spiegel, P., Guntzer, F., Lummer, M., Götz, J. (2008), "Modelling of Helicopter Noise in Arbitrary Maneuver Flight using Aeroacoustics Database", *Conference Proceedings*, 9th Onera-DLR Aerospace Symposium, Châtillon, France

[14] Spiegel, P., Guntzer, F., Le Duc, A., Buchholz, H. (2008), "Aeroacoustic Flight Test Data Analysis and Guidelines for Noise-Abatement-Procedure Design and Piloting", *Conference Proceedings*, 34th European Rotorcraft Forum, Liverpool, United Kingdom

[15] Guntzer, F., Spiegel, P., Lummer, M. (2009), "Genetic Optimization of EC-135 Noise Abatement Flight Procedures using an Aeroacoustic Database", *Conference Proceedings*, 35th European Rotorcraft Forum, Hamburg, Germany

[16] Olsman, W.J.F., Lummer, M. (2012), "Influence of Wind on the Noise Footprint of a Helicopter Landing", *Conference Proceedings*, 38th European Rotorcraft Forum, Amsterdam, The Netherlands

[17] Cruz, L., Massaro, A., Melone, S., D'Andrea, A. (2012), "Rotorcraft Multi-Objective Trajectory Optimization for Low Noise Landing Procedures", *Conference Proceedings*, 38th European Rotorcraft Forum, Amsterdam, The Netherlands

[18] Zhao, Y.J., Jhemi, A.A., Chen, R.T.N. (1996), "Optimal Vertical Takeoff and Landing Helicopter Operation in One Engine Failure", *Journal of Aircraft*, **33**(2), pp. 337-346

[19] Jhemi, A.A., Carlson, E.B., Zhao, Y.J., Chen, R.T.N. (2004), "Optimization of Rotorcraft Flight Following Engine Failure", *Journal of the American Helicopter Society*, **49**(2), pp. 117-126

[20] Jhemi, A.A., Zhao, Y.J., Chen, R.T.N. (1996), "Real-time Generation of Optimal Helicopter Trajectories for Cockpit Display", *Conference Proceedings*, AIAA 34th Aerospace Sciences Meeting and Exhibit, Reno, Nevada, USA

[21] Okuno, Y., Kawachi, K., Azuma, A., Saito, S. (1991), "Analytical Prediction of Height-Velocity Diagram of a Helicopter Using Optimal Control Theory", *Journal of Guidance, Control, and Dynamics*, **14**(2), pp. 453-459

[22] Okuno, Y., Kawachi, K. (1994), "Optimal Control of Helicopters Following Power Failure", *Journal of Guidance, Control, and Dynamics*, **17**(1), pp. 181-186

[23] Bottasso, C., Croce, A., Leonello, D., Riviello, L. (2004), "Optimization of Critical Trajectories for Rotorcraft Vehicles", *Conference Proceedings*, 64th American Helicopter Society Annual Forum, Baltimore, Maryland, USA

[24] Tsuchiya, T., Ishii, H., Uchida, J., Ikaida, H., Gomi, H., Matayoshi, N., Okuno, Y. (2009), "Flight Trajectory Optimization to Minimize Ground Noise in Helicopter Landing Approach", *Journal of Guidance, Control and Dynamics*, **32**(2), pp. 605-615

[25] Visser, H.G., Pavel, M.D., Tang, S.F. (2009), "Optimization of Rotorcraft Simultaneous Non-Interfering Noise Abatement Approach Procedures", *Conference Proceedings*, AIAA 47th Aerospace Sciences Meeting, Orlando, Florida, USA

[26] Visser, H.G., Wijnen, R.A.A. (2001) "Optimization of Noise Abatement Departure Trajectories", *Journal of Aircraft*, **38**(4), pp. 620-627

[27] Visser, H.G., Wijnen, R.A.A. (2003), "Optimisation of Noise Abatement Arrival Trajectories", *The Aeronautical Journal*, **107**(1076), pp. 607-615

[28] Wijnen, R.A.A., Visser, H.G., (2003), "Optimal Departure Trajectories with respect to Sleep Disturbance", *Aerospace Science and Technology*, **7**, pp. 81-91

[29] Visser, H.G. (2005), "Generic and Site-Specific Criteria in the Optimization of Noise Abatement Trajectories", *Transportation Research Part D: Transport and Environment*, **10**(5), pp. 405-419

[30] Hartjes, S., Visser, H.G., Hebly, S. (2010), "Optimisation of RNAV Noise and Emission Abatement Standard Instrument Departures", *Aeronautical Journal*, **114**(1162), pp. 757-767

[31] Betts, J.T. (1998), "Survey of Numerical Methods for Trajectory Optimization", *Journal of Guidance, Control, and Dynamics*, **21**(2), pp. 193-207

[32] Bryson, Arthur E. Jr., Ho, Yu-Chi (1975), "Applied Optimal Control: Optimization, Estimation and Control, Revised Printing", Levittown, PA: Taylor & Francis

[33] Pontryagin, L.S.,Boltyanskii, V., Gamkrelidze, R., and Mischenko, E. (1962), "The Mathematical Theory of Optimal Processes", New York: Interscience

[34] Huntington, G.T. (2007), "Advancement and Analysis of a Gauss Pseudospectral Transcription for Optimal Control", *Ph.D. Thesis*, Department of Aeronautics and Astronautics, Massachusetts Institute of Technology, Cambridge, Massachusetts, USA

[35] Betts, J.T. (1997), "SOCS Sparse Optimal Control Software", *Technical Report*, The Boeing Company, Seattle, Washington, USA

[36] Ross, I.M., Fahroo, F. (2004), "Pseudospectral Knotting Methods for Solving Optimal Control Problems", *Journal of Guidance, Control, and Dynamics*, **27**(3), pp. 397-405

[37] Fahroo, F., Ross, I.M. (2008), "Advances in Pseudospectral Methods for Optimal Control", *Conference Proceedings*, AIAA Guidance, Navigation and Control Conference and Exhibit, Honolulu, Hawaii, USA

[38] Gong, Q., Lewis, L.R., Ross, I.M., "Pseudospetral Motion Planning for Autonomous Vehicles", *Journal of Guidance, Control, and Dynamics*, **32**(3), pp. 1039-1045

[39] Rao, A.V., Benson, D.A., Darby, C.L., Patterson, M.A., Francolin, C., Sanders, I., Huntington, G.T. (2010), "Algorithm 902: GPOPS, A MATLAB Software for Solving Multiple-Phase Optimal Control Problems Using the Gauss Pseudospectral Method", *ACM Transactions on Mathematical Software*, **37**(2), pp. 22.1-22.39

[40] Garg, D., Patterson, M.A., Hager, W.W., Rao, A.V., Benson, D.A., Huntington, G.T. (2009), "A Unified Framework for the Numerical Solution of Optimal Control Problems Using Pseudospectral Methods", *Automatica*, **46**(11), pp. 1843-1851

[41] Benson, D.A. (2004), "A Gauss Pseudospectral Transcription for Optimal Control", *Ph.D. Thesis*, Department of Aeronautics and Astronautics, Massachusetts Institute of Technology, Cambridge, Massachusetts, USA

[42] Benson, D.A., Huntington, G.T., Thorvaldsen, T.P., Rao, A.V. (2006), "Direct Trajectory Optimization and Costate Estimation via an Orthogonal Collocation Method", *Journal of Guidance, Control, and Dynamics*, **29**(6), pp. 1435-1440

[43] Huntington, G.T., Benson, D.A., Rao, A.V. (2007), "Design of Optimal Tetrahedral Spacecraft Formations", *The Journal of the Astronautical Sciences*, **55**(2), pp. 141-169

[44] Huntington, G.T., Rao, A.V. (2008), "Optimal Reconfiguration of Spacecraft Formations Using a Gauss Pseudospectral Method", *Journal of Guidance, Control, and Dynamics*, **31**(3), pp. 689-698

[45] Huntington, G.T., Benson, D.A., How, J.P., Kanizay, N., Darby, C.L., Rao, A.V. (2007), "Computation of Boundary Controls Using a Gauss Pseudospectral Method", *Conference Proceedings*, Astrodynamics Specialist Conference, Mackinac Island, Michigan, USA

[46] Stamatiadis, S., Prosmiti, R., and Farantos, S.C. (2000), "AUTO_DERIV: Tool for Automatic Differentiation of a Fortran Code", *Computer Physics Communications*, **127**, pp. 343-355

[47] Garg, D., Patterson, M.A., Darby, C.L., Francolin, C., Huntington, G.T., Hager, W.W., Rao, A.V. (2009), "Direct Trajectory Optimization and Costate Estimation of General Optimal Control Porblems Using a Radau Pseudospectral Method", *Conference Proceedings*, AIAA Guidance, Navigation and Control Conference, Chicago, Illinois, USA

[48] Garg, D. (2011), "Advances in Global Pseudospectral Methods for Optimal Control", *Ph.D. Thesis*, University of Florida, Gainsville, Florida, USA

[49] Gill, P.E., Murray, W., Saunders, M.A. (2008), "User's Guide for SNOPT Version 7: Software for Large-Scale Nonlinear Programming", Department of Mathematics, University of California, San Diego, La Jolla

[50] Gill, P.E., Murray, W., Saunders, M.A. (2002), "SNOPT: An SQP Algorithm for Large-Scale Constrained Optimization", *SIAM Journal on Optimization*, **12**(4), pp. 979-1006

[51] Pavel, M.D. (2001), "On the Necessary Degrees of Freedom for Helicopter and WindTurbine Low-Frequency Mode Modeling", *Ph.D. Thesis*, Delft University of Technology, Delft, The Netherlands

[52] Drzewiecki, S. (1920), "Thorie gnrale de l'hlice", Paris: Gauthier-Villars et cie

[53] Glauert, H. (1926), "The Elements of Aerofoil and Airscrew Theory", Cambridge: Cambridge University Press

[54] Frost, W., Bowles, R.L. (1984), "Wind Shear Terms in the Equations of Aircraft Motion", *Conference Proceedings*, AIAA 22nd Aerospace Sciences Meeting, Reno, Nevada, USA

[55] Bennett, J.A.J. (1940), "Rotary Wing Aircraft", *Aircraft Engineering*, **12**(131-138), pp. 7-9, 40-42, 65-67, 109-112, 139-141, 174-176, 208-209, 237-241, 246

[56] Rindlisbacher, Th. (2009), "Guidance on the Determination of Helicopter Emissions", *FOCA Technical Report*

[57] Eurocopter (1993), "Bo-105 CB/CBS Approved Rotorcraft Flight Manual", Fourth issue

[58] Magliozzi, B., Metzger, F., Bausch, W., King, R.J. (1975), "A Comprehensive Review of Helicopter Noise Literature", *Technical Report*, FAA-RD-75-79

[59] Brentner, K.S., Farassat, F. (2003), "Modeling Aerodynamically Generated Sound of Helicopter Rotors", *Progress in Aerospace Sciences*, **39**(2-3), pp. 83-120

[60] Yang, C., Aoyama, T., Kondo, N., Saito, S. (2004), "Numerical Analysis of Interaction Noise Between Main Rotor and Tail Rotor of Helicopter", *Conference Proceedings*, 24th International Congress of the Aeronautical Sciences, Yokohama, Japan

[61] Yang, C., Aoyama, T., Kondo, N., Saito, S. (2009), "Numerical Analysis for Main-Rotor/Tail-Rotor Interaction of Helicopter", *JAXA Research and Development Report*, JAXX-RR-08-006E

[62] Gennaretti, M., Bernardini, G. (2006), "Aeroelastic Response of Helicopter Rotors Using a 3-D Unsteady Aerodynamic Solver", *The Aeronautical Journal*, **110**(1114), pp. 793-801

[63] Gennaretti, M., Bernardini, G. (2007), "Novel Boundary Integral Formulation for Blade-Vortex Interaction Aerodynamics of Helicopter Rotors", *AIAA Journal*, **45**(6), pp. 1169-1176

[64] Gennaretti, M., Bernardini, G. (2012), "Aeroacousto-elastic Modeling for Response Analysis of Helicopter Rotors", in Buttazzo, G., Frediani, A. (Eds.), "Variational Analyis and Aerospace Engineering: Mathematical Challenges for Aerospace Design, Springer Optimization and its Applications 66", New York: Springer Science+Business Media

[65] Bernardini, G., Serafini, J., Ianniello, S., Gennaretti, M. (2007), "Assessment of Computational Models for the Effect of Aeroelasticity on BVI Noise Prediction", *International Journal of Aeroacoustics*, **6**(3), pp. 199-222

[66] Piccione, E., Bernardini, G., Molica Colella, M., Gennaretti, M. (2011), "Structural and Aeroelastic Modeling of Curved Rotor Blades Using a Galerkin Approach", *Conference Proceedings*, 3rd CEAS Air & Space Conference - XXI AIDAA Congress, Venice, Italy

[67] Hodges, D.H., Dowell, E.H. (1974), "Nonlinear Equation for the Elastic and Torsion of Twisted Nonuniform Rotor Blades", *NASA Technical Note*, NASA TN D-7818

[68] Hodges, D.H., Ormiston, R.A. (1976), "Stability of Elastic Bending and Torsion of Uniform Cantilever Rotor Blades in Hover with Variable Structural Coupling", *NASA Technical Note*, NASA TN D-8192

[69] Ffowcs Williams, J.E., Hawkings, D.L. (1969), "Sound Generation by Turbulence and Surfaces in Arbitrary Motion", *Philosophical Transactions of the Royal Society of London, Series A, Mathematical and Physical Sciences*, **264**(1151), pp. 321-342

[70] Farassat, F. (1981), "Linear Acoustic Formulas for Calculation of Rotating Blade Noise", *AIAA Journal*, **19**(9), pp. 1122-1130

[71] Farassat, F., Brentner, K.S. (1988), "The Uses and Abuses of the Acoustic Analogy in Helicopter Rotor Noise Prediction", *Journal of the American Helicopter Society*, **33**(1), pp. 29-36

[72] Gopalan, G., Schmitz, F.H. (2003), "A Sensitivity Analysis of the Quasi-Static Acoustic Mapping of Helicopter Blade-Vortex Interaction (BVI) Noise During Slowly Maneuvering Flight", *Conference Proceedings*, 9th AIAA/CEAS Aeroacoustics Conference and Exhibit, Hilton Head, SC, USA

[73] Sabbatini, D., Janssens, K., Hartjes, S., Visser, H.G., Gennaretti, M., Bernardini, G. (2013), "Sound Synthesis Approach for Noise Annoyance Assessment of Rotorcraft Operations", *Conference Proceedings*, Noise-Con 2013, Denver, CO, USA

[74] Franke, S.J., Swenson, G.W. Jr. (1989), "A Brief Tutorial on the Fast Field Program (FFP) as Applied to Sound Propagation in the Air", *Applied Acoustics*, **27**(3), pp. 203-21

[75] Leontovich, M.A., Fock, V.A. (1946), "A Method for the Solution of the Propagation of Electromagnetic Waves along the Surface of the Earth", *Izvestiya Akademii Nauk SSSR*, **16**, pp. 557-582

[76] Gilbert, K.E., White, M.J. (1989), "Application of the Parabolic Equation to Sound Propagation in the Atmosphere", *Journal of the Acoustical Society of America*, **85**(2), pp. 630-637

[77] Salomons, E.M. (2001), "Computational Atmospheric Acoustics", Dordrecht: Springer Science+Business Media

[78] Spencer, G.H., Murty, M.V.R.K. (1962), "General Ray-Tracing Procedure", *Journal of the Optical Society of America*, **52**(6), pp. 672-676

[79] Ruijgrok, G.J.J. (1993), "Elements of Aviation Acoustics", Delft: Delft University Press

[80] Plovsing, B. (2006), "Nord2000. Comprehensive Outdoor Sound Propagation Model. Part 1: Propagation in an Atmosphere without Significant Refraction", Delta, no. AV1849/00

[81] Plovsing, B. (2006), "Nord2000. Comprehensive Outdoor Sound Propagation Model. Part 2: Propagation in an Atmosphere with Refraction", Delta, no. AV1851/00

[82] Boor, C. de (1978), "A Practical Guide to Splines", New York: Springer

[83] Lamancusa, J.S., Daroux, P.A. (1993), "Ray Tracing in a Moving Medium with Two-Dimensional Sound-Speed Variation and Application to Sound Propagation over Terrain Discontinuities", *Journal of the Acoustical Society of America*, **93**(4), pp. 1716-1726

[84] Chessell, C.I. (1977), "Propagation of Noise Along a Finite Impedance Boundary", *Journal of the Acoustical Society of America*, **62**(4), pp. 825-834

[85] Delany, M.E., Bazley, E.N. (1970), "Acoustical Properties of Fibrous Absorbent Materials", *Applied Acoustics*, **3**(2), pp. 105-116

[86] International Civil Aviation Organization (ICAO) (2008), "International Standards and Recommended Practices, Environmental Protection, Annex 16, Volume I, Aircraft Noise, Fifth Edition"

[87] Arntzen, M., Rizzi, S.A., Visser, H.G., Simons, D.G. (2012), "A Framework for Simulation of Aircraft Flyover Noise Through a Non-Standard Atmosphere", *Conference Proceedings*, 18th AIAA/CEAS Aeroacoustics Conference, Colorado Springs, CO, USA

[88] Engineering Sciences Data Unit (ESDU) (2004), "Prediction of Sound Attenuation in a Refracting Turbulent Atmosphere with a Fast Field Program", *ESDU Data Item*, ESDU 04011

[89] Suzuki, Y., Takeshima, H. (2004), "Equal-Loudness-Level Contours for Pure Tones", *Journal of the Acoustical Society of America*, **116**(2), pp. 918-933

[90] American National Standards Institute (2006), "American National Standard Specification for Sound Level Meters", ANSI S1.4-1983/ANSI S1.4A-1985

[91] American National Standards Institute (2011), "Design Response of Weighting Networks for Acoustical Measurement", ANSI/ASA S1.42-2001

[92] Federal Interagency Committee on Aviation Noise (1997), "Effects of Aviation Noise on Awakenings from Sleep"

[93] Ollerhead, J.B., Jones, C.J., Cadoux, R.E., Woodley, A., Atkinson, B.J., Horne, J.A., Pankhurst, F., Reyner, L., Hume, K.I., Van, F., Watson, A., Diamond, I.D., Egger, P., Holmes, D., McKean, J. (1992), "Report of a Field Study of Aircraft Noise and Sleep Disturbance", London: Civil Aviation Authority

[94] Fidell, S., Pearsons, K., Howe, R., Tabachnick, B., Silvati, L., Barber, D.S. (1994), "Noise-Induced Sleep Disturbance in Residential Settings", *Armstrong Laboratory Final Report*, AL/OE-TR-1994-0131

[95] Fidell, S., Pearsons, K., Howe, R., Tabachnick, B., Silvati, L., Barber, D.S. (1995), "Field Study of Noise-Induced Sleep Disturbance", *Journal of the Acoustical Society of America*, **98**(2), pp. 1025-1033

[96] Fidell, S., Howe, R., Tabachnick, B., Pearsons, K., Sneddon, M. (1995), "Noise-Induced Sleep Disturbance in Residences near Two Civil Airports", *NASA Technical Report*, NAS1-20101

[97] Integrated Aeronautical Information Package Netherlands, available at http://www.ais-netherlands.nl/aim/2013-04-18-AIRAC/eAIP/html/index-en-GB.html, (Accessed 11 June 2013)

[98] Newman, D., Wilkins, R. (1998), "Rotorcraft Integration into the Next Generation NAS", *Conference Proceedings*, 54th American Helicopter Society International Annual Forum, Washington, DC, USA

[99] Hogenhuis, R.H., Hebly, S.J., Visser, H.G. (2011), "Optimization of Area Navigation Noise Abatement Approach Trajectories", *Proceedings of the Institution of Mechanical Engineers, Part G: Journal of Aerospace Engineering*, **225**(5), pp. 513-521